



HAL
open science

High content cell imaging reveals actin cytoskeleton-mediated control of the immunological synapse

Yolla German

► **To cite this version:**

Yolla German. High content cell imaging reveals actin cytoskeleton-mediated control of the immunological synapse. Immunology. Université Paul Sabatier - Toulouse III, 2020. English. NNT : 2020TOU30015 . tel-02980214

HAL Id: tel-02980214

<https://theses.hal.science/tel-02980214>

Submitted on 27 Oct 2020

HAL is a multi-disciplinary open access archive for the deposit and dissemination of scientific research documents, whether they are published or not. The documents may come from teaching and research institutions in France or abroad, or from public or private research centers.

L'archive ouverte pluridisciplinaire **HAL**, est destinée au dépôt et à la diffusion de documents scientifiques de niveau recherche, publiés ou non, émanant des établissements d'enseignement et de recherche français ou étrangers, des laboratoires publics ou privés.

Université Fédérale



Toulouse Midi-Pyrénées

THÈSE

En vue de l'obtention du DOCTORAT DE L'UNIVERSITÉ DE TOULOUSE

Délivré par l'Université Toulouse 3 - Paul Sabatier

Présentée et soutenue par

Yolla GERMAN

Le 25 février 2020

**L'imagerie cellulaire à haut débit révèle le contrôle de la synapse
immunologique par le cytosquelette d'actine**

Ecole doctorale : **BSB - Biologie, Santé, Biotechnologies**

Spécialité : **IMMUNOLOGIE**

Unité de recherche :

CPTP - Centre de Physiopathologie de Toulouse Purpan

Thèse dirigée par

Loïc DUPRÉ et KAAN BOZTUG

Jury

M. Christophe LE CLAINCHE, Rapporteur

Mme Delphine MURIAUX, Rapporteur

M. Fernando SEPULVEDA, Rapporteur

Mme Maha AYYOUB, Examinatrice

M. Loïc DUPRE, Directeur de thèse

Acknowledgements.....	7
Summary.....	10
Résumé des travaux.....	12
Acknowledgements.....	14
Preface.....	17
Abbreviations.....	20
Figures and tables.....	23
Introduction.....	25
1. General overview of the immune system and immune cell activities.....	25
1.1 Innate immunity.....	27
1.2 Cells at the interphase of the innate and adaptive immune systems.....	27
1.3 Adaptive immunity.....	27
A. B lymphocytes.....	28
B. T lymphocytes.....	28
2. The cytotoxic function: the weapon of defense of the immune system.....	28
2.1 Natural killer cells.....	29
A. NK cell receptors.....	29
a. Natural cytotoxicity receptors.....	29
i. CD16.....	30
ii. NKp46.....	30
iii. NKp30.....	30
iv. NKG2D.....	31
v. NKp44.....	31
b. Inhibitory NK receptors (iNKR).....	32
c. Costimulatory molecules.....	32
B. NK cell cytotoxicity: from target binding to target lysis.....	33
a. NK receptors involved in immunological synapse formation.....	33

b.	NK cell degranulation	34
A.	Receptors, adhesion and co-stimulatory and inhibitory molecules involved in CD8+ T cell cytotoxicity	36
a.	The T-cell receptor	37
b.	The role of the integrin LFA-1 in cytotoxicity	39
i.	LFA-1 activation	39
ii.	Inside-out signaling	41
iii.	Outside-in signaling	41
	Costimulatory molecules	41
	Inhibitory molecules	42
B.	CD8+ T cell cytotoxicity: from naïve cells to professional killers	42
a.	Differentiation into professional killers	43
	CD8+ T cell cytotoxicity	44
2.3	Remodeling of the actin cytoskeleton governs the cytotoxicity of NK and CD8+ T cell cytotoxicity	45
2.4	Dynamic steps of cytotoxicity	46
A.	Cell migration	46
B.	The immunological synapse: the platform for cytotoxicity	47
a.	Immunological synapse of CD8+ T cells	47
b.	Immunological synapse of NK cells	49
3.	Cytotoxicity in the clinical context	51
3.1	Cancers	51
3.2	Autoimmunity	51
3.3	Primary immunodeficiencies	52
A.	Hemophagocytic lymphohistiocytosis	52
a.	Perforin deficiency (FHL2)	53
b.	Munc13-4 deficiency (FHL3)	53
c.	STX11 deficiency (FHL4)	54

d.	Munc18-2 deficiency (FHL5)	54
e.	Rab27a deficiency (Griscelli syndrome).....	55
f.	LYST deficiency (Chediak-Higashi syndrome).....	55
B.	Severe combined immunodeficiency	56
a.	B cell immunodeficiencies	56
b.	Innate immunodeficiencies	56
C.	PIDs related to defects in the actin cytoskeleton	56
a.	Wiskott Aldrich protein deficiency	57
b.	WASp Interacting protein deficiency.....	59
c.	ARHGEF1 deficiency	59
d.	WDR1 deficiency	60
e.	Coronin1A deficiency	61
f.	Ccd42 deficiency.....	63
g.	RhoA deficiency.....	63
h.	RhoH deficiency.....	63
i.	DOCK2 deficiency	64
j.	DOCK8 deficiency	64
k.	PSTPIP1 deficiency.....	66
l.	STK4 deficiency.....	66
m.	RASGRP1 deficiency	67
n.	MKL1 deficiency	68
o.	Moesin deficiency	68
p.	Rac2 deficiency	69
q.	Myosin deficiency	69
r.	ARPC1B deficiency	70
4.	Methodologies to assess defects in cytotoxicity	73
5.	Microscopy imaging of biological objects.....	74

5.1 The basics of microscopy	74
A. Light sources to illuminate a sample	74
B. From an object to an image.....	75
5.2 The timeline of microscopy in biology	76
5.3 High content imaging: A game changer.....	79
A. High content imaging: microscopy at a large scale	80
a. HCI screens may be used to define gene function.	81
b. HCI screens can be effective in determining gene interactions.	81
c. HCI screening is a useful tool to assess alterations to cell morphology in response to chemical compounds.	82
d. HCI screens are a powerful tool to image disease models.....	82
B. Instrumentation: High content imaging requires specialized devices.....	84
C. High content imaging analysis requires specialized software	86
a. CellProfiler.....	87
b. EBImage	87
D. Image analysis pipeline in high content imaging screens	88
a. Image analysis.....	89
b. Image quality control	89
c. Processing the extracted features	90
d. Dimensionality reduction.....	90
e. Single-cell data aggregation.....	91
f. Profile similarity measurement.....	91
g. Assay quality assessment.....	92
h. Downstream analysis and result interpretation	92
i. Linear dimensionality reduction: Principle component analysis	92
ii. Non-linear dimensionality reduction.....	93
a) Isomap.....	93

b) Diffusion map	93
c) t-distributed stochastic neighborhood embedding	93
d) Uniform manifold approximation and projection	94
E. Statistics	96
Implementation of a high content imaging pipeline to study the immunological synapse of cytotoxic lymphocytes	99
Rationale	99
Objectives	100
Results	101
1. Setting up assays in the NK-92 cell line	102
2. Setting up assays in primary NK cells.	104
3. High content imaging of the immunological synapse	107
Materials and methods: optimizations on NK-92 and primary NK cells	138
1. NK-92 cells	138
1.1 Migration	138
1.2 Conjugate formation kinetics	138
1.3 NK-92 – K562 conjugate assessment by microscopy	138
1.4 NK-92 cytotoxicity	139
1.5 TIRF microscopy	139
2. Primary NK cells	139
2.1 Primary NK cell expansion	139
2.2 Migration	139
2.3 Conjugate formation kinetics	140
2.4 Primary NK– K562 conjugate assessment by microscopy	140
2.5 Primary NK cell cytotoxicity	140
Discussion and perspectives	141
1. HCI as a methodological advance in imaging the immunological synapse assembly	142

2. HCI validates the role of the actin cytoskeleton in governing IS assembly	143
3. HCI coupled to robust statistics reveal important and sometimes unexpected IS morphological features	145
4. HCI could be indicative of a defect in the cytotoxic function	146
5. HCI of the immunological synapse reveals discrepancies in the regulation between cell lines and primary cells.	147
6. HCI reveals the lack of a standard “normal” or “disease” phenotype	148
7. HCI as a first step preceding functional assays	149
8. HCI of the immunological synapse as a useful tool in the field of personalized medicine	150
9. HCI could be the method study different functional steps of cytotoxicity	151
10. Limitations of HCI of the immunological synapse	153
References	155
Annexes	183
.....	184

Acknowledgements

This manuscript is the culmination of three years of doctoral studies, for which acknowledgments to various people are due. I apologize in advance if I have forgotten some people, who are nonetheless appreciated.

First, I would like to thank my supervisors: Drs Loïc Dupré and Kaan Boztug, without whom none of this would have been possible. Loïc, thank you for all your advice, help, support, the long hours and fruitful discussions, and for being a humane supervisor.

Drs Joerg Menche and Audrey Ferrand for their help and input in shaping the project.

My three reviewers Drs. Christophe Le Clainche, Delphine Muriaux and Fernando Sepulveda for taking the time to read this manuscript, advise and for agreeing to partake in the thesis jury, and Dr. Maha Ayyoub, the jury president.

A major thanks is due to Loan Vulliard, none of this would have been possible without your hard work, and the countless times you have helped me sort things out. Thank you for trying to make bioinformatics understandable for me, and for the much-appreciated occasional sarcasm.

The organoid platform of the IRSD, especially Aude Rubio, Muriel Quaranta-Nicaise and Dr. Isabelle Fernandes, for all the long hours spent acquiring, analyzing and transferring (and re-transferring) images, and for making me fall in love with the Opera Phenix.

The ladies of both the cytometry and microscopy platforms of the CPTP, for all your help not only during experiments but also your kind and encouraging words from the start until the very end. Drs Sophie Allart and Fatima L'faquih-Olive, you are strong, knowledgeable and amazing boss ladies. Danièle Daviaud and Fatima, thank you for always being extremely sweet and helpful. Anne-Laure Iscache, Valérie Duplan-Eche and Lydia De La Fuente, I cannot forget to thank you for the times you have come to “rescue” me at the cytometers. “Maître” Astrid Canivet-Laffitte, I really appreciate every time you have helped me with ImageJ.

A huge thank you to all the colleagues in both Dupré /Lesourne and Boztug teams in Toulouse and Vienna: Dr. Renaud Lesourne, thank you for your feedback, advice and comprehension.

Nelly Rouquié, Cui Yang and Suzanne Mélique, you have been amazing ladies all the way. To the past members and now Drs Gaëtan Blaize and Jeremy Argenty, as well as Aurélie Mougel, it was a pleasure being in the same team with you. To Claire, our most recent newcomer, thank you for you for your

company along experiments, and of course for taking care of my cells along with H el ene. Dr. H el ene Daniels, thank you for the discussions, advice and feedback.

I cannot thank each member of the big Boztug team individually, but a huge thanks to every member for their sweetness, help, and for making the 9 months I spent in Vienna so memorable. Dr Artem Kalinichenko and Jakob Huemer, thank you for always being up for discussing anything NK. Dr. Wojciech Garnarcz, you are a hero and no words can do you justice. Drs. Ana Krolo and Ozelm Yuce, you ladies are sweethearts. Ewa Lenartowicz, thank you for your kind and encouraging words, always. Dr. Johannes Pfeifenschneider, thank you for your sweetness and positive mood.

To the Valitutti team (Dr. Salvatore Valitutti, Dr. Eric Espinosa, Dr. Marie-Pierre Puissegur, recent Drs. Roman Jugel e and Yoan Eliasse, and Liza Filali Sabina Mueller), and the previous members of the Dupr e team (Drs. Javier Rey-Barroso and Ra issa Houmadi, and Alice Munaretto) thank you for making me feel welcome among you, your help, sweetness and support, and for making the beginning of this journey a bit easier. Every single one of you has helped me throughout this experience whether it was through advice, support or even words of encouragement over a coffee. To Dr. Delphine Guipouy, thank you for helping me with the French administration, sharing your knowledge with me, and answering my endless questions. Thank you infinitely Dr. Cat.

A special thank you to my colleagues Tala Shahin, Maximilian Rau, Laur ene Pfajfer and Marianne Guisset, colleagues who also became great friends. Afterall, it is friends who make some days more bearable.

The colleagues at CPTP who have given feedback and input to help better shape this project through listening to my presentations and advising. Moreover, thanks to Drs Anne Quillet-Mary, Ga el Menasch e and Abdelhadi Saoudi for their advice and feedback as part of my thesis committee.

An immense thank you to Dr. Nabila Jabrane-Ferrat for all her advice, support and help. You are the best “godmother” I could have asked for. I would also like to thank the NJF team: Drs Hicham El Costa (thank you for your encouragement through your sarcasm), Jordi Gouilly and Qian Chen, and finally the wonderful Ana Espino, also known as “my hero”.

To my friends in Toulouse and away, and my family and friends back in Lebanon who have been there for me throughout this journey. From the bottom of my heart I would like to thank Celine, Ranine and Elio, you have become a family away from home.

To my small family. Whatever I say, words will never be enough. To my adorable grandma whom I love beyond words, and who has always believed in me. To my little brother Georges, thank you for

always being by my side and for all your wise words and encouragement, and for always encouraging me to have faith in myself. To my Georges (the other special Georges in my life), I could not have done this without you, without your endless support and patience. I cannot thank you enough for being there every single day on this journey.

And finally, the most important people in this journey (and my life): my parents. Without you I could not be here today. Thank you for all the sacrifices you have made for me to be who I am and where I am. Thank you for your unconditional love and for always believing in me and making sure I knew it. I cannot possibly thank you enough for everything you have done for me. If superheroes existed, my parents would be ones. Everything I am and everything I will ever be, I owe to you. I love you beyond words and I am eternally grateful for you. Mom, dad, this (and everything I am and ever will be) is for you.

Summary

High content cell imaging reveals actin cytoskeleton-mediated control of the immunological synapse

Cytotoxic lymphocytes rely on actin cytoskeleton remodeling to achieve their function. In particular cytotoxic T lymphocytes and NK cells assemble the immunological synapse (IS), a complex actin-rich structure that allows the interaction with target cells, such as infected cells or tumor cells, and permits the polarized delivery of lytic granules. Although actin cytoskeleton remodeling is known to be a driving force of IS assembly and dynamics, our understanding of the molecular control of actin remodeling sustaining IS dynamics remains fragmented. This PhD project consisted in developing a high-content imaging approach to unbiasedly define the metrics of IS from human T and NK lymphocytes and to characterize the requirements for actin cytoskeleton integrity in organizing the IS architecture.

For that purpose, the stimulation and staining of cell lines and primary cells in multiwell plates and acquisition of a unique set of >100.000 confocal images with a fully automatized high-content imager was optimized. The images were analyzed with two complementary CellProfiler analytical pipelines to characterize the morphological features associated with different treatments and disease status. We first extracted 16 morphological features pertaining to F-actin, LFA-1 or lytic molecules based on prior knowledge of IS assembly, and included features pertaining to the nucleus. We show that IS assembly in Jurkat and NK-92 cells is characterized by increased F-actin intensity and cell area. For Jurkat cells, we report an increase in LFA-1 intensity and surface area, and for NK-92 cells an increase in lytic granule detection at the IS plane. We then treated NK-92 cells with seven drugs known to affect different aspects of actin dynamics and investigated the associated effects on IS features. We report concentration dependent effects, not only on F-actin intensity, as expected, but also on lytic granule polarization. Furthermore, using a high-resolution morphological profiling based on >300 features, we show that each drug inflicts distinct alterations of IS morphology. In a next step, we applied our experimental pipeline to primary NK cells isolated from the blood of healthy donors. Distinct morphological features were characterized among the NK cells from different donors, highlighting the sensitivity of our approach, but also revealing an unsuspected variability of immune cell morphologies among donors. We then further applied our approach to primary CD8⁺ T cells from patients with a rare immunodeficiency due to mutations in the gene encoding the actin regulator ARPC1B. ARPC1B deficiency results in decreased F-actin intensity, as well as in lytic granule polarization. This prompted us to assess the ability of these cells to kill target cells, which was markedly reduced. These results

illustrate how the systematic analysis of the IS might be used to assist the exploration of functional defects of lymphocyte populations in pathological settings.

In conclusion, our study reveals that although assembly of the IS can be characterized by a few features such as F-actin intensity and cell spreading, capturing fine alterations of that complex structure that arise from cytoskeleton dysregulation requires a high-content analysis. The pipeline we developed through this project holds promises for the morphological profiling of lymphocytes from primary immunodeficiency patients whose genetic defect has not yet been identified. Moreover, the discriminative power of our high-content approach could be exploited to characterize the response of lymphocytes to various stimuli and to monitor lymphocyte activation in multiple immune-related pathologies and treatment settings.

Résumé des travaux

L'imagerie cellulaire à haut débit révèle le contrôle de la synapse immunologique par le cytosquelette d'actine

Les lymphocytes cytotoxiques dépendent du remodelage du cytosquelette d'actine pour atteindre leur fonction. En particulier, les lymphocytes T cytotoxiques et les cellules NK assemblent la synapse immunologique (SI), structure complexe riche en actine qui permet l'interaction avec des cellules cibles et la distribution polarisée de granules lytiques (GL). Bien que le remodelage du cytosquelette d'actine soit connu pour être une force motrice de l'assemblage et de la dynamique de la SI, la compréhension du contrôle moléculaire du remodelage de l'actine soutenant la dynamique de la SI reste fragmentée. Ce projet de thèse a consisté à développer une approche d'imagerie à haut débit pour définir de manière impartiale les métriques de la SI des lymphocytes T et NK et caractériser les exigences d'intégrité du cytosquelette d'actine dans l'organisation de l'architecture de la SI.

À cette fin, la stimulation et coloration des lignées cellulaires et cellules primaires dans des plaques à puits multiples et l'acquisition d'un ensemble unique d'images confocales avec un imageur à haut contenu entièrement automatisé ont été optimisées. Les images ont été analysées avec deux pipelines complémentaires avec CellProfiler pour définir les caractéristiques morphologiques associées aux différents traitements et à l'état de la maladie. Nous avons d'abord extrait 16 caractéristiques morphologiques se rapportant à la F-actine, LFA-1 ou aux GL, sur la base d'une connaissance préalable de l'assemblage de la SI, et inclus des caractéristiques relatives au noyau. Nous montrons que l'assemblage de la SI dans les lignées est caractérisé par une augmentation de l'intensité de la F-actine et la surface cellulaire. Pour les cellules Jurkat, nous rapportons une augmentation de l'intensité et de la surface LFA-1, et de la de la détection des LG sur le plan SI pour les cellules NK-92. Le traitement des cellules NK-92 avec 7 drogues affectant différents aspects de la dynamique de l'actine et l'étude des effets associés sur les caractéristiques de la SI montrent des effets dépendants de la concentration sur l'intensité de l'actine et sur la polarisation des GL. De plus, un profilage morphologique à haute résolution basé sur > 300 caractéristiques montre que chaque drogue inflige des altérations distinctes sur la morphologie de la SI. Nous avons appliqué ce pipeline à des cellules NK primaires isolées du sang de donneurs sains. Des caractéristiques morphologiques distinctes définissent les cellules NK de différents donneurs, soulignant la sensibilité de notre approche, mais révélant également une variabilité insoupçonnée des morphologies des cellules immunitaires parmi les donneurs. Nous avons appliqué notre approche aux cellules T CD8+ primaires de patients présentant une immunodéficiences rare due à des mutations dans le gène codant pour le régulateur d'actine ARPC1B. La carence en ARPC1B entraîne une diminution de l'intensité de l'actine et de la polarisation des GL. Cela nous a incités à

évaluer la capacité lytique de ces cellules, qui a été considérablement réduite. Ces résultats illustrent comment l'analyse systématique de la SI pourrait être utilisée pour aider à l'exploration des défauts fonctionnels des populations de lymphocytes dans des contextes pathologiques.

En conclusion, notre étude révèle que, bien que l'assemblage de la SI puisse être caractérisé par quelques caractéristiques telles que l'intensité de l'actine et la propagation cellulaire, la capture de fines altérations résultant de la dérégulation du cytosquelette nécessite une analyse à haut débit. Le pipeline développé est prometteur pour le profilage morphologique des lymphocytes de patients atteints d'immunodéficiences primaires dont le défaut génétique n'a pas encore été identifié. De plus, le pouvoir discriminant de notre approche pourrait être exploité pour caractériser la réponse des lymphocytes à divers stimuli et surveiller leur activation dans de multiples pathologies et traitements.

Acknowledgements

This manuscript is the culmination of three years of doctoral studies, for which acknowledgments to various people are due. I apologize in advance if I have forgotten some people, who are nonetheless appreciated.

First, I would like to thank my supervisors: Drs Loïc Dupré and Kaan Boztug, without whom none of this would have been possible. Loïc, thank you for all your advice, help, support, the long hours and fruitful discussions, and for being a humane supervisor.

Drs Joerg Menche and Audrey Ferrand for their help and input in shaping the project.

My three reviewers Drs. Christophe Le Clainche, Delphine Muriaux and Fernando Sepulveda for taking the time to read this manuscript, advise and for agreeing to partake in the thesis jury.

A major thanks is due to Loan Vulliard, none of this would have been possible without your hard work, and the countless times you have helped me sort things out. Thank you for trying to make bioinformatics understandable for me, and for the much-appreciated occasional sarcasm.

The organoid platform of the IRSD, especially Aude Rubio, Muriel Quaranta-Nicaise and Dr. Isabelle Fernandes, for all the long hours spent acquiring, analyzing and transferring (and re-transferring) images, and for making me fall in love with the Opera Phenix.

The ladies of both the cytometry and microscopy platforms of the CPTP, for all your help not only during experiments but also your kind and encouraging words from the start until the very end. Drs Sophie Allart and Fatima L'faqihi-Olive, you are strong, knowledgeable and amazing boss ladies. Danièle Daviaud and Fatima, thank you for always being extremely sweet and helpful. Anne-Laure Iscache, Valerie Duplan-Eche and Lydia De La Fuente, I cannot forget to thank you for the times you have come to “rescue” me at the cytometers. “Maître” Astrid Canivet-Laffitte, I really appreciate every time you have helped me with ImageJ.

A huge thank you to all the colleagues in both Dupré /Lesourne and Boztug teams in Toulouse and Vienna: Dr. Renaud Lesourne, thank you for your feedback, advice and comprehension.

Nelly Rouquié, Cui Yang and Suzanne Mélique, you have been amazing ladies all the way. To the past members and now Drs Gaëtan Blaize and Jeremy Argenty, it was a pleasure being in the same team with you. To Claire, our most recent newcomer, thank you for you for your company along experiments, and of course for taking care of my cells along with Hélène. Dr. Hélène Daniels, thank you for the discussions, advice and feedback.

I cannot thank each member of the big Boztug team individually, but a huge thanks to every member for their sweetness, help, and for making the 9 months I spent in Vienna so memorable. Dr Artem Kalinichenko and Jakob Huemer, thank you for always being up for discussing anything NK. Dr. Wojciech Garnarcz, you are a hero and no words can do you justice. Drs. Ana Krolo and Ozelm Yuce, you ladies are sweethearts. Ewa Lenartowicz, thank you for your kind and encouraging words, always. Dr. Johannes Pfeifenschneider, thank you for your sweetness and positive mood.

To the Valitutti team (Dr. Salvatore Valitutti, Dr. Eric Espinosa, Dr. Marie-Pierre Puissegur, recent Drs. Roman Jugelé and Yoan Eliasse, and Liza Filali Sabina Mueller), and the previous members of the Dupré team (Drs. Javier Rey-Barroso and Raïssa Houmadi, and Alice Munaretto) thank you for making me feel welcome among you, your help, sweetness and support, and for making the beginning of this journey a bit easier. Every single one of you has helped me throughout this experience whether it was through advice, support or even words of encouragement over a coffee. To Dr. Delphine Guipouy, thank you for helping me with the French administration, sharing your knowledge with me, and answering my endless questions. Thank you infinitely Dr. Cat.

A special thank you to my colleagues Tala Shahin, Maximilian Rau, Laurène Pfajfer and Marianne Guisset, colleagues who also became great friends. Afterall, it is friends who make some days more bearable.

The colleagues at CPTP who have given feedback and input to help better shape this project through listening to my presentations and advising. Moreover, thanks to Drs Anne Quillet-Mary, Gaël Menasché and Abdelhadi Saoudi for their advice and feedback as part of my thesis committee.

An immense thank you to Dr. Nabila Jabrane-Ferrat for all her advice, support and help. You are the best “godmother” I could have asked for. I would also like to thank the NJF team: Drs Hicham El Costa (thank you for your encouragement through your sarcasm), Jordi Gouilly and Qian Chen, and finally the wonderful Ana Espino, also known as “my hero”.

To my friends in Toulouse and away, and my family and friends back in Lebanon who have been there for me throughout this journey. From the bottom of my heart I would like to thank Celine, Ranine and Elio, you have become a family away from home.

To my small family. Whatever I say, words will never be enough. To my adorable grandma whom I love beyond words, and who has always believed in me. To my little brother Georges, thank you for always being by my side and for all your wise words and encouragement, and for always encouraging me to have faith in myself. To my Georges (the other special Georges in my life), I could not have

done this without you, without your endless support and patience. I cannot thank you enough for being there every single day on this journey.

And finally, the most important people in this journey (and my life): my parents. Without you I could not be here today. Thank you for all the sacrifices you have made for me to be who I am and where I am. Thank you for your unconditional love and for always believing in me and making sure I knew it. I cannot possibly thank you enough for everything you have done for me. If superheroes existed, my parents would be ones. Everything I am and everything I will ever be, I owe to you. I love you beyond words and I am eternally grateful for you. Mom, dad, this (and everything I am and ever will be) is for you.

Preface

Having come from a background in microbiology and virology, immunology was not always the most evident of topics for me, as I had done my masters in a lab that worked on mice, where I had mostly done Western blots and Real-time PCR. The decision to embark on a PhD in immunology was quite the challenge for me, but the idea of putting in place a screen of cytotoxic cells by high content imaging sure was appealing. I began my PhD in the Dupré lab in January 2017, in the Valitutti team.

The team is an expert on cytotoxic cells, and the Dupré team is an expert on the immunological synapse of T cells, especially in the context of primary immunodeficiencies. At the time I joined, the Dupré team was composed of a postdoc: **Javier Rey-Barroso**, three PhD students: **Delphine Guipouy**, **Raissa Houmadi** and **Laurène Pfajfer**, and an engineer: **Alice Munaretto**.

Javier Rey-Barroso was passionate about motility and was studying the different migration patterns of B cell lines on Collagen and Fibronectin, as well as their ability to remain and individual cells or cluster based on the matrix. He did so by seeding these cells in 96 well plates and imaging them by TIRF microscopy. He also studied the roles of actin branching and actoMyosin contractility by using two drugs: the ROCK1 inhibitor Y-27632 and the ARP2/3 inhibitor CK-869. He also did live imaging of chemotaxis of B cells over a CCL19 gradient. Javier loved to perform his experiments and allowed me to observe, while giving me thorough explanations. Indeed, he was my first exposure to chemotaxis, as well as the potential that multiwell plates offer in terms of efficiently imaging cells under different conditions.

Alice Munaretto was also working on migration, but as opposed to Javier who was working on a B cell line, she was working on cells from CLL patients, to assess the migratory behavior of specific cell populations pre- and post-treatment. To do so, she was using a protocol of barcoding to phenotype her cells and was assessing their migration in response to chemokines. She did so by trans well assays, whose readout is by flow cytometry. Observing these experiments with Alice was my first exposure to flow cytometry. Moreover, to minimize bias in sample readout, Alice would set up an automatic sample mixing and acquisition, which was the first time I saw “automated” experiments.

Delphine Guipouy was in her last year of PhD when I met her. She was working on a specific type of cytotoxic Tregs referred to as ova-Tr1 T cells, that are capable of specific elimination myeloid target cells via their granzyme and granulysin. Delphine was highly passionate about cytotoxic cells, and she showed me how to set cytotoxicity assays in 96 well plate formats and how to analyze the results acquired by Flow cytometry. She also showed me how to perform live microscopy assays to assess cytotoxicity in real-time. Delphine also spoke to me about a killing experiment she had done in real-

time, by using a high content microscope (The Operetta), where she could sort single CD8+ T cells and seed one cell per well in a 96 well plate, to observe their cytotoxicity over time. She also showed me how to perform imaging of the immunological synapse of cytotoxic cells incubated with target cells, on microscopy slides.

Raissa Houmadi was also in her 3rd year of PhD, and she was working on developing a super-resolution microscopy approach. Indeed, she revealed how LFA-1 is spatially organized in nanoclusters and how this assembly is regulated by WASP to ensure proper granule docking in CD8+ T cells.

Laurène Pfajfer was a first year PhD student who was doing a part of her PhD at the LBI-RUD in Vienna, where she had worked on two primary immunodeficiencies: WIP and WDR1 to show how these defects lead to defective immunological synapse assembly and cytotoxicity.

Delphine, Raissa and Laurène, as well as Loïc's background in WASp and other primary immunodeficiencies provided me the exposure I needed to primary immunodeficiencies, and the immunological synapse.

In the context of primary immunodeficiencies, NK cells are sometimes overlooked in cell biological assays due to their low numbers and the difficulty to expand them. I fell in love with NK cells only by working with the NK-92 cell line, but I admired these cells for their cytotoxic potential. The journey with these cells was not easy and being the first in the lab to have to grow them and use them in experiments was not an easy challenge. For that I would like to thank Delphine Guipouy, for her advice, feedback and help.

Despite the challenges that these cells presented, the difficulty to transduce the NK-92 cell line, not due to lack of trying, and their fragility and erratic behavior sometimes, I am glad have been able to set up the functional approaches routinely used in our lab on CD8+ T cells on the NK cells, as well as an approach that allows the high content imaging of the immunological synapse of these poorly adherent cells. Our lab is an expert of CD8+ T cells and their cytotoxicity, as well as the defects in the context of primary immunodeficiencies.

Taken together, the expertise of my host team has led me to optimize several assays established in the lab on the NK-92 cell line and eventually primary NK cells, as well as being the first in our lab to put in place the protocol for conjugation assay, which has later on been applied by colleagues to expanded CD8+ T cells.

Most importantly, the past three years have led me to develop the protocol of high content imaging of the immunological synapse of NK-92 and Jurkat cell lines, as well as primary NK cells and expanded

CD8+ T cells from patients suffering from a primary immunodeficiency caused by mutations in the ARPC1B gene of the ARP2/3 complex.

This project would not have been possible without the help of the smart, dedicated and through bioinformatician Loan Vulliard, whose expertise has helped take this project to the next level. I was lucky to have been able to work closely with Loan during my 9-month stay at the Center for Molecular Medicine in Vienna, as a guest scientist in the Boztug team.

Prior to the results section, I will briefly introduce the immune system, with a focus on cytotoxic cells and highlighting the role of the actin cytoskeleton and the immunological synapse in achieving the cytotoxic function. The second part will address dysregulations that can affect the cytotoxic functions, while focusing particularly on primary immunodeficiencies where the cytotoxic function is perturbed. The last part will comprise information of the various types of microscopy approaches, with a focus on high content imaging.

In the coming pages I hope to be able to highlight the importance of the cytotoxic function, as well the importance of the immunological synapse in this context. I also hope to convince the people reading this manuscript that high content imaging is the revolutionary step that they should invest in, and that, with some effort, even poorly adherent cells are amenable to being imaged with this method. Most importantly, I hope to shed light on the importance of morphology in predicting disease.

Abbreviations

ADP: Adenosine diphosphate

APC: Antigen presenting cell

ATP: Adenosine triphosphate

BCR: B cell receptor

CTL: Cytotoxic T lymphocyte

CTLA: Cytotoxic T lymphocyte antigen

Coro1A: Coronin 1A

DC: Dendritic cell

DIC: Differential interference contrast

F-actin: Filamentous actin

FRAP: fluorescence recovery after photobleaching

FRET: Förster resonance energy transfer

GBD: G protein binding domain

GDP: Guanine diphosphate

GFP: Green fluorescent protein

GTP: guanine triphosphate

Gzm: Granzyme

HCI: High content imaging

hESC: Human embryonic stem cells

HLA: Human leukocyte antigen

HLH: Hemophagocytic lymphohistiocytosis

ICAM: Intracellular adhesion molecule

IFN- γ : Interferon gamma

Ig: Immunoglobulin

IL: Interleukin

ILC: Innate lymphoid cell

IS: Immunological synapse

KD: Knock-down

LAT: Linker for activation

LED: Light emitting diode

LFA-1: Lymphocyte function associated antigen 1

ITAM: Immune tyrosine-based activating motif

KIR: Killing inhibitory receptor

mAb: Monoclonal antibody

MHC: Major histocompatibility complex

MSN: Moesin

MTOC: Microtubule organizing center

mp-value: multidimensional perturbation value

MyH: Myosin heavy chain

NCR: Natural cytotoxicity receptor

NK: Natural killer cell

NKT: Natural killer T cell

ORF: Open reading frame

PALM: Photo-activated-localization microscopy

PCA: Principal component analysis

PD-1: Programmed cell death protein 1

PID: Primary immunodeficiency

PSTPIP1: Proline-serine-threonine phosphatase-interacting protein 1

Rac2: Ras-related C3 botulinum toxin substrate 2

SCID: Severe combined immunodeficiency

SMAC: Supramolecular activation cluster

STED: Stimulated emission depletion microscopy

TCR: T cell receptor

Th: T helper cell

TIRF: Total internal reflection fluorescence

TNF: Tumor necrosis factor

t-SNE: t-distributed stochastic neighborhood embedding

UMAP: Uniform manifold approximation and projection

VLA: Very late after activation

WAVE: WASp family-Verprolin homologous protein

WASp: Wiskott-Aldrich Syndrome Protein

WDR1: WD repeat 1 gene

WIP: WASp interacting protein

Figures and tables

Figure 1: Overview of the immune system

Figure 2: Natural killer cell surface receptors involved in cytolytic activity, and their association to signaling molecules

Figure 3: Schematic representation of T cell activation and differentiation in response to APC stimulation

Figure 4: The TCR and its association with CD3

Figure 5: Pathways of TCR signal transduction

Figure 6: Changes undergone by CD8⁺ T cells before/after infection

Figure 7: Schematic representation of the different components of the LFA-1 molecule in its different conformations

Figure 8: Overview of families of actin-binding proteins involved in the different processes pertaining to actin

Figure 9: Dynamic steps of cytotoxicity

Figure 10: Top view model of the spatial organization of the immunological synapse

Figure 11: NK cells from STX11 deficient patients do not fail to polarize their perforin granules to the IS

Figure 12: NK cells from a normal donor and an STXBP2 deficient patient stained for F-actin and perforin reveal a normal granule polarization in patient cells

Figure 13: Wiskott–Aldrich syndrome protein activation, molecular partners, and cytoskeleton remodeling

Figure 14: The role of Coronin1A in the immunological synapse of NK cells

Figure 13: DOCK8 suppression leads to diminished F-actin and lytic granules at the IS

Figure 16: Defective RASGRP1-deficient NK cell IS assembly

Figure 17: Crystal structure of the ARP2/3 complex from *Bos taurus* access protein data bank:1K8K

Figure 18: PID-associated actin regulators

Figure 19: The timeline of microscopy

Figure 20: A typical high-content workflow pipeline

Figure 21: Schematic representation of the confocal light path of the Opera Phenix high content screening system.

Figure 22: Representative workflow for image-based cell profiling

Figure 23: Visualization of 6000 handwritten digits from the MNIST data set by t-SNE

Figure 24: Visualization of 6000 handwritten digits from the MNIST data set by UMAP

Figure 24: Functional assays on the NK-92 cell line

Figure 25: Functional assays on primary NK cells

Table 1: HLH classification, causes and underlying defects

Table 2: Main criteria used in the assessment of a defective immunological synapse in cytotoxic lymphocytes by immunofluorescence.

Introduction

The following pages will comprise an introduction on the immune system with a focus on cytotoxic lymphocytes, their mechanism of action and receptors. In particular, the role of the actin cytoskeleton rearrangements and the immunological synapse in supporting cytotoxicity will be presented. Next, pathology-related defects in cytotoxicity will be addressed with a focus on primary immunodeficiencies, including a chapter on the methodologies used to assess defects in the cytotoxic function.

The second section of the introduction will focus on microscopy as a rapidly evolving collection of methodologies. In particular will be addressed how high content cell imaging applications provide novel opportunities to explore cell biology. This introduction will then provide a rationale for the implementation of high content cell imaging for the study of cytotoxic lymphocytes.

1. General overview of the immune system and immune cell activities

The human immune system is composed of a complex association of lymphoid organs, tissues, cells, humoral and soluble factors, which evolve simultaneously with the environment the body is exposed to, to ensure its protection against pathogens. Moreover, the immune system ensures the elimination cancer cells, as well as ensuring tissue reparation to maintain homeostasis. Also, it ensures symbiosis with the microorganisms of the microbiota.

For long, the immune system has been divided into innate and adaptive immunity, due to the types of cells involved, as well the specificity and duration of their effector function. However, research is showing that cells of both types are highly interconnected. Therefore, an increasing number of immune cells is to be found at the interface between the innate and the adaptive immunity (Figure 1).

Innate immunity

Adaptive immunity

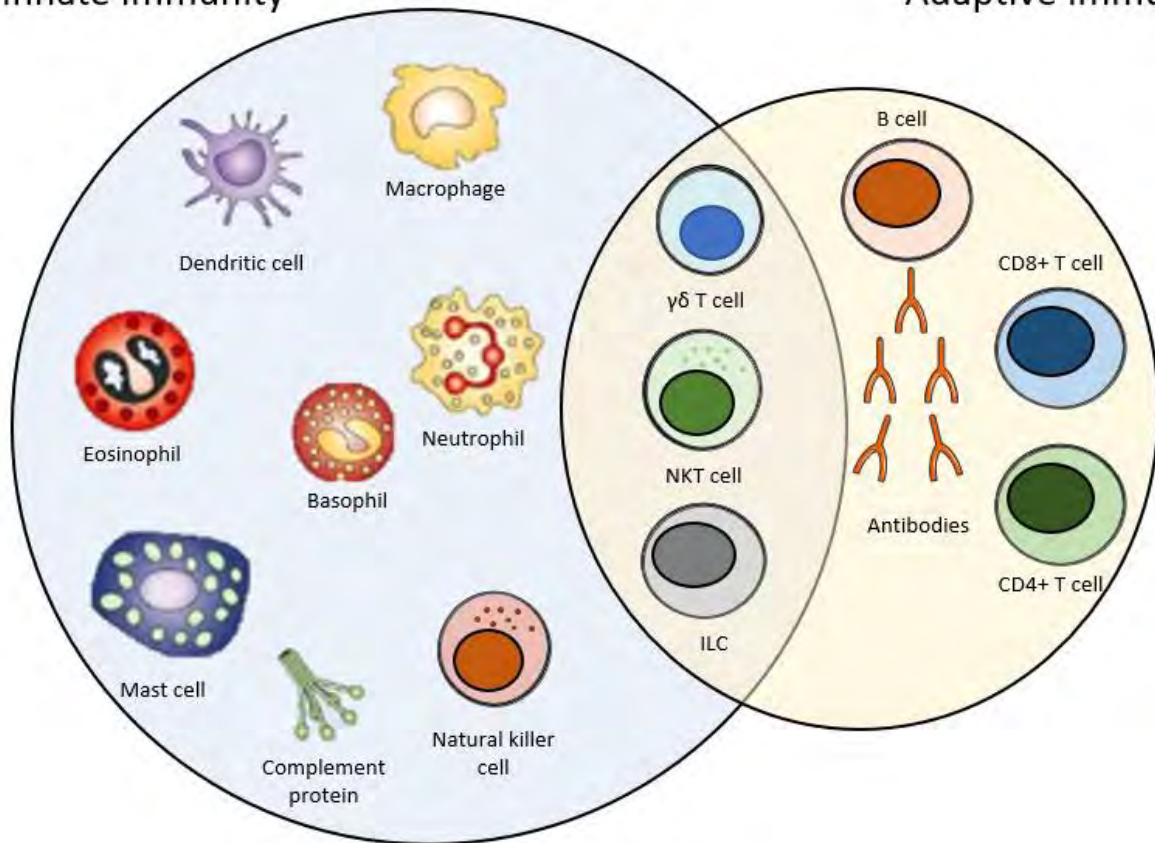


Figure 1: Overview of the immune system. The immune system is composed of the innate arm, the adaptive arm and cells at the interface of both arms. Adapted from¹.

1.1 Innate immunity

Innate immunity is a quick reaction which follows a non-specific recognition of various microorganisms, and can take as little as a few hours to be put in place². The cells implicated are tissue resident natural killer cells, macrophages, mast cells, monocytes, neutrophils, basophils, eosinophils and dendritic cells (DC). However, only natural killer (NK) cells will be detailed in a section of this manuscript.

1.2 Cells at the interphase of the innate and adaptive immune systems

Innate lymphoid cells (ILC) are a new category of cells which were discovered in the past decade. Three groups of ILCs exist, based on the expression of transcription factors and cytokines that they produce³. NK cells were officially classified as the prototypical members of the group 1 innate lymphoid cells (ILC), which are defined by capacity to secrete interferon gamma (IFN- γ), but not type 2 cytokines⁴. **Natural killer T** (NKT) cells, which share surface markers of both natural killer and T cells. They express a semi-invariant receptor resembling that on T cells and which reacts with major histocompatibility complex (MHC) CD1d, as well as receptors present on NK cells such as CD161⁵. NKT cells are both cytotoxic cells and capable of releasing cytokines, such as IFN- γ , IL-4, IL-10 and IL-13. **T $\gamma\delta$** cells are CD3⁺ T cells that express the gamma/delta alternative T cell receptor (TCR) (as opposed to the conventional alpha/beta). They are cells that produce cytokines and exert a cytotoxic activity. They recognize bacterial phosphoantigens and non-classical MHCI molecules, and in response can either exhibit cytotoxicity or secrete cytokines such as IFN- γ ⁶⁻⁸.

1.3 Adaptive immunity

Adaptive immunity requires a longer time to take place than innate immunity, as it requires the action of antigen-specific cells, some of which would eventually become memory cells. Such a process requires several days to be put in place². The players in this immune response are T and B lymphocytes.

However, and as previously mentioned, innate and adaptive immune responses are interconnected. An adaptive immune response cannot be initiated without the dendritic cells, which are antigen presenting cells (APC). DCs will migrate into the lymphoid organs, where they will activate the T cells specific to their antigen. Through V(D)J rearrangements through their development, T cells would be endowed with unique and antigen specific TCR^{9,10}.

A. B lymphocytes

B cells are CD19⁺ lymphocytes. B lymphocytes recognize specific antigens by B cell receptors (BCR) or membrane bound immunoglobulins. BCRs recognize either soluble foreign antigens or ones bound to cell surface. Antigens are then internalized and processed in lysosomal/endosomal compartments, and subsequently expressed on the cell surface as antigenic peptides bound to MHC-II molecules for presentation to T helper cells (discussed in the next section). Activated B cells develop into plasma cells, which are antibody secreting cells.

B. T lymphocytes

T cells are CD3⁺ cells that can also be CD4⁺ or CD8⁺. **CD4⁺ T** cells are known as helper T (Th) cells and can be further subclassified into Th1, Th2 and Th17, based on the cytokines and interleukins they produce. Special subsets include follicular helper T cells (Tfh) and regulatory T cells (Treg). Their main role is aiding in B cell activation and antibody production. Follicular helper T cells are essential for B cells to mature into plasma cells and achieve proper immune functions¹¹. Regulatory T cells suppress immune reactions and maintain immune homeostasis. **CD8⁺ T** cells were thought to be the only cytotoxic cells, prior to the identification of a subpopulation of cytotoxic CD4⁺ T cells¹². CD8⁺ T cells are cytotoxic T cells (CTLs) and will be discussed in detail in the next section.

2. The cytotoxic function: the weapon of defense of the immune system

Natural killer cells and CD8⁺ T cells are two cell types belonging to the innate and the adaptive arms of the immune system respectively. Even though they, broadly speaking, appear to serve the same function, which is to eliminate target cell, their mechanism of action, cell surface receptors and regulation are not the same, and will be elaborated in detail in this section. The cytotoxic activity of NKT, T γ δ and cytotoxic CD4⁺ T cells will not be addressed.

Cytotoxicity is achieved when the cytotoxic cells kill their targets by the means of releasing lytic molecules through the process of degranulation. CD8⁺ T cells and NK cells can kill target cells by a tightly regulated secretion of cytotoxic granules containing pore-forming proteins perforin and/or granulysin and combinations of granzyme (Gzm) family effector proteases (in humans: Gzm A, B, K, M and H). However, a deep immune profiling of CTLs and NK cells has shown that NK cells have more abundant granulysin than CTLs¹³.

Lytic granules are delivered to the interface of the cytotoxic lymphocyte and target cell, and their exocytosis requires clearances in the actin cytoskeleton¹⁴. Released perforin monomers insert into the

target cell membrane and polymerize to form a pore through which granule contents including the effector protease enzymes are delivered, and subsequently cleave caspases to initiate cell death.

2.1 Natural killer cells

Natural killer cells are cytotoxic lymphocytes of the innate immune system, and which play a role in protection against viral infections and solid and hematological malignancies. They comprise about 10-15% of circulating lymphocytes. For a long time, NK cells were simply identified as cytotoxic cells that could kill without prior activation. They specifically target cells that lack MHC-I expression, without expressing clonally-distributed antigen receptors¹⁵. Moreover, they release cytokines that cause an inflammatory response which mediate the response of the adaptive immune system. Further details on the cytotoxic activity of NK cells will be addressed in the next chapter, “cytotoxicity”.

Two major markers to characterize natural killer cells are CD16 and CD56. That being said, it should be noted that approximately 90% of natural killer cells are CD16^{bright} CD56^{dim} and those are the ones capable of generating the cytolytic response, also known as antibody-dependent cellular cytotoxicity (ADCC)¹⁶. The other 10% are CD16^{dim} CD56^{bright} and are the ones that secrete cytokines. When it comes to expression of lytic molecules, among NK cells, CD56^{bright} and CD56^{dim} CD16+ NK cells showed clearly different cytotoxic molecule expression patterns: CD56^{bright} NK cells had low Gzm B, but high Gzm K expression, whereas the CD56^{dim} CD16+ NK cell subset expressed high Gzm B but lacked Gzm K¹³.

The cytotoxic activity of NK cells is tightly regulated by a complex interplay between stimulatory and inhibitory receptors and their ligands expressed on the target cells, which will be discussed in the coming section^{17,18}.

A. NK cell receptors

Natural killer cells receive signals through different receptors on target cells and use a multiple receptor recognition strategy and will kill cells that have an increased or a decreased expression of “self” proteins, and cells that express foreign proteins.

a. Natural cytotoxicity receptors

Natural cytotoxicity receptors (NCR) are key in recognizing virus infected and tumor cells and their clearance. The expression of these NCRs has been shown to correlate with the magnitude of the cytolytic activity of the NK cells.

i. CD16

CD16 is an Fc receptor (FcγIII) present on the CD56^{dim} population of the natural killer cells. Signaling through CD16 delivers a powerful signal that enables the natural killer cells to kill target cells mainly by cytolysis. CD16 binds to the IgG portion of antibodies. In NK cells, CD16A is expressed and co-localizes with CD3ζ and Fc-εRI-γ, thus inducing the stimulatory signals. CD16 activation following binding to its ligand induces the transcription of the genes encoding interleukin-2 receptor (IL-2R) and cytokines, and even though binding to anti-CD16 induces a strong cytolytic reaction, it does not lead to NK cell proliferation^{19,20}. Moreover, it has been shown that the levels of expressions of CD16 may vary, and this variation correlates with the strength of serial killing²¹.

ii. NKp46

NKp46 (also known as CD335) is a member of the natural cytotoxicity receptor family, and is, along with NKG2D, one of the main receptors. In 1997, a 46 kDa molecule was shown to play a role in NK mediated cytolytic activity, cytokine secretion as well as Calcium ion mobilization²². NKp46 is encoded in the leukocyte receptor complex on chromosome 19^{23,24}. NKp46 has been shown to be expressed on subsets of natural killer cells, while it was not expressed in T and B cells²⁵. NKp46 expression was shown to be decreased in post-transplant lymphoproliferative disease in all natural killer subsets, accompanied by an increase in programmed cell death protein 1 (PD-1), which may give a hint on the dysregulation in natural killer functions²⁶. Cross-linking of NKp46 with a monoclonal antibody (mAb) resulted in an increase in cytolytic activity, cytokine secretion and Calcium ion mobilization. NKp46 molecules are coupled to intracytoplasmic transduction machinery through associating with CD3ζ and Fc-εRI-γ adaptor proteins that contain immune tyrosine-based activating motifs (ITAM).

iii. NKp30

NKp30 is encoded in the class III region of the MHC locus on chromosome 6²⁴. It has been demonstrated that NKp30 expression varies depending on the organ in which NK cells are examined: it is highest in spleen, lowest in liver and intermediate in blood, despite the absence of a general receptor down-regulation, thus suggesting either an organ-specific regulation of NKp30 receptors, or a preferential homing of NKp30+ NK positive cells²⁷. Expression of the ligands of NKp30 on DCs is the main regulator of the supply of dendritic cells, as NKp30 can mediate the promotion or termination of dendritic cell maturation. One of the ligands of NKp30 is BAG6. Soluble BAG6 has been shown to be present in elevated levels in patients with hematological diseases^{28,29}. Galectin-3 has also been shown to be a soluble NKp30 target, and to play a role in tumor evasion from NK cells³⁰. B7-H6,

another soluble NKp30 ligand was shown to be associated with a down-regulation of NK cells in neuroblastoma patients³¹. Another NKp30 ligand is BAT6, a nuclear factor also released by tumor cells in exosomes rather than a soluble protein, which triggers cytokine release (tumor necrosis factor alpha (TNF- α), IFN- γ) and enhances NK-cell mediated killing^{27,32}. The cytoplasmic region of NKp30 lacks ITAM motifs.

iv. NKG2D

NK receptor member D of the lectinlike receptor family (NKG2D) is a natural killer receptor that binds to cells which have an upregulated expression of self-proteins. It is also expressed on CD8+ T cells, $\gamma\delta$ T cells and Natural Killer T cells^{33,34}. NKG2D binds to NKG2D-L on target cells, thus activating an effective anti-tumor response in early stages³⁵. However, a sustained NKG2D-L expression and shedding of soluble ligands counteracts NKG2D-dependent NK cell activity in later stages. Contrary to NKG2A, NKG2D does not bind to CD94. The ligand for NKG2D is stress-inducible MICA, a distant homolog MHC I, and the expression of NKG2D on NK cells is increased by IL-15^{34,36}. The structures of NKG2D–ligand complexes indicate that NKG2D binds diagonally over the $\alpha 1$ and $\alpha 2$ helices of the ligands, which bears a striking resemblance to the way T-cell receptors bind over MHC molecules. DAP10 is the membrane-bound signal transducing subunit of the NKG2D receptor³⁷. It has been shown that one tumor evasion mechanism is the release of soluble NKp30 and NKG2D ligands, as well as a down-regulation of the expression of NCR ligands^{38,39}.

v. NKp44

NKp44 is another member of the NCR family, and is about 44 kDa in size. The gene encoding NKp44 is encoded on chromosome 6. While NKp30 and NKp46 are expressed on resting and activated NK cells, NKp44 is exclusively expressed on activated NK cells in the presence of IL-2⁴⁰. NKp44 ligands include glycoproteins and proteoglycans expressed on the surface of target cells, nuclear proteins that can be exposed outside the cell, and molecules that can be either soluble or in vesicles⁴¹. In the same fashion as NKp46, monoclonal antibody cross-linking of NKp44 enhances the cytolytic activity of NK cells. NKp44, which does not contain any ITIM motif in the cytoplasmic region, associates with the adaptor molecules DAP12 and KARAP, which contain an ITAM motif in the cytoplasmic region^{40,42}.

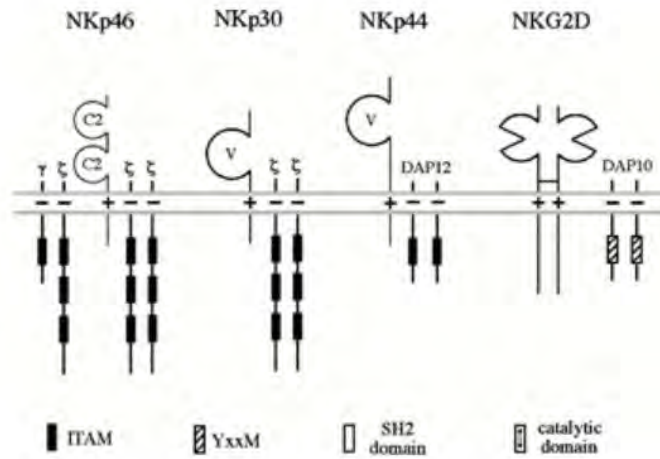


Figure 2: Natural killer cell surface receptors involved in cytolytic activity, and their association to signaling molecules²⁴.

b. Inhibitory NK receptors (iNKR)

Regulation of the cytotoxicity of NK cells is also a crucial process and depends on killing inhibitory receptors (KIR), whereby the signals that NK cells receive completely bring their cytolytic activity to a halt. It has been shown that inhibiting the cytolytic activity of NK cells depends on the recognition of MHC-I molecules. Killer Ig-like KIR and NKG2A/B (heterodimer with CD94) are major human leukocyte antigen I (HLA-I) specific inhibitory receptors. The CD94/NKG2A/B recognize the HLA-E molecule (a non-classical MHC-Ib) and subsequently protect the target cells from cytolysis⁴³. KIRs include but are not limited the p49, p50, p58, p70 and p140^{17,38}. However, each KIR is expressed on a fraction of NK cells, thus allowing the NK cells to recognize a larger pool of MHC-I deficient cells. It has been shown that once an NK cell is in contact with an MHC-I expressing cell, KIRs accumulate at the contact area in a central area surrounded by LFA-1 and ICAM-1 to drive NK cell migration⁴⁴. F-actin is a somewhat expendable player in this process, whereby it can accelerate KIR recruitment to the synapse but is not crucial for this process⁴⁴.

c. Costimulatory molecules

2B4 (CD44) which binds to CD48, and NTBA are two members of the CD2 family which can play either an activating or inhibitory function, depending on the availability of downstream regulating element of the signaling pathway termed signaling lymphocyte activation molecule-associated protein (SAP). Both 2B4 and NTBA trigger NK cytolytic activity in cells that express high levels of NCRs^{45,46}. NTBA promotes a strong production of IFN- γ and TNF- α ^{46,47}. 2B4 may also enhance the cytolytic activity of NK cells⁴⁸. 2B4 does not associate with ITAM-bearing polypeptides but has functional

signaling motifs in the intracellular domain. The 2B4-CD48 interactions appear to take place at the center of the synapse⁴⁴. Sivori and colleagues have shown that 2B4 can initiate cytolysis in the subset of NK cells that have a high level of NKp46 expression, without altering the expression of 2B4, but also that 2B4 may function as an inhibitory molecule at early stages of NK cell differentiation^{49,50}. Other co-stimulatory molecules include CD80 and CD86, which have been shown to enhance the cytotoxic activity of NK cells⁵¹.

B. NK cell cytotoxicity: from target binding to target lysis

Natural killers were long compared to cytotoxic T cells. However, they are unique in the sense that they use specific NK receptors, and that their response is faster than that of CTLs. Being part of the innate immune system, natural killer cells do not need prior activation to achieve their cytotoxic function. Therefore, they do not express antigen-specific receptors, but rather the activation and inhibition receptors discussed in the previous chapter “NK cell receptors”. The cytotoxicity of NK cells can be broken down into several steps, leading to the formation of the immunological synapse (IS) and achievement of the cytotoxic function by release of lytic molecule content, and then detachment of scanning for another target cell.

a. NK receptors involved in immunological synapse formation

NK cell receptors can associate with ITAM bearing molecules. FcR γ and TCR ζ chains can form either homodimers or heterodimers which interact with CD16. NKp30 and NKp46 associate with FcR γ and TCR ζ , while NKG2D associates with DAP10⁵². After patrolling their environment, NK cells attach to a target cell through adhesion receptors, which include CD2, NKG2D and DNAM-1. By using tweezers and confocal microscopy, it has been demonstrated that upon NK cell contact with its target, NKG2D is recruited to the IS and forms a ring type of structure which marks a border in which lytic granules are secreted⁵³. Moreover, stimulation through NKG2D was shown to lead to the formation of an F-actin ring at the periphery of the IS, and that NKG2D leads to a more stable synapse than CD16^{21,53}. NKp44 associated with DAP12, a homodimer with a single ITAM motif. While signaling through CD16 is sufficient to cause NK cell – target conjugates and degranulation, stimulation of other receptors alone does not cause NK degranulation^{21,54,55}. Other receptors only stimulate degranulation in pairs, suggesting a synergistic activation. CD16 binds to the Fc portions of antibodies and NK cells can therefore kill target cells coated with antibodies and eliminate them by ADCC. NKG2D signaling

leads to adhesion, granule polarization and degranulation⁵⁶. DNAM-1, NKp80 and NKp65 also have activating potential. However, there is limited information of their signaling properties. The immunological synapse of NK cells will be touched upon further in the section pertaining to the steps of cytotoxicity.

b. NK cell degranulation

Degranulation of NK cells is not random process, and it has been shown that NK cells must converge their lytic granules to prevent bystander killing and achieve a more efficient elimination of target cells⁵⁵. Moreover, it has been shown that receptor activation must occur in a specific sequence, as initial engagement of CD16 did not affect subsequent stimulation via NKG2D, whereas stimulation through CD16 was impaired after activation via NKG2D²¹. Once firmly tethered to its target, the NK cell undergoes a change in shape and becomes more flattened, and a lytic cleft is formed⁵⁷. Following actin rearrangement as well as *de novo* actin synthesis, the MTOC undergoes reorientation to allow polarization of the lytic granules towards the synapse, and this is mediated by the formin homolog hDia, which in NK cells is not essential for actin branching⁵⁸.

DNAM-1 has been found to physically associate with lymphocyte function associated antigen 1 (LFA-1), thus indicating that it plays a role in LFA-1 mediated signaling⁵⁹. Indeed, LFA-1 engagement was shown to mediate granule convergence, and to induce more targeted degranulation at the IS, along with CD16 than CD16 alone⁵⁵. Therefore, the co-engagement of LFA-1 and CD16 leads to a monodirectional granule convergence, thereby reducing bystander killing rates and increasing the rates of specific killing. Only a small fraction express the open conformation of LFA-1, and LFA-1 in NK cells requires activation to through the aforementioned adhesion receptors, which can induce inside-out signaling⁶⁰. LFA-1 induces a downstream signaling cascade, changes in F-actin reorganization, as well as an arrest signal and symmetrical spreading⁶¹. Talin is also recruited to the sites of LFA-1 prior to granule polarization, and, via constitutive association of vinculin (an actin-binding protein that was shown to act as “leaky capper” of the barbed end of the actin filament) to talin and Arp2/3, recruits ARP2/3⁶²⁻⁶⁴. Moreover, talin is essential for lytic granule polarization⁶⁵. Furthermore, LFA-1 also leads to WASp recruitment, which in turn promotes Arp2/3 mediated actin polymerization⁶². Lytic granules must converge along the MTOC, and this step is independent of actin dynamics and of CD107a, and is rather mediated by dynein and does not imply a commitment for neither granule polarization nor for cytotoxicity⁶⁶. However, formation of an organized synapse where LAMP-1 is retrieved at the center depends on the interaction of LFA-1 with the lipid bilayer⁴⁴. Following lytic granule polarization, they dock at the IS membrane and fuse with the plasma membrane. The docking

is primarily mediated by Rab27a and Munc13-4, followed by priming, which occurs as a result of Munc13-4-mediated activation of Syntaxin 11 or bridging of the plasma membrane with lytic granule⁶⁶⁻⁶⁸. Fusion occurs as a result of the formation of a complex whose components are not all known, but include syntaxin11, VAMP 4 and VAMP 7⁶⁶.

Following lytic granule delivery to the IS, it has been shown that only a fraction of the lytic granules are exocytosed, and that granules are highly mobile, independently of F-actin dynamics, but may depend on Myosin II A(MyH9) to generate the necessary forces^{14,69}. Indeed, MyH9 heavy chain knock-out impaired cytotoxicity, membrane fusion of lytic granules, and granzyme secretion⁷⁰. It has also been shown that MyH9 constitutively physically interact with lytic granules, and lytic granule secretion was shown to be impaired in patients suffering from MyH9 mutations⁷¹. While Myosin IIa is not needed for the formation of an organized IS in NK cells, it is crucial for the final exocytosis step⁴⁴. Following degranulation, the cell must undergo a termination process, followed by detachment. These steps are elaborated in details in⁶⁶. Moreover, it has been shown that lytic granules require a pervasive actin meshwork of hypodense F-actin (which can be achieved through NKG2D and LFA-1 co-ligation) to pass through and that the actin clearances in which they pass are granule-sized^{53,72}. However, actin dynamics are independent of the presence of granules, since actin clearances are observed prior to granule arrival. It has also been demonstrated by super resolution microscopy that the center of the NK IS contains thin F-actin filaments, as opposed to the previous belief that the IS formation leads to F-actin clearance from the center^{53,72}.

2.2 Cytotoxic T cells: the killers of the adaptive immune system

CD8+ T cells have a classical $\alpha\beta$ T-cell receptor TCR. Through a random process of genetic rearrangements, lymphocytes express on their surface unique TCR that have single antigen specificity, which is their capacity to recognize one type of peptide-MHC complex.

Progenitor lymphoid cells leave the bone marrow and reach the thymus to proceed to differentiate, where they undergo a negative and a positive selection. Following this selection, the remaining cells will be capable of recognizing APC, and not react against self-molecules. Naïve CD8+ T cells must be activated by CD4+ cells in order to produce lytic and effector molecules⁷³. CD8+ lymphocytes recognize MHC I molecules presented on the surface of APCs, therefore most cells can be APC- as opposed to CD4+ T cells which recognize MHC II molecules on “professional” APC such as DC and B cells. Naïve T cells will give rise to several subpopulations, culminating in effector cells. Effector

CD8+ T cells express lytic molecules and have high migratory capacity. Following stimulation of their TCR, they undergo reorganization of their actin cytoskeleton, slow down their motility and establish firm adhesions with their targets leading to the assembly of the IS⁷⁴.

The delivery of lytic granules from CD8+ T cells is a highly regulated process, and the signaling and cytotoxic activity of CD8+ T cells will be elaborated in detail in the section “CD8+ T cell Cytotoxicity”.

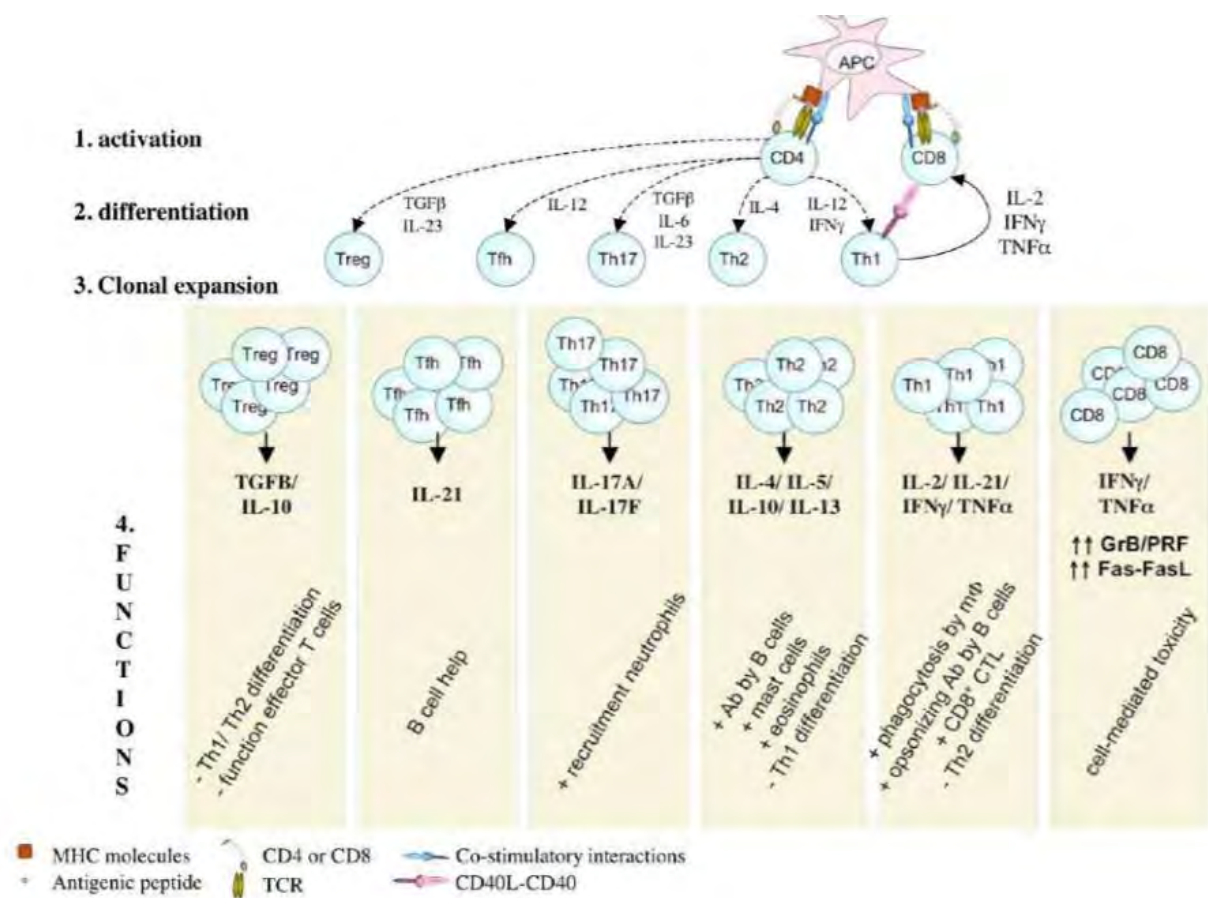


Figure 3: Schematic representation of T cell activation and differentiation in response to APC stimulation. Adapted from the thesis manuscript of Julie De Meester (Thesis, 2011).

A. Receptors, adhesion and co-stimulatory and inhibitory molecules involved in CD8+ T cell cytotoxicity

The activity of cytotoxic T cells is governed by the interplay between several receptors and co-stimulatory molecules, which will be elaborated in the following pages.

a. The T-cell receptor

The $\alpha\beta$ TCR on CTLs is composed of two transmembrane glycosylated polypeptide chains belonging to the immunoglobulin superfamily and linked through a disulfide bond. These glycoproteins contain a short intracytoplasmic tail composed of 4-12 amino acids and a hydrophobic transmembrane domain of 20 positively charged amino acids, thus allowing the TCR to achieve a stable association with the negatively charged transmembrane domain of the CD3 molecules (Figure 4)⁷⁵.

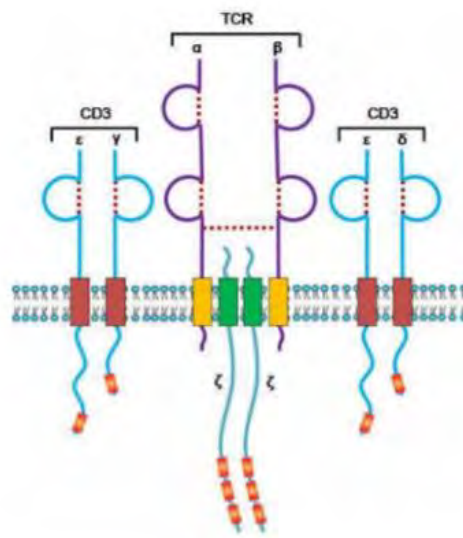


Figure 4: The TCR and its association with CD3. The TCR is composed of the α and β chains and forms a complex with CD3. From the thesis manuscript of Roxana El Khazen, 2016.

T cell activation requires sustained signaling by the pMHC specific to the TCR. However, the duration of the TCR-pMHC contact has been shown to be very short^{76,77}. Therefore, it was proven that despite the rapidity of TCR-MHC interaction, sustained TCR signaling occurs via multiple rounds of TCR-MHC binding^{78,79}. Interestingly, as little as 1 MHC molecule can induce calcium ion increase in T cells, and that T cell activation can be achieved by TCR recognizing as little as 10-15 MHC molecules, and CTLs can kill target cells expressing 1-10 MHC molecules⁸⁰⁻⁸³. This can be explained by the proposed model of “serial TCR engagement”, which suggests that one MHC molecule could trigger and internalize approximately 180 TCRs, thus leading to a sustained TCR signaling despite the small number of MHC molecules via a sequential high TCR occupancy⁸⁴. However, another model referred to as “kinetic proofreading” suggests a prolonged TCR-MHC interaction, leading to modifications

which will be amplified only by highly specific interactions⁸⁵. However, it is most likely that these two types of interactions are not mutually exclusive and may be dependent on the number of MHC molecules on the APC surface.

Briefly, the steps of TCR signaling include the translocation of LCK and Fyn, two members of the Src tyrosine kinase family, into the membrane following TCR engagement, which eases the phosphorylation of ITAM motifs. ZAP-70 also associates to ITAM motifs and activates Linker for activation of T cells (LAT) protein which will allow more signaling molecules to bind (Figure 5).

However, TCR engagement is not enough and T cell activation requires signaling from co-stimulatory molecules. These include CD8 for CTLs, CD28 and the adhesion molecules CD2 and LFA-1⁸⁶.

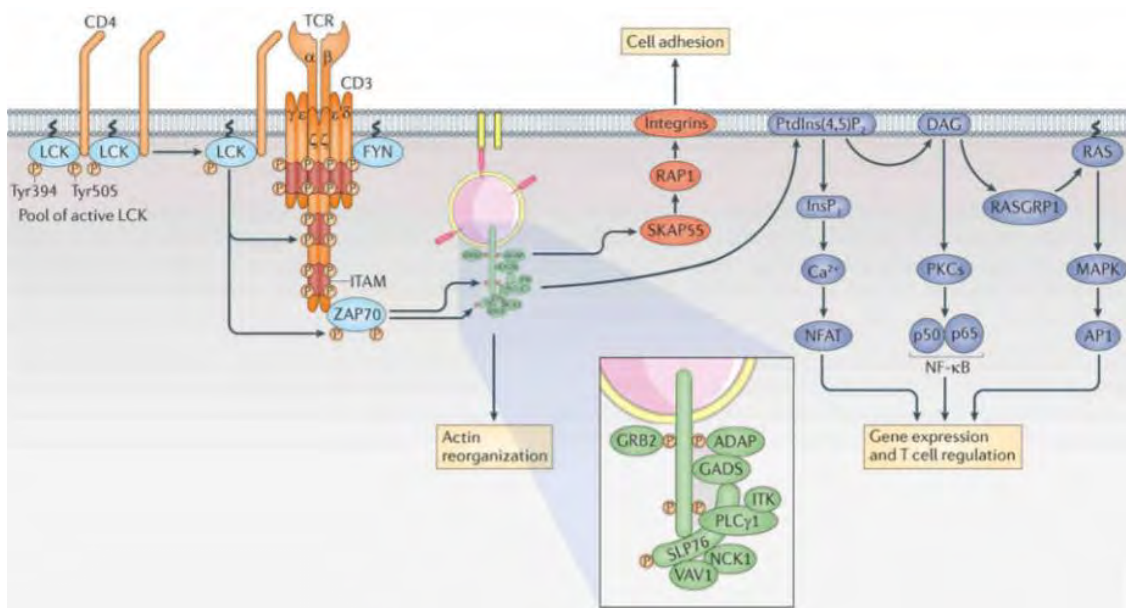


Figure 5: Pathways of TCR signal transduction⁸⁷.

b. The role of the integrin LFA-1 in cytotoxicity

Integrins are heterodimeric adhesion proteins, which allow leukocyte adhesion and play a role in their migration. Integrins play an essential role in infection control, where their absence leads to recurrent infections. They also have a role in immune homeostasis, and perturbations can lead to cancers and autoimmunity. Integrins have a crucial role in the recruitment of lymphocytes from the blood into infection sites, and for lymphocyte adhesion onto their target cells. Moreover, integrins make intracellular adhesion therefore playing a role in the activation of several signaling pathways.

Being heterodimeric proteins, they are formed of one of 18 α and one of 8 β subunits. They can be one of 24 different combinations^{88,89}. The very late after activation (VLA) family of integrins which comprises VLA-1 to 5 has also been identified. Of the LFA-1 family, three members have been identified: LFA-1, 2 and 3⁹⁰. In this manuscript, only the integrin LFA-1 will be addressed.

LFA-1 is required for the migration of T and NK lymphocytes. It is composed of the CD11a (α L) and the CD18 (β 2) subunits. LFA-1 plays a role in immunity, as its deficiency is characterized by recurrent bacterial infection⁹¹. LFA-1 is a transmembrane protein comprised of an extracellular domain, a transmembrane domain and a cytoplasmic domain. LFA-1 binds to intracellular adhesion molecule ICAM-1, among other ICAMs (ICAM-2 and 3, as well as JAM-1). In this manuscript, only the LFA-1 – ICAM-1 interaction will be addressed. LFA-1 binding to ICAM-1 is a temperature-dependent energy requiring process, which also requires the presence of magnesium ion and an intact cytoskeleton⁹².

ICAM-1 (CD54) is a transmembrane glycoprotein expressed on the surface of leukocytes and endothelial cells. ICAM-1 is required for the interaction of LFA-1 on immune cells with their target cells or DCs, or between the immune cells and their environment⁹²⁻⁹⁴. Moreover, full LFA-1 activation requires ICAM-1 on the target cell to provide a physical resistance to allow for F-actin flow⁹⁵.

i. LFA-1 activation

Integrins in circulating lymphocytes are inactive and get activated through binding to chemokine receptors. LFA-1 activation is characterized by both affinity to ICAM-1, and avidity.

Affinity is defined as the capacity of a ligand to bind to its receptor, depending on the available number of molecules. FRET experiments have revealed that the constant of dissociation between LFA-1 and ICAM-1 to be 17.93 ± 1.34 nM⁹⁶.

Avidity is defined as the strength of interaction between two molecules. The increased probability of an LFA-1 – ICAM-1 interaction due to the aggregation of LFA-1 molecules indirectly leads to an increased adhesion strength⁹⁷. Avidity varies based on the conformation (openness) of the LFA-1 molecule. LFA-1 has been described to have three conformations: the closed conformation corresponds to a low affinity and thus an inactive LFA-1 (Figure 6). The intermediate conformation corresponds to an intermediate affinity, while the open conformation corresponds to a high affinity.

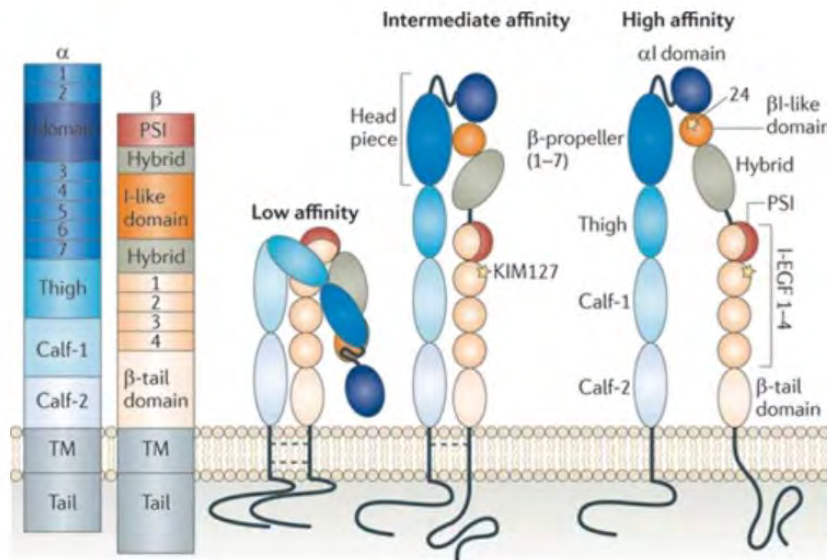


Figure 6: Schematic representation of the different components of the LFA-1 molecule in its different conformations. A. Resting, B. Intermediate and C. Open conformations⁹⁸.

LFA-1 activation is modulated by bidirectional signaling: inside-out and outside-in signaling.

ii. Inside-out signaling

Inside-out signaling is mediated by intracellular signals, resulting from the activation of other receptors such as the TCR or chemokine receptors, to mediate extracellular changes to the adhesive state of LFA-1⁹⁹. Chemokines such as CCL19 and CCL21 only activate the LFA-1 to its intermediate conformation and lead to a binding to ICAM-1 with intermediate affinity¹⁰⁰. However, to fully activate LFA-1 and cause T cell arrest, shear forces were shown to be necessary¹⁰⁰

Inside-out signaling mediated by the TCR occurs upon the formation of the IS. TCR activation induces Rap1 activation through ADAP and SKAP55, leading to LFA-1 inside-out signaling. As previously mentioned, PLC, among others, plays a role in LFA-1 activation. Inside-out signaling cascades increase the ligand binding affinity of LFA-1 receptors and cause their redistribution on the T cell surface into highly organized patch-like clusters. Comrie et al. have shown that LFA-1 in the extended conformation is enriched in the pSMAC, while open LFA-1 was concentrated in a smaller and more central ring of the IS, which will be elaborated further in section pertaining to the IS⁹⁵. A recent study by Houmadi et al. in our laboratory, shows that the nanoscale topology of LFA-1 at the T cell IS consists of a belt of nanoclusters embedded in the interstices of the cortical actin cytoskeleton meshwork¹⁰¹.

iii. Outside-in signaling

Outside-in signaling refers to the final stages of LFA-1 adhesion to its ICAM-1, which initiates an integrin-proximal tyrosine kinase cascade of signaling events. It is caused by extracellular changes which regulate the adhesiveness of LFA-1⁹⁹. Vav1, talin, kindlin3 and ZAP70, all proteins who are bound to the cytoplasmic tail of LFA-1 play a role in outside-in signaling, where the changes they undergo lead to a signaling cascade. Extended LFA-1 is bound with a “closed” head to ICAM-1, but following the signaling cascade, the headpiece changes shape to allow high affinity binding to LFA-1. This consequently increases the avidity and affinity of LFA-1 binding to ICAM-1⁹⁹.

c. Costimulatory molecules

The critical costimulatory receptor **CD28**, when engaged by its primary ligand CD80 becomes enriched in TCR MCs. The CD28-CD80 complex is transported to the central supramolecular

activation cluster of the immunological synapse, where a CD28-PKC θ arrays around this structure¹⁰². The adhesion molecule **CD2** (LFA-2) not only facilitates T cell adhesion but also functions as a costimulatory molecule, by lowering the threshold for T cell activation. Following TCR activation, the avidity of the interaction between CD2 and CD58 is increased¹⁰³. The engagement of CD2 induces phosphorylation of PLC γ 1 via Fyn kinase thus potentiating intracellular calcium levels above those achieved in response to TCR triggering alone¹⁰².

d. Inhibitory molecules

Cytotoxic T lymphocyte antigen-4 (**CTLA-4**) can outcompete CD28 for binding to CD80 and CD86. CTLA-4 co-ligation leads to an increased threshold of T cell triggering, thus reducing the likelihood of activation. Programmed-death 1 receptor (**PD1**) generally binds with PD-L1 but can interact with CD80 to generate inhibitory signals. It is also a marker for exhausted antigen-specific T cells, where T cells have reduced proliferation and are incapable of producing cytokines. PD-1 signaling inhibits CD28-dependent PI3K activation and blocks Akt activation¹⁰².

B. CD8+ T cell cytotoxicity: from naïve cells to professional killers

When compared, the cytotoxicity of NK and CTLs differ in the migration dynamics, the duration of contact with their targets, whereby it was shown that CTLs decrease their migration speed when patrolling the tumor environment, and establish longer contacts with their targets, while NK cells establish more dynamic contacts¹⁰⁴. The contact with an antigen presenting cell is what triggers TCR mediated signaling which, along with other costimulatory signals leads to the differentiation into CTLs in the primary lymphoid organs.

Following the first stimulation with antigen, most effector CD8+ T cells will die, and only a fraction will become memory cells (Figure 7).

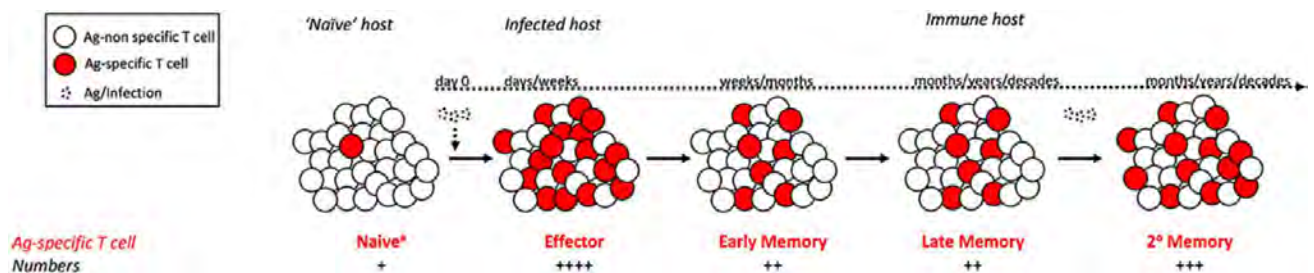


Figure 7: Changes undergone by CD8+ T cells before/after infection. Antigen-specific naïve CD8+ T cells undergo differentiation into effector, early memory late memory and secondary memory cells¹⁰⁵.

The pattern of expression of lytic molecules varies based on the stage of differentiation they are at¹³. 20–60% of early differentiated T cells express all granzymes (GzmB expression was minimal) and intermediate levels of perforin., granulysin or high-levels of perforin. Late differentiated cells express high levels of perforin and GzmB. The accumulated expression of Gzm B, granulysin and perforin as T cells differentiate to effector memory cells is in line with greater cytotoxicity observed in late differentiated effectors compared to early differentiated central memory or naïve CD8 T cells.

a. Differentiation into professional killers

First, naïve CD8+ T cells must scan their environment and interact with antigen presenting cells, to become activated via their TCR. Such CD8/APC interactions are possible thanks to the motility of both the CD8 and the dendritic cells. This capacity to interact with APCs and high motility allows CD8+ T cells to quickly scan through DCs, wherein it is supposed that in one hour, a single DC can be probed by about 500 CD8+ T cells¹⁰⁶. However, CD8+ T cells must reduce their motility and come to a halt in order to establish an interaction with the APC. This process is enabled by the interaction of their TCR with MHC molecules, where an adhesion ring is formed due to centripetal actin flow¹⁰⁷. The IS of a T cell was first defined in the late 1990s, and was defined as “a molecular machine controlling T cell activation”¹⁰⁸.

CD8-APC interactions were initially thought to be a timely process, where activation of the T cell was thought to require long hours of CTL-APC contact, where the T cell remains in contact with one APC for a time ranging between 6 and 30 hours^{108,109}. However, evidence in later years supported a more dynamic type of interactions, in which the CTL will have several brief and short-lived interactions with multiple DCs¹¹⁰. This has suggested the presence of a short-term memory that allows T cells to perform a “signal summation” from these intermittent interactions, which were termed “kinapses”^{111–113}. The activation signal that is subsequently generated from these interactions was shown to last for several hours¹¹². However, the immunological synapse is a productive and more stable interaction between the T cell and the APC¹¹³. It has been shown that for T cells to be arrested and primed, they must interact with a DC that expresses high levels of adhesion molecules, a high quantity of co-stimulatory molecules, as well as a high quantity of high affinity MHC-I molecules¹¹⁴.

CTL-APC interaction leads to a fast tyrosine phosphorylation cascade, thus triggering several signaling pathways and a Ca^{++} induction of the transcription of genes involved not only in lymphocyte activation, but also proliferation^{115,116}. The calcium signaling depends on a stable IS, therefore on the actin cytoskeleton. Indeed, inhibition of actin filaments by Latrunculin B which binds G-actin reduces the number of TCR that can be stimulated, subsequently rendering the cell unable to maintain calcium ion release¹¹⁷.

CD8+ T cell cytotoxicity

CTL-mediated cytotoxicity requires a direct contact between the CTL and the antigenic peptides presented on the MHC-I molecules on the target cell. Following contact with the target an immunological synapse is formed and the lytic machinery of the CTL is quickly assembled. The formation of the CTL-target stable immunological synapse relies on the binding of the integrin LFA-1 to ICAM-1 on the target cell¹¹⁸. TCR signaling following TCR-peptide-MHC-I engagement drives the ARP2/3 dependent polymerization of branched actin filaments at the edge of the site of contact between the T cell and the target cell.

The MTOC polarizes towards the target cell, causing the release of soluble lytic molecules such as perforin and granzymes and membrane-anchored effector molecules such as the Fas ligand^{103,119}. It has also been shown that polarization of the lytic molecules to the IS requires a strong TCR signal, whereas weak TCR signaling cannot induce granule recruitment to the IS, despite proper MTOC polarization¹²⁰. The activity of Lck, Fyn, and ZAP-70 are all essential for promoting MTOC polarization to the lytic synapse, where Lck is essential for signal propagation through ZAP70¹⁰³. ZAP 70 phosphorylates LAT which recruits several proteins including SLP76, PLC γ 1 and Vav1 to form the LAT signalosome. SLP76 and Itk mediate PLC γ 1 activation, therefore inducing MTOC polarization and calcium ion influx, as well as inducing a cascade of signaling events which contribute to MTOC polarization¹⁰³. Ca^{2+} influx into the cell is essential for degranulation, but not for MTOC polarization, reinforcing the observation that MTOC polarization is not a requirement for granule polarization and exocytosis¹⁰³. The granules are then released from the secretory cleft and into the target cell¹²¹. However, not all granules that are polarized will fuse with the synapse, as determined by total internal reflection microscopy¹²². Moreover, granule secretion relies heavily on the actin cytoskeleton remodeling, which will be addressed in detail in the next chapter.

2.3 Remodeling of the actin cytoskeleton governs the cytotoxicity of NK and CD8+ T cell cytotoxicity

Cytotoxicity is a dynamic process which involves several steps, in which the actin cytoskeleton and the rearrangements it undergoes play a pivotal role.

The actin cytoskeleton is a filamentous network composed of globular actin (G-actin) monomers, which polymerize to form filamentous actin (F-actin), and then these filaments may be severed. This involves the interplay of several actin binding proteins. This is a highly dynamic process involving several players. Nucleation involves the formation of actin dimers followed by actin trimers, which allows the start of the elongation through the process of polymerization. The next step involves adenosine triphosphate (ATP) hydrolysis.

To further elongate the actin filaments, formins such as mDia in mice (hDia in humans), and FMNL1 must interact with the barbed wire to allow monomers to be added to it, thus creating parallel elongated bundles^{123,124}. Formins also acts as “leaky cappers”, whereby they slow down the elongation and dissociation rates of the actin filament¹²⁵.

Arp2/3 binds to the “mother” actin filament to allow the formation of a “daughter” filament in a dendritic fashion at a 70-degree angle. Arp2/3 is composed of seven subunits of which five unique components: ARP2, ARP3, ARPC2, ARPC3 and ARPC4, together with one molecule each of the isoform pairs ARPC1A and ARPC1B, and ARPC5A and ARPC5B. Arp2/3 generally requires activation by a nucleation-promoting factor from the Wiskott-Aldrich Syndrome protein (WASp) family, the WASp family-Verprolin homologous protein (WAVE), and the cortactin family. WASp bound to ARP2/3 will bind to profilin bound G-actin to perform actin nucleation, until the process is stopped by capping proteins¹²⁶.

On the other hand, proteins that prevent actin polymerization include cofilin and profilin. Cofilin-mediated actin severing has been shown to be necessary in achieving T cell spreading and the formation of a proper immunological synapse, as well as cell motility^{127,128}. Profilin is a protein that binds to the barbed end G-actin and prevents its addition to the nascent actin filament¹²⁹.

Some major players in this process can be summarized in Figure 8.

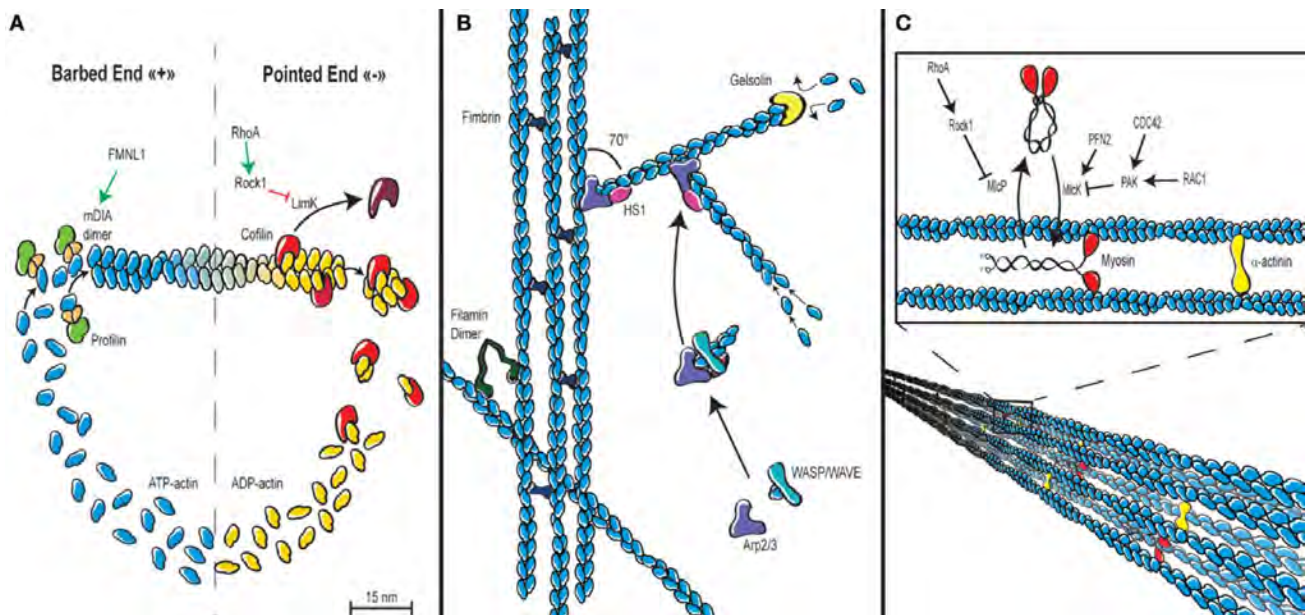


Figure 8: Overview of families of actin-binding proteins involved in the different processes pertaining to actin¹⁰¹.

2.4 Dynamic steps of cytotoxicity

A. Cell migration

Chemokine receptors allow lymphocytes to sense the chemokine gradients and migrate to where their targets cells are. Migrating cells transform from round cells to cells with a leading edge at the front, and a uropod at the back. The leading edge, also named the lamellipodium, is a thin and spread structure, composed of highly branched actin fibers. Also in the leading edge are filipodia, which are protrusions with an exploratory function, and made up cross-linked actin fibers arranged in a parallel fashion¹³⁰. The uropod is composed of actin filaments coupled to Myosin, which allows the cell to generate the tension necessary to migrate forward. To achieve cytotoxicity, the cytotoxic T or NK lymphocyte must bind to different targets and scan them. In order to do so, lymphocytes must halt their motility upon contact with the target^{106,109}. Upon binding to the potential target cell, the cell's machinery is shifted from locomotion towards immunological synapse formation, where actin polymerization continues to take place without the cell moving. The lymphocyte spreads a lamellar sheet over the target, and outward radial actin polymerization takes place.

More information on the mobility of T lymphocytes can be found in¹³¹.

B. The immunological synapse: the platform for cytotoxicity

Once the lymphocytes reach their target, they must establish a stable contact, which is the immunological synapse (discussed in the next section). Following the establishment of the immunological synapse, cytotoxic lymphocytes must polarize their lytic vesicles and their MTOC towards the area of contact in order to release perforin and create pores in the target, followed by granzyme release into the target⁶⁴. The MTOC is polarized in a way to deliver the lytic granules in the open areas of the actin meshwork⁵³.

The immunological synapse in the cytotoxic context, is defined as the interaction between a cytotoxic lymphocyte and a target cell. As inferred from the previous sections, the immunological synapse assembly plays a crucial role in cytotoxicity and will only be discussed in that context.

IS formation takes place when the lymphocyte halts its movement and establishes a transient but controlled contact with the target cell. However, the immunological synapse is far from being a static process, it is highly dynamic and tightly regulated and involves reorganization of cellular components as well as signaling proteins.

a. Immunological synapse of CD8+ T cells

Analysis of the structure of the mature immunological synapse of T cells has revealed a “bullseye” structure with radially distributed and spatially segregated rings which Kupfer has named supramolecular activation clusters (SMAC), where the TCR-MHC cluster in the center, surrounded by a ring of LFA-1-ICAM-1, which is itself surrounded by a distal ring which comprises CD45, a transmembrane tyrosine phosphatase¹³²⁻¹³⁴. These clusters are referred to, from the inside-out as: central, peripheral and distal SMAC (cSMAC, pSMAC and dSMAC) (Figure 10), and the bullseye pattern has been suggested to be a mechanism to confine lytic granules and prevent bystander killing^{44,135}. The cSMAC, as its name indicates, is the center of the synapse and the area of TCR aggregation, and was postulated to be formed of microclusters of about 100 TCR^{136,137}. The pSMAC directly surrounds the cSMAC and is composed of proteins such as talin and LFA-1. The dSMAC is the most distal area, and is also referred to as radial lamellipodium that allows the cell to sense chemical and physical properties of the APC^{134,138}.

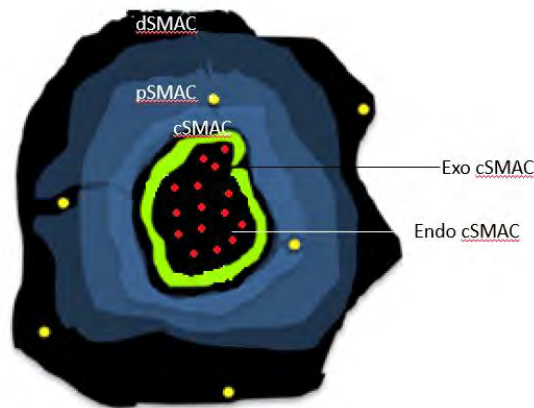


Figure 10: Top view model of the spatial organization of the immunological synapse¹³⁵. The immunological synapse is organized into a central, peripheral and distal supramolecular activation clusters (SMAC), where distinct molecules aggregate in each SMAC.

Methods based on fluid supported lipid bilayers showed that in the case of CD8+ T cells, TCR-MC form at the dSMAC and move centripetally through the pSMAC to the cSMAC, initially aided by actin filaments undergoing retrograde flow and subsequently through dynein-mediated movement along the microtubules toward the centrosome that translocates beneath the cSMAC following TCR stimulation^{139–141}. LCK is, however, found at the dSMAC, and the cSMAC can be further divided into the endo-cSMAC, a poor actin region where the TCR are located, and the exo-cSMAC, a TCR poor region where CD28 molecules are located^{142,143}. TCR signaling following TCR-peptide-MHC-I engagement drives the ARP2/3 dependent polymerization of branched actin filaments at the edge of the site of contact between the T cell and the APC. This drives initial T cell spreading and the centripetal flow of the acto-Myosin network, and aids in the retrograde flow towards the cSMAC. This retrograde flow may be inhibited by using Jasplakinolide, a drug that directly binds the actin filament and leads to the depletion of the G-actin pool. Jasplakinolide addition leads to the formation of a dense actin ring between the pSMAC and the cSMAC¹⁴⁴. Centripetal actin flow also plays a role in the conformational change of integrins, thereby causing the T cell to adhere to its APC and plays a role in the outside-in signaling. Indeed, removing the synapse symmetry leads to the restoration of the lymphocyte motility by creating a retrograde actin flow, which in turn creates an LFA-1 focal zone⁴⁴.

The pSMAC is made up of a lamella-like actin arc network that outlines the radial symmetric contractile ability of this part of the IS. It has been shown that the assembly of the pSMAC actin arc is

mediated by formins and organized by Myosin II into antiparallel concentric arcs^{143–146}. Indeed, the role of formins validated by the fact that mDia depletion leads to failure in the formation of the linear actin filaments needed generate the typical concentric Myosin IIA-rich arcs, as well as the treatment with the pan-formin inhibitor SMIFH2, which decreases the presence of actin arcs within the pSMAC¹⁴⁶.

b. Immunological synapse of NK cells

Most of the available information on the IS comes from the study of T cells. However, some groups have been interested in the study of the IS on NK cells. In NK cells, distinct IS properties have been identified.

For NK cells, much like T cells, cytotoxicity is mediated by the NK cell emptying its granule content into the target cell. In addition to the receptor interplay mentioned above, the actin cytoskeleton plays a crucial role in the NK cell synapse. In NK cells, cytotoxicity requires the formation of a mature immunological synapse¹⁴⁷. Moreover, the fact that lytic granules exist in NK cells even prior to activation, the accidental release of these granules must be prevented, and the directed release of lytic granules must be ensured. The contact between the NK cell and its target is followed by adhesion, mediated by LFA-1 among other adhesion molecules¹⁴⁷. In the absence of inhibitory signals, the stable IS begins to form, involving F-actin rearrangements and morphological changes to NK morphology, which occur downstream of Vav1, and is WASp dependent¹⁴⁷. It has been shown that NKp46 aggregates into clusters which are enriched at the IS. It has also been shown to play a role in F-actin accumulation at the IS. Even though the NK cell synapse was thought to be static and stable at the micrometer scale, it has been shown to exhibit local nanoscale dynamism, where actin filament rearrangement appears to be mediated by ARP2/3 and MyosinIIA⁷². As opposed to the retrograde F-actin flow observed in T cell synapse, NK cells appear to only display short sequences of outward F-actin polymerization⁷².

While lytic granules aggregate around the MTOC, the MTOC also begins to polarize towards the immunological synapse, and the signals to cause this polarization include ERK, VAV1 and PYK2¹⁴⁷. Lytic granules appear to be accumulated at the cSMAC, and adhesion molecules in the pSMAC⁵⁷. As in T cells, reorganization of the actin cytoskeleton must take place for MTOC and lytic granule polarization to the IS, and discrete actin hypodense regions in the cytoskeleton must exist to allow lytic granule access to the plasma membrane^{14,72,147}. However, these clearances are not mediated by a unidirectional or radial actin flow, but rather by a local nanoscale dynamism where these clearances are opening and closing⁷². ARP2/3 and Myosin IIA also play a role in the structuring of these clearances, where ARP2/3 depletion leads to the formation of long bundled actin filaments at the IS,

and MyosinII A impairment decreases the number of permissive clearances⁷². Interestingly, these clearances were observed prior to granule arrival⁷². Docking of the granules requires members of the Rab family of GTPases, such as Rab27a, and the SNARE family member Munc13-4 which interacts with Rab27a, as well as LFA-1 engagement^{72,147}. The ARP2/3 complex, as well as MyosinIIA have also been shown to play a role in granule secretion, where their absence appears to impair exocytosis⁷². Indeed, MyosinII A not only plays a role in the actin clearances, but also in lytic granule movement towards the secretory domain of the cSMAC⁷¹. In NK cells, it has been demonstrated that the granule-sized clearances are maintained after degranulation, and so were local filament dynamics, suggesting that the formation of these clearances is independent from granule presence, despite the necessity for these clearances for a successful degranulation⁷².

Cytotoxicity resolves by the detachment of cytotoxic lymphocyte from its target. These steps can be summarized in the figure 9 below.

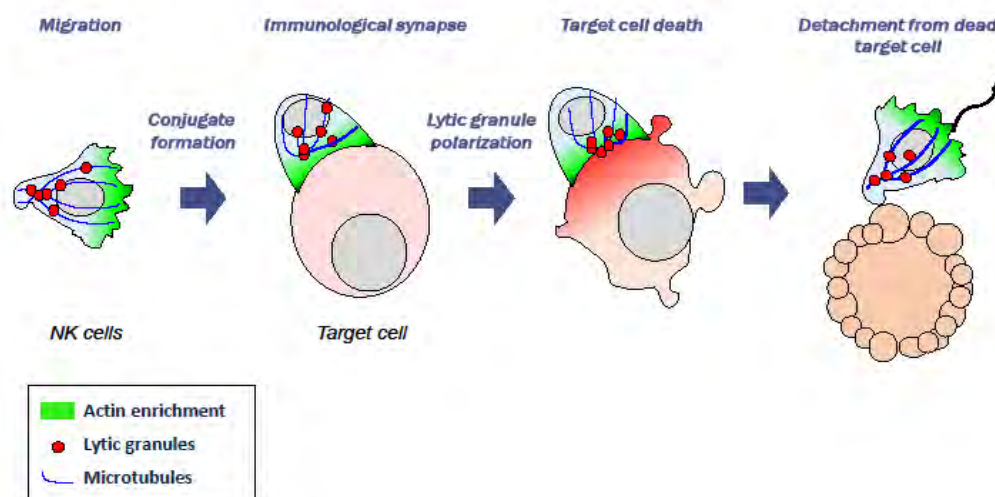


Figure 9: Dynamic steps of cytotoxicity. The main steps of cytotoxicity include migration towards the target cell, conjugate formation, lytic granule polarization followed by degranulation, and end with the detachment from the target cell

3. Cytotoxicity in the clinical context

Cytotoxic T and NK cells have long been known as essential pillars in the clearance of infected cells and tumor cells. Dysregulation in the function of these cells can lead to harmful consequences, which will be elaborated in the next pages.

3.1 Cancers

Cancer is defined as a disease of immune dysregulation, characterized by a failed immune recognition leading to the proliferation of malignant cells¹⁴⁸.

The infiltration of a tumor by activated CD8⁺ T cells is considered a good prognosis and can be predictive of a better response to chemotherapy and immune checkpoint blockade therapy. However, in several cancers, CD8⁺ T cells are unable to access the tumor and will accumulate outside the tumor cell cluster. However, some CD8⁺ T cells can infiltrate tumors and it is speculated that the dense fiber region surrounding the tumor might not be able to protect against this infiltration¹⁴⁹. However, Li et al. speculate that in the case of tumors that are indeed being infiltrated, it is due to CD8⁺ T cells that slow down then regain cell motility and chemotaxis¹⁴⁹. NK cells were also demonstrated to play a role in cancer immunosurveillance¹⁵⁰. Due to their potency to eliminate cancer cells, T and NK cell research aiming to use them as cancer immunotherapy is currently booming.

3.2 Autoimmunity

Autoimmune diseases are defined as aberrant responses towards “self”. They have a high prevalence of 7-9% in the population and affect women more than men. It is thought that women are more predisposed to autoimmune diseases due to hormones as well as the direct effects of X chromosomes as well as a sex-specific microbiota¹⁵¹. Autoimmune diseases can be mediated by autoantibodies or CD8⁺ T cells, but T_h cells are always implicated. Autoimmune diseases are usually caused by a combination of genetic and environmental factors (such as infections, microbiome and UV light) which culminate in an imbalance between the effector and the regulatory responses^{152–159}. They include type I diabetes, multiple sclerosis, rheumatoid arthritis and inflammatory bowel disease. Despite the large spectrum of organs they affect and their different clinical manifestations, autoimmune diseases usually undergo an initiation phase, often asymptomatic, followed by a propagation phase characterized by inflammation and tissue damage caused by cytokine production and the imbalance between the effector and regulatory functions of T cells¹⁶⁰. The last stage is the resolution, in which patients have some restored balance between the regulatory and effector functions, but often relapse. Interestingly, and contrary to a previous belief, a larger portion than previously thought of self-reactive CD8⁺ T cells manage to

escape the process of clonal deletion^{161,162}. Therapies for autoimmune diseases are mainly cytokine antagonists, which aim at establishing a long-term resolution by increasing regulatory mechanisms^{163,164}.

3.3 Primary immunodeficiencies

Primary immunodeficiencies (PID) are a heterogeneous group of approximately 400 rare genetic diseases characterized by severe defects in one or several components of the innate and/or the adaptive immune system. The clinical presentations of PIDs are variable, but PID patients usually suffer from recurrent infections, cancers and autoimmunity, which may be life-threatening. Characterized PIDs are monogenic disorders, but more complex polygenic disorders certainly remain to be discovered. In this section, only an overview on PIDs will be presented, and the focus on PIDs where defects in the cytotoxicity or the actin cytoskeleton/immunological synapse were reported will be discussed in a later section. An exhaustive list of PIDs can be found in¹⁶⁵.

A. Hemophagocytic lymphohistiocytosis

Hemophagocytic lymphohistiocytosis (HLH) is a severe condition characterized by a heightened inflammatory response and an expansion of polyclonal CD8+ T cells, most likely due to defects in the cytotoxic machinery of T and NK cells, despite their normal numbers¹⁶⁶. HLH patients present with mutations in the perforin, MUNC13/4, RAB27a, LYST, Syntaxin11 genes, all of which are associated with the perforin-containing lytic granules in cytotoxic cells (Reviewed in¹⁶⁷). These defects are comprised in the category of primary HLH, while secondary HLH occurs as a complication of infection, cancer or autoimmunity. The fact that several of the mutations in some of these genes such as perforin were found in families has led to terming some HLH as familial hemophagocytic lymphohistiocytosis (FHL). These defects, summarized in Table 1, will be elaborated in further details in the coming pages, as they entail a defect in cytotoxicity.

Primary HLH	Inheritance	Cytogenetic localization	Involved gene	Protein	Function
FHL					
FHL1	AR	9q21.3-22	Unknown		Unknown
FHL2	AR	10q21-22	<i>PRF1</i>	Perforin	Pore formation
FHL3	AR	17q25	<i>UNC13D</i>	Munc13-4	Granule priming
FHL4	AR	6q24	<i>STX11</i>	Syntaxin-11	Granule fusion
FHL5	AR	19q13	<i>STXBP2</i>	Munc18-2	Granule fusion
CHS	AR	1q42-43	<i>LYST</i>	LYST	Granule trafficking
Griscelli syndrome type 2	AR	15q21	<i>Rab27A</i>	Rab27A	Granule docking
HPS type 2	AR	5q14.1	<i>AP3B1</i>	AP3B1	Granule trafficking
XLP type 1	XR	Xq25	<i>SH2D1A</i>	SAP	Signaling in T and NK cells
XLP type 2	XR	Xq25	<i>BIRC4</i>	XIAP	Signaling pathways involving NF- κ B
IL-2-inducible T-cell kinase deficiency	AR	5q34	<i>ITK</i>	ITK	Signaling in T cells
CD27 deficiency	AR	12p13	<i>CD27</i>	CD27	Lymphocyte costimulatory molecule
Secondary HLH				Inducer	
Infection-associated			Epstein-Barr virus, herpes simplex virus, cytomegalovirus, adenovirus etc.		
Lymphoma-associated			NK/T-cell lymphoma nasal type, anaplastic large cell lymphoma etc.		
Autoimmune disease-associated			Systemic idiopathic juvenile arthritis, systemic lupus erythematosus etc.		
Post-allo-HSCT-associated			Immunologic reaction at engraftment		
Drug hypersensitivity-associated			Carbamazepine, phenobarbital, sulfamethoxazole, etc.		

Table 1: HLH classification, causes and underlying defects¹⁶⁸.

a. Perforin deficiency (FHL2)

The pore forming 70 kDa perforin glycoprotein is encoded by the *PRF1* gene on chromosome 22 and is stored in the lytic granules of CTLs and NK cells. Patients with complete perforin deficiency present with HLH symptoms, and present an impaired CD8+ T cell and NK cell cytotoxicity^{169,170}. Partial loss of perforin leads to certain malignancies, and perforin loss may lead to certain autoimmune diseases such as a systemic lupus erythematosus, Hashimoto's disease and Grave's disease¹⁷¹. A missense mutation in the *PRF1* gene has also been shown to lead to neurological manifestations¹⁷². In certain cases where cytotoxicity of CD8+ is impaired, some CD4+ T cells may become perforin positive¹⁷³. Perforin polymerizes and binds target cells through membrane phospholipids, forming a channel in the target cell membrane through which Gzms may be released. T cell gene therapy has been proposed as a curative mechanisms for HLH patients with perforin defects¹⁷⁴.

b. Munc13-4 deficiency (FHL3)

Munc13-4, a member of Munc13 family of proteins involved in vesicle priming function, has been described as a positive regulator of secretory lysosome exocytosis. It is encoded by the *UNC13D* gene located on chromosome 17. Patients presented with fever, hepatosplenomegaly, pancytopenia, coagulation abnormality, liver dysfunction, and features of hemophagocytosis in the bone marrow or cerebrospinal fluid¹⁷⁵. Confocal and TIRF microscopy imaging reveal that Munc13-4 is dispensable for granule polarization and docking at the IS membrane, but is required through its association with Rab27a for the regulated secretion of cytotoxic granules at the priming stage of the exocytic

pathway^{176,177}. Therefore, Munc13-4 deficient CD8+T and NK cells exhibit defective cytotoxicity and express more perforin than healthy controls^{175,176,178}.

c. *STX11* deficiency (*FHL4*)

The syntaxin11 (*STX11*) protein is encoded by a gene on chromosome 6. Patients with defective *STX11* present with HLH symptoms. *STX11*-causes defects in cytotoxicity and degranulation, and patients have a higher perforin expression levels than healthy controls. However, confocal microscopy imaging reveals that *STX11* deficient cells can efficiently polarize their perforin granules but fail to degranulate, due to defective granule fusion with the membrane¹⁷⁸ (Figure 11). These defects may be reversed by IL-2 administration¹⁷⁹.

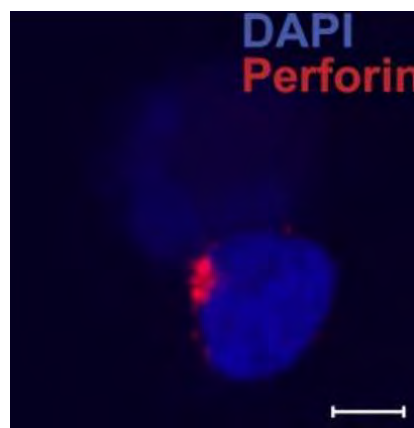


Figure 11: NK cells from *STX11* deficient patients do not fail to polarize their perforin granules (red) to the IS¹⁷⁸.

d. *Munc18-2* deficiency (*FHL5*)

Munc18-2, also known as syntaxin binding protein 2 (*STXBP2*) is encoded by a gene on chromosome 19. Its deficiency leads to symptoms of HLH. T and NK cells deficient in Munc18-2 have impaired degranulation and cytotoxicity which can be in part corrected by IL-2 administration^{180,181}. Much like *STX11* deficiency, confocal microscopy reveals that *STXBP2* mutant NK cells are capable of normal granule polarization (Figure 12). Moreover, Syntaxin 11 is stabilized through a *STXBP2*/Syntaxin 11 interaction which is abolished in *STXBP2* deficiency.

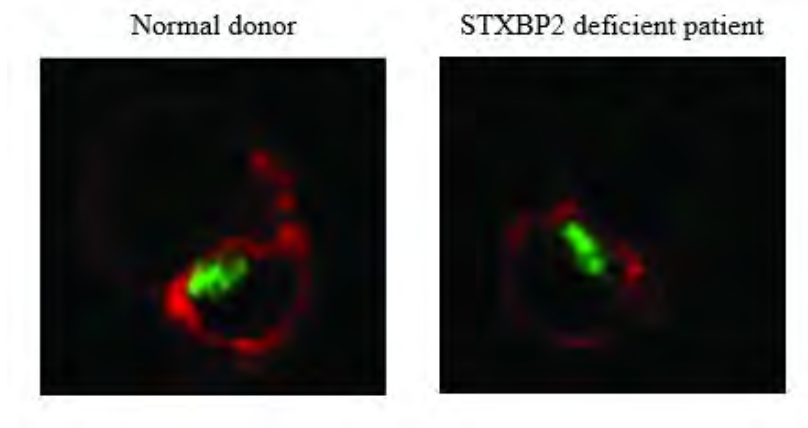


Figure 12: NK cells from a normal donor and an STXBP2 deficient patient stained for F-actin (red) and perforin (green) reveal a normal granule polarization in patient cells¹⁸¹.

e. Rab27a deficiency (Griscelli syndrome)

Rab27a is a member of a large family of Ras-related small GTPases, and the gene encoding it is located on chromosome 15. Loss-of-function mutations in the Rab27A gene result in Griscelli syndrome, a rare autosomal disorder in which patients suffer partial cutaneous albinism where a pigmentary dilution of the skin and the hair is observed, as well as clumps of pigment in hair shafts and an accumulation of melanosomes in melanocytes. Patients often develop hemophagocytic syndrome, which is the uncontrollable activation of lymphocytes and macrophages. Rab27a is required for granule secretion, as Rab27a-deficient T cells exhibited reduced cytotoxicity and cytolytic granule exocytosis despite the presence of a normal amount of lytic granules of the proper size¹⁸²⁻¹⁸⁴. Confocal microscopy images revealed that Rab27a co-localizes with Gzm B-containing granules¹⁸³.

f. LYST deficiency (Chediak-Higashi syndrome)

The *LYST* gene is located on chromosome 1. Patients with *LYST* deficiency suffer from Chediak-Higashi syndrome, a rare autosomal recessive disease characterized by partial oculocutaneous albinism, recurrent infections, a progressive primary neurological disease, and often causing HLH^{185,186}. NK cells from *LYST* deficient patients show no cytotoxicity and impaired degranulation, similarly to T cells^{185,187-189}. Lytic granules from *LYST* deficient patients show an aberrant morphology. There are distinct granules in patient NK cells, and not a giant granule as previously thought. However, they are larger than granules in normal NK cells, and they do not converge at the MTOC, as revealed by confocal microscopy imaging¹⁸⁹. The granules containing cytokines, and cytokine release are not affected by *LYST* mutation¹⁸⁹.

B. Severe combined immunodeficiency

Severe combined immunodeficiency (SCID) are a group of genetic diseases caused by mutations in genes regulating the development and function of T, NK and often B cells. SCID patients that lack T cells and can be sub-classified further based on the presence or absence of NK and B cells. However, since antibody production from B cells requires functional T cells, patients in which T cells are absent usually have a combined T and B deficiency¹⁹⁰. Moreover, within the same family, two siblings suffering from SCID may present with different cellular phenotypes¹⁹¹. SCID patients often present with symptoms early on, in the first weeks or months of life. They fail to thrive and suffer from viral and fungal infections which include infections by rare microorganisms¹⁹². One symptom that SCID patients present with and that physicians often overlook is lymphopenia.

a. B cell immunodeficiencies

B cell immunodeficiencies, also known as antibody deficiency, are the most common type of PIDs, making up for about 50% of diagnosed PIDs. Clinical manifestations include a susceptibility to bacterial respiratory tract infections. They are characterized by the reduction or absence of serum immunoglobulins (Ig), or an increased Ig level but with impaired function. More than twenty Ab deficiency disorders have been defined, and include X-linked agammaglobulinemia and common variable immunodeficiency¹⁹³.

b. Innate immunodeficiencies

Innate immunodeficiencies are usually associated with defects in phagocytes, Toll-like receptor mediated signaling and complements. Clinical manifestations comprise bacterial and fungal infections. Innate immunodeficiencies include severe congenital neutropenia, presented as an extremely low neutrophil count. Phagocyte defects are characterized by chronic granulomatous disease, which often has an X-linked inheritance. Innate immunodeficiencies also include defects in the IL-2/IFN- γ signaling pathway. PIDs associated with complement defects are the rarest category of PIDs, comprising less than 1% of all diagnosed cases, and are often associated with autoimmunity.

C. PIDs related to defects in the actin cytoskeleton

Even though primary immunodeficiencies with a defective actin cytoskeleton are not a category per se, we must focus on them as a group in this manuscript, since its emphasis is cytotoxic cells and several of these defects are causative of impaired cytotoxicity. As previously mentioned, much of the information available to us today on the role of the actin cytoskeleton and its regulation, especially in

the control of the immunological synapse, comes from the study of PID patients. In the context of my thesis project, we are particularly interested in the regulation of the immunological synapse, and the interplay between the actin cytoskeleton and the lytic granules. The genes which cause such defects appear to belong to same signaling pathway in several instances, as seen by similar symptoms in the patients and similar functional defects. Some of these defects may also be accompanied by a defective cytotoxic activity.

a. Wiskott Aldrich protein deficiency

The Wiskott Aldrich syndrome (WAS) was first described in 1953 by Wiskott, then by Aldrich in 1954¹⁹⁴. Both have identified that patients suffering from a defect linked to the X chromosome present with microthrombocytopenia, eczema and recurrent otitis among other infections. In certain cases, the pathology of WAS would evolve to include tumors such as B cell lymphomas, and autoimmunity, and treatment often requires stem cell transplantation^{195,196}. The gene behind WAS is located on the short arm of the X chromosome, specifically at Xp11.22–p11.23, and it encodes the WAS protein (WASp), a 501 amino-acid protein expressed in the cytoplasm of nonerythroid hematopoietic cells¹⁹⁵. Neuronal WASp (N-WASp) is expressed in neuronal cells. WASp has been of interest for my host team in Toulouse, as my supervisor Dr. Loïc Dupré has had ongoing research on this protein for almost two decades.

WASp is a multidomain protein comprised, from the N to the C terminus, of a WH1 domain, followed by a basic domain, a G protein binding domain (GBD), a proline-rich region and a VCA domain. WASp is autoinhibited by a set of intramolecular interactions, mainly between the basic and GBD domains and the VCA domain, therefore preventing binding of the Arp2/3 to the VCA domain and initiation of actin polymerization¹⁹⁷. Indeed, WASp is involved in actin polymerization through the nucleation of nascent actin filaments in response to the TCR or chemokine receptors (Figure 13). In fact, WASp, (as well as the WAVE complex) controls the activation of the ARP2/3 complex. For more information on the detailed activation of WASp, I invite you to read¹⁹⁷.

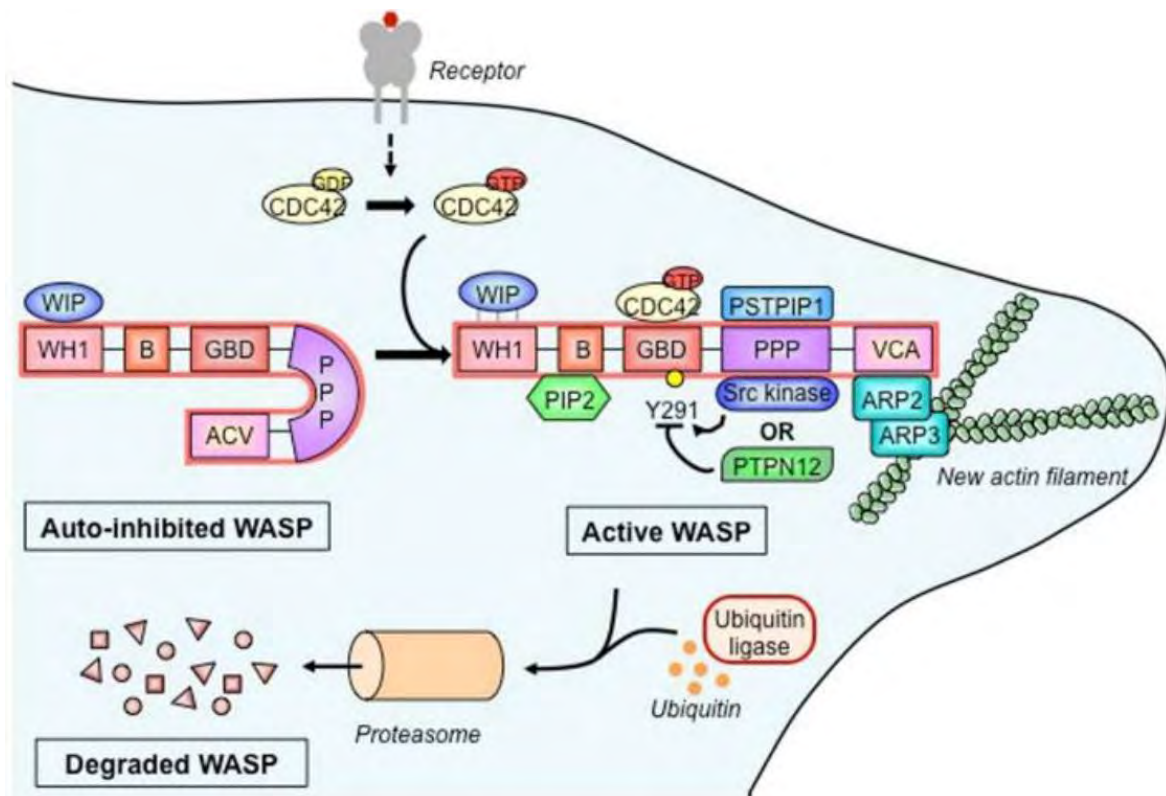


Figure 13: Wiskott–Aldrich syndrome protein activation, molecular partners, and cytoskeleton remodeling¹⁹⁸.

The role of WASp in the immunological synapse assembly has been demonstrated about 20 years ago. WASp is not only recruited to lipid rafts following TCR activation, but is essential for lipid raft clustering¹⁹⁹. WASp deficiency also causes a decreased F-actin accumulation at the IS, as well as a decreased density of LFA-1 clusters at the IS^{57,101,200}.

Moreover, WASp deficiency was shown to cause a mild defect in the cytotoxicity of CTLs and an even more severe defect in NK cells. Indeed, WASp deficient cells, despite a normal expression level of lytic molecules, show an aberrant synapse morphology as well as a defect in the recruitment of the lytic molecules to the synapse, as well as the exocytosis of these molecules^{57,201,202}. That is because lytic granule polarization relies on the WASp-dependent actin polarization. Interestingly, treatment with IL-2 corrects the defect in NK cells from WAS patients and restores their normal cytotoxic function, by activating WAVE2^{203,204}. This was demonstrated by blocking WAS using the inhibitor Wiskostatin, which stabilizes WASp in its autoinhibited conformation and blocks its actin branching promoting activity. Using platinum replica electron microscopy, Orange et al. showed that treatment with Wiskostatin abolished the branched actin meshwork in treated NK cells, but IL-2 restored this branched network, suggesting that IL-2 can activate a mechanism to circumvent WASp inhibition²⁰⁴.

They also showed that IL-2 treatment is effective in restoring F-actin content and cytotoxicity in WAS patients.

b. WASp Interacting protein deficiency

WASp is found in association with WASp interacting protein (WIP), which plays a role in the control of WASp activation, by easing its activation by Cdc-42 and WASp recruitment to the IS²⁰⁵. WIP was shown to be recruited to the IS in NK cells²⁰⁰. WIP is activated by phosphorylation but interestingly, this phosphorylation is independent of the WIP-WASp interaction, thus suggesting an additional role for WIP²⁰⁰. It has been shown by triple-color FRET that both the activation and degradation of WASp are dependent on the phosphorylation state of WIP²⁰⁶

The mutation in the *WIPF1* gene located on chromosome 2 causes a decrease in the expression levels of the WIP, which consequently leads to the absence of WASp, despite the absence of mutations in the *WAS* gene. Moreover, expression of WIP in the cells of the patient restores the expression of WAS to normal levels²⁰⁷.

The clinical presentations of WIP deficiency resemble those of WAS, which include a failure to thrive, eczema, thrombocytopenia, ulcerative skin lesions, pneumonia and cytomegalovirus infection^{207,208}. The patient suffered from a reduced number of CD3+ cells, with a more notable decrease in CD8+ than CD4+ cells, as well as a reduction in B cells and an increase in NK cells. WIP was also shown to negatively impact the migration of T cells towards CXCL12 and CCL19, and the cells displayed a failure to elongate²⁰⁸.

Despite the normal expression of perforin in WIP patient CD8+T cells, the cells displayed a reduced ability to degranulate, which translates into a defect in cytotoxicity and elimination of target cells²⁰⁸. That can be explained by the fact that the patient cells were shown to be incapable of assembling the IS, rendering them incapable of polarizing their lytic granules. Moreover, patient T exposed an aberrant actin organization, where the dominant actin structures were elongated and filamentous, and oriented in one direction. This evidence supports the role of WIP in the control of the actin cytoskeleton and lamellipodia formation, therefore an essential role in the proper assembly of the immunological synapse.

c. ARHGEF1 deficiency

ARHGEF1 is an intracellular protein that has been shown to regulate migration and adhesion through its regulation of G protein-coupled receptor signaling and RhoA activation. It acts by stimulating the release of guanine diphosphate (GDP) to allow the binding of guanine triphosphate (GTP)²⁰⁹. The gene encoding ARHGEF1 is located on chromosome 19. ARHGEF1 deficiency symptoms include

respiratory tract infections including pneumonia. They also showed defective antibody production²¹⁰. One patient presented with mucoepidermoid carcinoma.

Both patients had low B cell counts with an elevated frequency of transitional B cells, with almost no memory B cells. NK, CD4+ and CD8+ T cells were within the normal range, with one patient showing an increase in naïve CD8+ T cells and a decrease in memory CD8+ T cells. The cells from these patients displayed normal levels of RhoA, but reduced RhoA activity, suggesting that the defect could be due to a Rho regulator. F-actin levels were lower in the patients than the healthy controls. Moreover, treatment of patient and normal donor T cells with the ROCK inhibitor Y-27632 caused no effect on F-actin levels in the patients but reduced their levels in normal donors to those comparable in the patients, indicating a role of ARHGEF1 in the RhoA-ROCK mediated actin polymerization. ARHGEF1 was also shown to play a role in mediating the LFA-1 dependent T cell adhesion to ICAM-1, but this was confirmed by siRNA not in patient cells²¹¹.

d. WDR1 deficiency

The deficiency in the WD repeat 1 gene, located on chromosome 4, leads to a deficiency in the actin interacting protein 1 (Aip1). WDR1 is composed of 9 repeats, which are 30-40 amino acids long. The patients present with mucosal and skin ulcerations, respiratory tract infections, stomatitis, periodic fevers and one patient died of sepsis. Patients present with mild to severe lymphopenia and suffer from recurrent infections. It has been shown that patients with WDR1 deficiency have neutrophil adhesion and migration defects, but such findings are beyond the scope of this manuscript^{212,213}.

WDR1 promotes actin filament disassembly through cofilin, and with the involvement of coronin. Indeed, WDR1 binds to cofilin-loaded F-actin to induce their rapid severing. THP1 cells transduced with shRNA targeting WDR1 do not show a defect in actin polymerization when assessed by flow cytometry, most likely because of mechanisms enabling the cells to compensate for the defects caused by WDR1²¹⁴. However, T cells from WDR1 patients left to adhere on slides coated with anti-CD3 Ab show increased spreading, as well as aberrant actin structures such as arcs, filopodia and spikes²¹³. Increased filopodia suggest an involvement of formins.

Even though B cells from patients migrate normally towards a CCL19 gradient, they display an increased adhesion and thin protrusions. They also display an increased accumulation of polymerized actin in the ventral plane of the cell, as shown by TIRF microscopy²¹³. This suggests that a WDR1 mutation affects BCR functions.

T cells from WDR1 deficient patients show a diminished to normal response to stimulation with anti-CD3 antibody, which may be explained by the need for the forces generation by the actin cytoskeleton

to activate T cells^{213,214}. However, the fact that WDR1 deficiency does not hinder the ability of patient T cells to migrate in response to CXCL12 or accomplish normal cytotoxicity suggest that WDR1 is not crucial in these aspects relying on TCR activation²¹³.

e. Coronin1A deficiency

The Coronin family is a family of highly conserved actin regulatory proteins. They bind to the Arp2/3 complex, but unlike other proteins, their role is the inhibition of actin nucleation²¹⁵. They contain 5 WD40 repeats, and their structure is reviewed in more details in^{215,216}. The gene encoding coronin 1A (*Coro1A*) is located on chromosome 16, and the Coro1A protein is a 57kDa protein that has the conserved WD repeats, and a leucine zipper motif²¹⁷

Coro1A, which is the member of the coronin family expressed mostly on hemopoietic cells, was shown to cause lymphopenia in mice, especially in T cells. SCID patients with *coro1A* deficiency were identified and exhibited T-B+ (NK+) SCID phenotype, as well as increased double-negative $\gamma\delta$ T-cells^{216,218–220}. The absence of naïve CD4+ T despite the presence of a thymus cells is attributed to the fact that Coro1A deficiency leads to distorted mitochondria, therefore leading to apoptosis²²¹. Coro1A deficient patients also suffered from upper respiratory tract infections; ear and sinus infections and inability to control EBV, associated with fatal lymphoproliferative syndrome and lymphoma at a particularly young age^{216,218}. In one patient, this was due to a mutation in one copy of Coro1A coding region, as well as a heterozygous deletion of p11.2 on chromosome 16²¹⁸. In this patient, this deletion is suggested to have predisposed her to attention deficit hyperactivity disorder.

Early assays of two-color confocal microscopy on mouse T cells and Jurkat cells showed co-localization between Coro1 and F-actin, within the T cell subcortical zone and in membrane protrusions, and that Coro1 accumulates in the protrusions caused by actin polymerization following cell contact with anti-CD3 Ab²²².

Coro1A plays its role in actin depolymerization in association to cofilin and WDR1. It performs its function mostly by redirecting the spatial organization and activity of cofilin in a way to disassemble older actin filaments²²³.

Mace and Orange have shown by confocal microscopy that Coro1A accumulates at the IS of NK cells in contact with their targets (Figure 12)²²⁴. A FRAP experiment in the same study shows that Coro1A is recruited to the synapse along with F-actin, and that it remains there for the duration of the mature synapse. Knock-down (KD) of Coro1A by shRNA in an NK cell line leads to a defective killing in these cells, due to a defect in degranulation (granule exocytosis), as shown by the decreased levels of

CD107a expression^{168,224}. However, confocal microscopy experiments show that Coro1A deficient cells can form conjugates with their targets, with no alteration of the size of the IS, the accumulation of LFA-1 at the IS and effective granule and centrosome polarization, all of which are actin-dependent processes (Figure 12). STED microscopy revealed that Coro1A KD does not hinder ARP2/3 recruitment but causes the accumulation of a greater density of F-actin in smaller area. This dense F-actin accumulation at the IS may be the reason the exocytosis of lytic granules is hindered, since degranulation requires a pervasive actin meshwork through which the lytic granules can be released, and since STED microscopy reveals that Coro1A KD leads to smaller clearances, and the association of the lytic granules with more dense actin, making Coro1A a probable key player in the residence of lytic molecules in the actin hypodense regions but not their movement²²⁴. NK cells from a patient presenting with a Coro1A deficiency show that, similarly to what is observed in the shRNA KD, the actin presents a smaller area, as well as smaller and fewer clearances, leading to a defect in granule exocytosis (Figure 14). The patient also displays a defective cytotoxic activity.

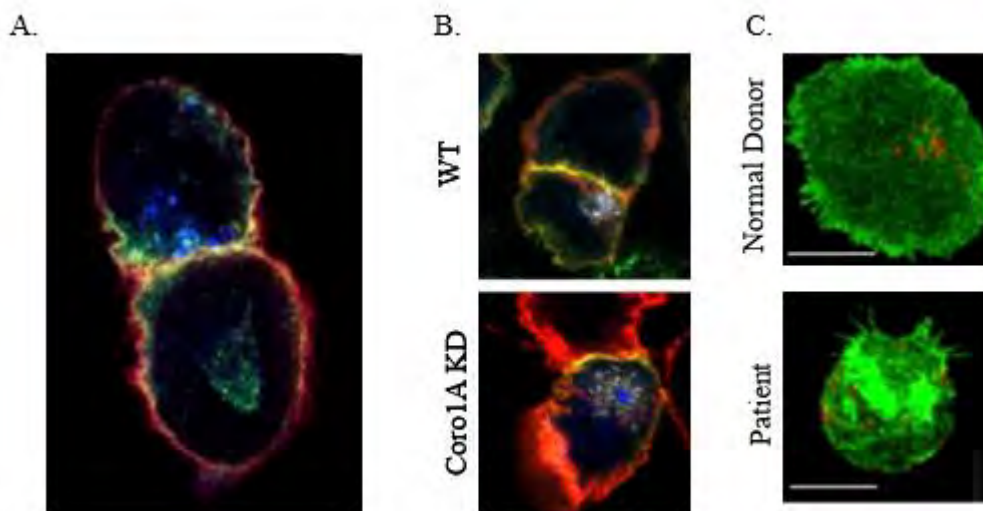


Figure 14: The role of Coronin1A in the immunological synapse of NK cells. A. Coro1A (red) colocalizes with F-actin (green) and polarized lytic granules (blue) at the NK cell immunological synapse. B. Coro1A KD does not alter IS size, F-actin (red), LFA-1 (green) recruitment to the IS and perforin (gray) and pericentrin (blue) polarization²²⁴. C. STED microscopy reveals a smaller but more intense F-actin (green) area with less pervasive areas, thereby hindering granule (red) release.

f. Cdc42 deficiency

Cdc42 is a RhoGTPase that acts upstream of WASp to activate it (when in its GTP bound state) and recruit protein kinase C θ (PKC θ) and talin to the cSMAC and pSMAC, respectively. Indeed, GTP bound Cdc42 binds to WASp, thus releasing the VCA region and allowing WASp binding to ARP2/3²²⁵. Cdc42 is activated more effectively by the β 1 integrin than by CD3, and the absence of the β 1 integrin can be partially compensated by LFA-1²²⁶. Ezrin has been shown to play a role in its activation. It has been shown that following TCR engagement, Cdc42, along with WASp, is recruited to the IS^{226,227}. T cells defective in Cdc42 fail to polarize F-actin at the IS when in contact with target cells, but this did not affect IL-2 production²²⁸. Therefore, Cdc42 has a role in multiple cellular processes involving the actin cytoskeleton, such as motility and endocytosis.

Patients with mutations in Cdc42 appear to have mid frontal bossing, failure to thrive, hepatosplenomegaly, transaminitis, recurrent febrile episodes, urticaria-like rashes, and significant cytopenia²²⁹. It has also been shown that when the Cdc42 defect is in the GTPase, the defect triggers the formation of broad lamellipodia and stress fiber assembly, while a defect where the rate of GDP/GTP exchange is elevated triggers filopodia formation and stress fiber dissolution²³⁰.

g. RhoA deficiency

RhoA, a 23kDA protein which is active when bound to GTP, plays a role in BCR signaling and induces the positive selection of CD8+ T cells. RhoA plays a role in T cell development and is important for the survival and proliferation of T cell progenitors in the thymus, as well as playing a role in thymocyte adhesion²³¹. RhoA inhibition also prevented Rac1 activation of integrins in thymocytes. Moreover, RhoA increases LFA-1 activation during lymphocyte migration, and most likely during the IS²³². RhoA can bind Rho-associated, coiled-coil-containing protein kinase (ROCK) and mDia. It also plays a role in uropod retraction, and microtubule formation at the uropod, and its absence leads to elongated cell tails. It is also important for the maintenance of cell shape. RhoA is also speculated to play a role in the control of IS size. (Reviewed in ²³³). Patients with low RhoA suffer from a defective antibody production, and in T and B cells there is a defect in F-actin polymerization as indicated by low levels of F-actin upon stimulation²¹⁰

h. RhoH deficiency

The RHOH gene located on chromosome 4 encodes an atypical, hematopoietic cell-specific member of the Rho GTPase family, which function as intracellular switches to transduce signals from several membrane receptors including the TCR and BCR. RHOH is constantly in its active GTP-bound active conformation^{234,235}. Moreover, it is essential for positive thymocyte

selection and for pre-TCR and TCR signaling because it allows the efficient interaction of ZAP70 with the LAT signalosome, thus regulating thymocyte development^{236,237}. Its interaction with ZAP70 is also essential for ZAP70 translocation to the IS^{237,238}. RhoH also plays a role in reducing the migration in response to chemokines and maintaining the contact with APC, by increasing both Rap1 activity and LFA-1 adhesion²³⁹. Indeed, cells that lack RhoH migrate faster in response to chemokines, while RhoH relocates along with LFA-1 to the IS upon T cell:target conjugate formation²³⁹. The patients suffered from Epidermodysplasia verruciformis and a human betapapilloma virus (EP-HPV). Consistent with findings in mice, RhoH deficient patients lack naïve T cells, and ZAP70 phosphorylation in response to stimulation with anti-CD3 Ab is defective, further enforcing the role of RhoH in TCR signaling²⁴⁰. It is most likely that these patient cells would display a defect in there is, given the role of RhoH in TCR signaling and IS stimulation.

i. DOCK2 deficiency

The DOCK180 related superfamily includes conserved genes which are guanine exchange factors, and that were shown to play a role in phagocytosis, cell migration and immune homeostasis. These proteins harbor a DOCK Homology Region-2 (DHR-2) domain that binds and activates Cdc42, Rac or another Rho family member to exchange GDP for GTP²⁴¹. Therefore, the DOCK family of proteins may be considered as guanine exchange factors (GEF). DOCK2 has been shown to be essential for the Rac1 signaling downstream of the TCR. Mice defective in DOCK2 harbor T and B cells fail to activate via Rac in response to chemokines, thus leading to migratory defects and suggesting a role of DOCK2 in cytoskeletal organization^{242,243}. DOCK2 patients presented with T and B cell lymphopenia, defective T cell proliferation, recurrent respiratory infection and pneumonia episodes²⁴⁴. One of the patients suffered multiorgan failure which caused his death. Similarly to mouse models, DOCK2 deficient patient cells exhibit defective Rac1 activation, as well as defective migration and F-actin polymerization²⁴⁴. NK cell cytotoxicity and IFN- γ were reduced, as well as the number of circulating NKT cells.

j. DOCK8 deficiency

Director of cytokinesis (DOCK 8) is a direct interactor GEF of Cdc42 (with little activity towards Rac1 and none with RhoA), and has been shown to mediate Cdc42 activation via its DHR-2, and was shown to be crucial for Cdc42 activation at the leading edge, therefore important in amoeboid migration^{245,246}. DOCK8 patients were reported to have SCID and be susceptible to viral (most common is herpes simplex virus) and cutaneous infections, therefore suggesting a defect of cytotoxic lymphocytes. Patients also presented with high levels of serum IgE and hypereosinophilia, low numbers of T cells and B cells, low serum IgM levels²⁴⁶⁻²⁴⁸. DOCK8 patient CD8 T cells show a decrease in naïve cells,

and the circulating cells display an exhausted phenotype and become unresponsive to TCR stimulation with anti-CD3²⁴⁹. Moreover, cells from these patients show a defect in proliferation, which is not overcome by the addition of exogenous IL-2²⁴⁹. Clonal expansion of CD4 T cells was also diminished.

In cell lines, DOCK8 was shown to be expressed in NK cell lines, but not the Jurkat T cell line, rendering it an incompatible model for such studies, even though Jurkat cell line is the most commonly used T cell line. In NK cell lines, Ham et al. have shown that depletion of DOCK8 with siRNA leads to a dose-dependent defect in cytotoxicity, as well as a decreased redirected cytotoxicity through FcR and NKG2D receptors, implying a role for DOCK8 in the cytotoxic function of NK cells²⁴⁶. Moreover, they have shown that DOCK8 plays a role in the upstream step of conjugate formation, where primary and NK cell lines deficient in DOCK8 showed defective conjugate formation despite the normal expression levels of CD18²⁴⁶. In primary DOCK8 deficient NK cells, the defect in cytotoxicity was confirmed, and it was shown that, similarly to T cells, it cannot be rescued by exogenous IL-2²⁵⁰.

It has been demonstrated by confocal microscopy that the CD8 T cells of mice harboring a DOCK8 deficiency show a defect in recruitment of LFA-1 to the IS, whereby the distribution of LFA-1 is reported to be uneven. Moreover, DOCK8 deficient mice cells failed to polarize actin to the IS²⁴⁹. Consistent with these findings, NK cell lines in which DOCK8 expression is suppressed by siRNA or shRNA, as well as primary NK cells from DOCK8 deficient patients show weaker accumulation of LFA-1 at the pSMAC, as well as a diminished F-actin accumulation, as well as a defective granule polarization (Figure 15)^{246,250}. Notably, the F-actin content in DOK8 deficient cells is the same as in healthy cells, as opposed to WASp deficient cells in which the overall actin content is reduced. Taken together, these data suggest a role for DOCK in cytotoxicity.

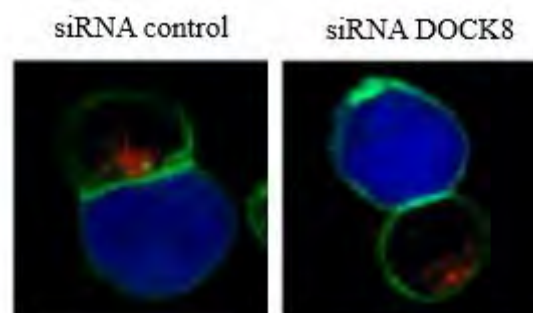


Figure 15: DOCK8 suppression leads to diminished F-actin (green) and lytic granule (red) at the IS²⁴⁶.

DOCK8 was also shown to be a direct interactor of WASp and talin, and to mediate their polarization to the IS in NK cells, therefore indicating a role for DOCK8 in actin reorganization and IS maturation²⁴⁶. However, the DOCK8 deficiency remains less severe than the DOCK2 deficiency.

k. PSTPIP1 deficiency

Proline-serine-threonine phosphatase-interacting protein 1 (PSTPIP1) gene located on chromosome 15, also known as CD2-binding protein 1 (CD2BP1) encodes for a cytosolic adaptor protein involved with activation, differentiation, and migration of T cells²⁵¹. PSTPIP1 also acts as a scaffolding protein for signal transduction towards the nucleus²⁵². PSTPIP1 has been identified in patients with pyogenic sterile arthritis with PG and acne syndrome, a rare autoinflammatory disorder with autosomal dominant inheritance^{251,253,254}. Patients with PSTPIP1 deficiency presented with an immunodeficiency phenotype, but no symptoms of autoinflammation. They also presented with recurrent viral and bacterial respiratory tract infections and low IgG and IgA levels (low IgM for one patient). Their T cells were mostly naïve T cells, there was a reduction of CD4+ T cells in one patient, and there was a reduction in B cell numbers²⁵². PSTPIP1 acts a scaffold protein to allow protein tyrosine phosphatase (PTP-PEST) to dephosphorylate WASp²⁵⁵. Therefore, through its interactions with CD2 and WASp through PTP-PEST, PSTPIP1 plays a role in F-actin dynamics and the establishment of a stable IS. In one patient, CD4+ T cells showed a pre-activated F-actin status, therefore failing to modulate their actin cytoskeleton in response to stimulation with anti-CD3 Ab, as well as higher baseline levels of calcium ion than normal controls²⁵². CD4+ T cells from patients were also more motile, which may explain their failure to respond to TCR/CD2 stimulation. Jurkat T cells transfected with plasmids encoding PSTPIP1 mutation and either left unstimulated or stimulated with antiCD3/anti-CD28 beads and imaged with confocal microscopy showed more baseline F-actin levels when unstimulated, but a failure to recruit F-actin to the IS upon stimulation²⁵².

l. STK4 deficiency

Serine threonine kinase 4 (STK4), previously named Mammalian sterile-like protein 1 (MST1), encoded by a gene on chromosome 3, is a ubiquitous protein that plays a dual proapoptotic and antiapoptotic role. Its proapoptotic role is suggested by the fact that in resting conditions it is a 63kDa cytosolic protein which becomes cleaved by caspases²⁵⁶. STK4 deficient patients presented with neutropenia, recurrent fever and recurrent respiratory tract infections, mouth ulcers, sinusitis, eczema-like rashes and skin abscesses²⁵⁶⁻²⁵⁸. Patients also presented lower levels of CD4+ and low to normal CD8+ T cells, as well as slightly lower B cell count, and a normal NK cell count^{256,257}. T cells from

MST1 deficient patients exhibit a defect in proliferation, and higher apoptosis rates than healthy controls^{256,257}. Recurrent episodes of neutropenia also suggest a role for STK4 in neutrophils. Unfortunately, the data on patients deficient in MST1 is limited. Moreover, MST1 was shown to play a role in the regulation of the IS, where it plays a role in the transport of TCR to cSMAC²⁵⁹. It also phosphorylates VASP, which is a player in the F-actin polymerization. More on the role of MST1 can be found in the review²⁵⁹

m. RASGRP1 deficiency

RASGRP1 is a guanine nucleotide exchange factor whose gene is on chromosome 15. RASGRP1 is an activator of the RAS-MAPK pathway following TCR signaling. Following TCR stimulation, RASGRP1 translocates to the membrane and converts RAS, a GTPase, from an inactive GDP-bound form to an active GTP-bound form, which in turn processes mediates activation of the MAP-kinase. Therefore, and as confirmed by mouse studies, RASGRP1 plays an important role in T cell proliferation and development and survival^{260,261}. The RASGRP1 deficient patient presented with recurrent infections including pneumonia, failure to thrive, and finger clubbing²⁶². The patient presented a decreased CD4+ T cell and B cell count, increased CD8+ T cells of which T $\gamma\delta$ cells were increased. Moreover, T $\alpha\beta$ CD8+ displayed an exhausted phenotype. CD4+ and CD8+ T cells displayed a failure to proliferate upon anti-CD3/CD28 Ab stimulation. Despite the increased expression of perforin and Gzm B in patient CD8+ T and NK cells, they failed to eliminate target. In NK cells, it was shown by confocal microscopy that this defect was due to the defective IS formation, with decreased F-actin accumulation, increased distance from the MTOC to the synapse and defective granule convergence (Figure 16), as well as reduced granule motility as shown by video microscopy. Defects in granule motility and convergence may be attributed to the inability of RASGRP1 to bind dynein. CD8+ T cells showed a reduced migratory speed in response to CXCL12 gradient, which due to a slower actin turnover. B cells also showed defective BCR stimulation and defective MAPK activation.

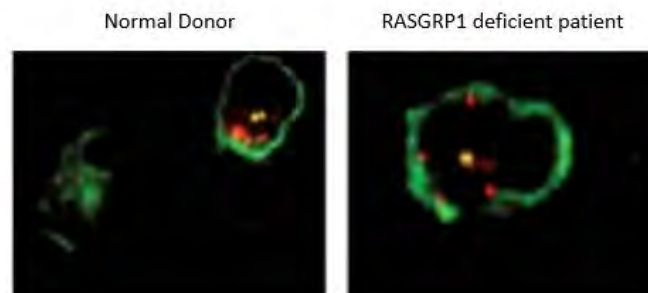


Figure 16: Defective RASGRP1-deficient NK cell IS assembly. Immunological synapse from a healthy donor and RASGRP1 deficient patient shows reduction in F-actin (green) accumulation, increased MTOC distance from IS (pericentrin; yellow) and a defect in lytic granule (red) convergence²⁶².

n. MKL1 deficiency

Megakaryoblastic leukemia 1 (MKL1), also known as MAL or myocardin-related transcription factor A (MRTF-A) and encoded by a gene on chromosome 22, is a coactivator of serum response factor, which regulates transcription of actin and actin cytoskeleton-related genes. Indeed, MKL1 exists in the cytoplasm in its inactive state as a reversible complex with actin. Rho GTPase stimulation promotes incorporation of G-actin into F-actin filaments, thereby releasing MKL1 from G-actin and allowing its import to the nucleus. In the nucleus, MKL1 functions as coactivator of serum response factor (SRF) and stimulate SRF-mediated transcription of actin and actin cytoskeleton-related genes^{263,264}. The patient presented with malignant otitis, as well as *P. aeruginosa* infection, chickenpox and painful skin lesions. Blood counts were normal, but T cells failed to activate in response to stimulation with anti-CD3 Ab²⁶⁵. F-actin levels in both myeloid and lymphoid cells were reduced. shRNA inhibition of MKL1 in THP1 cells (DC cell line) showed depletion of F-actin, poor adhesion to fibronectin, reduced spreading, and defective podosome assembly, as well as impaired fibroblast migration along with altered cell shape and loss of cortical actin and stress fibers. In neutrophils, chemotaxis was aberrant and disruption of Myosin II interaction with F-actin using Blebbistatin produced impaired uropod retraction similar to that in MKL1 deficient cells, suggesting that MKL1 deficiency could impair neutrophil migration through effects on Myosin II.

o. Moesin deficiency

Moesin (MSN) belongs to the ezrin- radixin-moesin (ERM) proteins, which are a family of widely distributed membrane-associated proteins that link plasma membrane proteins with actin filaments in the cell cortex. They exist in the cytosol in their auto-inhibited form, and can be activated by binding to membrane phosphatidylinositol 4,5-bisphosphate²⁶⁶. Lymphocytes express primarily ezrin and moesin. MSN is expressed on the X chromosome. Mice with MSN deficiency exhibit lymphopenia and a systemic lupus erythematosus -like disease, suggesting a role of MSN in the regulation of Treg homeostasis²⁶⁷. MSN deficient patients presented with varicella zoster virus infections, as well as respiratory tract infections²⁶⁸. Blood cell counts revealed low NK, CD4+T, CD8+ T (as well as exhausted CD8+ T cells) and B cell count, and neutropenia and microcytopenia^{268,269}. T cell proliferation following stimulation with anti-CD3/CD28 Ab was impaired. IS was not impaired in MSN deficient cells and neither was F-actin content, but migration and adhesion were. However,

cytotoxicity was not assessed, but it may be affected given that MSN is a regulator of the actin cytoskeleton.

p. Rac2 deficiency

Ras-related C3 botulinum toxin substrate 2 (RAC2) is a hematopoietic-specific member of the Rho family of guanosine triphosphatases (Rho GTPase) and encoded on chromosome 22. Rac2GDP can be activated by a GEF and RAC2-GTP drives several cellular functions through association and activation of downstream effector proteins. Activation of these downstream targets leads, among other, to actin cytoskeleton rearrangement and thymic T-cell selection. Indeed, RAC2 is involved in the cycling of actin between G-actin and F-actin states through interactions with cofilin and the ARP2/3 complex²⁷⁰. The patients presented with failure to thrive, recurrent pneumonia, followed by edema, proteinuria, urinary tract infections, cellulitis and membranous glomerulonephritis, undetectable IgA and increased IgG, a normal T cell count and a slightly decreased B cell count in one patient and a reversed CD4+:CD8+ T cell ratio and severe B cell lymphopenia in the other^{271,272}. Rac2 is mainly studied in neutrophils, and patient neutrophils from Rac2 deficient patients exhibit an abnormal chemotaxis, and constantly high levels of F-actin, suggesting that the role of Rac2 in actin cycling between its two forms is impaired^{272,273}.

q. Myosin deficiency

Myosins are actin-dependent molecular motors that use the energy of ATP hydrolysis to move along actin filaments. Myosin II in non-muscle cells plays important roles in cytokinesis and cell migration, and the most abundant form is IIA (MyH9). Indeed, to migrate forward the cell must retract its trailing edge by combining both the acto-myosin contractility and the disassembly of adhesions at the rear (uropod)¹²⁵. The actin filaments generated via ARP2/3 elongation are organized by Myosin II into antiparallel concentric arcs in the pSMAC, as revealed by SIM imaging of Jurkat cells and primary mouse T cells²⁷⁴. It has been shown that upon LFA-1 binding to ICAM-1, LFA-1 associates with MyH9²⁷⁵. Treatment with Blebbistatin, a MyH9 ATPase inhibitor, and siRNA inhibition of MyH9 both result in a polarized cell morphology, in which the uropod was extended in length as opposed to shorter uropods in untreated cells. This suggest that MyH9 binding to LFA-1 and the force it exerts is essential for the LFA-1 de-adhesion at the uropod²⁷⁵. However, MyH9 association to LFA-1 is not required for LFA-1 activation nor its recruitment to the leading edge of the cell.

In 2004, Jacobelli et al. Showed that MyH9 function is essential for maintenance of the uropod and for T cell motility but is dispensable for synapse formation, even though Ilani et al. show that it is recruited to the IS and essential for its stability^{276,277}. However, mouse experiments revealed that siRNA

inhibition of MyH9 leads to more spread IS, suggesting that MyH9 plays a role in constricting IS size, as well as playing a role in pSMAC and cSMAC formation regardless of the concentration of MHC available, but not for TCR microcluster transport²⁷⁸. Conversely, Yu et al. demonstrate that Myosin is required in the TCR transport in the first two minutes of IS formation, and that its inhibition by Blebbistatin affects the directed TCR movement²⁷⁹. Treatment of Jurkat cells with Blebbistatin and shRNA inhibition in primary CD4+ T cells and observation with TIRF microscopy of supported planar lipid bilayers reveals, on the other hand, that MyH9 activity is required for centripetal TCR microcluster movement, but not for microcluster formation²⁷⁷. Ilani et al. also show a role for MyH9 in TCR signaling²⁷⁷. Moreover treatment with Y-27632, which inhibits Myosin-II contractility by specifically targeting rho-associated protein kinase (ROCK) leads to a perturbed IS²⁸⁰. In NK cells it was shown that NK MyH9 deficiency causes an inability of NK cells to properly polarize their granules to the immune synapse and subsequently degranulate and lyse target cells²⁸¹. Moreover, it was shown to polarize at the IS but its absence does not affect IS formation. MyH9 constitutively associates with lytic granules and plays a role in their fusion with the cell membrane, as shown by siRNA inhibition or Blebbistatin treatment⁷⁰. MyH9 also plays a role in B cell migration but not BCR signaling, as shown by use of Blebbistatin and mouse models²⁸². Mutations in the motor domain Myosin II heavy chain lead to MYH9-related disease, characterized by hematologic defects such as macrothrombocytopenia and in some cases cataracts, deafness, and glomerulonephritis²⁸³. However, mutations in the tail domain of Myosin IIA lead to no relevant clinical symptoms²⁸⁴.

r. ARPC1B deficiency

The actin nucleator ARP2/3 is composed of 7 subunits (Figure 17) The Arp2 and Arp3 subunits act as monomers from which new actin filaments elongate in a 70-degree orientation and recruit and hydrolyze ATP²⁸⁵. The remaining subunits (the isoforms ARPC1A, ARPC1B (encoded by a gene on chromosome 7), ARPC5, and ARPC5L, and ARP4) organize to form the structural core of the complex, providing an interface for binding to preexisting actin filaments and regulatory cofactors. Indeed, activated WASp binds to ARP2/3 and delivers the first G-actin via its VCA domain, and WAVE binds to the complex as well^{286,287}.

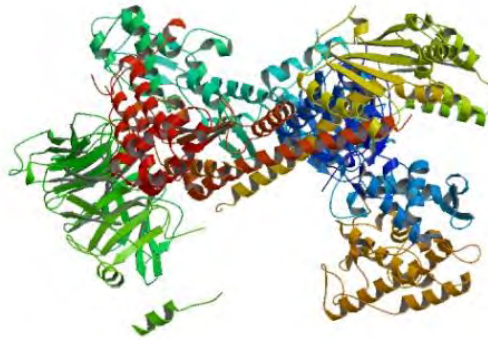


Figure 17: Crystal structure of the ARP2/3 complex from *Bos taurus* access protein data bank:1K8K²⁸⁸

Patients with ARPC1B deficiency present with a very early onset of 2 months on average. The first patients with an ARPC1B mutation were reported in 2017, and more have been reported since then. ARPC1B deficient patients presented with failure to thrive (due a partial growth hormone impairment), recurrent bacterial and viral infections and hemorrhages, platelet abnormalities, eosinophilia, enterocolitis, small vessel vasculitis, eczema and other indicators of inflammatory/immune disease, and such a phenotype was described as “WAS-like”^{288–291}. The patients presented with an increased amount of B cells, and decreased CD4+ and CD8+ T cells, including a reduction of naïve T cells²⁸⁹.

ARP2/3 was recently shown to colocalize with actin at the IS and at lamellipodia, suggesting that the defects observed in ARPC1B deficiency may be attributed to defects in cytoskeletal organization, especially that ARPC1B cells display a defect in actin polymerization^{288,291,292}. Moreover, in patients with ARPC1B deficiency, levels of ARPC1B in PBMCs are reduced and the distribution is, as revealed by confocal microscopy, in large patches instead of an even distribution along the actin cortex²⁸⁸.

ARPC1B deficient patient T cells fail to spread radially on an ICAM-1/Anti-CD3 Ab coated surface, and they emit thin filopodia, which are under the control of formins, as can be inferred from their abolishment upon treatment with SMIFH2^{274,288,292}. Moreover, they require more time to form weak conjugates and a very narrow, F-actin poor contact area with target cells, due to the failure to accumulate or deplete F-actin^{288,292}. Treatment of T cells with the ARP2/3 inhibitor CK-666 - which like CK-869 maintains the ARP2/3 complex in an inactive state blocking formation of the short pitch Arp2-Arp3 dimer - was shown to reduce T cell cytotoxicity, as well as reduced actin accumulation as compared to the inactive CK-689^{292,293}. Inhibition with CK-666 also abolished lamellipodia (which

were replaced by small blebs), and treated cells showed a slower migratory speed²⁹². Therefore, the ARP2/3 complex is involved in CTL migration and cytotoxicity.

ARPC1B deficient T cells show a reduced migration in response to CXCL12, reduced degranulation, reduced centrosome polarization and a reduced ability to lyse targets, which are due to defective TCR signaling, as well as a reduced Gzm B content²⁹². Of note, even though ARPC1B deficient cells could secrete granules, the defect in degranulation can be traced back to the fact that only a minority of lytic granules are polarized to the IS. Some ARPC1B deficient CTLs (perforin positive) showed a loss of CD8 as well. ARPC1B deficient CD16^{neg}CD56^{bright} NK cells also show defects of degranulation and cytotoxicity, which may be partially restored with IL-2²⁸⁹.

The study of patients with several immunodeficiencies related to the cytotoxic function lead to the observation that ARP2/3 is a key player in the regulation of the cytotoxic function in lymphocytes. Therefore, it would be interesting to study the response of the ARPC1B deficient cells to different levels of activation by anti-CD3 and assess their cytotoxic potential under these different levels of activation.

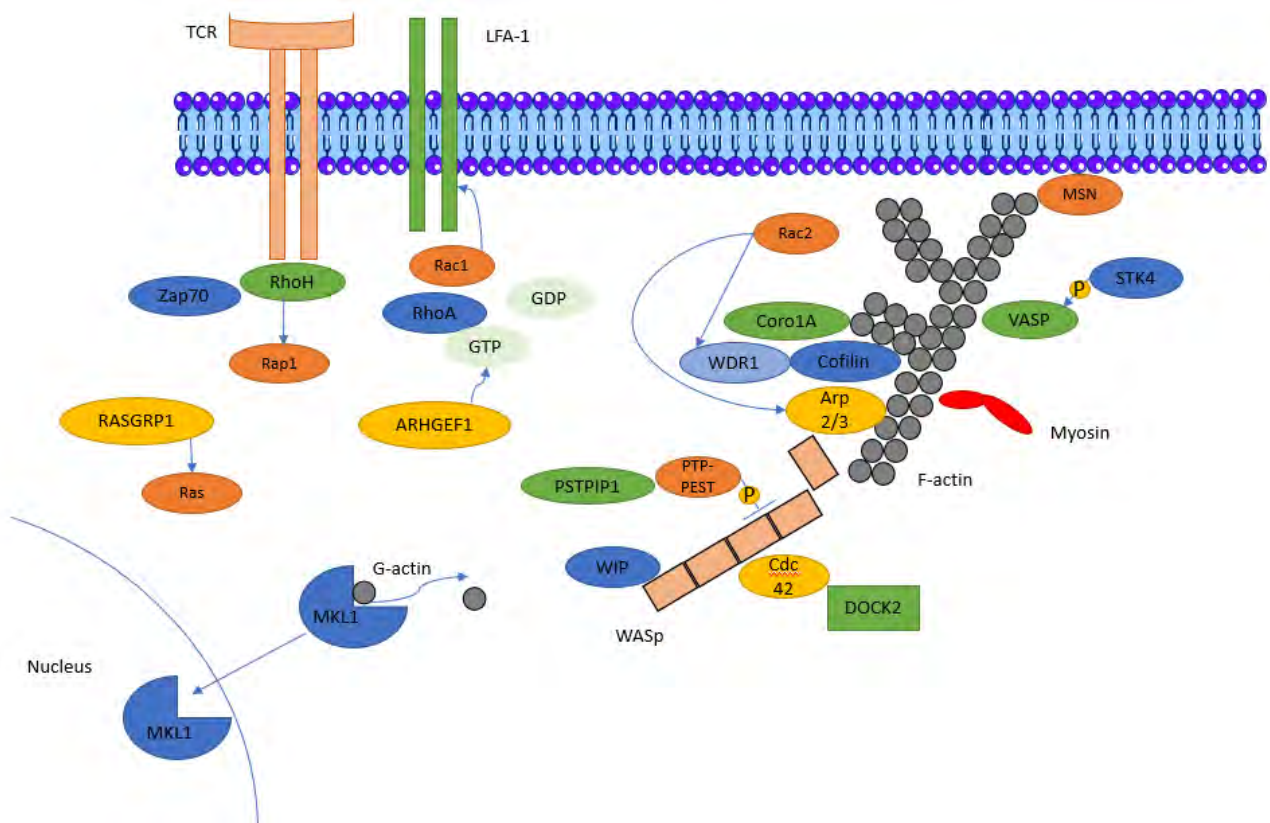


Figure 18: PID-associated actin regulators

4. Methodologies to assess defects in cytotoxicity.

To assess the defects in cytotoxic lymphocytes in patients or mouse models, different methodologies exist. In this chapter, the methods employed to assess functional defects in the PIDs mentioned in this chapter will be elaborated, following the logical order of the steps of cytotoxicity.

A defect in actin content or polymerization may be assessed by flow-cytometry, as done for WDR1, DOCK2, DOCK8, Rac2 and ARPC1B^{214,244,250,273,291}.

Defects in lytic granule content are generally assessed by flow cytometry, as was done for RASGRP1²⁶².

Conjugate formation capacity can be assessed by flow cytometry or immunofluorescence, as was done for DOCK8 and Coro1A respectively^{224,250}.

The immunological synapse is typically monitored by confocal microscopy. It has been shown that WIP deficient cells display actin organization and form improper IS²⁰⁸. WDR1 deficient cells are more spread and form actin arcs²¹³. Coro1A cells form a synapse of normal size while Myh9 deficient cells appear to spread more than control cells and ARPC1B deficient cells display a failure to spread radially^{224,278,292}. DOCK8, PSTPIP1, RASGRP1 fail to recruit actin to the IS^{246,252,262}. Coro1A deficient cells can successfully recruit LFA-1 to the IS, which is not the case for DOCK8 deficient cells^{224,246}. Granule convergence at the MTOC appears defective in Lyst deficient cells, and the granules appear larger in size than controls²⁹⁴.

Defective degranulation can be monitored by flow cytometry, by monitoring the levels of CD107a exposure by flow cytometry, as was done for WIP, Coro1a, Rab27a and Lyst^{183,185,208,224}. It can also be monitored by observing the recruitment of lytic granules to the IS, where it has been shown that while Munc13-4, Munc18-2, Coro1A can usefully polarize their granules to the IS, DOCK8 and STX11 and MyH9 deficient cells fail to do so^{176-178,181,224,246,249,250,281}.

Finally, the ability of cytotoxic cells to eliminate target cells can be assessed by flow cytometry, where it has been shown that WASp, WIP, Coro1A, DOCK8, Rab27a, Munc18-2, Lyst and ARPC1B have impaired ability to eliminate target cells with respect to healthy controls^{180,182,202,208,224,246,250,292}.

Table 2 below summarizes the criteria used to assess IS defects in cytotoxic cells by immunofluorescence.

Defect	Assessment measurement
Actin Organization	Actin intensity at IS

Cell Spreading	Cell area
Radial spreading	Cell width to length comparison
Lamellipodia formation	Cell Roundness
Granule polarization	Distance from lytic granules to IS
Granule size	Individual granule size measurement
Degranulation	Granule fusion with the IS
LFA-1 recruitment	LFA-1 intensity at the synapse

Table 2: Main criteria used in the assessment of a defective immunological synapse in cytotoxic lymphocytes by immunofluorescence.

This shows that there is currently no systematic and unified process of detecting defects in the cytotoxic activity of lymphocytes, and that several tests are usually performed to assess it. Therefore, there is a need for an approach which can predict a functional defect in the cytotoxic activity of NK and CD8+ T cells.

5. Microscopy imaging of biological objects

In the previous section, I have tried to highlight the importance of the cytotoxic function of T and NK cells, as well as the important role of the immunological synapse in the context of cytotoxicity. In the next section, I will highlight the importance of microscopy in immunology, as well as the advantages of high content imaging pipelines as opposed to traditional low throughput microscopy.

The human eye is highly capable of viewing different objects of varying sizes. However, the smallest it can see is an object of around 100 μ M, when that object is about 25 cm away.

The human eye is thus incapable of seeing infectious organisms such as bacteria, without an object that would enhance their size. For that reason, the microscope, which was invented by Antoni Van Leeuwenhoek and Robert Hooke, has proven to be a vastly useful tool. A microscope is therefore a tool that allows one to see samples while enhancing their size through one or multiple lenses. Any sample that allows light to pass through it may be viewed with a microscope.

5.1 The basics of microscopy

A. Light sources to illuminate a sample

Every microscope essentially needs a light source, and the light is composed of an electromagnetic wave having a specific wavelength, and photons. Lights can illuminate a sample either directly

(transmission) or can be reflected through a mirror before hitting the sample (reflection). Light can be divided into two main categories: brightfield and fluorescence.

Widefield microscopy consists of the microscope forming an image of the object on the camera. For widefield imaging, traditional lighting methods include xenon, mercury and halogen lamps, combined with excitation and emission filters, as well as shuttering devices which control the duration of illumination. Light emitting diodes (LEDs) are also a cheap and stable alternative. LEDs can be turned on and off rapidly, eliminating the need for shutters²⁹⁵.

Fluorescence microscopy relies on the use of fluorophores (fluorescent dyes) which absorb one wavelength of light and emit another. Techniques to introduce fluorescence to biological cells include fluorescent antibodies which bind to specific proteins (a process termed immunofluorescence), and genetic manipulation to introduce fluorescent proteins into the cell. LEDs can also be used for fluorescent microscopy due to a narrow emission spectrum, as have been designed to provide illumination at very specific wavelength bands from UV to infrared^{295,296}. Confocal microscopy is also used to illuminate fluorophores, where the sample is illuminated by a laser beam at a single point in the focal plane²⁹⁷.

B. From an object to an image

When light passes through lenses, the image can be enlarged to different sizes, depending on the magnification of a given lens. Light exiting a lens and rays parallel to the optical axis may only be converged onto one focal point if the lens is spherical. The objective lens typically determines the magnification and resolution of an image, as well as the sensitivity of the microscope with regards to how much light will be collected from the sample. Magnification refers to how large the final collected image will be with respect to the sample.

The object being detected by a microscope is referred to as a sample, and it should be placed on a support in order to be illuminated. Therefore, an essential characteristic of a sample is that it should allow the passage of light.

The human eye is the structure that detects the image in the context of a simple light microscope.

However, most commonly used nowadays is a camera, which also allows saving images. However, noises may occur and interfere with proper image detection. Notably we name the black noise

generated by the camera, the reading noise caused by the electronic signal amplification and the photonic noise due to the random nature of the light.

The term “resolutive” is employed to refer to a microscope that can detect two close points as separate. In other terms, the resolution of a microscope is defined as the smallest distance between two points of a sample at which they can still be distinguished as two separate points. This distance, as demonstrated by Abbe in 1873, has been shown to depend on the light diffraction from the sample through the lens. The formula to determine resolution is:

$$d = \lambda / NA,$$

where λ is the wavelength of light and NA is the numerical aperture of the objective lens.

Technological advancements in the field of microscopy are always aiming to increase the resolution.

5.2 The timeline of microscopy in biology

The discovery of microorganisms through microscopes began in the 17th century with the Dutch scientist Antony Van Leeuwenhoek, who created lenses with 300x magnification, and used single lenses to view his samples, and referred to what he saw as “animalcules”. Hooke, a contemporary of Van Leeuwenhoek, also created settings that allowed object magnification and imaged seeds, the eyes of a fly and the structure of a cork. He however used compound lenses, which resulted in more aberrations due to the lenses themselves at the time.

In the nineteenth century, the theoretical and technical aspects of the modern light microscope were developed. The most notable are diffraction-limit theory, aberration-corrected lenses and an optimized illumination mode called Köhler illumination.

In 1868, Abbe invented the apochromatic lens, using more fused lenses, which better corrected chromatic and spherical aberrations. In 1883, he collaborated with Schott, a glass chemist, to produce the first lenses that were engineered with sufficiently high quality to produce diffraction-limited microscopes.

Fritz Zernike developed phase contrast microscopy in the 1930s to overcome the poor contrast of transparent biological samples²⁹⁸. Smith and invented Nomarski invented differential interference contrast (DIC) in 1955, as an alternative to phase contrast²⁹⁹. The images produced are exceptionally sharp in comparison with other transmission modes. DIC is still the current standard technique for

imaging unstained microbiological samples in having an exceptional ability to reveal the boundaries of cells and subcellular organelles.

To improve contrast in biological samples, stains have proved to be quite a useful tool, especially stains that allow staining of specific parts of a sample.

The first reported staining of a biological sample was reported by von Gerlach in 1858, who managed to differentially stain the cytoplasm and the nucleus of brain tissue with carmine. Golgi introduced silver staining in 1873, through which he visualized the nervous system. In 1884, Gram introduced the Gram staining, which is until now still used to stain different bacteria. However, the revolution in microscopy staining of biological samples occurred upon the introduction of fluorescent stains. Stokes was the first to define fluorescence in 1852, as the emission of light at a wavelength different from that of excitation. In 1941, Albert Coons published the first work on immunofluorescence, where he used a fluorescein-derivative-labelled antibody and showed that it could still bind to its antigen³⁰⁰. This was the first steps towards the use of fluorescent antibodies as highly specific stains.

The first natural fluorescent stain used was green fluorescent protein (GFP), isolated from jellyfish in 1962³⁰¹. However, it was not expressed outside of jellyfish until 1994, when it was incorporated into a promoter gene for β -tubulin and shown to be useful in determining expression levels³⁰². A real breakthrough was optimizing a method to fuse the genes of a protein of interest with a GFP and express this in a cell while also leaving it relatively unperturbed. This was performed in 1994 by Wang and colleagues by fusing green fluorescent protein GFP to the *bcd* transcription factor in *Drosophila*³⁰³. Blue and yellow fluorescent proteins were produced by mutating GFP, while red fluorescent protein was produced from *Anthzoa*, a species of coral, in 1999^{304,305}. In 1980, Roger Tsien introduced the first calcium probe, capable of detecting cell membrane voltages and ion concentration³⁰⁶.

In 1946, Förster postulated that if a donor and acceptor molecule were sufficiently close together, non-radiative transfer of energy could occur between the two, now known as Förster resonance energy transfer (FRET)³⁰⁷. Fluorescence can be used as a metric of putative molecular interaction through FRET in the event that the donor and acceptor molecule are fluorescent dyes. Stryer & Haugland showed in 1967 that this phenomenon could be used as a molecular ruler over a length scale of approximately 1–10 nm³⁰⁸. Since then, FRET has been widely used to image molecular interactions and the distances between biological molecules, and also in fluorescence lifetime imaging³⁰⁹.

In 1964, Curtis introduced the principles of interference reflection microscopy (IRM), where the interference of reflected light waves generates images with high contrast and definition. This technique has been improved and is now used to study cell adhesion or cell mobility on a glass coverslip³¹⁰.

With all these advancements came the fluorescent microscope, specifically designed for samples to be stained and imaged with fluorescent dyes or probes. Fluorescent imaging techniques include confocal microscopy, total internal reflection fluorescence (TIRF) introduced in the 1980s, fluorescence recovery after photobleaching (FRAP) introduced in the 1970s, and two-photon and light-sheet microscopy. TIRF microscopy is based on the principle that when excitation light is totally internally reflected in a transparent solid at its interface with liquid, the evanescent wave (an electromagnetic field), is generated in the liquid at the solid-liquid interface and is the same frequency as the excitation light. The intensity of the evanescent wave exponentially decays with distance from the surface of the solid, and only fluorescent molecules within a few hundred nanometers of the solid are efficiently excited³¹¹.

Two-photon scanning laser microscopy was introduced by Denk in 1990 and has since been used to observe molecules in live tissues³¹².

The confocal microscope was invented by Minsky in 1955 but the nomenclature “Confocal” was first used by Brakenhoff in 1979, to refer to a microscope where the illumination is in a diffraction-limited spot within the specimen, and where the detection is also confined by positioning an aperture in front of the detector in a position that would be optically conjugate to the focus spot³¹³. Confocal microscopy aims to eliminate the signals from fields other than the imaging plane, through the use of a pinhole, which would be situated in front of the detector. Laser-scanning confocal microscopes typically use point detectors instead of cameras to record an image point by point and are therefore less sensitive. To overcome this limitation, systems which scan multiple focus spots across the sample simultaneously and image the resulting emission on a camera have been designed. The spinning disk confocal is the most common, and it uses a disk of pinholes which sweep across the sample in a way that a revolution of the disk scans over every point in the sample during a single exposure³¹⁴. Spinning disk confocal microscopes have gained popularity given their high speed and sensitivity.

Even though the imaging of biological samples had come a long way, the size of the smallest object that could be imaged was still a limiting factor. Two objects could be separated (or resolvable) as long as the nearest-neighbor separation of the dye is greater than the limit of the optical resolution. In other words, the wavelength of the light used, as well as the objective used were the barrier to imaging single molecules. Hell and Wichmann were the first to show that it was possible to break the diffraction limit with a technique he called stimulated emission depletion microscopy (STED), and Hell and Klar implemented it in 1999^{315,316}. Alexa dyes also came to use in the late 1990s and are more fluorescent than the dyes previously used. Alexa derivatives coupled to phalloidin can be used to visualize F-actin,

and may also be used to detect antibodies³¹⁷. Currently, a common approach to stain cells is indirect immunofluorescence, where the cells are fixed, labeled with a primary antibody specific to the protein to be detected, followed by staining with secondary antibodies, which generally have a broad specificity and can be coupled to Alexa dyes.

In 2006, two new techniques were introduced. Photo-activated-localization microscopy (PALM) was used by Hess and Betzig, in which photoactivable proteins which change colors when exposed to UV light change colors^{318,319}. The main difference is that Hess and colleagues used TIRF while Betzig and colleagues used confocal microscopy. In 2006 as well, Rust and colleagues showed that by using a technique called stochastic optical reconstruction microscopy (STORM), they could generate a super resolution by using a Cy5/Cy3 switchable probe³²⁰. When the probe is illuminated by a red laser, Cy5 is kept in a dark state, while the pair is brought back to an excited state by a green laser.

Advancements have also been made in 3D imaging microscopy which allow the reconstitution of cells and even organoids. However, they will not be addressed in this manuscript.

The timeline of microscopy is summarized in Figure 19 below.

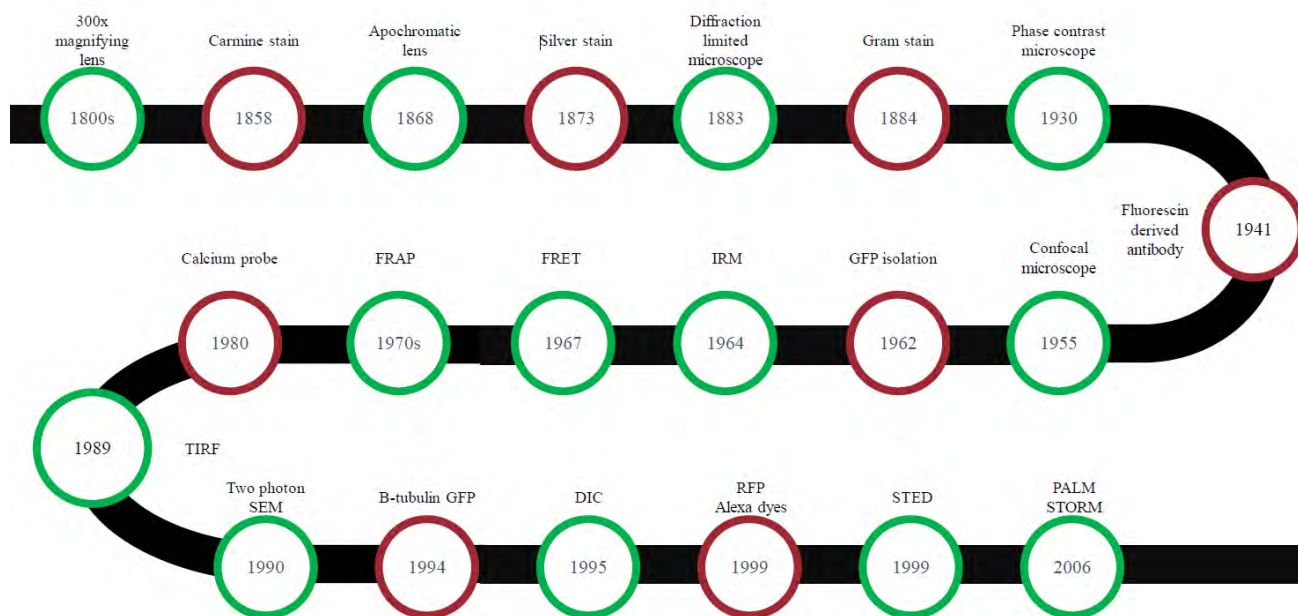


Figure 19: The timeline of microscopy

5.3 High content imaging: A game changer

One problem microscopy has faced is the time image acquisition and processing can take. This is true especially in a time where screens have become highly popular as an approach, and the fact that

phenotypic analysis can be a powerful technique to reveal information. Indeed, phenotypic analysis has been employed by Brenner who performed a screen on *Caenorhabditis elegans* to assess how different mutations could impact behavior, and by Nüsslein-Volhard and Wieschaus who performed a screen on the *Drosophila melanogaster* embryos to assess the effect of different mutations on the number and the polarity of the segmental patterns of the larva^{321,322}. However, these screens were manual and consequently laborious, which explains the need for an automated approach. Screens may be conducted in several different ways and may include biochemical assays, neurite growth assays, as well as translocation and differentiation assays (reviewed in³²³).

Screens can also include specific inhibitions with small interfering RNA (siRNA), short hairpin RNA (shRNA) and CRISPR cas9 screens, and include genome wide screens^{324–326}. Indeed, Carlin and colleagues have designed an siRNA screen and images samples using fluorescence lifetime imaging microscopy (FLIM), which is the optimized FRET technique to image protein interactions, and monitored the activity of Cdc42 and its interactors³²⁷. However, CRISPR cas9 screens are growing in popularity since shRNA and siRNA may generate off-target effects and incomplete inhibition³²⁸

High content screens are a useful tool in the identification of small molecules that may be used for drug development, as well as determining interactions between different proteins or compounds.

A. High content imaging: microscopy at a large scale

High content imaging (HCI), a term which began to be employed in the early 2000s, combines approaches of automated imaging and image analysis of cells and cellular organelles, to quantify phenotypic and functional parameters, usually linked to genetic or pharmacological perturbations. High content imaging, with its corresponding analysis methods, has become increasingly popular in the fields of drug or chemical compound discovery, as well as identification of gene functions, especially because it allows for quick, efficient and lower cost screens^{329–336}.

Some low content imaging approaches may be amenable to screening by high content imaging. Sieprath and colleagues have optimized an HCI protocol on fibroblasts seeded in 96 well plates, where they use live imaging to assess the levels of reactive oxygen species as well as mitochondrial membrane potential and mitochondrial morphology³³⁷. Szalai and Engedal have optimized a protocol for the assessment of real-time cell proliferation and death in a prostate carcinoma cell line³³⁸. Massey has developed an HCI approach to measure target engagement in living adherent cells based on the principle of altered protein thermal stabilization or destabilization in response to ligand binding³³⁹.

HCI has several biological applications and may be used to answer different biological questions. The following pages will focus on the questions that may be answered with HCI, and the tools needed for such screens.

a. HCI screens may be used to define gene function.

Bai et al. used an siRNA HCI screen to knock-down 26 genes whose function was not previously assessed, in a prostate carcinoma cell line and showed that 25 of these genes affected cytoskeletal organization or cell shape³⁴⁰. Indeed, they used 14 morphological including parameters pertaining to F-actin, cell shape and area. Chia et al. showed, by using an HCI on a genome-wide siRNA screen in human embryonic stem cells (hESC), that PRDM14 is a crucial transcription factor required for the maintenance of hESC identity and the re-acquisition of pluripotency in human somatic cells³⁴¹. It has been shown that an HCI RNA screens can be useful to determine genes involved in mitotic spindle formation in yeast³⁴². Indeed, an HCI screen coupled to gene knock-down has served to identify mutants with aberrant spindle morphology, by using 78 spindle-specific features for the analysis, as well as to identify new candidate genes that may play a role in spindle disassembly.

Billmann et al. have used an RNAi screen in *Drosophila*, to screen for modulators of the cell cycle. They started with a genome-wide RNAi screen where, following image analysis for nuclear and mitotic parameters, they selected 300 candidates to connect novel genes to known regulators of the cell cycle³⁴³.

b. HCI screens can be effective in determining gene interactions.

Genetic interactions can be assessed by using pairwise gene perturbations to generate interaction profiles. An image-based genome-wide RNAi screen in *Drosophila* cells has identified 168 genes whose phenotypic profiles are sensitive to MEK, involved in the MAP/ERK pathway³⁴⁴. Genes may also be co-depleted by RNAi and imaged by HCI to determine genetic interactions and generate correlation networks. Using this technique, it was determined that there is a link between Ras signaling and chromatin remodeling³⁴⁵.

Chong et al. have applied an HCI screen to budding yeast open reading frame (ORF) – GFP collection, where each of the ~4,100 strains carries a unique fusion gene construct in which an ORF is fused to the GFP gene, generating a full-length protein with a COOH-terminus GFP fusion, whose expression is driven by the endogenous ORF promoter³⁴⁶. They also introduced a cytosolic RFP, to create an automated platform to quantify the abundance and localization of these fusion genes, instead of the manual quantification that was applied³⁴⁷. Their results led to the generation of the abundance

localization map with 2834 proteins connected to at least one of the 16 quantitative localization scores that they defined for each protein and which reflect 16 defined subcellular compartments.

c. HCI screening is a useful tool to assess alterations to cell morphology in response to chemical compounds.

Coupling treatment with compounds to genetic perturbations may reveal how genes are sensitive to specific inhibitions³⁴⁴.

Bray and colleagues showed that it is possible to use six fluorescent dyes to perform what they describe as “Cell Painting”, in which they can reveal eight cellular components and organelles³³¹. Subsequently, they could extract roughly 1500 morphological features to describe their cells, and profile them accordingly. They then show that it is possible to profile cells treated with different chemical compounds and detect even subtle morphological differences.

A recent study by Caldera et al. has shown that it is possible to benefit from the interactome of the physical interactions of more than 16000 proteins and perturb them with chemical compounds, which they summarized in a 3D perturbation space^{348,349}. For that, they applied an HCI approach in the adherent MCF 10A cell line and showed that it is possible to use cell morphology to evaluate the interaction between different perturbations in high dimensionality space.

HCI may be used to determine levels of protein interactions in response to different chemical compounds. Priestly et al. have developed an immunocytochemical protocol in which they use HCI to determine the specific binding of Dickkopf-related protein 1, whose elevated levels have been linked to Alzheimer’s disease³⁵⁰. Using HCI they measured the specific binding of the protein to its receptor in response to treatment with different inhibitors.

d. HCI screens are a powerful tool to image disease models.

Schulte and colleagues show that high content imaging screens can be used to build a Huntington’s disease model and identify compounds which can rescue dystrophic neurite formation³⁵¹. Puls and colleagues have shown that it is possible to develop a 3D model of tumor invasion that is amenable to high content imaging screens, in which they could test potential drugs³³⁵.

Zahir et al. have recently shown that it is possible to use a high content imaging screen coupled to morphological profiling to assess the response of different strains of *E. coli* to different antibiotics³⁵².

Chakraborty et al. have shown that it is possible to design a FRET screen to determine the constant of dissociation between LFA-1 and ICAM-1, by using an LFA-1 molecule coupled to AF488 and an ICAM-1 molecule coupled to AF555⁹⁶.

The advantage that high content screens offer is the large assay format, where samples may be placed in 96 or 384 well plates instead of the traditional microscopy slides. Moreover, robotics has also been developed to minimize sample processing time and human error. High content imaging relies on fluorescence. Therefore, the typical fluorescent antibodies, proteins and dyes that are used in low throughput microscopy are commonly used. HCI may be used to establish a process of machine learning, where image “fingerprints” are extracted to define a specific cellular morphology, corresponding to a specific biological state. Once these fingerprints have been established, prediction models may be used to extract features from images and predict biological states³⁵³. Supervised training models refers to using a part of a whole set of images in order to establish these fingerprints, and then apply these models to the set and test their predictive performance. These steps can be summarized in figure 20, and image-based profiling will be elaborated further in the HCI analysis section.

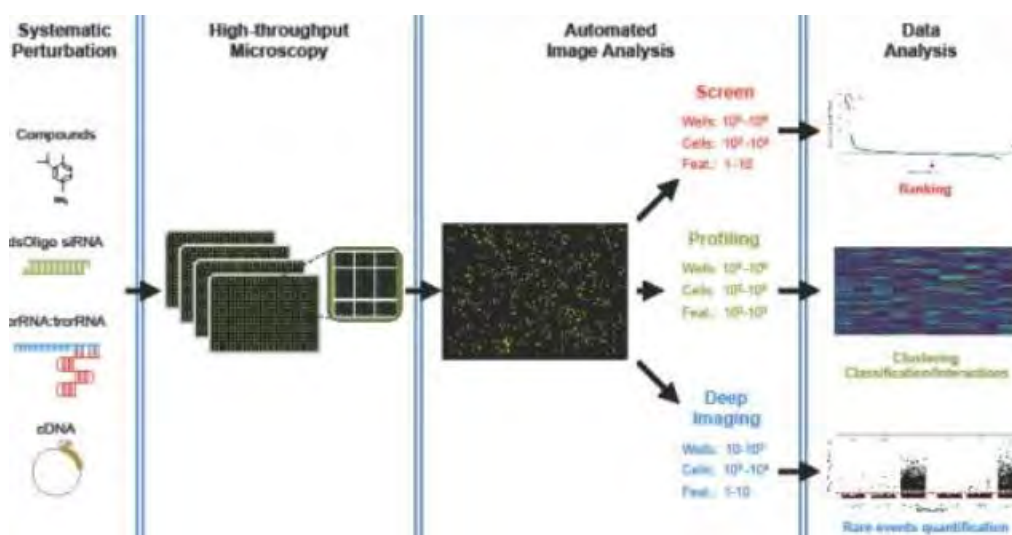


Figure 20 : A typical high-content workflow pipeline³⁵⁴.

B. Instrumentation: High content imaging requires specialized devices

Several companies have now worked on building high content imaging devices, to account for the growing need for such technologies in both basic research and drug discoveries.

ThermoFisher Scientific introduced the “ArrayScan” in 1999 and have over the years continues to produce several high content analyzers. They have recently released their latest model: the **CellInsight CX7 LZR** high content analysis platform, which comprises fluorescence microscopy, as well as automated image analysis tools to extract relevant information from the imaged samples. Their latest system is endowed with objectives that range from 2x to 60x magnification, a seven-color laser illumination source for confocal imaging with spinning disk technology, a 5 color LED array for brightfield imaging and HCS Studio Cell Analysis Software which allows a user-friendly image acquisition setup and result analysis.

From: ThermoFisher website.

BioTek have also developed two automated cell imagers: the **Lionheart LX** and the **Lionheart FX** automated microscopes. Both have objectives that can go up too 100x (oil immersion), can image more than 20 fluorescent colors, are endowed with image-based and laser-based autofocus, and allow for fluorescence, brightfield and high contrast brightfield microscopy. The Lionheart FX also allows color brightfield and phase contrast microscopy, and is endowed with CO₂ and pressure chambers, and temperature control. The Lionheart FX allows for fluorescent imaging in four channels and illumination with twenty filter/LED cubes, and can images cells in microscope slides, Petri dishes, flasks and microplates. They also offer “**Cytation5**”, which can go up to 60x magnification in fluorescence, brightfield, high contrast brightfield, color brightfield and phase contrast. It offers temperature and CO₂ control, and has aSony CMOS camera and imaging LED cubes and filter cubes to detect a wide range of fluorophores. Images acquired with BioTek devices can be analyzed with the Gen5 software.

From: the BioTek website

Molecular Devices offer the **ImageXpress Pico** automated cell imaging system, where images can be acquired by either brightfield or fluorescence with objectives that range from 4x to 63x magnification, humidity, temperature, CO₂, O₂ controls and pre-configured analysis protocols to facilitate image

analysis. It is illuminated with LEDs and has a Sony CMOS camera. It offers digital confocal deconvolution, which enhances image contrast, thus decreasing exposure time and allowing for imaging of clearer cell structures, therefore a more robust image analysis.

From: Molecular Devices website

Logos Biosystems offers “**Celena®**” **X** high content imaging system, which offers laser autofocus, live cell assay support, objectives that range from 1.25x to 100x, a vast selection of LED filter cubes adapted to a wide array of fluorophores. It offers fluorescence imaging in four channels, brightfield, color brightfield, and phase contrast imaging, and a user-friendly interface for both image acquisition and data analysis. It has a monochrome CMOS and an optional dual camera module.

From: Logos Biosystems website.

GE Healthcare Life Sciences offer the **IN Cell Analyzer 6500HS** system which comes as a successor to previous models, and which features the IRIS confocal technology for a better visualization and segmentation of biological objects, especially in thicker samples. It is a high content screening confocal microscope adapted for fixed and live-cell imaging and is illuminated with four lasers and has a sCMOS camera. Objectives range from 2x to 100x magnification, and the autofocus is maintenance is laser-based. The acquisition software of this device is user-friendly, and image analysis is performed with the IN Carta software, which also has an intuitive interface.

From: GE Life Sciences website

Another high content imaging system is the **Opera Phenix™**, developed by Perkin Elmer. It is a confocal microscope endowed with a Nipkow spinning disk with dual view confocal optics and up to four sCMOS cameras that allow simultaneous acquisition in up to four channels, with the advantage of a low signal: background noise ratio, a wide dynamic range and high resolution.

Being a spinning disk confocal microscope, it has an array of illuminated pinholes equally paced to illuminate the whole field of view and positioned at one of the microscope's intermediate image planes will create a de-magnified array of tiny excitation focal volumes at the nearest objective lens object plane. The spinning disk optics and precise excitation laser and camera synchronization lead to minimal phototoxicity and photobleaching. This minimalized spectral cross-talk allows for high

quality images and a reduced acquisition time (Figure 21). This microscope also offers the advantage of water immersion objectives, which capture more photons, thus increasing image resolution. Moreover, the system has a fast laser-based autofocus, thus ensuring the maintain of focus throughout different fields. The system also benefits from a CO₂ chamber and temperature control, to allow live cell imaging.

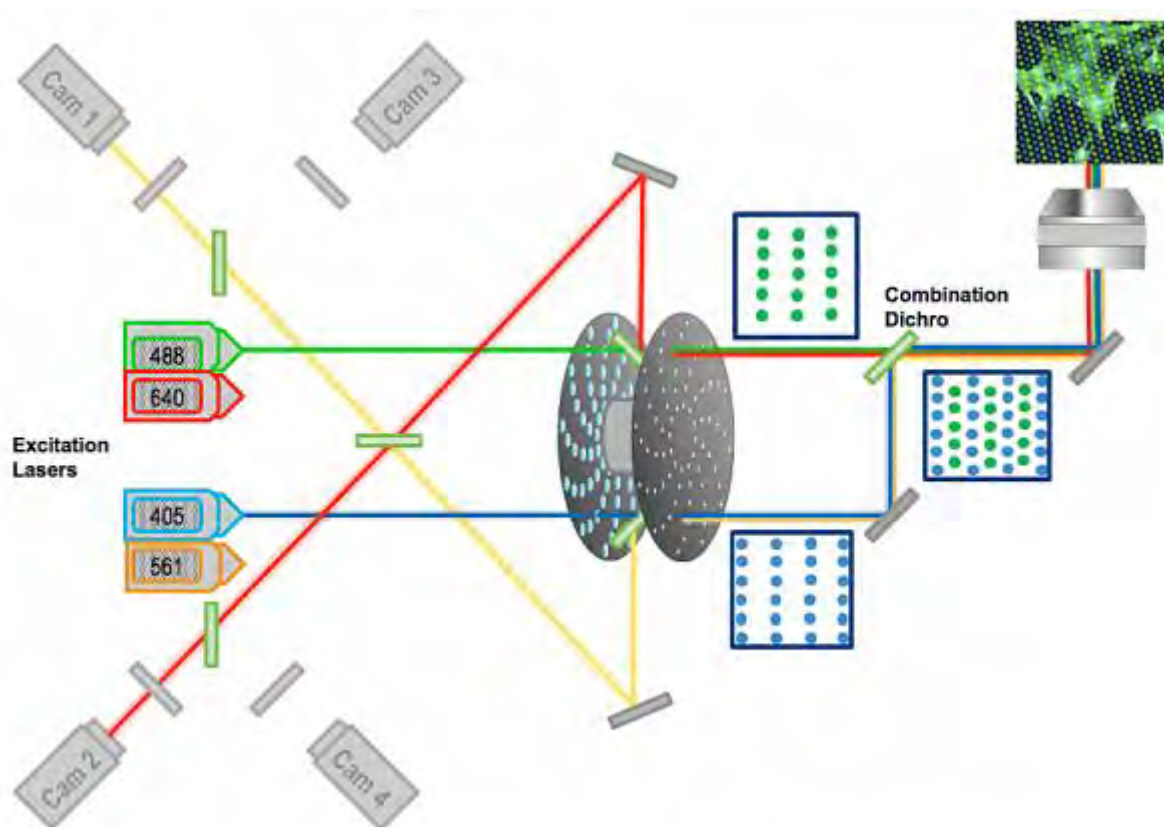


Figure 21: Schematic representation of the confocal light path of the Opera Phenix high content screening system. The projection of non-overlapping excitation pinhole patterns onto the sample achieves the separation of excitation and emission wavelength in space. Excitation lasers are placed into two groups in a way that adjacent laser lines are separated, and are focused through different quadrants, to allow the emission light passage only through the pinhole disc in the respective quadrant.

From: The Perkin Elmer website

C. High content imaging analysis requires specialized software

Companies developing and selling HCI microscopes usually develop in parallel compatible analysis software that may be purchased in parallel. Such software are specifically designed for the analysis of data from HCI screens. They are generally user-friendly and easy to navigate and may include pre-

designed analysis pipelines. They may be used to detect specific phenotypes of alterations to cell morphology or intensities of a fluorophore. However, such software may not be adapted for more complex questions which go beyond basic biology and require knowledge of bioinformatics to a certain extent. Therefore, there is the need for software that are more adapted to deal with such demands.

a. *CellProfiler*

CellProfiler is an open source image analysis software, developed by the Carpenter lab at the Broad Institute of Harvard and MIT. It allows the user to measure, simultaneously, several parameters related to cell size, shape, intensity and texture. Moreover, it is specifically designed to perform the analysis of data incoming from screens, in a high throughput and automated manner^{355–358}. CellProfiler is an easy to use software which can be installed on a personal computer to analyze a small number of images, while a larger number of images will have to be processed on a cluster. The details on how the software works, its advantages and its applications can be found in ³⁵⁵. Caldera et al. have used CellProfiler to analyze fluorescent microscopy images of cells treated with an array of drugs and extracted 78 morphological features (out of 438) to position each treatment within the 78-dimension morphological space³⁴⁸.

b. *EImage*

EImage is an image processing toolbox for R whose features include multi-dimensional image processing, a range of fast image processing functions, support of more than 80 image formats, fast interactive image display. It allows for automated phenotyping of images by performing the steps of segmentation, feature extraction and statistical analysis, as used in the screens by Breinig et al, and Heigwer et al. ^{344,359,360}.

High content imaging screens have come a long way in recent years. The first screens were 2D, but the need to mimic *in-vivo* conditions has led to the development of microscopes and image analysis software capable of handling 3D structures. The advantage that 2D screens offer are the simplicity and the lower cost, but cells cultured and subsequently imaged in 2D layers lose some of their morphological properties, giving 3D screens an advantage in terms of physiological value^{361–363}. One limitation of high content screens is the difficulty to apply them to cells in suspension, thus hindering the study of several diseases such as lymphomas or primary immunodeficiencies.

3D screens will not be addressed in this manuscript.

D. Image analysis pipeline in high content imaging screens

As previously mentioned, high content imaging screens generate a significant bulk of data to be processed, which require analysis to quantify the phenotypes of interest. ImageJ and Metamorph, can be a tedious tool to analyze many images, even with the use of macros. That is because any change that needs to be made to the analysis pipeline will require a direct intervention with the code (Matlab, Java), which may be prone to errors. Therefore, they will not be discussed in this manuscript. However, they have been reviewed in ³⁵⁵.

There are however specialized tools for HCI data analysis and image-based cell profiling. In image-based profiling, hundreds of morphological features are measured, and the morphological profile refers to this collection of measurements³⁶⁴. The typical analysis work flow for image based profiling can be divided into eight main steps³⁶⁴. Assuming the cellular model, fluorescent probes and image acquisition have been performed successfully, the transition from images to phenotypes can take place³⁶⁵

The typical workflow of image-based cell profiling is represented in figure 22 below and will be elaborated in the following pages.

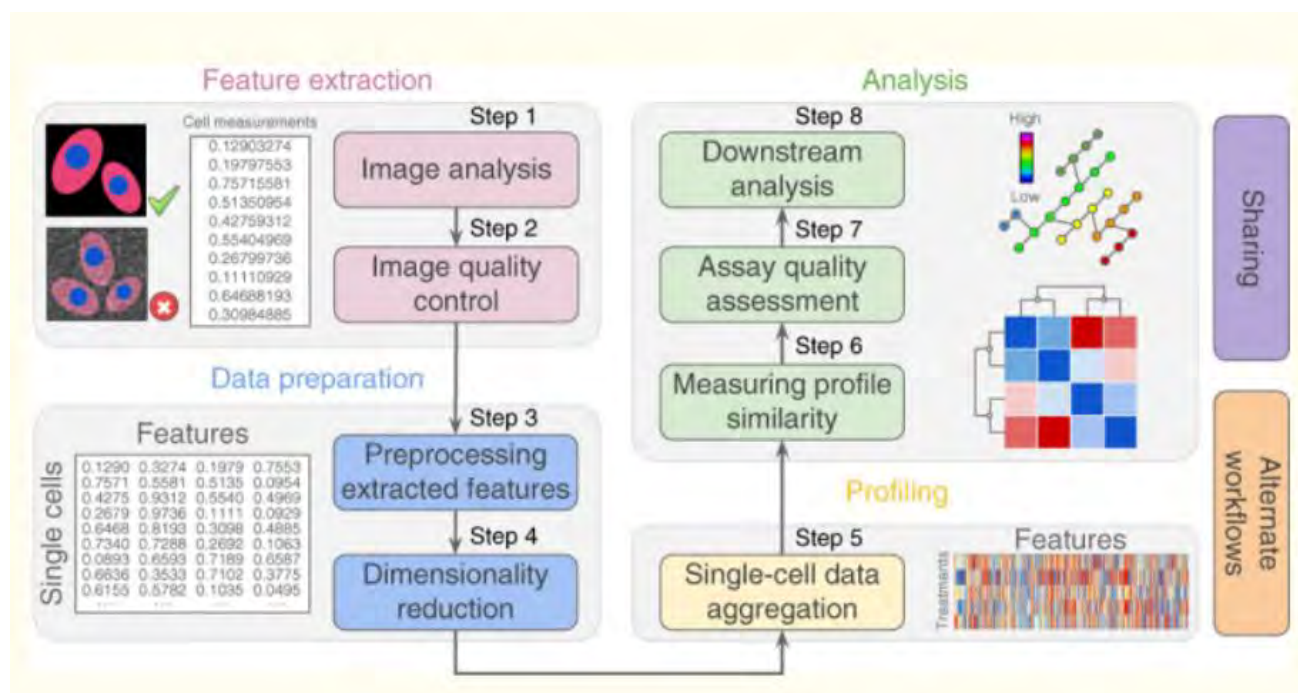


Figure 22: Representative workflow for image-based cell profiling. Image-based cell profiling involves eight main steps which lead to the transformation of images into quantitative information from which conclusions can be drawn³⁶⁴.

a. Image analysis

First, **image analysis** must transform images into measurements (features) describing the state of each cell. Every image must undergo **field of view illumination correction**, as intensities can vary between the center and the edges of a field of view, due to optic artifacts. This process recovers the true image to avoid corruption of an accurate segmentation and intensity measurements³⁶⁶. Illumination correction can be achieved by building corrections from dark and bright images with no sample acquired along with the imaged samples, in a process termed “prospective methods”³⁶⁷. However, such an approach often yields an incomplete correction. Alternatively, retrospective single-image methods can correct illumination by calculating corrections on a per image basis, which can alter relative intensities³⁶⁴. Retrospective multi-image methods correct illumination by using the totality of the images acquired in an experiment^{364,367,368}. This approach usually produces more robust results. Next, the images must undergo **segmentation**, which allows the distinction between pixels that belong to the object of interest and background pixels. This approach is typically used in CellProfiler analyses and requires adjustments for each experiment. Segmentation can be model-based and performed manually based on visual parameters, or by machine learning, where a classifier is trained to find the optimal segmentation solution. Next is **feature extraction**, which measures the phenotypic characteristics of each cell. It includes shape features such as boundaries on nuclei and cells, perimeter, area and roundness. Intensity-based features are computed from actual intensity values per channel, on a single cell basis and separately within each segmented compartment. They include simple statistics such as minimum, maximum and mean intensity. Texture features are used to quantify the regularities of intensities in an image and rely on mathematical equations such as cosines and correlation matrices^{364,368}. Microenvironment features include counts and special relationships among cells in a given field of view.

b. Image quality control

The second step is **image quality control**, and an automated approach must be put in place to remove defective images. It has to be done a field of view level to account for blurring, saturation and the presence of debris. Cell-level quality control must also be performed to remove cells that exhibit a highly unusual phenotype. Outliers can be detected in a model-free fashion by the use of robust

statistics such as the mean and media, or multivariate methods such as principal component analysis (PCA) and Mahalanobis-based outlier detection. The latter is based on robust estimation of mean and covariance matrix to detect outliers^{364,369}. Model-based outlier detection is based on training a model to detect outliers.

c. Processing the extracted features

The third step is the **processing of extracted features**, which must consider several factors in order to yield the proper conclusions. Features extracted may present with **non-finite values**, which can be problematic for statistics and machine learning approaches. Therefore, cells with such values may be removed if they are a minority, or the feature itself may be removed if it appears to be missing in a large proportion of the sample. A third way, which should generally be avoided as it may create a bias and false conclusion, is the imputation of missing values. The **effect of the plate layout** must also be corrected, to account for artifacts that may be present in a plate or across a batch. Ideally, samples should be placed in random positions in the plate, and in different positions in multiple replicated. However, this is not a practical approach in the absence of robotic sample distribution. Caicedo et al. recommend using a two-way median polish to correct for these effects when the samples are randomized, via iterative median smoothing of rows and columns to get rid of positional effects, followed by the division of each well value by the plate median absolute deviation to generate a *B* score³⁶⁴. Local smoothing may also be applied via 2D polynomial regression or running averages. **Batch effect** must also be corrected via standardization and quantile normalization to plates if the samples are placed in a random order in each experiment. Otherwise, canonical correlation analysis could be applied. **Feature transformation and normalization** must be applied to features that display varying shapes of statistical distribution. These include logarithmic transformations used to obtain approximate normal distributions for features that have highly skewed values or require range correction either by the logarithmic functions or one of its adaptations, or relative normalization whereby the population is scaled and centered with respect to one part of the population in which statistics have been computed. Confounding effects must also be removed for subtle phenotypes, to avoid masking a phenotype of interest³⁶⁸.

d. Dimensionality reduction

The fourth step involves **dimensionality reduction**, which aims to remove related, redundant or uninformative features. **Feature selection** includes finding correlated features by computing the feature-feature correlation matrix and keeping only the features with the largest mean absolute correlation³⁶⁴. Replicate correlation filtering keeps only the features that provide the highest additional

information content. Minimum redundancy–maximum relevance adds a constraint based on mutual information to the selection algorithm. The resulting selected features have high replicate correlation while preserving a diverse set of measurements. Support-vector-machine-based recursive-feature elimination involves a support vector trained machine that is trained to weigh feature usefulness. **Linear transformation** methods can be performed to achieve lower-dimensional subspaces of higher-dimensional data that maintain information content. An additional step of decorrelation must be implemented in the case of a technical bias, such as the choice of features to measure. In that instance, the output space becomes biased as well, as should be accounted for.

From the fifth until the eighth step, the pipeline becomes less straightforward, as steps may be skipped or reordered, based on the experimental setup and the answers sought.

e. Single-cell data aggregation

The fifth step is **single-cell data aggregation**, from which population-level morphological states can be concluded. Aggregation can rely on the mean profile which assumes a normal feature distribution and where a profile is built from the means of each feature for the entire population. It can also rely on the median profile, which can provide more robustness for non-normal distributions and minimize outlier effect. It appears to perform better than other profiling strategies³⁶⁴. KS profile compares the probability distribution of a feature in a sample with respect to negative controls by using the KS nonparametric statistical test and yields a profile where the KS statistics reveal how the sample behaves differently with respect to the control. Next is **subpopulation identification and aggregation**, where cells are first identified and clustered according to their morphological phenotypes from single cell profiles. This can be either supervised or unsupervised. Single cell data points are then classified to one of the identified subpopulations and aggregated to calculate the number of cells within each of the identified subpopulations.

f. Profile similarity measurement

The sixth step is **measuring profile similarity**, to compare experimental conditions. **Similarity metric calculation** involves three main types of metrics which allow a simpler data visualization and analysis. They include distance measures to calculate how far apart two features are in the feature space and quantify the magnitude between two given profiles. They include Euclidian, Mahalanobis and Manhattan distances. Similarity measures compute a statistical estimation of how likely two profiles are to be related and to find groups that share common properties. They include Pearson's correlation, cosine similarity and Spearman's and Kendall's rank correlations. Machine learning-based learned similarity measures involve training models with prior knowledge about the samples to

highlight patterns that may not be discriminated by regular metrics. **Concentration-effect handling** must be taken into consideration to identify similarities among different compounds that may occur at different concentrations. Titration-invariant similarity score computes a score between each dose and the negative control, and the scores are sorted in a concentration-dependent fashion. Maximum correlation is practical when a small number of concentrations is used, and the correlation matrix is computed between all concentration pairs³⁷⁰. The maximum value is used as the dose-independent similarity score.

g. Assay quality assessment

The seventh step is the **assessment of the assay quality**. **Comparison to ground-truth** relies on the use of known similarities between pairs of treatments. Classification accuracy may be applied if treatment results are known to fall into specific classes, and concentrations of the same treatment are expected to cluster together. **Replicate reproducibility** should also be achieved, where the similarity between replicates should be higher than the similarity to profiles of other treatments or conditions³⁶⁴. **Effect size** computes the difference between the positive and negative controls but may lead to a bias as some phenotypes which do not particularly distinguish a control may be ignored.

h. Downstream analysis and result interpretation

The final step is **downstream analysis**, which allows the interpretation of the results of morphological profiling. **Clustering** is an effective way to extract meaningful relationships between different morphological profiles. Hierarchical clustering is the most commonly used strategy to identify correlation as well as positive and negative connections, and is computed by a similarity matrix which can reveal patterns in the data^{371,372}. The data from the heat map is structured as a dendrogram to link features together based on proximity in the feature space. Next comes data **visualization**, which usually takes the form of a 2D (sometimes 3D) map to reduce dimensionality and allow for an easier interpretation and less crowding. While tools to represent data in more than two dimensions have been used, which include the Chernoff faces and the pixel-based techniques, they are a mere visual tool where the user is let to interpret the data. Visualization can include data projections or hierarchical visualizations. Data projection includes the following:

i. Linear dimensionality reduction: Principle component analysis

PCA is a linear dimensionality reduction technique which has long been the most employed tool, as it relies on simple linear algebra and is faster than most other methods. It consists in finding a low-dimensional embedding of the data points in a way to best preserve their variance, as it was measured in the high-dimensional space, and representing them as a new set of orthogonal and uncorrelated

variables called the principal components^{373,374}. A comprehensive and recent review on PCA was published in 2016 by Jolliffe and Cadima³⁷⁴.

ii. *Non-linear dimensionality reduction*

The need and usefulness of new tools is being recognized, in order to extract not only linear relationships between input dimensions (as in PCA), but any kinds of relationships. Such non-linear dimensionality reductions include but are not limited to the following:

a) *Isomap*

Also known as complete isometric feature mapping, the Isomap consists of a three-step algorithm. The first step determines neighboring points, the second estimates the geodesic distances and the third applies multidimensional scaling to the distances in the matrix, thus culminating in an embedding of the data in a d-dimensional Euclidian space. This technique is well elaborated in ³⁷⁵

b) *Diffusion map*

Diffusion maps were introduced by Coifman and colleagues in 2005. Diffusion maps consist in computing the data set into the often low-dimensional Euclidian space, where the Euclidian distance between two points in the embedded space would be equal to the diffusion distance between the probability distributions which are centered at those points³⁷⁶.

c) *t-distributed stochastic neighborhood embedding*

t-distributed stochastic neighborhood embedding (t-SNE) has stochastic neighbor embedding (SNE) as its basis, which converts the high-dimensional Euclidean distances between datapoints into conditional probabilities ($p_{j|i}$) that represent similarities. The mathematical aspect of SNE is elaborated in ³⁷⁷. The limitation of SNE is the crowdedness of the data points and a suboptimal cost function, whereas t-SNE is an improvement since it uses a symmetrized thus simpler cost function and a student-t rather than a Gaussian distribution. t-SNE is elaborated in further detail in ³⁷⁷.

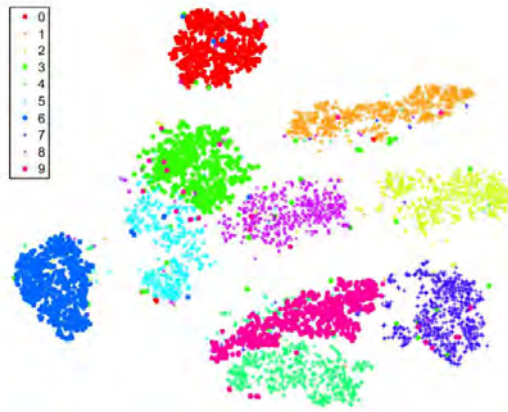


Figure23: Visualization of 6000 handwritten digits from the MNIST data set by t-SNE ³⁷⁷

However, the disadvantage of tSNEs is that such a representation causes the loss of large scale information such as the inter-cluster relationships, while it is precise for local structures rather than global trends³⁷⁸. Therefore, a tSNE might not be the best adapted method to extract meaningful relationships between large-scale clusters

d) Uniform manifold approximation and projection

When compared to other tools, the uniform manifold approximation and projection (UMAP) proved to have not only the fastest run times and highest reproducibility, but also and most importantly, the most relevant organization of clusters³⁷⁹. They are a recent technique, introduced by McInnes and colleagues in 2018. The algorithm of UMAPs assumes a uniform distribution of the data in a Riemannian manifold, that the Riemannian metric is locally constant, and that the manifold is locally connected³⁸⁰. The subsequent manifold, which has a fuzzy topology, can then be made into a low dimensional projection.



Figure 24: Visualization of 6000 handwritten digits from the MNIST data set by UMAP ³⁸⁰.

Several more methods of nonlinear dimensionality reduction exist, and they are reviewed in ^{377,381}.

The last step in classification and result interpretation is **classification**, which may be only applied if the transfer of labels from annotated samples to unknown data points is possible. If this is possible, classification can provide meaningful information and insights into the effects of given compounds or treatments. The most commonly used classification rule in morphological profiling experiments is the nearest-neighbors algorithm, which finds the closest data points in the collection of annotated samples and recommends a label for the new sample, as well supervised prediction models such as neural networks and random forest classifiers.

Supervised prediction models follow certain paths to predict a “correct answer”, and classifiers can be generated to recognize cells with a phenotype of interest. The training set must be chosen with as many cells as possible, and not only from the control group, to avoid overfitting. The number of rules or features where the cutoff for a decision are then set and refined repeatedly until the classifier reaches the desired accuracy³⁶⁸. An increased number of rules usually correlates with more accurate predictions of the classifier.

Neuronal networks mimic human brain behavior and provide powerful modeling algorithms that allow or non-linearity between feature variables and output signals³⁸². The network has a layer of input nodes which receive features variables from raw data, and a layer of output nodes. The more complex the classification, the more layers are required. The data is split into a training and a test set, to assess

the predictive ability of the network. **Deep learning models** are composed of multiple layers of latent variables, where hierarchical structuring can be found from complex images³⁸³. Deep learning methods can overcome the limitations associated with extracted feature sets by jointly learning optimal feature representations and the classification task directly from pixel level data. More complex network such as convolutional networks are considered deep learning methods and have achieved an accuracy of prediction higher than the human eye³⁸⁴.

Random forest classifier algorithms use a series of classification or decision trees to map the features of a samples and profile it in a class output. The decision trees consist of branches which are features conjugated in paths where a particular combination will trickle down to a class output. Random forest classifiers rely on uncorrelated decision trees with random combinations of features to reduce data variance and reduce overfitting the data to the training set^{385,386}.

Unsupervised methods aim to find internal structure or relationships in a data set instead of trying to determine how best to predict a “correct” answer and reveal clusters and associations within the data set without any prior teaching model. They are useful especially when class data labels are unavailable. They include **hierarchical clustering on principal components**, because PCA allows the reduction of the number of variables without losing important information and is a very stable method compared to other unsupervised machine learning techniques^{387,388}. Unsupervised clustering finds clusters without a pre-determined number of clusters and the data is divided into clusters in a way where the data within one cluster bares high similarity among themselves, and dissimilarity to data in other clusters³⁸⁹.

The performance of a classifier can be determined by comparing the prediction of the classifier to the expected outcome. These include binary classifications and multilabel classifications. The **F1 score** is a measure that can express the counts of true positives, false positives and false negatives³⁹⁰.

E. Statistics

The performance of a high content screen is usually quantified with statistical parameters. When performing a high content screen, it is assumed that the data is normally distributed, and **logarithmic transformations** (usually log2) are often applied in the pre-processing stage, to generate data that is more symmetrically distributed around the mean, to facilitate the understanding between positive and negative values^{391,392}

The next step involves dealing with outliers and can be achieved in two ways: classical and robust. Instead of eliminating outliers, **Robust statistics**, which have gained in popularity in high content screens, may be applied. Robust statistics are less sensitive to outliers as they use the median and median absolute deviation instead of the mean and standard deviation. This diminished the effect of outliers on the final results³⁹². The robustness of a technique can be determined by a breakdown point, which is the number of outliers allowed before the parameters become no longer representative of the original dataset. The median and median absolute deviation have a breakdown point of 50, while the mean and standard deviation have a breakdown point of 0%, implying that robust statistics can successfully handle a data set where 50% of the data points are outliers³⁹².

Data must be normalized to account for and reduce assay variability, as well as to eliminate false positives and negatives which may be caused by plate patterns³⁹¹. **Data normalization** can be **control-based**, where the positive and negative controls are used as the 100% and 0% bounds respectively, and the features of the other data points are calculated with respect to these values. The activity of the sample can be calculated as percent of control or normalized percent inhibition.

Non-control-based data normalization is favored in high content screens, as it assumes that most samples are inactive and serve as their own control. IT can be calculated as percent of samples, robust percent of samples, Z-score or robust Z-score. The Z-score accounts for signal variability in the samples. This method is usually favored as it leads to a better understanding of the overall activity but can be quite misleading in screens where the basal activity shifts upwards.

Data analysis must also consider variability detected in experiment-wise patterns. **Median polish** accounts for row and column effect (the spatial trends in a plate), and the **B-score** utilized to account for inter-plate variability uses the residual values calculated in median polish and the mean absolute deviation^{368,391,392}. **Background correction** must also be applied by calculating the average activities within each well and generating a background surface for each experiment. **Well correction** is performed in a similar manner to background correction, but the fitting is performed for each individual well, proving to be successful for hit selection³⁹². **Diffusion-state model** corrects variability in environmental factors such as temperature or humidity distribution across well and is generated from a control column.

Quality control statistics include **signal/background** which is the ratio of the mean of the positive control to the mean of the background signal, **signal/noise** which is similar to signal/background but takes into account signal variability, **signal window** which measures the data range in an assay, **assay variability ratio** which measures the data variability in the positive and negative controls, the **Z²**-

factor which assumes a normal distribution to account for variability in the control wells, the **Z-factor** which is a modification of the Z' -score where the sample mean and standard deviation replace that of the negative control, and the **SSMD**, which relies on probability and statistics and has been shown to be more effective than Z' and Z scores in handling controls with different effects^{392,393}.

To assess HCI results, specific statistical analyses must be employed to analyze and interpret the large amount of data generated. The different analysis methods and requirements include normalization, logarithmic transformation and quality control.

To compare any two treatments, a **multidimensional perturbation value** (mp-value) may be calculated. The difference between a treated condition and a control is considered as activity, while no difference is considered inactivity. An mp-value to the Mahalanobis distance is assigned, and permutation tests are used to determine statistical significance. This is done by a permutation approach, where under the null hypothesis, shuffling the replicate labels would not result in a drastically different Mahalanobis distance between the two groups, while if the treatment replicates are significantly different, the Mahalanobis distance would likely be smaller after randomly shuffling the replicate labels¹²⁰. Significance values are interpreted in the same way as significance values from parametric statistical analyses, where an mp-value < 0.05 is considered significant.

Implementation of a high content imaging pipeline to study the immunological synapse of cytotoxic lymphocytes

Rationale

Despite the great advancements made in the field of high content imaging in terms of techniques and analysis, these assays lack standardized protocols. The work towards standardization is however in progress.

The cytotoxic function is highly important, and a tightly regulated process. Moreover, the immunological synapse involves a complex interplay between a plethora of molecules, in order to drive the successful delivery of lytic molecules into the target cells. All the aforementioned research suggests a crucial role for the actin cytoskeleton and the process of polymerization and depolymerization in maintaining immune homeostasis, and that cytoskeletal defects such as defective immunological synapse and cytotoxicity may lead to several life-threatening illnesses. In the context of primary immunodeficiencies, the data is not systematic, and the analysis methods vary. Current advancements in the field of imaging and image analysis have made high content imaging of a large number of samples feasible, with a good image resolution that allows the detection of subtle morphologies, and robust statistics specially designed for such approaches. However, microscopy is not widely used among immunologists, but the advancements made in that field have undeniably helped our understanding of the mechanisms governing the cytotoxic activity, actin dynamics and the assembly of the immunological synapse.

Taking together the crucial role of the immunological synapse in cytotoxicity, and the findings that perturbations of the cells can alter morphology, the following could be hypothesized the following:

- The immunological synapse of CD8⁺ T cells and NK cells should present different morphological features
- Different perturbations to the actin cytoskeleton of cytotoxic lymphocytes should yield distinct immunological synapse morphologies.
- The immunological synapse of ARPC1B deficient patients should have a morphology that is distinct from that of normal donors

Driven by the importance of the role of the immunological synapse in cytotoxicity and the need for a systematic method to screen for PIDs that may display a defective cytotoxic activity, I have

elaborated a new high content imaging and analysis pipeline of the immunological synapse. This pipeline could be a first step to assess defects in the immunological synapse assembly, from which functional defects may be inferred. Such a pipeline, which overcomes the bottleneck of low throughput microscopy typically used to image the immunological synapse, could be systematically applied to screen cytotoxic lymphocytes from PID patients and adapted to screen other types of immune cells.

Objectives

Therefore, the objectives of my thesis project were the following:

1. Set up a high content imaging and analysis pipeline of the immunological synapse of cytotoxic lymphocytes
2. Provide an understanding of the actin-driven mechanisms regulating IS architecture in cytotoxic lymphocytes
3. Apply this pipeline in the clinical context, by providing an insight as to how the IS architecture may vary in patients with actinopathies.
4. Assess how a defect in the IS morphology could imply a functional defect in cytotoxicity

Results

I first started by optimizing assays on the NK-92 cell line and primary NK cells isolated from the PBMCs of normal donors.

Indeed, the review by Emily Mace entitled: “**Cell biological steps and checkpoints in accessing NK cell cytotoxicity**”⁶⁶, as well as the expertise of our lab on lymphocytes inspired me to set up functional assays to assess the main steps of cytotoxicity in NK cells. During the first year of my PhD, I learned a lot about the cytotoxic function, and had the chance to establish assays on a new cell type that was not used in our lab.

Indeed, I have established a methodology where the functional steps of cytotoxicity can be assessed in parallel. Migration, conjugation and cytotoxicity were amenable to assessment high throughput cytometry readings in 96 well plates. However, the step of imaging the immunological synapse which is done by low throughput confocal microscopy revealed to be tedious in terms of the time required for image acquisition, the analysis approach to adopt and the parameters to analyze. I was therefore driven to test the feasibility of staining the immunological synapse in a high content format, to match this assay format to that of the other steps. It was also interesting to benefit from imaging the cells in a high content format and apply a compatible analysis. For that reason, I imaged the IS using the Opera Phenix microscope, and its compatible analysis software Harmony, to analyze the individual wells.

However, the number of parameters that may be analyzed by such approaches remain limited, and the analysis on a per well basis can hide some interesting phenotypic features. It was evident that a more powerful bioinformatics approach was needed to extract hundreds of relevant IS features on a per cell basis, and with statistics on hundreds of cells. With my thesis supervisor, we therefore established a close collaboration with the Menche lab at the CeMM in Vienna, to benefit from their expertise in morphological profiling in high content imaging screens³⁴⁸.

I will first start by showing the results of experiments that I set up and optimized on the NK-92 cell line and primary NK cells isolated from PBMCs, followed by the setup of a high content imaging approach of the IS. This approach should be overcome the technical bottleneck of low throughput imaging, and its power in terms of the number of cells and the parameters to be analyzed, and resolute power should lead to identifying meaningful biological morphological features of the immunological synapse.

1. Setting up assays in the NK-92 cell line

Cell migration is a crucial step in the function of cytotoxic cells. Indeed, cytotoxic cells migrate along a chemokine gradient.

Our results show that NK-92 cells migrate in response to CXCL12, even at low chemokine concentrations (Figure 24a). However, the response to chemokines appears to stop beyond a certain threshold. Indeed, cells appear to stop responding to the two highest CXCL12 concentrations tested. Alternatively, cells may undergo chemorepulsion, as shown in other cell models at high chemokine concentrations, which has been previously described for mature T cells³⁹⁴

In order to achieve their cytotoxic function, NK cells must establish conjugates with their targets. Conjugate formation is assessed by flow cytometry by staining NK cells and K562 target cells with two different stains and assessing the percentage of NK cells bound to K562 cells.

Our results show that NK-92 cells establish conjugates with their targets after 15 minutes of incubation, and conjugate formation seems to plateau at 45 minutes (Figure 24b).

Our lab has quite an expertise in confocal microscopy imaging of cytotoxic lymphocytes. Therefore, I had the opportunity to perform staining of NK-92 cells incubated with their targets to visualize the formation of the immunological synapse. Our results show that upon formation of the immunological synapse, NK-92 cells polarize their lytic granules towards the area of contact with the target cell (Figure 24c). After 1 hour of incubation, the mean distance between the lytic granules and the synaptic area is about 4.3 μ m, providing support to the visual observation that NK-92 cells do not polarize all their lytic granule content.

Also benefitting from the expertise of our lab in performing cytotoxic assays, I could perform killing assays where NK-92 cells and stained K562 cells are incubated for 4 and 24 hours and evaluated by flow cytometry. Cells are also stained with 7AAD which only stains dead cells and allows the discrimination of alive cells. The percentage of lysis is determined by evaluating the residual number of 7AAD-/stain+ K562 cells. Our results indicate that NK-92 cells are efficient at eliminating target cells starting 4 hours, and it appears that to achieve maximum cytotoxicity an excess of effector NK-92 cells is needed with respect to target cells (Figure 24d). Indeed, we observe a better killing efficiency at a 5:1 effector to target ratio than 1:1. I was also the first in the lab to set up IRM and TIRF microscopy imaging of NK-92 cells in 8-well chambers for a collaboration, with the help of Javier Rey-Barroso and Astrid Canivet-Laffitte from the microscopy platform. Our results show that most WT NK-92 cells spread efficiently over a coating of ICAM-1 and anti-NKp30 Ab and form an IS

where they display a large peripheral belt of tight adhesion and a less adherent central patches, and that lytic granules dock in these loose adhesion patches (Figure 24e). We report a defect in synapse formation and granule docking in NK-92 cells knocked down for a yet unpublished gene, so these results may not be disclosed. The manuscript revealing the role of that gene has been submitted.

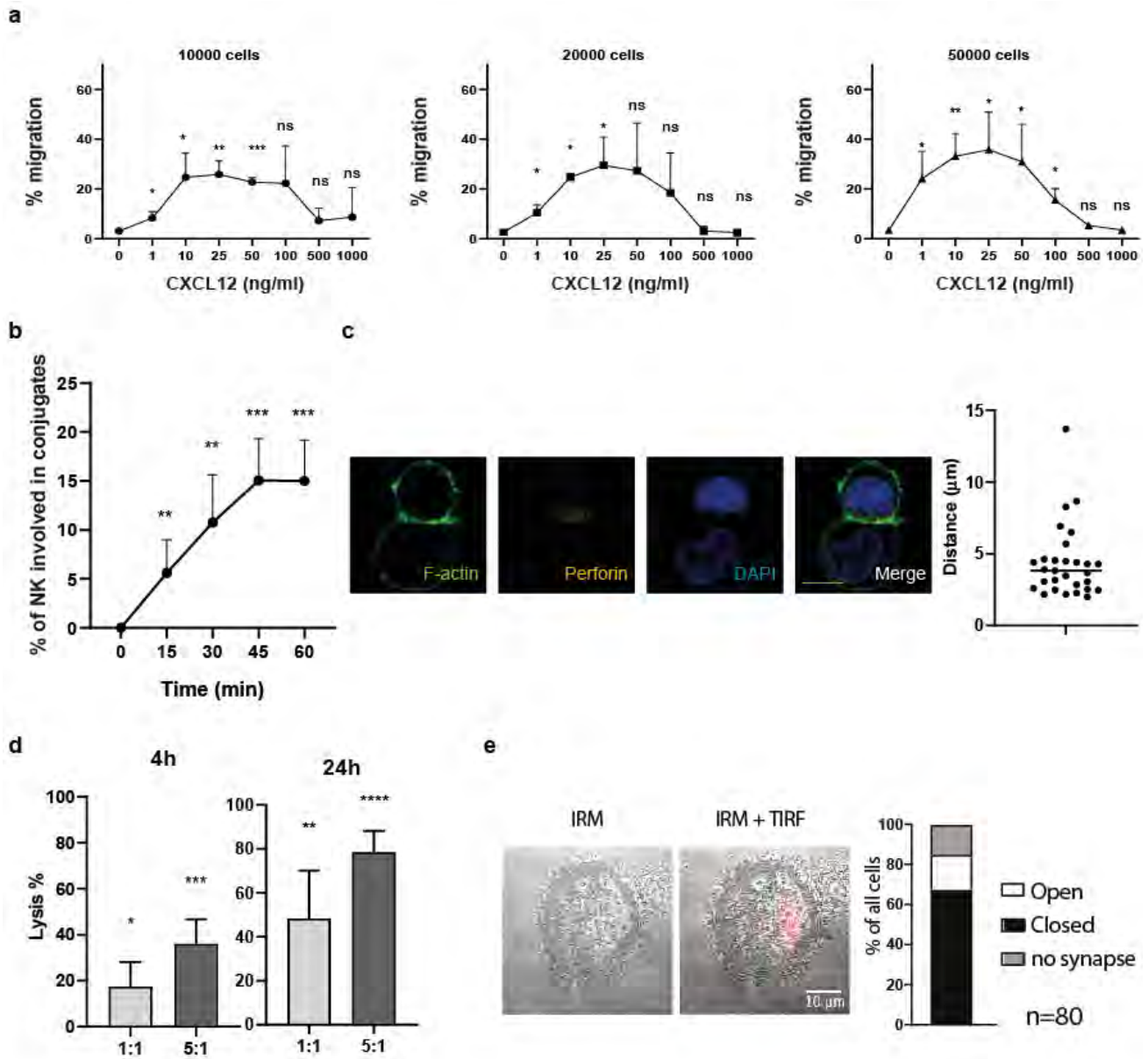


Figure 24: Functional assays on the NK-92 cell line. A. % migration of 10000, 20000 and 50000 NK-92 was determined in response to a CXCL12 gradient (n=2). B. % conjugate formation between NK-92 cells and target K-562 cells was determined over the course of 1 hour, at 15-minute intervals (n=3). C. Confocal microscopy images of an NK-2 forming a conjugate and an immunological synapse

with a target cell, and stained for F-actin (green), perforin granules (yellow) and nuclei (DAPI). Scale bar: 10 μm . Mean distance of lytic granules to the synaptic interface was calculated in 30 cells. D. 4 and 24h cytotoxicity assays to determine the lytic activity of NK-92 cells against target cells ($n=3$). Student's *t*-test was used to determine statistical significance. Values represent means and the error bars show SD. Significance is noted as * $P<0.05$, ** $P<0.01$, *** $P<0.001$, **** $P<0.0001$. E. Representative image of an NK-92 cell forming a synapse imaged by IRM and lytic granules (red) imaged by TIRF microscopy using lysotracker.

2. Setting up assays in primary NK cells.

Once assays were set up and optimized in the NK-92 cell line, the next logical step was to apply them to primary NK cells.

For that, I tried to optimize the expansion on primary NK cells from PBMCs by using a feeder system, like the expansion of CD8⁺ T cells using a feeder system routinely performed in our team. PLH cells, which are EBV transformed lymphoblastoid cell line, kindly provided by DR. Martin Villalba were used as feeder cells.

The expansion process was not optimal, as it does not yield large numbers of NK cells, and the cells are only viable for two weeks and needed stimulation with feeder every 2-3 days. Moreover, the protocol is optimized for NK cells isolated from umbilical cord blood which yields a much higher starting number of PBMCs than a 10ml blood tube. Moreover, there are other expansion protocols using another type of irradiated feeder referred to as NK cell feeder (NKF)^{395,396}, which I could not try.

However, I could manage to set up functional assays on the primary NK cells.

Even though primary NK cells appear to be spontaneous migrators, they are also capable of a specific migratory response towards both CXCL10 and CXCL12 (Figure 25a). They are also capable of forming conjugates with target K562 cells, and similarly to NK-92, the % of primary NK cells forming conjugates appears to increase over time (Figure 25b). The expanded primary NK cells appear to be cytotoxic and capable of efficient ADCC, even at 4h and in a surplus of target cells (Figure 25c). Our results also show that an excess of primary NK cells is not needed to efficiently eliminate most target cells, and a ratio of 2 NK cells for 1 K562 cell efficiently removes all target cells at 24 hours. Primary NK cells could also be assessed by confocal microscopy for the formation of the immunological

synapse when conjugated with target K562 cells, and to polarize their lytic granules (Figure 25d). However, the % of granules polarized and the mean distance to the IS was not assessed in these cells.

I also performed some microscopy experiments on NK cells isolated from frozen PBMCs of normal donors and a PID patient for a collaboration where a reduced lytic granule content and a defect in granule polarization were observed, but these have not yet been published and the gene name and specific results shall not be disclosed in this manuscript.

In conclusion, I was the first to set up the functional assays routinely performed on CD8+ T cells in our lab on an NK cell line and primary NK cells, and add the conjugation assay. However, if our lab is to start performing experiments on primary NK cells (especially from patient material), the expansion of primary NK cells should be tested using the feeder system developed by Bae and Lee³⁹⁶.

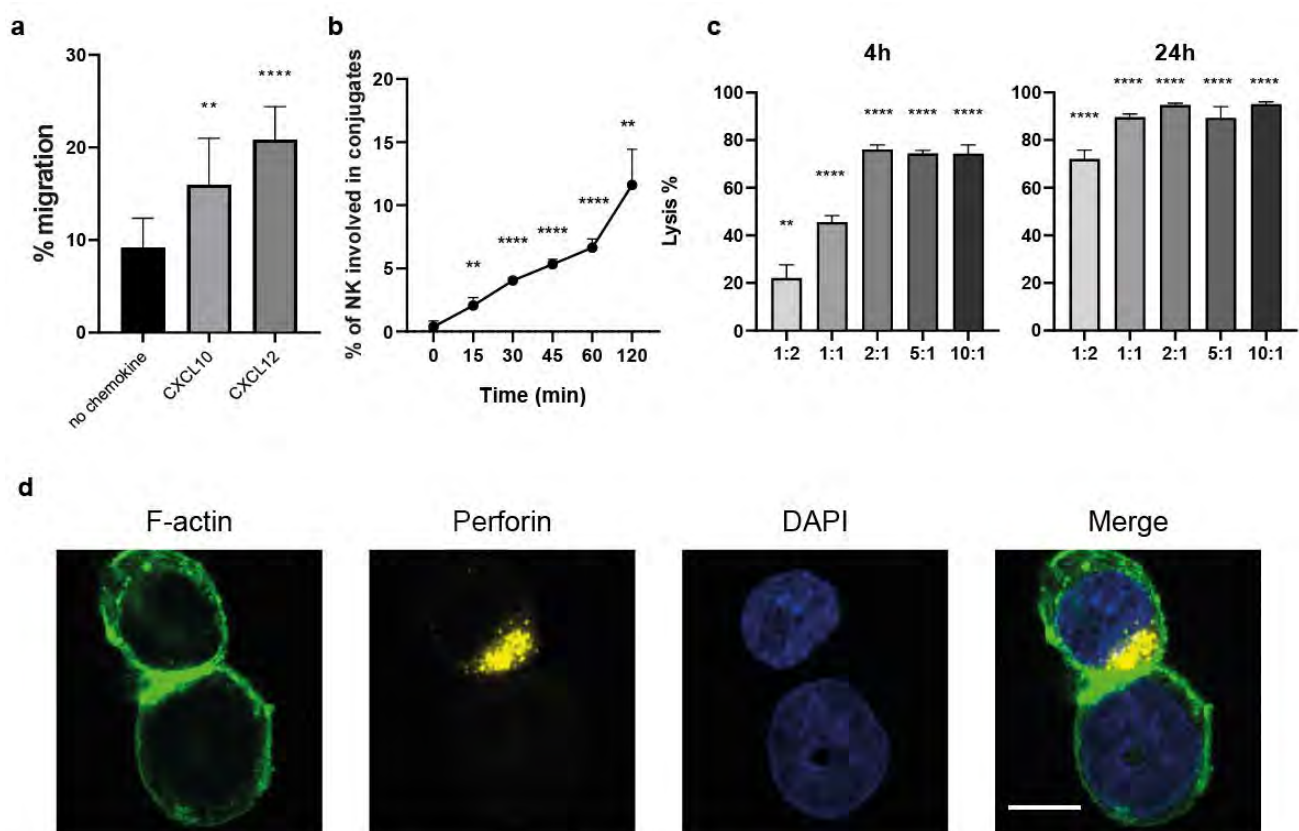


Figure 25: Functional assays on primary NK cells. A. % migration of 50000 primary NK cells was determined in response to CXCL10 and CXCL12 (n=2). B. % conjugate formation between NK cells and target K-562 cells was determined over the course of 2 hours (n=2). C. 4 and 24h cytotoxicity assays to determine the lytic activity of primary NK cells against target cells (n=2). Student's t-test was used to determine statistical significance. Values represent means and the error bars show SD. Significance is noted as *P<0.05, **P<0.01, ***P<0.001, ****P<0.0001. D. Confocal microscopy

images of an NK cell forming a conjugate and an immunological synapse with a target cell, and stained for F-actin (green), perforin granules (yellow) and nuclei (DAPI). Scale bar: 10 μ m.

Seeing how important the immunological synapse is for the cytotoxicity process, we posited that imaging the immunological synapse under different conditions can be predictive of the cytotoxic potential of CD8⁺ T cells and NK cells. However, traditional confocal microscopy revealed to be limited in terms of the conditions that were amenable to imaging, and the limitation of the parameters that can be assessed, as well as the time required for image analysis.

These optimizations led to the development of my main project, which is the establishment of a high content imaging approach of the immunological synapse under different conditions, to determine the role of the actin cytoskeleton in regulating cytotoxic activity.

We established a close collaboration with the Institut de Recherche en Santé Digestive (IRSD), who had acquired the Opera Phenix, to set up the high content imaging on the IS. This collaboration, as well as a close collaboration with the Menche team at the Center for Molecular Medicine (CeMM) in Vienna made it possible for me to conclude my PhD work in a scientific paper that is soon to be submitted (to Nature Communications), and of which I will share co-first authorship with Loan Vulliard, a PhD student in bioinformatics in the Menche lab.

3. High content imaging of the immunological synapse

Morphological profiling of human T and NK lymphocytes identifies actin-mediated control of the immunological synapse

Yolla German,^{1,2,3,4+} Loan Vulliard,⁵⁺ Aude Rubio,^{2,6} Kaan Boztug,^{4,5,7,8} Audrey Ferrand,^{2,6} Jörg Menche⁵ and Loïc Dupré*^{1,2,3,4}

The detection and neutralization of infected cells and tumors by cytotoxic lymphocytes is a vital immune defense mechanism. The immunological synapse orchestrates the target recognition process and the subsequent cytotoxic activity. Here, we present an integrated experimental and computational strategy to systematically characterize the morphological properties of the immunological synapse of human cytotoxic lymphocytes. Our approach combines high-content imaging with an unbiased, data-driven identification of high-resolution morphological profiles. Such profiling discriminates with high accuracy immunological synapse perturbations induced by an array of actin drugs in both model cell lines and primary lymphocytes. It reveals inter-individual heterogeneity in lymphocyte morphological traits. Furthermore, it uncovers immunological synapse alterations in functionally defective CD8⁺ T cells from immunodeficient patients carrying *ARPC1B* mutations. Our study thus provides a foundation for the application of morphological profiling as a powerful and scalable approach to monitor lymphocyte activation status in experimental and disease settings.

The immunological synapse (IS) is a complex cellular structure that sets lymphocyte activation and function during encounter with antigen-presenting cells and target cells. The canonical IS is characterized by a symmetrical architecture consisting of concentric rings of F-actin and integrins, while the antigen receptors occupy a central position^{1,2}. The lymphocyte spreading associated with IS assembly, as well as the molecular organization defining IS architecture, rely on actin cytoskeleton dynamics. In cytotoxic lymphocytes, including CD8⁺ T cells and NK cells, the IS is particularly important because it sustains the polarized delivery of cytolytic molecules such as perforin and granzymes towards target cells³. Indeed, activation of the integrin LFA-1 via an inside-out signaling from the T-cell receptor (TCR) in T cells, and several stimulatory receptors in NK cells⁴⁻⁷, leads to the formation of a tight adhesive ring allowing confinement of the degranulation process. Additional layers of control of lytic granule delivery at the IS are their polarization via the orientation of the microtubule organizing center^{8,9} and their restricted passage through pervasive actin cytoskeleton clearances¹⁰. Given the key events occurring at the IS, this structure is a window of choice to monitor lymphocyte activation and function. Indeed, the positioning and dynamic behavior of multiple receptors and signaling molecules have been characterized within the IS¹¹, and alterations of the its architecture have been reported in multiple disease settings^{12,13}. However, the various microscopy approaches employed so far to characterize spatial organization of the IS have remained low throughput and have been restricted to the analysis of a limited number of morphological features. A more systematic in-depth assessment of the IS would better exploit this structure as a pivotal read-out for the characterization of lymphocyte activation and function.

Recent advances in high content imaging (HCI) now allow for the profiling of cells at a much richer level of detail and in an unbiased fashion. It has therefore been widely employed in cancer and toxicology research, in particular for

screening drug effects on adherent cell lines and implementing genetic screens based on the siRNA, shRNA and CRISPR technologies¹⁴⁻¹⁷. However, HCI has not yet been applied to the study of leukocytes because of the difficulty to overcome the relatively poor adherence of these cells.

In this study, we report the implementation of an HCI approach that allows the high-resolution confocal imaging of T and NK cells stimulated over 2D surfaces functionalized with ICAM-1 and stimulatory antibodies, and the effect of pharmaceutical and genetic perturbations on the IS morphology. In addition to extracting a previously studied features related to staining of F-actin, LFA-1 and perforin, we develop an unbiased analytical approach allowing high-dimensional profiling and clustering of IS morphologies. Our data shows non-identical perturbations caused by drugs affecting different facets of actin cytoskeleton remodeling and highlights that actin cytoskeleton integrity is required not only for lymphocyte spreading but also for lytic granule polarization and LFA-1 distribution. Application of our HCI pipeline to lymphocytes isolated from human blood reveals distinct morphological profiles in individual healthy donors. Furthermore, our method allows characterizing synapse defects in untransformed CD8⁺ T cells from ARPC1B-deficient patients, illustrating its potential to identify disease-related synapse alterations and to predict functional defects, such as cytotoxicity.

Results

Morphological profiles of T cell and NK cell immunological synapses.

In order to systematically analyze the morphological profile of lymphocyte populations, we here sought to develop an adapted HCI workflow. It consisted in seeding cells of interest on stimulatory surfaces in microwells of 96- or 384-well plates, fixation and staining with combinations of fluorescent dyes and antibodies. Confocal images were acquired on an Opera Phenix high-content screening system and analyzed with CellProfiler¹⁸ to

automatically segment individual cells and extract features pertaining to cell morphology and each of the fluorescent markers (**Fig. 1a**). As proof of concept, we first applied our approach to NK-92 and Jurkat cells, two human cell lines commonly used as models for NK cells and T cells, respectively. Cell morphologies were compared upon interaction with a neutral poly-L-lysine (PLL) surface or co-stimulation with the LFA-1 ligand ICAM-1 and stimulatory antibodies (Ab) in order to evoke IS assembly. Upon co-stimulation with ICAM-1 and anti-NKp30 / NKp46 Ab, NK-92 cells spread, emitted F-actin-rich peripheral pseudopodia and polarized perforin-containing granules towards the center of the cell to substrate interface (**Fig. 1b** and **Fig. S1a**). These observations are in line with the characteristics of the IS from cytotoxic lymphocytes^{11,19}, therefore validating our high-throughput stimulation and staining procedure. Based on literature describing the IS and reporting a polarization of F-actin and lytic granules in NK cells²⁰⁻²², we first selected quantitative features pertaining to the F-actin and perforin stainings and extracted them as mean values per field of view averaged across 3 experiments. We also included features related to the nucleus, available since the DAPI staining was used in a primary nucleus segmentation step before the identification of the cytoplasm around the nuclei (**Fig. 1c** and **Table S1**). Increase in F-actin intensity and cell area were prominent features of the stimulation, as compared to the PLL condition. Furthermore, the number of perforin-containing granules detected at the cell to substrate interface increased upon stimulation, which is indicative of their polarization towards the IS. Interestingly, this polarization process was associated with a relative spreading of the area covered by lytic granules, supporting the notion of multiple docking domains at the synapse²³. Our analysis also highlights that increase of nucleus area is a typical feature of the IS in the NK-92 cells. Interestingly, nucleus area appears to increase along with F-actin intensity when

assessed across 3 experiments (**Fig. 1d**), suggesting that nucleus flattening and F-actin polymerization are related events, probably as components of the cell spreading mechanism. Of note, the absolute values for F-actin intensity were higher in one of the 3 experiments, possibly resulting from differences in staining quality. This indicates that absolute value for staining intensities across experiments should be considered with caution. To further estimate morphological heterogeneity in individual cells, F-actin intensity was assessed on a per-cell basis (**Fig. 1e**), rather than on a per field of view basis. The unimodal increase of F-actin intensity driven by the stimulation of NK-92 cells indicates a relatively homogenous activation and IS assembly in these cells. It also validates our approach to consider mean cell measurements on a per field of view basis.

We then applied our HCI workflow to Jurkat cells, which were co-stimulated with ICAM-1 and anti-CD3 Ab. We selected 12 features pertaining to the F-actin, LFA-1 and DAPI stainings to monitor hallmarks of the T cell IS¹¹. As compared to the neutral PLL stimulation, LFA-1/CD3 co-stimulation led to cell spreading, assembly of a peripheral F-actin ring-like structure and redistribution of the integrin LFA-1 as an inner belt at the cell to substrate interface (**Fig. 1f** and **Fig. S1b**), which are characteristic for the IS^{11,24}. Our quantification over multiple fields showed that similarly to NK-92 cells, F-actin intensity, cell area, LFA-1 intensity and LFA-1 area are prominent features of the Jurkat cell IS (**Fig. 1g** and **Table S2**). Likewise, F-actin and LFA-1 intensities correlated in individual fields of view with a Pearson correlation coefficient of 0.50 (**Fig. 1h**). At the single cell level, F-actin clearly increased in response to the ICAM-1 and anti-CD3 Ab stimulation, despite noticeable heterogeneity in both stimulated and unstimulated cells (**Fig. 1i**). When taken together, the data collected on the

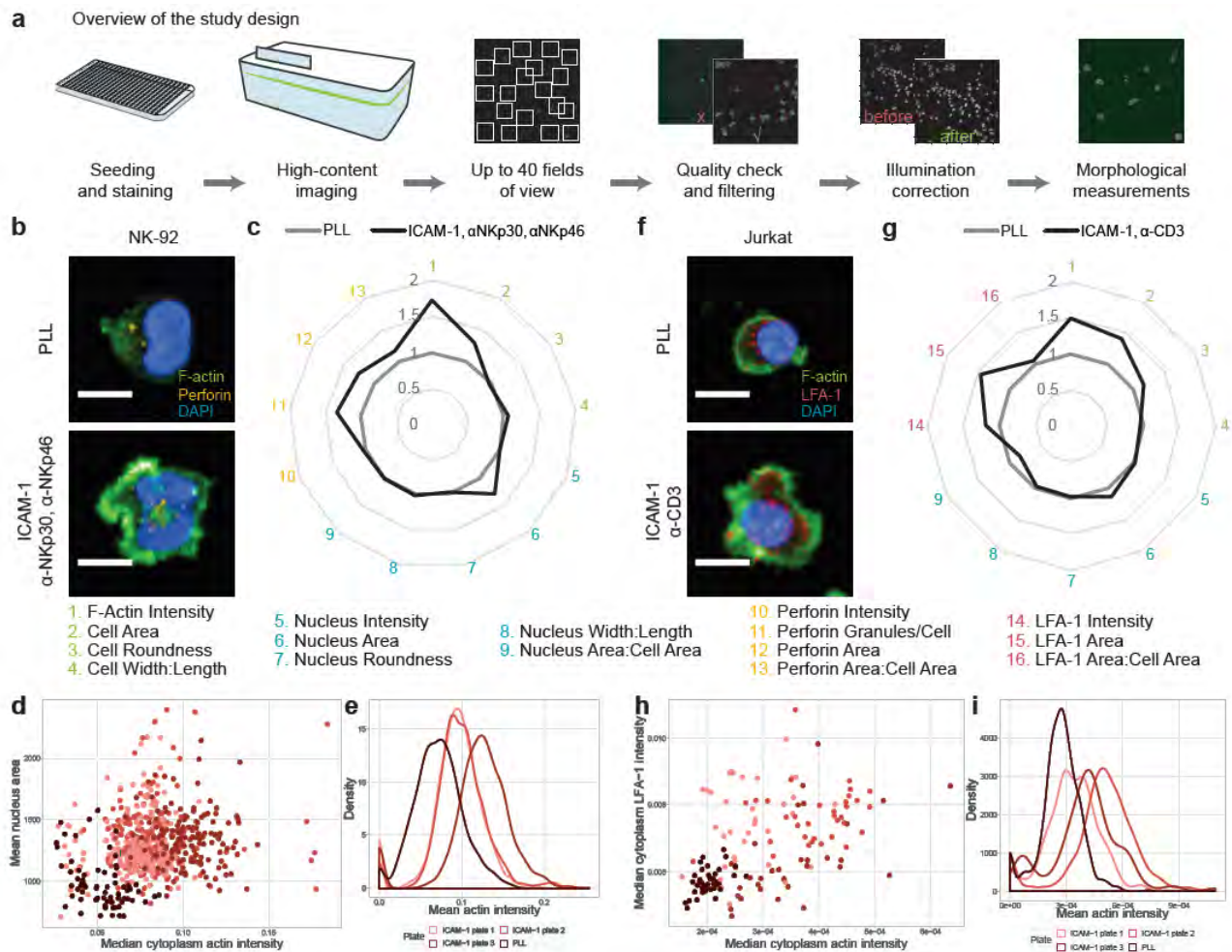


Fig. 1 | High content imaging of the immunological synapse in lymphocytic cell lines. **a.** Schematic representation of the High content imaging pipeline. **b.** Representative images of NK-92 cells seeded on Poly-L-Lysine (PLL) or ICAM-1 plus anti-NKp30 / NKp46 Ab, stained for F-actin (green), perforin (yellow) and the nucleus (DAPI). Scale bars: 10 μ m. **c.** Selected IS features analysed as fold change of ICAM-1 plus anti-NKp30 / NKp46 Ab over PLL. The data represent the mean of three separate experiments (n= 933-5860 cells). **d.** Mean nucleus area in pixels and median F-actin intensity per image across PLL and ICAM-1 plus anti-NKp30 / NKp46 Ab conditions. **e.** F-actin intensity distribution per cell across PLL and ICAM-1 plus anti-NKp30 / NKp46 Ab conditions. **f.** Representative images of Jurkat cells on PLL or ICAM-1 plus anti-CD3 Ab, stained for F-actin (green), LFA-1 (red) and the nucleus (DAPI). Scale bars: 10 μ m. **g.** Selected IS features analysed as fold change of ICAM-1 plus anti-CD3 Ab over PLL. The data represent the mean of triplicates (n= 125-940 cells). **h.** Median F-actin and LFA-1 intensity per image across PLL and ICAM-1 plus anti-CD3 Ab conditions. **i.** F-actin intensity distribution per cell across PLL and ICAM-1 plus anti-CD3 Ab conditions.

assembly of the IS in NK-92 and Jurkat cells highlight F-actin intensity rise and cell spreading as common traits. However, in line with the distinct appearance of their actin rich peripheral protrusions, Jurkat cells, but not NK-92 cells, became rounder upon activation. Furthermore, while NK-92 flattened their nucleus, the effect was not marked in Jurkat cells, indicating a distinct cell spreading behavior. Overall, our data validate the reliability and power of HCI with high spatial resolution to unbiasedly define the

morphological profiles of lymphocytes in response to stimulatory regimens.

Cytoskeleton drugs induce non-identical alterations of the NK cell IS.

Given the prominent actin remodeling activity sustaining IS assembly, we next exploited our HCI approach to monitor how pharmacological modulation of cytoskeletal dynamics would affect

IS architecture. NK-92 cells were treated with seven drugs known to target distinct aspects of actin and acto-Myosin dynamics, which were used at 3 concentrations in order to detect possible dose-dependent effects. NK-92 cells were pre-treated with drugs for 30 minutes before seeding on ICAM-1 and anti-NKp30 / NKp46 Ab. In a first step, the effects of these drugs on the previously selected quantitative morphological features of the IS were assessed.

Upon treatment with Latrunculin B, which binds actin monomers and inhibits actin

polymerization, a concentration-dependent decrease in F-actin intensity was detected as compared to the untreated control (**Fig. 2a**), in concordance with an expected reduction in actin polymerization. However, IS assembly was not fully impeded as revealed by a minor reduction of cell area. Remarkably, Latrunculin B treatment elicited an increase of the number of perforin granules and the area they occupied at the cell to substrate interface. This might reflect impaired exocytosis and accumulation of aberrantly

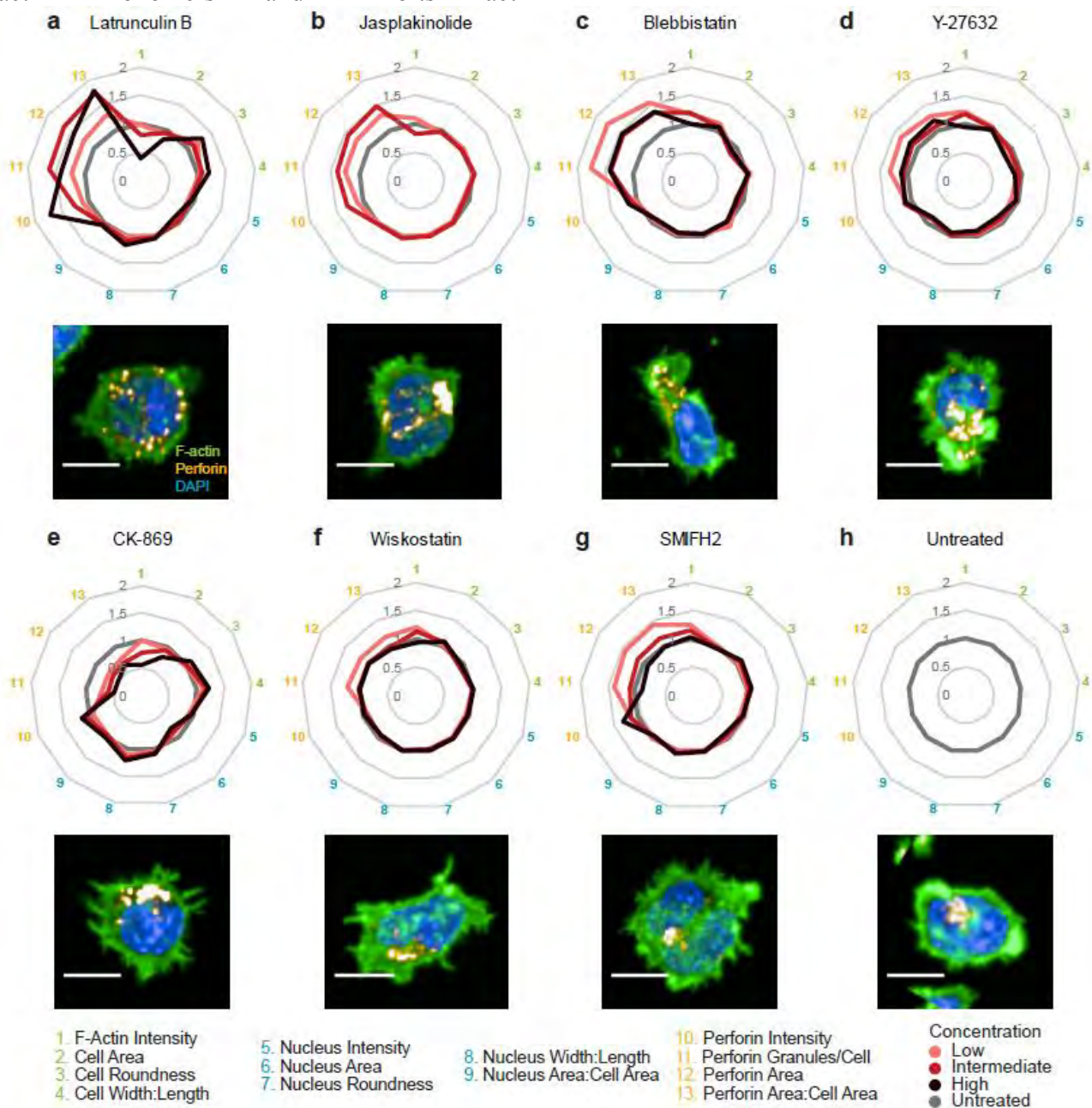


Fig. 2 | Drug treatments yield changes to immunological synapse morphology. Graphs representing the fold change of IS parameters and representative images of NK-92 cells seeded on ICAM-1, anti-NKp30 and anti-NKp46, stained for F-

actin (green), perforin granules (yellow) and nuclei (DAPI) and treated with three concentrations of **a.** Latrunculin **b.** Jasplakinolide, **c.** Blebbistatin, **d.** Y-27632, **e.** CK-968, **f.** Wiskostatin, and **g.** SMIFH2 with respect to the untreated control. **h.** Untreated control. The data represent the mean of triplicates for each concentration (1425-5541 cells). Scale bars: 10 μ m.

spread lytic granules at the IS. Such explanation is in agreement with the role of actin dynamics in facilitating the docking and exocytosis of lytic granules^{21,25}. Upon treatment with Jasplakinolide, which stabilizes actin, a mild decrease in F-actin intensity was detected at 1 μ M, supporting the notion that actin turnover is required to fuel polymerization^{26,27}(**Fig. 2b**). A higher concentration of 2.5 μ M was tested but could not be exploited because of its apparent detrimental effect on cell viability. In comparison to Latrunculin B, Jasplakinolide treatment elicited an increase in the perforin-related features, confirming that actin turnover is required for lytic granule exocytosis^{25,27}. Treatment with the Myosin inhibitor Blebbistatin induced a slight increase in F-actin intensity at 5 and 10 μ M (**Fig. 2c**). More strikingly it increased the number of granules detected at the synapse and the area they occupied, consistent with previous findings that Blebbistatin hinders granule exocytosis without affecting their polarization^{28,29}. Treatment with the ROCK inhibitor Y-27632 affected F-actin intensity, cell area and lytic granule features similar to those elicited by Blebbistatin treatment (**Fig. 2d**), in agreement with the activity of ROCK as an upstream regulator of acto-Myosin contractility. Upon CK-869 treatment, a concentration-dependent decrease in F-actin intensity was detected (**Fig. 2e**), showing, as expected, that ARP2/3 complex inhibition reduced actin polymerization³⁰. Moreover, CK-869 treated cells displayed reduced radial spreading, as shown by decreased area and increased cell width to length ratio, indicative of a severe impairment of IS assembly. A distinct property of CK-869 treatment was a reduction in the number of and area covered by perforin granules, possibly reflecting the inability of CK-869 treated cells to polarize lytic granules towards the stimulatory surface because of defective IS assembly. Upon treatment with Wiskostatin, an inhibitor of WASP, which drives ARP2/3-dependent actin branching, a slight increase in F-actin intensity was measured for the two lowest concentrations (**Fig. 2f**). In comparison with CK-

869, Wiskostatin displayed minor effects on perforin features. This suggests that the ARP2/3 activator WASP plays a limited role in the overall actin polymerization rate at the IS and in lytic granule polarization and secretion^{24,31}. Treatment with the pan-formin blocker SMIFH2 led to a concentration-dependent increase in F-actin intensity (**Fig. 2g**). Low-concentration SMIFH2 treatment resulted in an increase in perforin intensity and area. Collectively, these data indicate that drugs affecting different facets of actin remodeling differentially altered the assembly of the NK cell IS.

To further assess whether the morphological alterations inflicted by the drugs could be distinguished one from another, we trained a random forest classifier based on the 13 selected features. The image set was split to carry out a parameter optimization and to validate the performance of the model. The obtained overall accuracy of 69% and F_1 score of 0.7 confirmed that our method performed relatively well at distinguishing the morphological effects of the actin drugs. The confusion matrix shows that most drugs were predicted with high accuracy based on the corresponding image features, while the morphological effects of Blebbistatin and Y-27632 could not be easily distinguished, in line with their highly related mechanism of action (**Fig. S2a**). It also confirmed F-actin intensity as a major discriminating feature and identified cell eccentricity and roundness as key features to account for the morphological alterations induced by the drugs (**Fig. S2b**).

Overall, our comparative image-based analysis of the effects of different drugs affecting actin and acto-Myosin dynamics reveals that distinct effects on actin turnover and polymerization yield distinguishable IS morphologies but converge in affecting lytic granule positioning. This supports the notion that multiple actin-dependent steps control lytic granule docking and exocytosis³².

High-resolution morphology profiling of NK cells upon drug treatment.

To further enrich our morphological analysis of the IS in the context of drug treatment, we considered additional morphological features beyond the previously analyzed quantitative features. From 1898 measured features, a set of 383 features was retained following filtering of non-informative and redundant features. In order to visualize the information contained in this large feature set, as well as to quantify the significance of morphological changes upon drug treatment as compared to untreated cells, we applied a UMAP dimensionality reduction. This allows the visualization of all cell images, recapitulating in a ‘morphological space’ the relation between the morphology they display, by summarizing the

variation of the 383 features into two dimensions (Fig. S2c). By examining the relation between these features, we saw that both the different types of measurements acquired, and the different biological objects studied provided complementary and non-redundant information about the global changes occurring between images and between treatments (Fig. S2d). This also showed that none of these morphological features were repeating technical confounders, such as experimental plate position effect or cell count. As clearly visible in the morphological space, images of cells treated with Latrunculin B, Jasplakinolide and CK-869 clustered away from the untreated cells and from one another, most likely owing to these drugs having prominent and distinct

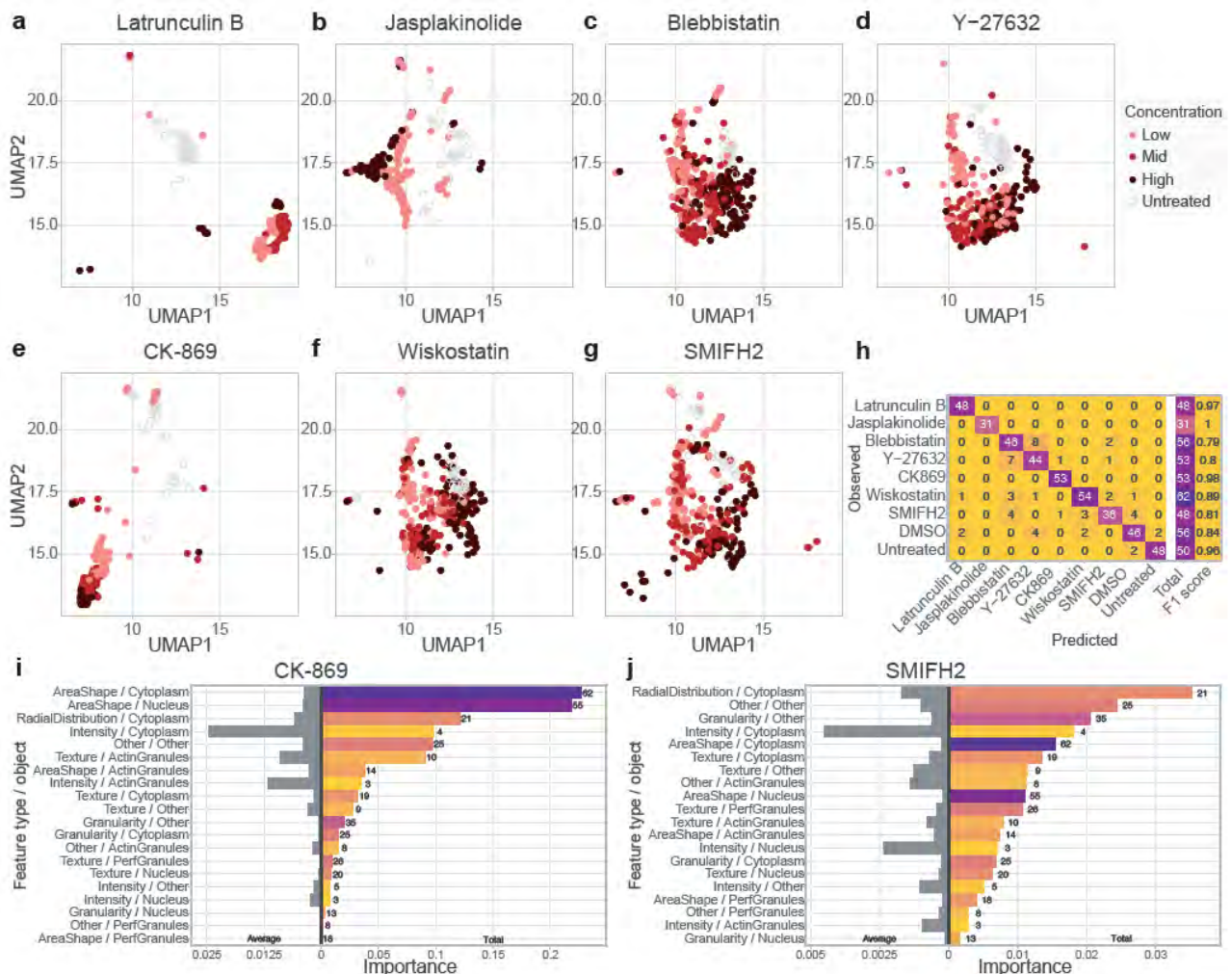


Fig. 3 | Morphological profiling of the NK cell immunological synapse upon drug treatment. Drug-treated NK-92 cell images were analysed with CellProfiler for an array of measurements and visualized using UMAP to position drug treated cells with respect to untreated cells from the same row. **a.** Latrunculin **b.** Jasplakinolide, **c.** Blebbistatin, **d.** Y-

27632, **e.** CK-968, **f.** Wiskostatin, and **g.** SMIFH2. **h.** Confusion matrix and class-wise performance on held-out data of a random forest model trained to predict drug treatment based on the morphology of NK-92 cells seeded on ICAM-1, anti-NKp30 and anti-NKp46. **i-j** Total and average importance for the prediction of morphological features per measurement type and biological object described of NK-92 cells seeded on ICAM-1, anti-NKp30 and anti-NKp46 and treated with **i.** CK-869 or **j.** SMIFH2.

effects on the ability of NK-92 cells to assemble the IS (**Fig. 3a, b and e**). In comparison, morphologies of cells treated with Blebbistatin, Y-27632, Wiskostatin and SMIFH2 appeared to be less distinct from the untreated condition and to cluster at close vicinity to one another (**Fig. 3c, d, f and g**). The three concentrations assayed per treatment fell into distinct sub-clusters, clearly indicating dose-dependent effects, as detailed for CK-869 and SMIFH2 (**Fig. S2e and f**). All drug-evoked morphological profiles were found to be significantly distant from the untreated state. Indeed, the median robust Mahalanobis distances between the fields of view per treatment and their matching negative controls are larger than expected at random (**Fig. S2g**)^{33,34}. To get insight into the nature of the changes that are causative of the observed clusters on the UMAP representation, we trained a random forest classifier on the set of 383 features. This achieved a satisfactory performance, as shown on the confusion matrix (**Fig. 3h**) with an F_1 score and an accuracy of 0.89 and 89%, respectively. The importance of each feature for the classification was proxied by the average increase in accuracy obtained by including the given feature in a decision tree. In particular, our analysis shows that CK-869 treatment mostly affected nucleus and cytoplasm shape descriptors (**Fig. 3i**), while SMIFH2 treatment altered radial intensity distributions in the cytoplasm (**Fig. 3j**). Only four features described intensities in the cytoplasm within our feature set. Interestingly, those few

features were in average increasing the model accuracy the most, strengthening the necessity, but not sufficiency, of actin intensity measurements to profile the IS. Features pertaining to lytic granules also played a determinant role in reinforcing model accuracy, providing further evidence of a tight regulation of lytic granule distribution at the IS. Our data therefore demonstrates the ability of the unbiased profiling to identify relevant spatially localized events and characterize perturbed cell states with high-resolution power.

Morphological profiling of primary human NK cells upon drug treatment.

We next applied our HCI approach to assess the susceptibility of primary human lymphocytes from different donors to cytoskeletal drugs. For that purpose, NK cells were purified from the peripheral blood of three normal donors, treated with four concentrations of either CK-869 or SMIFH2, and stimulated with ICAM-1 and anti-NKp30 / NKp46 Ab (**Fig. 4a**). Although the untreated cells from the three different healthy donors displayed variation in morphology, an actin-rich IS with the lytic granules concentrated in one area towards the cell periphery was observed upon stimulation. The four tested concentrations of CK-869 caused a marked decrease in F-actin intensity in the NK cells from the three donors, demonstrating the capacity of our approach to detect actin cytoskeleton

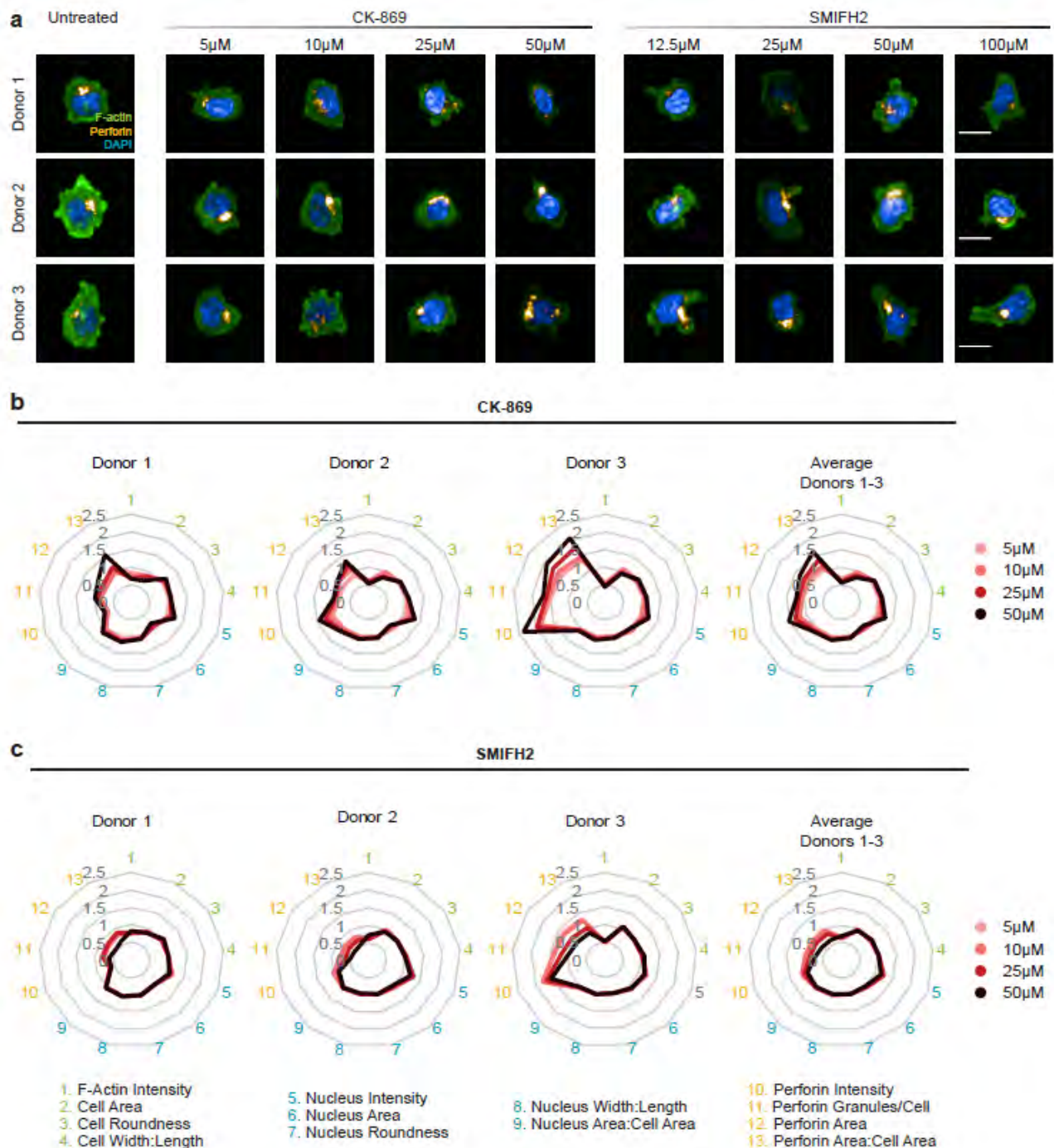


Fig. 4 | CK-869 and SMIFH2 treatments alter immunological synapse architecture and lytic granule polarization in primary NK cells. **a.** Representative images of primary NK cells isolated from PBMCs of three normal donors seeded on ICAM-1, anti-NKp30 and anti-NKp46, stained for F-actin (green), perforin granules (yellow) and nuclei (DAPI) and either untreated or treated with four concentrations of CK-869 or SMIFH2. Scale bars: 10 μ m. **b-c** Graphs representing the fold changes of immunological synapse parameters of primary NK cells treated with **(b)** CK-869 and **(c)** SMIFH2 with respect to untreated controls. The data represent the mean of 4 replicates for each drug concentration (60-409 cells).

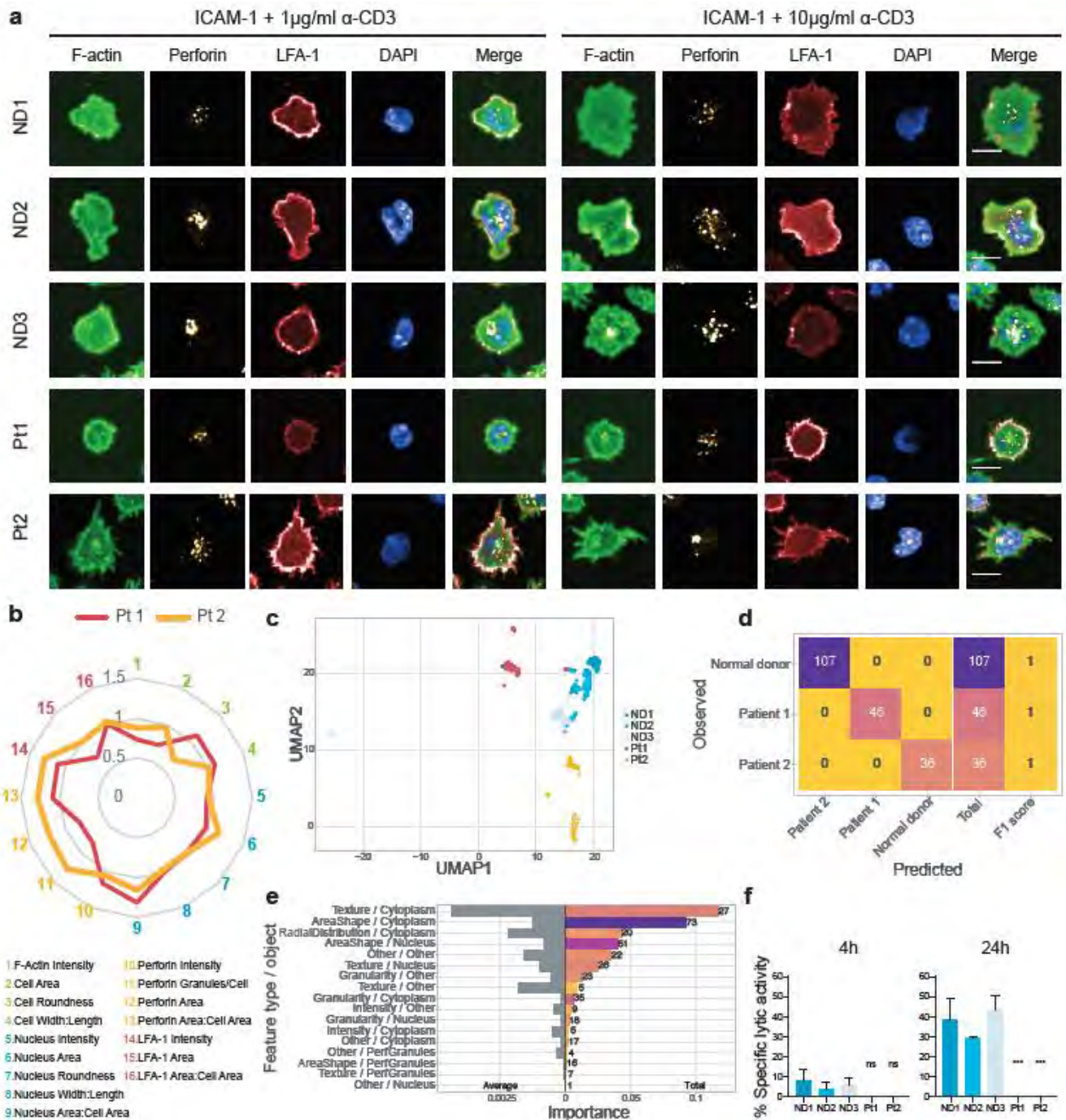
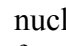


Fig. 5 | High content imaging of the immunological synapse in ARPC1B deficient CD8+ T cells. a. Representative images of CD8+ T cells from normal donors and ARPC1B deficient patients seeded on ICAM-1 and either 1 or 10 μ g/ml anti-CD3 and stained for F-actin (green), perforin granules (yellow), LFA-1 (red) and nuclei (DAPI). Scale bars: 10 μ m. **b.** Characteristics of the immunological synapse of CD8+ T cells of the two ARPC1B deficient patients represented as fold change with respect to the average of the three normal donors seeded on ICAM-1 and 1 μ g/ml anti-CD3. The data represents the mean of 6 replicates for each donor (10687-19353 cells) **c.** UMAP projection of CD8+ T cells morphological profiles from the two patients and the three normal donors seeded on ICAM-1 and 10 μ g/ml anti-CD3. **d.** Confusion matrix and class-wise performance on held-out data of a random forest model trained to discriminate between patient and normal donors based on the morphology of CD8+ T cells seeded on ICAM-1 and 10 μ g/ml anti-CD3. **e.** Total and average importance of morphological features per measurement type and biological object described for the prediction of patient and normal donor CD8+ T cells seeded on ICAM-1 and 10 μ g/ml anti-CD3. **f.** Specific lytic activity of patient and normal donor CD8+ T cells incubated with P815 cells coated with 10 μ g/ml anti-CD3 after 4 h and 24 h. Values represent the mean of triplicates and error bars show SD. Significance is noted as *($P < 0.05$).

alterations in primary lymphocytes. Notably, the area covered by the perforin granules, taken as an absolute value or divided by the cell area, was increased in the CK-869 treated NK cells from the three donors, showing a clear dose-dependent response (**Fig. 4b**). This effect is opposite to what was measured in the NK-92 cells, highlighting contrasting responses of model cell lines and primary cells. Moreover, the four tested concentrations of SMIFH2 also caused a decrease in F-actin intensity in the NK cells from the three donors, thereby highlighting the importance of formins for actin remodeling at the IS (**Fig. 4c**). SMIFH2 treatment also strongly affected the distribution of perforin granules. Interestingly, in NK cells from donors 1 and 2, a dose dependent reduction of both perforin granule number and covered area was observed, a response opposite to that to CK-869. In contrast with donors 1 and 2, low concentrations of SMIFH2 resulted in an increase of perforin granule number and covered area in NK cells from donor 3. It should be noted that lower number of perforin granules were detected in the untreated cells from this donor, possibly influencing the response to the tested drugs. Those observations highlight the potential of HCI to identify features underlying inter-donor variability upon stimulation and treatment of lymphocytes populations, which may be explained by the phenotypic variation of each donor's NK cells³⁵. Together, the dataset collected on primary NK cells demonstrates that HCI is amenable to the morphological profiling of primary human lymphocytes in the context of drug treatments and that it can discriminate specific responses from individual donors.

Immunological synapse defect is associated with impaired cytotoxicity in CD8⁺ T cells from ARPC1B deficient patients.

We then reasoned that the HCI approach might be adapted to characterizing lymphocyte impairments in the context of pathology. For that purpose, we implemented a morphological profiling of CD8⁺ T cells isolated from two patients suffering from a primary immunodeficiency caused by mutations in *ARPC1B*, which encodes one subunit of the ARP2/3 complex. Cells from the two patients and

three normal donors were stimulated with ICAM-1 and either 1 or 10 µg/ml anti-CD3 Ab, and stained for perforin and LFA-1, F-actin and the nucleus.  images suggests that the CD8⁺ T cells from both patients spread less than control cells and failed to assemble a typical IS (**Fig. 5a**). Analysis of 16 selected morphological features highlighted that F-actin intensity was decreased in T cells from the two patients, as compared to the cells from the normal donors, following stimulation with anti-CD3 Ab at both concentrations (**Fig. 5b** and **Fig. S3a**). This is comparable to the data collected above in cell lines and primary cells upon treatment with the ARP2/3 inhibitor CK-869. Cells from the two patients however displayed distinct morphological aberrations. While cell area was mostly affected in cells from patient 1, implying an impaired spreading ability, cell roundness was prominently decreased in patient 2, most likely resulting from aberrant peripheral actin spikes. T cells from patient 2 displayed an increased number and dispersion of perforin granules, similarly with what we observed in primary NK cells treated with CK-869. However, fewer perforin granules were detected in T cells from patient 1. Their dispersion was reduced in absolute terms but increased when normalized for the cell area, the latter being reduced. LFA-1 intensity was increased in the T cells from both patients and LFA-1 was localized at the cell rim rather than at the cell to substrate contact area, suggesting abnormal distribution of adhesive forces. Our morphological profiling clearly establishes that CD8⁺ T cells from the two considered ARPC1B-deficient patients have severe impairments in IS assembly. The distinct synaptic alterations revealed by our approach in the two patients could not be explained by differences in the phenotype of the cells, which showed similar expression of CD8, perforin, LFA-1, and granzyme B (**Fig. S3 f-i**). To further enrich our analysis, we applied once more a UMAP approach to explore the morphological space, which evidenced a marked segregation of the two patients from the control donors, but also among each other (**Fig. 5c** and **Fig. S3b**). This analysis therefore reinforces the finding that patient T cells have aberrant synaptic traits and that the nature of these aberrations is distinct

between the two patients. Interestingly, we noticed that even though the normal donors clustered closely to each other, donor 3 did not overlap with the other two at either anti-CD3 Ab concentration, confirming that heterogeneity in IS morphology exists among normal donors, as observed above for NK cells. A first random forest model showed that we could determine the concentration of anti-CD3 Ab used to stimulate the cells with an accuracy of 95% and F_1 score of 0.95 (**Fig. S3c**), and indicated that IS assembly varied according to the concentration of anti-CD3 Ab (**Fig. S3d**). This was associated with changes in shape and radial distribution in the cytoplasm, while cytoplasm intensities were the most discriminative feature category in average, fitting a scenario in which TCR stimulation strength would differentially remodel the actin cytoskeleton and associated synapse morphology. A second model showed that our approach is powerful enough to distinguish patient cells from normal donor cells seeded on ICAM-1 and 10 $\mu\text{g/ml}$ anti-CD3 Ab by achieving a perfect classification on a validation set (**Fig. 5d**), distinguishing ARPC1B deficient cells mostly on the basis of textural and intensity distribution changes within the cytoplasm (**Fig. 5e**). Moreover, some features changed not only between ARPC1B patients and normal donors but were as well discriminating between patient 1 and patient 2 (**Fig. S3e**), further reinforcing that the two patients have distinct IS architectures. The aberrant IS characterized in the patients through the morphological profiling approach alluded to a possible functional defect. We therefore assessed the cytotoxic activity of CD8^+ T cells towards anti-CD3 Ab-coated P815 target cells. Whereas, normal CD8^+ T cells started to kill target cells in four hours, CD8^+ T cells from the ARPC1B deficient patients failed to do so. The patient derived CD8^+ T cells remained defective at killing target cells over a prolonged 24-hour incubation (**Fig. 5f**). This indicates that the T cells from the patients most likely fail to secrete lytic molecules, despite a normal content in perforin and granzyme B (**Fig. S3g and i**). Our results therefore indicate that the defects in IS organization characterized in both patients are leading to a severe impairment of the cytotoxic activity.

Discussion

By combining automated cell imaging with computational image analysis pipelines, HCI provides novel opportunities to systematically analyze cellular mechanisms^{15,36,37}. However, the potential of such approach has not yet been explored for the study of immune cells. We here tailor a HCI approach for the high-resolution morphological profiling of various human cytotoxic lymphocyte population, and focus on the imaging of the IS as a mean to capture the activation state and effector potential of these cells. We validate our HCI approach by identifying distinct morphological signatures evoked by a panel of actin-targeting drugs. We further reveal the power of our HCI approach to discriminate individual donors on the basis of immune cell morphological traits. We also exemplify the clinical applicability of such approach by identifying cytotoxic lymphocyte aberrations in patients with a severe congenital immunodeficiency.

Although we use a minimalistic 2D static approach based on the adsorption of stimulatory molecules on the surface microwells, it proves to robustly stimulate the assembly of morphological structures qualifying as IS. We show that various human lymphocyte populations, including model cell lines, cells freshly isolated from the blood, as well as expanded primary cells can be stained and imaged with an automated confocal microscope at high resolute power in a 384-well format, allowing the analysis of several samples, activation conditions and perturbations in parallel. Computationally, we use robust statistics and work at an image-level resolution, typically gathering a few dozens of cells imaged over four z planes representing the 2- μm section of the cells most proximal to the stimulatory substrate. While most morphological profiling studies have been limited to average profiles over wells or replicates^{14,37,38}, a few approaches have defined profiles based on single cells^{39,40}. We here rather consider the variability in morphology displayed in each image by including measures of dispersion that are proven to be beneficial for morphological profiles and could potentially be further improved by adding a higher order joint statistical moment⁴¹. From an analytical point of

view, we elaborate two complementary methods. First, we focus on a pre-defined set of morphological features based on prior knowledge and including cell and nucleus shape parameters as well as intensities of F-actin, LFA-1 and perforin at the synaptic plane. We show that such method can be applied to relatively low numbers of images and provides meaningful identification of discriminative features when comparing experimental conditions. Second, we implement a high-resolution and unbiased morphological profiling pipeline, from which novel relevant features can be identified and from which high-performance classifiers can be trained to discriminate cell states corresponding to different stimulations, drug treatments or genetic defects.

Beyond the methodological advance provided in this study, we present data relevant to the understanding of lymphocyte activation in both a fundamental and medically relevant perspective. Among the pre-defined set of morphological features, we identify increase of F-actin as a hallmark of T and NK lymphocyte stimulation by combinations of ICAM-1 and antibodies directed against CD3 or NK receptors, respectively. This is in line with the previously established role of the actin cytoskeleton in driving the cell spreading behavior supporting IS assembly^{42,43}. The further investigation of the role of actin cytoskeleton remodeling by the treatment of NK cells with a drug array reveals distinct morphological alterations upon targeting actin polymerization, depolymerization and Myosin II. Our data also point to converging morphologies induced by some of the drugs with distinct modes of action, possibly related to a limited number of configurations of the cytoskeleton, as recently described in an adherent neuroblastoma cell line^{36,44}. Strikingly, most tested drugs yield prominent alteration of the distribution of perforin-containing granules, indicating that the different facets of actin cytoskeleton dynamics are all important to regulate the polarized delivery of lytic granules at the IS^{25,45}.

Owing to the distinct morphological profiles observed for each drug, and the detection of dose-dependent effects, both in cell lines and primary cells, such an approach could be applied in the context of immunotherapeutic drugs. A striking

finding of the application of morphological profiling to lymphocyte populations is that it reveals a previously unappreciated level of heterogeneity in cellular morphological traits among individuals. When considering the data pertaining to the NK cells freshly isolated from the blood, we cannot rule out that morphological differences arise from distinct activation states of the cells from different donors. However, *in vitro* stimulation and expansion of T lymphocytes, which is expected to robustly drive cells towards a differentiated phenotype⁴⁶, was also associated with distinct morphological traits. Further analysis of larger cohorts of donors and sorted subpopulations of lymphocytes will be required to precisely appreciate the degree of morphological heterogeneity among individuals and lymphocyte subsets. The detection of distinct morphological profiles among healthy individuals certainly highlights the extreme sensitivity of the HCI approach to characterize and compare cell populations. A further illustration of this property is provided by the characterization of IS alterations in T lymphocyte populations isolated from 2 patients with ARPC1B deficiency. Interestingly, again, our approach points to distinct morphological alterations in the cells from the 2 patients considered. Such differences might be inherent to the severity of the ARPC1B genetic defect.^{47,48} The study of larger cohorts of patients, which would be compatible with the herein developed approach, would be required to answer such question.

CD8⁺ T cells from ARPC1B patients display an aberrant IS morphology including defects pertaining to the distribution of perforin granules and LFA-1. Comparably to other studies, we show a reduced cell area and a failure to spread radially and emit lamellipodia upon TCR stimulation⁴⁷. The lack of lamellipodia formation was also observed upon NK-92 and primary NK cell treatment with CK-869. Our data reveals increased accumulation of lytic granules at the IS for one patient, which could indicate a defect in granule exocytosis, opposed to a decrease in perforin related parameters for the other patient, most likely indicative of failed lytic granule polarization. These observations are in agreement

with a recent study showing defective lytic granule polarization and degranulation in ARPC1B deficient CD8⁺ T cells⁴⁹. The detection of such IS defects is suggestive of a possible alteration of the cytotoxic activity. Our data shows that ARPC1B deficient cells fail to eliminate target cells, as recently reported⁴⁹. This illustrates the potential of HCI to provide guidance for the implantation of complementary low throughput assays to assess defects at the functional and molecular level. At this stage, we cannot generalize the case of the ARPC1B deficiency in establishing a systematic relationship between IS alteration and functional defect. However, it is interesting to mention that multiple primary immunodeficiencies have been found by us and others to associate IS defects and functional impairments^{50–53}. Previous reports have also shown that PIDs where the IS is defective fail to eliminate target cells^{51,53,54}. The systematic analysis of multiple such pathologies and corresponding cellular models would certainly provide a unique opportunity to establish rules linking morphology to function.

Overall, we provide here an innovative HCI approach to unbiasedly interrogate the biology of lymphocyte populations. It provides a rich way to identify and interpret details of the IS architecture and surpass current approaches in detecting morphological traits of specific lymphocyte populations, as illustrated by the distinct morphological profiles identified among the primary lymphocytes of individual donors. This hold promises to stratify patients based on specific morphotypes of lymphocytes or other leukocytes. Therefore, we thoroughly report both the experimental and computational methods employed and provide all scripts used in the analysis to maximize the reproducibility of the approach developed herein. We hope this encourages further research leveraging the application of HCI to blood-derived cell subsets, for potential translation in the field of cancer therapy and personalized medicine.

Materials and methods

Cell lines and primary cells

Jurkat cells were cultured in RPMI (Gibco) supplemented with 10% FBS, 1% penicillin/streptomycin, 1% sodium pyruvate, 1% non-essential amino acids and 1% HEPES (all from Thermo Fisher Scientific). NK-92 cells were cultured according to the recommendations from ATCC. Primary NK cells were purified from freshly isolated PBMCs using the MagniSort Human NK enrichment kit (Invitrogen) and maintained in RPMI supplemented with 5% human serum, 1% penicillin/streptomycin, 1% sodium pyruvate, 1% non-essential amino acids and 1% HEPES. Primary CD8⁺ T cells were purified from frozen PBMCs of 3 healthy donors and 2 ARPC1B deficient patients by negative selection using the EasySep Human CD8⁺ T cell enrichment kit. CD8⁺ T cells were stimulated in RPMI supplemented with 5% human serum, 1% penicillin/streptomycin, 1% sodium pyruvate, 1% non-essential amino acids, 1% HEPES 1 µg/ml PHA and 100 IU/ml IL-2. CD8⁺ T cells were expanded for further rounds every 2 weeks with a mixture of irradiated PBMCs from 3 normal donors. Peripheral blood from healthy donors and patients was obtained in accordance with the 1964 Helsinki declaration and its later amendments or ethical standards. Informed consents were approved by the relevant local Institutional Ethical Committees.

Culture and staining conditions used for High content imaging

CellCarrier Ultra tissue culture treated plates (Perkin Elmer) were coated with either 0.01% PLL (Merck) or a combination of 2 µg/ml ICAM-1 (R&D Systems), 1 µg/ml NKp30 (R&D systems, MAB18491) and 1 µg/ml NKp46 (BD Biosciences, 557487). NK-92 cells were cultured in IL-2 free medium overnight. 15000 NK-92 and 5000 primary NK cells were seeded per well and left for 30 min at 37°C to adhere and form the synapse. Cells were fixed with 3% paraformaldehyde (Merck) and stained with anti-perforin Ab and phalloidin-AF 488. Goat anti-mouse AF 555 was used to reveal perforin staining. Nuclei were stained with DAPI.

NK-92 were treated with 5, 10 and 50 µM Blebbistatin, 10, 25 and 50 µM CK-869 (Merck), 0.1, 1 and 2.5 µM Jasplakinolide (Merck), 0.1,

0.25 and 0.5 μM Latrunculin B (Merck), 50, 100 and 250 μM SMIFH2 (Merck), 10 50 and 100 μM Wiskostatin (Merck) and 5, 10 and 25 μM Y-27632 (Merck) for 30 min at 37°C and washed twice in PBS before seeding onto the plates and letting them adhere for 30 min. The same procedure was applied to primary NK cells treated with 5, 10, 25 and 50 μM CK-869 and 25 50, 100 and 250 μM SMIFH2.

CellCarrier Ultra multiwell tissue culture treated plates were coated with either 0.01% poly-L-lysine or a combination of 2 $\mu\text{g}/\text{ml}$ ICAM-1 and 10 $\mu\text{g}/\text{ml}$ anti-CD3 (eBioscience). 10000 Jurkat or 5000 CD8⁺ T cells were seeded per well and left for 15 min at 37°C to adhere and form the synapse. Cells were fixed with 3% paraformaldehyde and stained with anti-LFA-1 (BioLegend, 301202) and phalloidin-AF 488 (Thermo Fisher Scientific) in permeabilization buffer (eBioscience). Goat anti-mouse AF 647 antibody (Thermo Fisher Scientific, A-21240) was used to reveal LFA-1 staining. CD8⁺ T cells were in addition stained with anti-perforin and goat anti-mouse AF 555 (Life technologies) was used to reveal perforin staining. Nuclei were stained with DAPI (Thermo Fisher Scientific). Stained cells were kept in PBS at 4°C until imaging.

Image acquisition and processing

Images were acquired on an automated spinning disk confocal HCS device (Opera Phenix, Perkin Elmer) equipped with a 40x 1.1 NA Plan Achromat water immersion objective and a sCMOS camera. For each well, 40 randomly selected fields and 8 stacks per field (0.5 μm step) were acquired. Stacks of images were combined with maximum projection for four focal slices (z from 1 to 4 with a 0.5 μm step), then assembled in sets of images per field of view corresponding to DAPI, phalloidin and LFA-1 or perforin depending on the cell type imaged. These datasets were processed, and measurements were made using CellProfiler 3.0¹⁸ (see Supplementary Files [CellProfiler pipeline]). In brief, we assess the image quality, log-transform the intensities for experiments with high background noise, correct the illumination on each image based on background intensities, avoid DNA precipitations

by multiplying intensities on DAPI channel by phalloidin intensities before segmenting cell nuclei using global minimum cross entropy thresholding. We perform a secondary segmentation of the cytoplasm using the watershed method⁵⁵ and global minimum cross entropy thresholding on the phalloidin channel. Image sets with low maximal DNA intensity or showing no nucleus were discarded. Cells having more than 30% of their cytoplasm surface at less than 5 pixels of another cell were removed, in order to ignore clusters of cells and to focus on single cells displaying an IS. We segmented small actin speckles in the cytoplasm at more than 3 pixels from the membrane as well as speckles of perforin and secondary objects spanned around the nuclei by LFA-1 staining. Additionally, primary NK and expanded CD8⁺ T cells associated with less than 2 perforin granules were excluded from the analysis. Finally, we measured colocalization of these objects, intensities in the nuclei and cytoplasm, granularity on all channels, textural and shape features, intensity distributions, distance and overlap between objects and counted speckles neighbors less than 10 pixels away. We then kept the average and the standard deviation of these features per field of view. This led to 1898 and 2076 morphological features in NK92 and Jurkat cells respectively. For primary NK cells and expanded CD8⁺ T cells, features related to actin speckles were excluded, as they were not found to be informative, resulting in 2386 and 1517 features, respectively.

Stacks of images were combined with maximum projection for four focal slices (z from 1 to 4 with a 0.5 μm step), then assembled in sets of images per field of view corresponding to DAPI, phalloidin and LFA-1 or perforin depending on the cell type imaged. These datasets were processed, and measurements were made using CellProfiler 3.0¹⁸ (see the pipelines provided).

In brief, we assess the image quality, log-transform the intensities for experiments with high background noise, correct the illumination on each image based on background intensities, avoid DNA precipitations by multiplying intensities on DAPI channel by phalloidin intensities before segmenting cell nuclei using global minimum cross entropy thresholding. We

perform a secondary segmentation of the cytoplasm using the watershed method⁵⁵ and global minimum cross entropy thresholding on the phalloidin channel. Image sets with low maximal DNA intensity or showing no nucleus were discarded. Cells having more than 30% of their cytoplasm surface at less than 5 pixels of another cell were removed, in order to ignore clusters of cells and to focus on single cells displaying an IS. We segmented small actin speckles in the cytoplasm at more than 3 pixels from the membrane as well as speckles of perforin and secondary objects spanned around the nuclei by LFA-1 staining. Additionally, primary NK and expanded CD8⁺ T cells associated with less than 2 perforin granules were excluded from the analysis. Finally, we measured colocalization of these objects, intensities in the nuclei and cytoplasm, granularity on all channels, textural and shape features, intensity distributions, distance and overlap between objects and counted speckles neighbors less than 10 pixels away. We then kept the average and the standard deviation of these features per field of view. This led to 1898 and 2076 morphological features in NK92 and Jurkat cells respectively. For primary NK cells and expanded CD8⁺ T cells, features related to actin speckles were excluded, as they were not found to be informative, resulting in 2386 and 1517 features, respectively.

Data processing and visualization

We subsequently conducted analyses in R 3.5.1 with the data visualization package ggplot2 3.1.1 and Microsoft Excel (Version 1902). We further selected a smaller set of informative morphological features and checked the quality of processed images by (i) removing wells with low maximal DNA intensity and cell count, (ii) removing features and images generating missing values and (iii) removing constant features in the study dataset or the subset of negative controls used as reference.

From these images passing our quality checks, up to 16 raw summary variables were extracted based on their interpretability and on their known relevance to describe ISs. The fold changes compared to unstimulated or untreated controls were further reported and displayed in the form of

radar charts. On the other hand, for all features, per-image values X were transformed successively with the following functions f_1 and f_2 , with $X_{Control}$ the negative controls in X on which the data is normalized:

$$f_1(X) = \log(X + 1 - \min(X))$$

$$f_2(X) = X - \frac{\text{median}(X_{Control})}{\text{mad}(X_{Control})}$$

To remove redundancy in the set of features used for downstream analyses, we ensured that the selected variables were not excessively linearly correlated. To do so, all features were ordered from highest to lowest median absolute deviation (hence by variation in the experiment compared to negative controls). Starting from the top of this list, all other features linearly correlated to the first feature with a Pearson's coefficient higher than 0.6 were excluded. We sequentially went on with the next remaining feature in the list and iterated until the acquisition of a small and informative set of uncorrelated features.

This set of features was used for visualization and quantification of the overall morphological changes induced by perturbations. We then reduced the dimensionality of the data using the UMAP algorithm⁵⁶ to 2 dimensions for visualizations and 3 dimensions for computation of the statistical significance of morphological effects in the drug screen on NK92. This pipeline succeeded in selecting a wide range of features that were not excessively biased by confounders (**Fig. S2d**).

Robust Morphological Perturbation Value

To quantify the significance of overall changes in morphology between a perturbed state and a reference state (healthy or untreated cells), we define the Robust Morphological Perturbation Value. This extends the concept of Multidimensional Perturbation Value³³, which defines a single value summarizing the statistical significance of morphological changes in multidimensional spaces, by using robust statistics and the minimum covariance determinant³⁴ decreasing the sensitivity to technical (unfiltered artifacts) and biological

outliers (images displaying extreme morphologies or uncommon cell states). In brief, the RMPV is obtained for X the set of all filtered and uncorrelated features and X_{WT} the subset of the data corresponding to images of the reference population in five steps. First, the minimum covariance determinant estimator $M(X_{WT})$ is calculated to describe the variation of morphologies observed in the reference set, using its implementation in the R package *robustBase* version 0.93. Second, this value is used to determine R , the robust Mahalanobis distance of each images of X to X_{WT} [arXiv:1904.02596 [stat.ME]]. Third, the median value $\tilde{R} = \text{median}(R)$ was obtained for each drug tested. Fourth, for 2000 iterations the labels of the condition and the reference were randomly permuted to obtain an empirical distribution of \tilde{R} under the assumption that there was no difference between the multivariate location and scatter of the morphological parameters of the perturbation and the reference. Finally, the RMPV is defined as the empirical p-value obtained from these distributions after FDR adjustment for testing changes in multiple conditions and indicates the probability of observing at least half of the images displaying morphological changes of a similar intensity if the perturbation was similar to the reference.

Random forest classification and interpretation

Using the set of informative and uncorrelated morphological features – previously used for dimensionality reduction, we trained a random forest classifier⁵⁷ using the R package *randomForest* version 4.6.

Using the set of informative and uncorrelated morphological features – previously used for dimensionality reduction, we trained a random forest classifier⁵⁷ using the R package *randomForest* version 4.6. Each forest included 1000 decision trees. The data was split in 6 folds of equal size, each containing all possible classification label. To select the optimal number *mtry* of variables selected at each split, we incremented the parameter value from 20 to 90 by steps of 10 and assessed the performance using the macro F_1 score as defined below in a 5-fold

cross-validation scheme. One extra fold was used as validation set to estimate the performance of the model after selection of the optimal parameters and retraining on all of the 5 folds used for cross-validation. In the case of the drug screen on the NK-92 cell line, we used a similar approach using the 13 features of known relevance in describing the IS as input, and testing *mtry* values from 1 to 13 with steps of 3. Overall the performance was evaluated using the macro F_1 score:

$$F_1 = \frac{1}{n} \sum_{i=1}^n \frac{2 \times TP_i}{2 \times TP_i + FP_i + FN_i}$$

where n is the number of categories in the classification, and TP_i , FP_i and FN_i are respectively the number of true positives, false positives and false negatives for category i in the validation set. To interpret the feature importance in the prediction, we extracted the mean decrease in accuracy obtained when including each feature, either for the prediction of a given class or overall using micro averaging. The total and average importance of features split in distinct groups based on the type of measurements and biological object described were calculated as well. These feature groups were defined based on the corresponding CellProfiler measurement types and biological objects. Features that did not describe the cytoplasm, nucleus, perforin granules or actin granules were counted in the “Other” biological object category. Similarly, features that did not correspond to the “Texture”, “AreaShape”, “RadialDistribution”, “Granularity” or “Intensity” measurements were grouped under the term “Other”.

Cytotoxicity assay

Target P815 cells were stained for 30 min with Cell Tracker green CMFDA (Thermo Fisher Scientific) and coated with 10 $\mu\text{g}/\text{ml}$ anti-CD3 (eBiosciences, 16-0037-81) for one hour at 37°C. They were also treated with 0.2 $\mu\text{g}/\text{ml}$ of aphidicolin to prevent their proliferation. P815 were incubated with effector CD8⁺ T cells in U-bottom 96 well plates at an effector: target ratio of 1:1 for 4 and 24 hours⁵⁸. Cells were then stained with Amino-Actinomycin D (7-AAD) (BD Biosciences) to discriminate dead and alive

cells using the MacsQuant VYB (Miltenyi) and analyzed with FlowJo. The number of residual alive CMFDA⁺ / 7-AAD⁻ cells was assessed to calculate cytotoxicity. Student's *t*-test was used to calculate significance.

Phenotypic analysis

Expanded CD8⁺ T cells from normal donors and ARPC1B-deficient patients were stained with fluorochrome-coupled antibodies recognizing the extracellular markers CD8 (BioLegend, 344718) and LFA-1 (BioLegend, 363404) for 30 min at 4°C. Intracellular staining was performed following fixation and permeabilization, with the following antibodies perforin (BioLegend, 308110) and granzyme B (BDPharmigen, 561142) for 45 min at 4°C. The data were acquired on MacsQuant Q10 (Miltenyi) and analyzed with FlowJo. Student's *t*-test was used to calculate significance.

Data availability

All the CellProfiler pipelines and morphological measurements used in this analysis are made available on FigShare with the DOI 10.6084/m9.figshare.11619960 [already available for reviewers with the following private link: <https://figshare.com/s/3c06753839d77783a899>].

Code availability

The analyses can be found and reproduced using the Docker image and scripts provided on Github and identified with the DOI 10.5281/zenodo.3518233.

Acknowledgements

The authors thank Fatima-Ezzahra L'Faqihi-Olive, Valérie Duplan-Eche, Anne-Laure Iscache and Lydia De La Fuente-Vizueté from the cytometry platform of the CPTP and Isabelle Fernandes from the Organoid platform of the IRSD, Muriel Quaranta-Nicaise, Laurène Pfajfer, Michael Caldera, Marianne Guisset and Anton Kamnev for discussion and technical advice, Alessandro Aiuti, Marco Gattorno and Stefano Volpi for patient-derived cell lines. Y.G. performed the experiments, analyzed the results and wrote the paper, L.V. designed and

performed data analysis and wrote the paper. A.R. contributed in image acquisition. A.F., J.M. and K.B. participated in research design and scientific discussions. L.D. designed the research, supervised the experiment analysis and wrote the paper.

The authors declare no competing interests.

Funding

This work was supported by the Vienna Science and Technology Fund (WWTF-LS16-060 to K.B. J.M. and L.D.), the INSERM Plan Cancer program (C15092BS to L.D.) and the Association Laurette Fugain (to L.D.).

References

1. Grakoui, A. *et al.* The immunological synapse: A molecular machine controlling T cell activation. *Science (80-.)*. **285**, 221–227 (1999).
2. Monks, C. R. F., Freiberg, B. A., Kupfer, H., Sciaky, N. & Kupfer, A. Three-dimensional segregation of supramolecular activation clusters in T cells. *Nature* **395**, 82–86 (1998).
3. Somersalo, K. *et al.* Cytotoxic T lymphocytes form an antigen-independent ring junction. *J. Clin. Invest.* **113**, 49–57 (2004).
4. Anikeeva, N. *et al.* Distinct role of lymphocyte function-associated antigen-1 in mediating effective cytolytic activity by cytotoxic T lymphocytes. *Proc. Natl. Acad. Sci. U. S. A.* **102**, 6437–6442 (2005).
5. Bryceson, Y. T., March, M. E., Ljunggren, H.-G. & Long, E. O. Synergy among receptors on resting NK cells for the activation of natural cytotoxicity and cytokine secretion. *Blood* **107**, 159–166 (2006).
6. Zhang, M., March, M. E., Lane, W. S. & Long, E. O. A signaling network stimulated by 2 integrin promotes the polarization of lytic granules in cytotoxic cells. *Sci. Signal.* **7**, ra96–ra96 (2014).

7. Urlaub, D., Höfer, K., Müller, M.-L. & Watzl, C. LFA-1 Activation in NK Cells and Their Subsets: Influence of Receptors, Maturation, and Cytokine Stimulation. *J. Immunol.* **198**, 1944–1951 (2017).
8. Geiger, B., Rosen, D. & Berke, G. Spatial relationships of microtubule-organizing centers and the contact area of cytotoxic T lymphocytes and target cells. *J. Cell Biol.* **95**, 137–143 (1982).
9. Ilani, T., Vasiliver-Shamis, G., Vardhana, S., Bretscher, A. & Dustin, M. L. T cell antigen receptor signaling and immunological synapse stability require Myosin IIA. *Nat. Immunol.* **10**, 531–539 (2009).
10. Rak, G. D., Mace, E. M., Banerjee, P. P., Svitkina, T. & Orange, J. S. Natural Killer Cell Lytic Granule Secretion Occurs through a Pervasive Actin Network at the Immune Synapse. *PLoS Biol.* **9**, e1001151 (2011).
11. Dustin, M. L. & Long, E. O. Cytotoxic immunological synapses: NK and CTL synapses. *Immunol. Rev.* **235**, 24–34 (2010).
12. Burns, S. O., Zerafov, A. & Thrasher, A. J. Primary immunodeficiencies due to abnormalities of the actin cytoskeleton. *Curr. Opin. Hematol.* **24**, 16–22 (2017).
13. Mace, E. M. & Orange, J. S. Insights into primary immune deficiency from quantitative microscopy. *J. Allergy Clin. Immunol.* **136**, 1150–1162 (2015).
14. Joshi, P. & Lee, M. Y. High content imaging (HCI) on miniaturized three-dimensional (3D) cell cultures. *Biosensors* **5**, 768–790 (2015).
15. Priestley, R. S. *et al.* A novel high-content imaging-based technique for measuring binding of Dickkopf-1 to low-density lipoprotein receptor-related protein 6. *J. Pharmacol. Toxicol. Methods* **95**, 47–55 (2019).
16. Wu, L. S. & Li, J. High-Content Imaging Phenotypic Screen for Neurogenesis Using Primary Neural Progenitor Cells. in 101–113 (2018). doi:10.1007/978-1-4939-7847-2_8.
17. Papakonstantinou, S. & James O’Brien, P. High content imaging for the morphometric diagnosis and immunophenotypic prognosis of canine lymphomas. *Cytom. Part B - Clin. Cytom.* **86**, 373–382 (2014).
18. Adelman, C. H., Wang, T., Sabatini, D. M. & Lander, E. S. Genome-Wide CRISPR/Cas9 Screening for Identification of Cancer Genes in Cell Lines. in 125–136 (2019). doi:10.1007/978-1-4939-8967-6_10.
19. Caldera, M. *et al.* Mapping the perturbome network of cellular perturbations. *Nat. Commun.* **10**, 5140 (2019).
20. Sieprath, T., Corne, T., Robijns, J., Koopman, W. J. H. & de Vos, W. H. Cellular redox profiling using high-content microscopy. *J. Vis. Exp.* **2017**, (2017).
21. Yin, Z. *et al.* How cells explore shape space: A quantitative statistical perspective of cellular morphogenesis. *BioEssays* **36**, 1195–1203 (2014).
22. Yu, K. K. H. *et al.* High content screening of patient-derived cell lines highlights the potential of non-standard chemotherapeutic agents for the treatment of glioblastoma. *PLoS One* **13**, 1–17 (2018).
23. Massey, A. J. A high content, high throughput cellular thermal stability assay for measuring drugtarget engagement in living cells. *PLoS One* **13**, 1–17 (2018).
24. Rohban, M. H. *et al.* Systematic morphological profiling of human gene and allele function via Cell Painting. *Elife* **6**, (2017).
25. McQuin, C. *et al.* CellProfiler 3.0: Next-generation image processing for biology. *PLoS Biol.* **16**, e2005970 (2018).

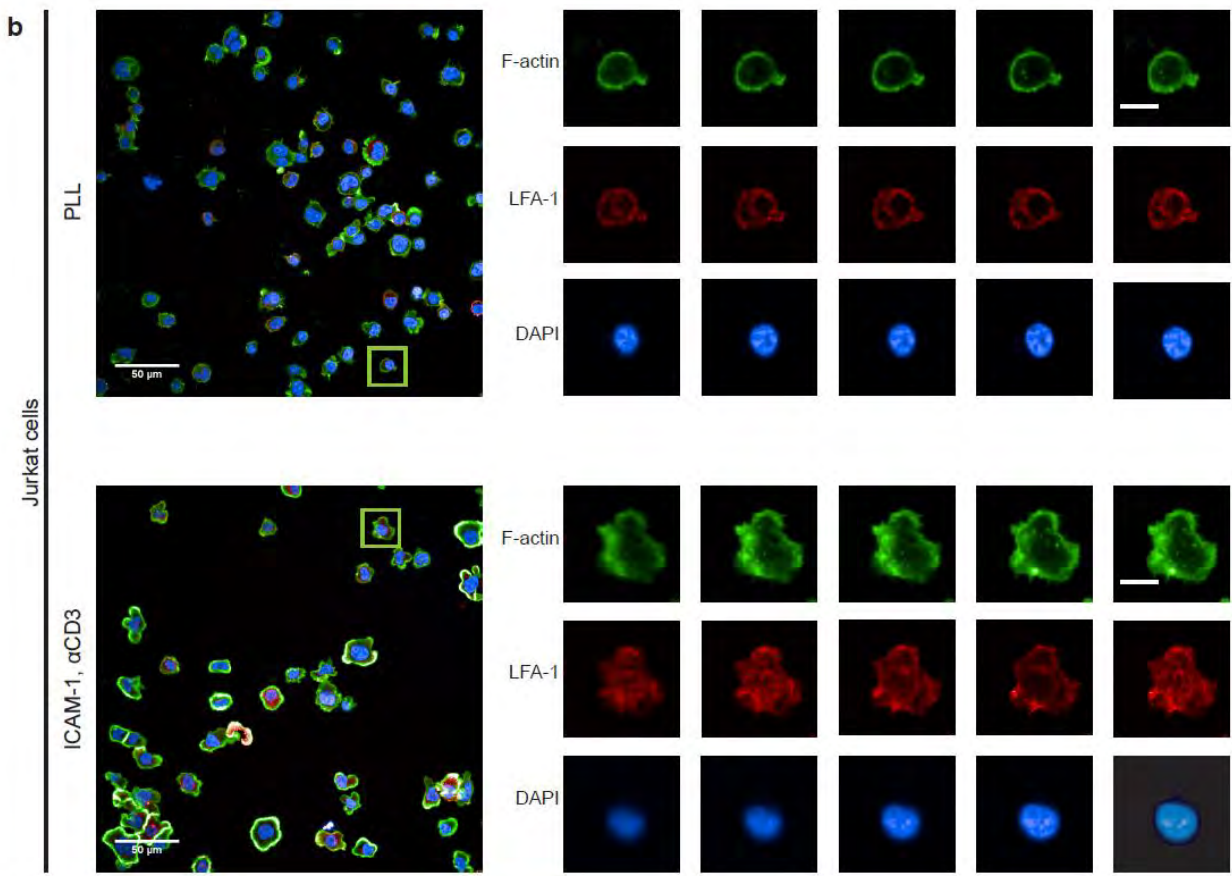
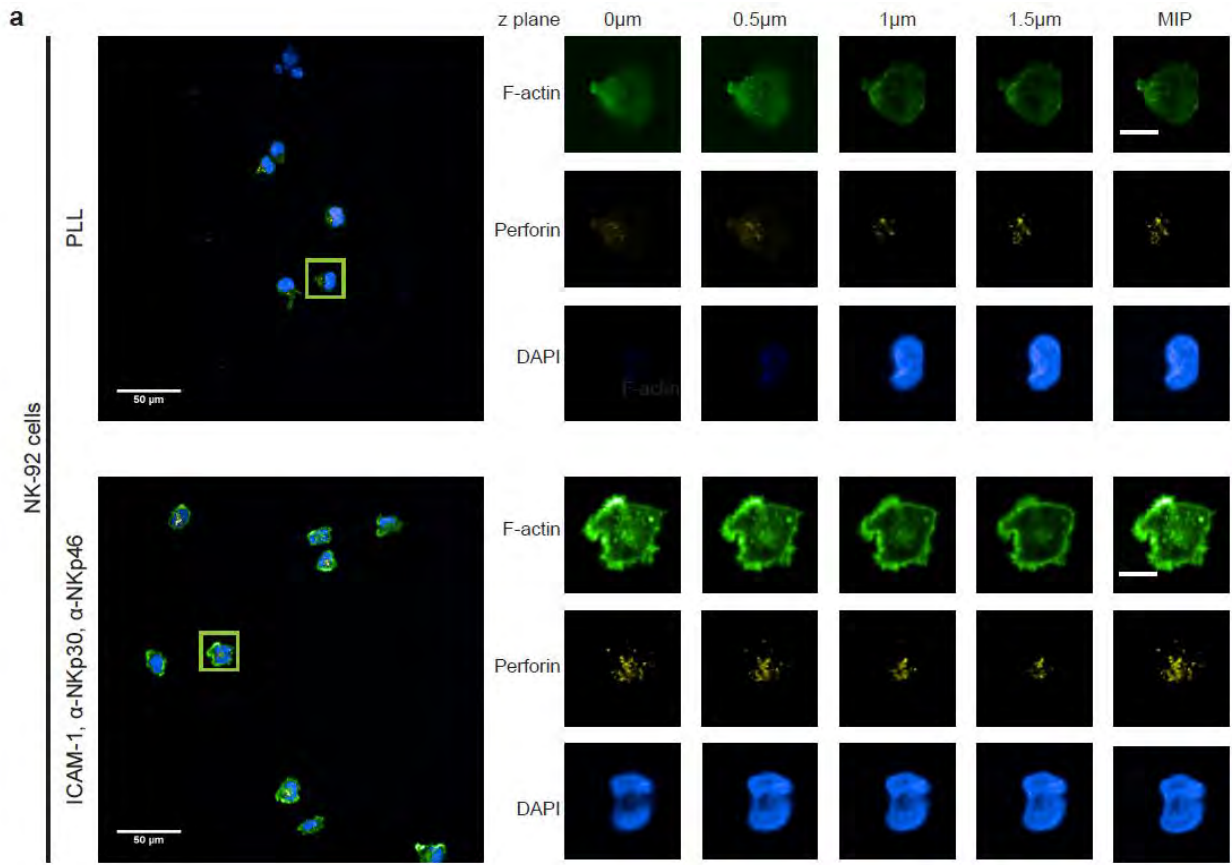
26. Dieckmann, N. M. G., Frazer, G. L., Asano, Y., Stinchcombe, J. C. & Griffiths, G. M. The cytotoxic T lymphocyte immune synapse at a glance. *J. Cell Sci.* **129**, 2881–2886 (2016).
27. Krzewski, K. & Coligan, J. E. Human NK cell lytic granules and regulation of their exocytosis. *Front. Immunol.* **3**, 1–16 (2012).
28. Mace, E. M. *et al.* NK cell lytic granules are highly motile at the immunological synapse and require F-actin for post-degranulation persistence. *J. Immunol. (Baltimore, Md. 1950)* **189**, 4870–4880 (2012).
29. Mace, E. M. *et al.* Cell biological steps and checkpoints in accessing NK cell cytotoxicity. *Immunol. Cell Biol.* **92**, 245–55 (2014).
30. Brown, A. C. N. *et al.* Remodelling of Cortical Actin Where Lytic Granules Dock at Natural Killer Cell Immune Synapses Revealed by Super-Resolution Microscopy. *PLoS Biol.* **9**, e1001152 (2011).
31. Lin, W. *et al.* Morphological change of CD4+ T cell during contact with DC modulates T-cell activation by accumulation of F-actin in the immunology synapse. *BMC Immunol.* **16**, 49 (2015).
32. Piragyte, I. & Jun, C.-D. Actin Engine in Immunological Synapse. *Immune Netw.* **12**, 71 (2012).
33. Houmadi, R. *et al.* The Wiskott-Aldrich Syndrome Protein Contributes to the Assembly of the LFA-1 Nanocluster Belt at the Lytic Synapse. *Cell Rep.* **22**, 979–991 (2018).
34. Carisey, A. F., Mace, E. M., Saeed, M. B., Davis, D. M. & Orange, J. S. Nanoscale Dynamism of Actin Enables Secretory Function in Cytolytic Cells. *Curr. Biol.* **28**, 489–502.e9 (2018).
35. Bubb, M. R., Spector, I., Beyer, B. B. & Fosen, K. M. Effects of Jasplakinolide on the Kinetics of Actin Polymerization. *J. Biol. Chem.* **275**, 5163–5170 (2000).
36. Lyubchenko, T. A., Wurth, G. A. & Zweifach, A. The actin cytoskeleton and cytotoxic T lymphocytes: evidence for multiple roles that could affect granule exocytosis-dependent target cell killing. *J. Physiol.* **547**, 835–847 (2003).
37. Andzelm, M. M., Chen, X., Krzewski, K., Orange, J. S. & Strominger, J. L. Myosin IIA is required for cytolytic granule exocytosis in human NK cells. *J. Exp. Med.* **204**, 2285–2291 (2007).
38. Sanborn, K. B. *et al.* Myosin IIA Associates with NK Cell Lytic Granules to Enable Their Interaction with F-Actin and Function at the Immunological Synapse. *J. Immunol.* **182**, 6969–6984 (2009).
39. Tabdanov, E. *et al.* Micropatterning of TCR and LFA-1 ligands reveals complementary effects on cytoskeleton mechanics in T cells. *Integr. Biol.* **7**, 1272–1284 (2015).
40. De Meester, J., Calvez, R., Valitutti, S. & Dupré, L. The Wiskott-Aldrich syndrome protein regulates CTL cytotoxicity and is required for efficient killing of B cell lymphoma targets. *J. Leukoc. Biol.* **88**, 1031–1040 (2010).
41. Hutz, J. E. *et al.* The Multidimensional Perturbation Value. *J. Biomol. Screen.* **18**, 367–377 (2013).
42. Rousseeuw, P. J. & Leroy, A. M. *Robust Regression and Outlier Detection.* (John Wiley & Sons, Inc., 1987). doi:10.1002/0471725382.
43. Angelo, L. S. *et al.* Practical NK cell phenotyping and variability in healthy adults. *Immunol. Res.* **62**, 341–356 (2015).
44. Bryce, N. S. *et al.* High-Content Imaging of Unbiased Chemical Perturbations Reveals that the Phenotypic Plasticity of the Actin Cytoskeleton Is Constrained. *Cell Syst.* **9**, 496–507.e5 (2019).

45. Breinig, M., Klein, F. A., Huber, W. & Boutros, M. A chemical–genetic interaction map of small molecules using high-throughput imaging in cancer cells. *Mol. Syst. Biol.* **11**, 846 (2015).
46. Caie, P. D. *et al.* High-Content Phenotypic Profiling of Drug Response Signatures across Distinct Cancer Cells. *Mol. Cancer Ther.* **9**, 1913–1926 (2010).
47. Caicedo, J. C., McQuin, C., Goodman, A., Singh, S. & Carpenter, A. E. Weakly Supervised Learning of Single-Cell Feature Embeddings. in *2018 IEEE/CVF Conference on Computer Vision and Pattern Recognition* 9309–9318 (IEEE, 2018). doi:10.1109/CVPR.2018.00970.
48. Lu, A. X., Kraus, O. Z., Cooper, S. & Moses, A. M. Learning unsupervised feature representations for single cell microscopy images with paired cell inpainting. *PLOS Comput. Biol.* **15**, e1007348 (2019).
49. Rohban, M. H., Abbasi, H. S., Singh, S. & Carpenter, A. E. Capturing single-cell heterogeneity via data fusion improves image-based profiling. *Nat. Commun.* **10**, 2082 (2019).
50. Fritzsche, M. *et al.* Cytoskeletal actin dynamics shape a ramifying actin network underpinning immunological synapse formation. *Sci. Adv.* **3**, (2017).
51. Roy, N. H. & Burkhardt, J. K. The actin cytoskeleton: A mechanical intermediate for signal integration at the immunological synapse. *Front. Cell Dev. Biol.* **6**, 1–7 (2018).
52. Hetrick, B., Han, M. S., Helgeson, L. A. & Nolen, B. J. Small Molecules CK-666 and CK-869 Inhibit Actin-Related Protein 2/3 Complex by Blocking an Activating Conformational Change. *Chem. Biol.* **20**, 701–712 (2013).
53. Litterman, A. J., Zellmer, D. M., LaRue, R. S., Jameson, S. C. & Largaespada, D. A. Antigen-Specific Culture of Memory-like CD8 T Cells for Adoptive Immunotherapy. *Cancer Immunol. Res.* **2**, 839–845 (2014).
54. Brigida, I. *et al.* T-cell defects in patients with ARPC1B germline mutations account for combined immunodeficiency. **132**, 2362–2374 (2019).
55. Somech, R. *et al.* Disruption of Thrombocyte and T Lymphocyte Development by a Mutation in ARPC1B. *J. Immunol.* **199**, 4036–4045 (2017).
56. Randzavola, L. O. *et al.* Loss of ARPC1B impairs cytotoxic T lymphocyte maintenance and cytolytic activity. *J. Clin. Invest.* (2019) doi:10.1172/JCI129388.
57. Salzer, E. *et al.* RASGRP1 deficiency causes immunodeficiency with impaired cytoskeletal dynamics. *Nat. Immunol.* **17**, 1352–1360 (2016).
58. Mace, E. M. & Orange, J. S. Lytic immune synapse function requires filamentous actin deconstruction by Coronin 1A. *Proc. Natl. Acad. Sci. U. S. A.* **111**, 6708–6713 (2014).
59. Gil-Krzewska, A. *et al.* An actin cytoskeletal barrier inhibits lytic granule release from natural killer cells in patients with Chediak-Higashi syndrome. *J. Allergy Clin. Immunol.* **142**, 914-927.e6 (2018).
60. Pfajfer, L. *et al.* WIP deficiency severely affects human lymphocyte architecture during migration and synapse assembly. *Blood* **130**, 1949–1953 (2017).
61. Mizesko, M. C. *et al.* Defective actin accumulation impairs human natural killer cell function in patients with dedicator of cytokinesis 8 deficiency. *J. Allergy Clin. Immunol.* **131**, 840–848 (2013).
62. Vincent, L. & Soille, P. Watersheds in digital spaces: an efficient algorithm based on immersion simulations. *IEEE Trans. Pattern Anal. Mach. Intell.* **13**, 583–598 (1991).
63. McInnes, L., Healy, J., Saul, N. &

Großberger, L. UMAP: Uniform Manifold Approximation and Projection. *J. Open Source Softw.* **3**, 861 (2018).

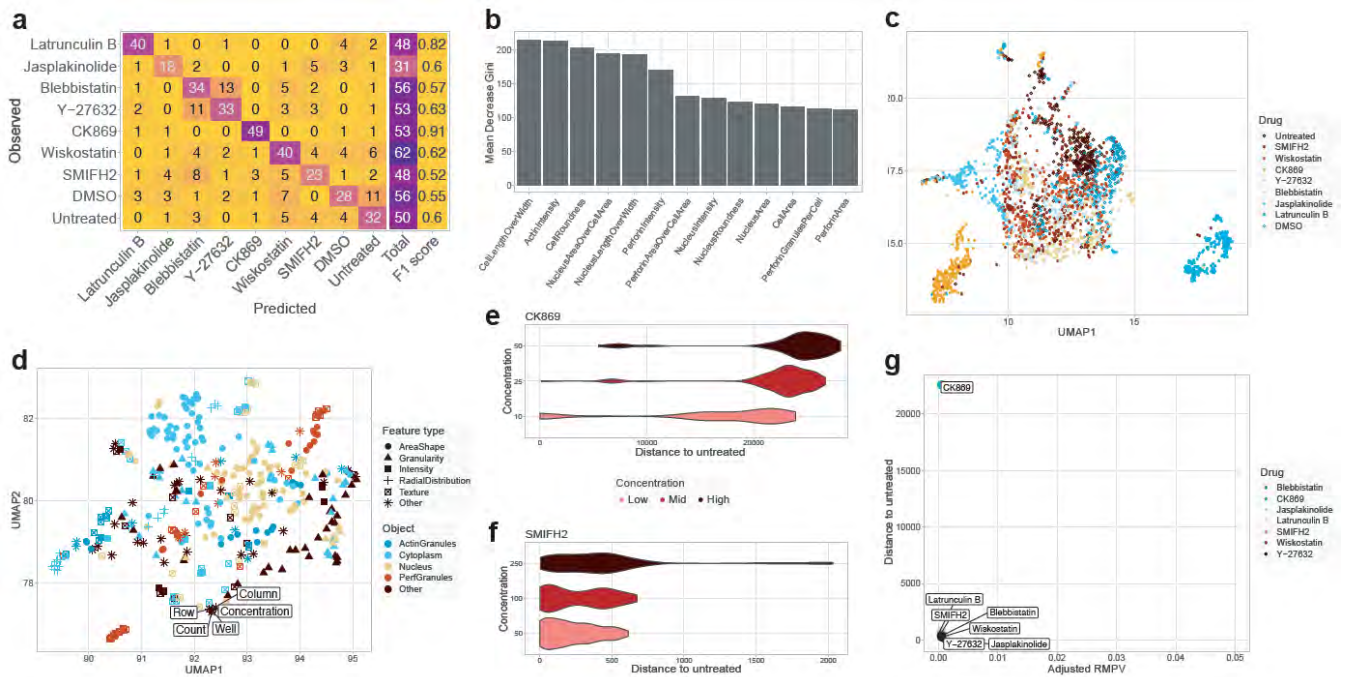
64. Breiman, L. Random Forests. *Mach. Learn.* **45**, 5–32 (2001).

Supplementary material

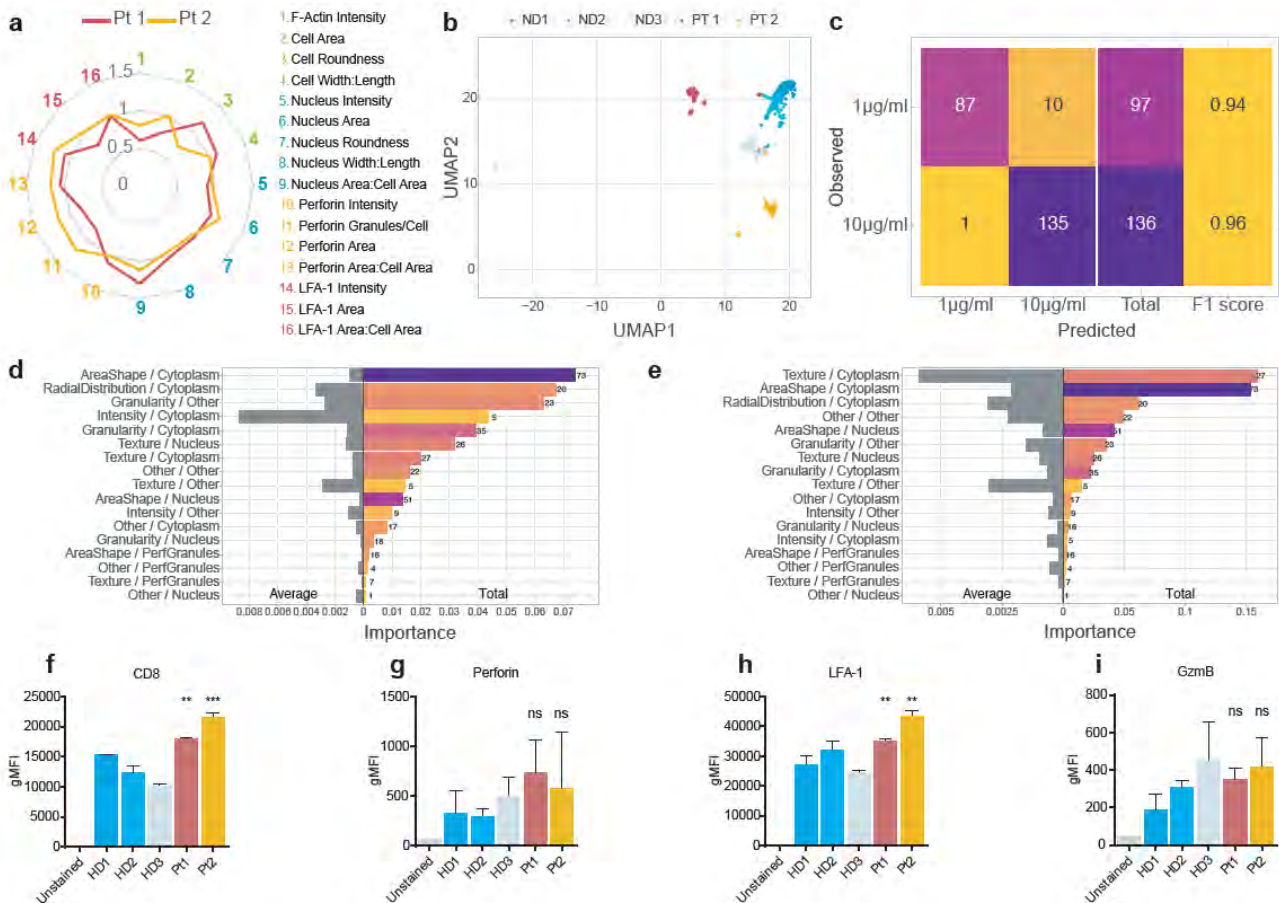


Supplementary Fig. 1 | Individual channels and z planes of single cells isolated from representative fields of view.

a. Maximum intensity projection (MIP) of a representative field of view of NK-92 cells seeded on PLL (top) or ICAM-1, anti-NKp30 and NKp-46(bottom), with zoom on a single representative cell stained for F-actin (green), perforin granules (yellow) and nuclei (DAPI) imaged at 4 z-planes with a step of 0.5 μm and its MIP. Scale bars: Field of view 50 μm and single cell 10 μm . **b.** MIP of a representative field of view of Jurkat cells seeded on PLL (top) ICAM-1, anti-CD3 (bottom), with zoom on a single cell stained for F-actin (green), LFA-1 (red) and nuclei (DAPI) and imaged at 4 z-planes with a step of 0.5 μm and its MIP. Scale bars: Field of view 50 μm and single cell 10 μm .



Supplementary Fig. 2 | Drug treatment leads to distinct immunological synapse phenotypes in NK-92 cells. a. Confusion matrix and class-wise performance of a random forest model trained to predict drug treatment based on 13 hand-picked morphological features of NK-92 seeded on ICAM-1, anti-NKp30 and anti-NKp46. **b.** Importance of the 13 morphological parameters for the classification described in panel (a). **c.** UMAP representing the clustering of all the drugs and the untreated conditions. **d.** UMAP representing the relations between confounders and morphological features, obtained by fitting the UMAP on the transpose of the data underlying panel (c). **e-f.** Violin plots representing the effect size of drug concentrations on morphological features for (e) CK-869 and (f) SMIFH2. **g.** FDR-corrected Robust Morphological Perturbation Value (RMPV) of the different drugs.



Supplementary Fig. 3 | Distinct immunological synapse phenotype in CD8+ T cells from ARPC1B-deficient patients.
a. Characteristics of the immunological synapse of the CD8+ T cells of the two ARPC1B deficient patients represented as fold change with respect to the average of the three normal donors seeded on ICAM-1 and 1 $\mu\text{g/ml}$ anti-CD3. The data represents the mean of 6 replicates for each donor (7525-17725 cells). **b.** UMAP of cells of the ARPC1B patients and the normal donors seeded on ICAM-1 and 1 $\mu\text{g/ml}$ anti-CD3. **c.** Confusion matrix and class-wise performance of a random forest model trained to predict the concentration of anti-CD3 antibodies based on the morphology of normal donors lymphocytes stimulated with ICAM-1 and either 1 or 10 $\mu\text{g/ml}$ anti-CD3. **d-e.** Total and average importance of measurement type and biological object described in the prediction of whether images corresponded to (d) normal donors CD8+ T lymphocytes seeded on ICAM-1 and 1 or 10 $\mu\text{g/ml}$ anti-CD3 or (e) to normal donors, patient 1 or patient 2 lymphocytes stimulated with ICAM-1 and 10 $\mu\text{g/ml}$ anti-CD3. **f-i** Phenotyping of expanded CD8+ T cells of ARPC1B patients and normal donors showing mean fluorescence intensity of (f) CD8, and (g) perforin, (h) LFA-1, and (i) Granzyme B in the CD8+ population. Values represent the mean of duplicates and error bars show SD. Significance is noted as ns ($P > 0.05$), ** ($P < 0.01$) and *** ($P < 0.001$).

	NK-92		
	PLL	ICAM-1, α -NKp30, α -NKp46	Fold increase
F-Actin intensity	0.065098277	0.110223848	1.69319149
Cell Area (μm^2)	2469.321237	3130.618434	1.26780525
Cell Roundness	0.674079624	0.444435641	0.65932217
Cell Width:Length	0.686074044	0.71563093	1.04308119
Nucleus Intensity	0.067203031	0.067329026	1.00187485
Nucleus Area(μm^2)	1037.718811	1333.179255	1.2847211
Nucleus Roundness	0.706061099	0.689874902	0.97707536
Nucleus Width:Length	0.685545171	0.706542199	1.03062822
Nucleus Area:Cell Area	0.427455169	0.431859895	1.01030453
Perforin Intensity	0.018403047	0.018502314	1.00539403
Perforin Granules/Cell	13.04941437	16.7196273	1.28125499
Perforin Area(μm^2)	86.05831253	117.5449158	1.36587521
Perforin Area:Cell Area	0.035039484	0.036882184	1.05258922

Supplementary Table 1 | Mean values and fold increase of immunological synapse parameters in NK-92 cells. Mean values of individual parameters pertaining to the immunological synapse in NK-92 cells seeded on PLL or ICAM-1, anti-NKp30 and anti-NKp46, and the fold change of the ratio of each mean value on the stimulated condition with respect to PLL. Intensity is measured in arbitrary units and area in μm^2 .

	Jurkat		
	PLL	ICAM-1, α -CD3	Fold increase
F-Actin intensity	0.000289437	0.000437181	1.5104544
Cell Area(μm^2)	1921.009837	2690.327023	1.4004754
Cell Roundness	0.530654443	0.61184158	1.15299436
Cell Width:Length	0.800192404	0.767932394	0.95968468
Nucleus Intensity	0.07313481	0.074429279	1.01769975
Nucleus Area(μm^2)	879.0221429	995.945146	1.13301486
Nucleus Roundness	0.830340643	0.806271514	0.97101295
Nucleus Width:Length	0.779080494	0.754652368	0.96864493
Nucleus Area:Cell Area	0.460560432	0.379756314	0.82455263
LFA-1 Intensity	0.006679646	0.007880989	1.17985131
LFA-1 Area(μm^2)	1728.306565	2526.153065	1.46163483
LFA-1 Area:Cell Area	0.900646361	0.938478533	1.04200558

Supplementary Table 2 | Mean values and fold increase of immunological synapse parameters in Jurkat cells. Mean values of individual parameters pertaining to the immunological synapse in Jurkat cells seeded on PLL or ICAM-1 and anti-CD3, and the fold change of the ratio of each mean value on the stimulated condition with respect to PLL. Intensity is measured in arbitrary units and area in μm^2 .

	Jurkat		
	PLL	ICAM-1, α -CD3	Fold increase
F-Actin intensity	0.000289437	0.000437181	1.5104544
Cell Area(μm^2)	1921.009837	2690.327023	1.4004754
Cell Roundness	0.530654443	0.61184158	1.15299436
Cell Width:Length	0.800192404	0.767932394	0.95968468
Nucleus Intensity	0.07313481	0.074429279	1.01769975
Nucleus Area(μm^2)	879.0221429	995.945146	1.13301486
Nucleus Roundness	0.830340643	0.806271514	0.97101295
Nucleus Width:Length	0.779080494	0.754652368	0.96864493
Nucleus Area:Cell Area	0.460560432	0.379756314	0.82455263
LFA-1 Intensity	0.006679646	0.007880989	1.17985131
LFA-1 Area(μm^2)	1728.306565	2526.153065	1.46163483
LFA-1 Area:Cell Area	0.900646361	0.938478533	1.04200558

Supplementary table 2. Mean values and fold increase of immunological synapse parameters in Jurkat cells.

Mean values of individual parameters pertaining to the immunological synapse in Jurkat cells seeded on PLL or ICAM-1 and anti-CD3, and the fold change of the ratio of each mean value on the stimulated condition with respect to PLL. Intensity is measured in arbitrary units and area in (μm^2).

Materials and methods: optimizations on NK-92 and primary NK cells.

1. NK-92 cells

1.1 Migration

NK-92 cells were resuspended at 0.2, 0.4 and 1×10^6 /ml in alpha-MEM + IL-2. 50 μ L of cell suspension was added on top of the 5 μ M polycarbonate transwell membrane. 100 μ L of 1, 10, 25, 50, 100, 500 and 1000 ng/ml CXCL12 were added to the bottom wells. Negative and positive controls were added. The cells migrated for 4 hours at 37°C. Following migration, cells in the bottom wells were corrected and the number of cells that migrated was assessed using the MacsQuant VYB. The percentage of migration in response to CXCL12 was calculated with respect to the negative control.

Student's t-test was used for statistical significance.

1.2 Conjugate formation kinetics

NK-92 cells were stained with CTV and K-562 cells were stained with CMFDA. 100 μ L of NK-92 cells and 100 μ L of K-562 cells at 1×10^6 cells/ml for 15, 30, 45 and 60 minutes at 37°C. Cells were fixed with 1% PFA and results were read at the MacsQuant VYB. Gentle automated sample mixing was performed, to ensure minimal conjugate disruption. The percentage of NK-92 cells involved in conjugates was calculated as the fraction of double positive cells with respect to the total CTV+ population.

Student's t-test was used for statistical significance.

1.3 NK-92 – K562 conjugate assessment by microscopy

Microscope slides were coated with Poly-L-Lysine overnight. NK-92 and K562 cells at 0.1×10^6 /ml were incubated for 30 minutes at 37°C in U-bottom 96 well plates. The cells were gently mixed, and a 50 μ L was deposited on each well. The cells were left to adhere for 5 minutes on the wells at 37°C. The cells were subsequently fixed with 3% PFA, permeabilized with 0.1% saponin and stained with mouse anti-human anti-perforin Ab for 1 hour at RT, followed by staining with phalloidin (AF-488) to reveal F-actin, goat-anti mouse IgG2b Ab (AF-647) to reveal perforin and DAPI to reveal nuclei. The sealed slides were imaged with the 63x oil-immersion objective at the LSM710, and the images were analyzed with ImageJ to calculate the mean distance of lytic granules to the IS.

Student's t-test was used for statistical significance.

1.4 NK-92 cytotoxicity

NK-92 cell suspensions were prepared at 0.25 and 1.25×10^6 cells/ml. K562 cells stained with CMFDA were prepared at 0.25×10^6 cells/ml. NK-92 cells were incubated with K562 cells at a 1:1 and a 5:1 effector: target ratio. Aphidicolin was added to prevent cell proliferation, and the cells were incubated at 37°C for 4 and 24h. 7AAD was added to the cell suspension prior to cytometry reading. Using the MacsQuant VYB, the number of residual alive target cells was assessed to calculate lysis, by assessing the number of CMFDA+ 7AAD- cells.

Student's t-test was used for statistical significance

1.5 TIRF microscopy

NK-92 cells were loaded with LysoTracker Red for 30 min at 37 °C. Cells were then washed and transferred to μ -Slide 8-well chambers pre-coated with ICAM-1 and anti-NKp30Ab, and rapidly transferred to a pre-warmed microscope stage. TIRFM experiments were performed using a 100×1.45 numerical aperture TIRF objective on a Nikon TE2000U microscope custom modified with a TIRF illumination module. The images were recorded at 1-sec intervals. Images were analyzed using ImageJ to quantify lytic granule position and movement within the TIRF plane.

2. Primary NK cells

2.1 Primary NK cell expansion

Primary NK cells were isolated from blood PBMCs of two normal donors using a CD3 negative selection kit. The negative fraction was stimulated with irradiated PLH cells at a ratio of 4 PLH for 1 NK cell, in RPMI 10% FCS containing 100U/ml IL-2 and 5ng/ml IL-15. The first cycle of stimulation was 5-7 days long, during which the cells were not used for experiment. The following cycles were 2-3 days long and involved stimulation with 1PLH cell for each NK RPMI 10% FCS containing 100U/ml IL-2 and 5ng/ml IL-15. The number of NK cells was calculated by using CD16 and CD56Ab, and 7AAD to exclude dead cells.

2.2 Migration

Primary NK cell cells were resuspended at 1×10^6 /ml in RPMI 10% FCS + IL-2. 50 μ L of cell suspension was added on top of the 5 μ M polycarbonate transwell membrane. 100 μ L of 50 ng/ml of either CXCL10 or CXCL12 were added to the bottom wells. Negative and positive controls were added. The cells migrated for 2 hours at 37°C. Following migration, cells in the bottom wells were

corrected and the number of cells that migrated was assessed using the MacsQuant VYB. The percentage of migration in response to CXCL10 and CXCL12 was calculated with respect to the negative control.

Student's t-test was used for statistical significance.

2.3 Conjugate formation kinetics

NK cells were stained with CTV and K-562 cells were stained with CMFDA. 100 μ L of NK-92 cells and 100 μ L of K-562 cells at 1×10^6 cells/ml for 15, 30, 45, 60 and 120 minutes at 37°C. The same protocol used for NK-92 cells was followed.

2.4 Primary NK– K562 conjugate assessment by microscopy

The same protocol used for NK-92 cells was applied. However, no calculations were performed on these cells.

2.5 Primary NK cell cytotoxicity

Primary NK cell suspensions were prepared at 0.1, 0.2, 0.4, 1 and 2×10^6 cells/ml. K562 cells stained with CMFDA were prepared at 0.2×10^6 cells/ml. NK-92 cells were incubated with K562 cells at a 1:2, 1:1, 2:1, 5:1 and 10:1 effector: target ratio. The same procedure as for NK-92 was followed.

Discussion and perspectives

The role of the cytotoxic lymphocytes in the immune response and host protection is undeniable, and their role is emphasized further by the consequences of the diseases in which they are defective^{165,397,398}. Moreover, their capacities are highlighted further by the developing cancer immunotherapies^{399,400}. Therefore, it is essential to understand the mechanisms governing the activation and the effector capabilities of these cells. Cytotoxicity involves several dynamic steps, of which the immunological synapse has been shown to play a crucial role⁶⁶. Indeed, the immunological synapse has been proposed to be the site of lytic granule convergence and their exocytosis in order to achieve target cell lysis^{44,147}. Low throughput imaging approaches are traditionally used to study the IS assembly and architecture, and these approaches have helped shape the current knowledge into IS regulation and the role of several genes in the dynamic process that is the formation of the lytic IS^{44,201,224}.

Given the crucial role that the immunological synapse plays in the process of cytotoxicity, we proposed a high content imaging approach coupled to robust morphological profiling to assess the IS architecture in various cytotoxic lymphocyte populations. We posit that such an approach could be relevant to determine the activation state of these cytotoxic lymphocytes, which may reflect on their cytotoxic functions.

1. HCI as a methodological advance in imaging the immunological synapse assembly

In our study, we provide a novel high content imaging and analysis pipeline of the immunological synapse in different cytotoxic lymphocyte subsets. We use a 2D imaging approach over 4 z planes which correspond to a 2 μ m slice encompassing the area of contact between the lymphocyte and a microwell surface coated with stimulatory molecules. We successfully manage to mimic the assembly of the immunological synapse, whereby the cells adhere successfully to the microwell surface, and that they are amenable to staining and imaging as such. In our study, the selection of the fields that are imaged is randomized, therefore eliminating the bias that may come into play when choosing the cells to image, which may in turn lead to the exclusion of “extreme” phenotypes that are a minority of the cells but may be of interesting biological relevance. This infers the need for an analysis pipeline which allows an extensive profiling of the IS. Coupling our imaging approach to robust statistics to evaluate the data on a per image (field of view basis) allows to account for the variability observed in each field of view. Therefore, this analysis pipeline comes as an intermediate between analyses of high content imaging screens on well/condition level and on a single cell level basis^{360,364,401}.

Our pipeline was applied to study the immunological synapse assembly and the use of robust statistics allowed us to draw conclusions that are statistically significant, and less sensitive to outliers while still able to identify distinct or striking morphologies. Moreover, such a pipeline allowed us to establish a classifier, which can discriminate treatment conditions and segregate normal donor from patient-derived cells.

It is to be noted that even though we imaged 8 z planes encompassing a height of 4 μ m, we only opted for the assessment of the first 2 μ m closest to the coated surface. Therefore, our data only captures the events at the synaptic plane and misses events occurring at higher planes. The large set of images generated might be of interest to study the 3D structure of the cells, which can provide a better understanding of granule positioning, and could potentially provide insight into granule polarization defects.

2. HCI validates the role of the actin cytoskeleton in governing IS assembly

As a first step, we validated our approach on the NK-92 and the Jurkat cell lines, and only considered a set of targeted morphological measurements that were compiled from previous knowledge about the IS assembly. These features include intensities of F-actin, the nucleus, perforin granules and LFA-1, as well as parameters pertaining to the size and morphology of the cell and the nucleus^{44,57,402}. At the field of view and single cell levels, our results reveal a positive correlation between actin intensity and nucleus area and LFA-1 intensity. However, there amount of correlation varies, indicating that cells in a given population may behave differently in response to a certain stimulus. Therefore, despite the usefulness of population-averaged assays and their ability to report how a population can respond to perturbations, these assays assume that the entire population behaves similarly to the mean cell, which leads to the loss of valuable information. Population distributions also lead to the exclusions of extreme phenotype that represent a minority, but that may have valuable biological relevance. Since our analysis pipeline eliminates any field of view that has less than three cells, as well as cell clusters, we offer a statistical robustness that permits the study of individual cells and their behavior. Having more than three cells per field of view eliminates the doubt of poor coating conditions in that particular field which may have led to poor cellular adhesion, while removing clusters allows the study of individual rather than collective cell behavior. Therefore, combining the approach of imaging a large number of cells with robust statistics decrease the sensitivity of our approach to outliers and artifacts and allows for keeping “extreme” phenotypes if they have a biological relevance.

Our results confirm the importance of the actin cytoskeleton in the assembly of the immunological synapse, whereby we show that synapse assembly entails actin accumulation and spreading. It also confirms that lytic granules polarize to the IS, and that LFA-1 accumulates there as well. There results highlight the importance of the actin cytoskeleton dynamics in the normal context, which led us to probe whether our approach identify changes to the immunological synapse assembly upon targeting the actin cytoskeleton whether it be by drug treatment or by using cells from patients presenting a genetic defect in an action-regulating gene. For that reason, we implemented an additional analysis approach, which goes beyond the analysis of a set of pre-defined morphological features to include a high-resolution analysis approach which includes a much larger set of morphological features.

We show that affecting actin cytoskeleton dynamics with drugs targeting the processes of actin polymerization and depolymerization yields alterations on the lytic granules, which is expected, as lytic granule polarization to the IS requires rearrangements to the actin cytoskeleton^{53,64}. However, the

changes caused by the drugs need to be considered in the context where these drugs may not be specific to only one mechanism, but could be affecting several mechanisms, as has recently been claimed for SMIFH2. Indeed, some recent data implies that SMIFH2 is not only a formin inhibitor but could also be targeting Myosins (unpublished data). Interestingly, we note that even though the parameters pertaining to perforin appear to change upon drug treatment or in ARPC1B deficient patient cells, the morphological features pertaining to perforin in the robust morphological profiling do not appear to have a high importance in the prediction of the drug treatment or distinguishing patient cell from normal donors. This suggests that the changes underwent by perforin granules are a consequence of the defects of the actin cytoskeleton, rather than a direct consequence of the drug treatment or genetic defect. This hypothesis is backed up by previous findings that there is a specific interplay between the actin cytoskeleton and the lytic granules from their polarization until their exocytosis^{44,69,224,403}.

3. HCI coupled to robust statistics reveal important and sometimes unexpected IS morphological features

Coupling our HCI approach to robust statistics has allowed us to perform a thorough morphological profiling of the IS, beyond the initial set of limited features. By performing a morphological analysis based on more than 300 morphological features, our results reveal the importance of some parameters which have been so far overlooked in the study of the IS. We show that targeting the IS with drugs that affect actin dynamics and analyzing cells from ARPC1B deficient patients reveals the importance of the shape of the cell, its radial distribution, its granularity as well as the shape of the nucleus are important determinants in the morphological profile of each treatment condition or deficiency. This finding is confirmed by the fact that the classifier performs with better accuracy when the model is trained to predict the treatment condition based on the 381 morphological features rather than only 13.

Interestingly, robust morphological profiling results reveal that the nucleus increases in area upon IS assembly, indicating a role of the actin cytoskeleton dynamics in shaping the morphology of the nucleus. It has been shown that the MTOC must translocate around the nucleus to IS, and that the nucleus must form an open arch structure toward the IS to allow this translocation^{404,405}. Robust morphological profiling highlights that the shape of the nucleus is indeed affected upon a defective IS assembly, and the morphological changes underwent by the nucleus upon IS formation may be linked to the formation of the open arch structure and facilitation of centrosome translocation. To explore further the effect of the changes of nuclear morphology on function, single cell RNA sequencing could be performed to check for a relationship between the nuclear morphology and transcription and try to answer whether changes in nucleus shape could relate to the changes in the IS assembly, and whether changes in the actin dynamics could impact on the functions of the nucleus.

Therefore, our results show a clear need for a morphological analysis of the immunological synapse that encompasses a large set of morphological features in order to properly understand the effect and impact of a given drug treatment or a mutation. However, we also note that morphological profiling is not enough to answer questions pertaining to function.

4. HCI could be indicative of a defect in the cytotoxic function

Our results reveal clear differences in the immunological synapse assembly of each of the two ARPC1B deficient patients compared to that of normal donors. The role of the immunological synapse assembly in the steps leading to successful cytotoxicity has been inferred from genetic defects where a defective IS assembly impacts on the cytotoxic activity^{208,224,262}. For that reason, it was evident that the cytotoxic activity of ARPC1B deficient CD8⁺ T cells was to be tested. We show that indeed, these cells harbor a defective cytotoxic activity at both a high and low anti-CD3 concentration. This could be due to a defect in the TCR signaling, since phenotyping analysis shows a normal expression of lytic molecules. Indeed, a recent study has confirmed that ARPC1B deficient CD8⁺ T cells have impaired TCR activation²⁹². In agreement with our results, they also report a decreased cytotoxic activity in these cells. Our analysis of the IS in these patients reveals distinct responses to stimulation with ICAM-1 and anti-CD3 Ab for each of these patients. While both of them display a reduced F-actin accumulation concordant with defective ARP2/3 and treatment with CK-869, we show that patient 1 has decreased perforin accumulation at the IS, while patient 2 appears to have more perforin granules at the IS^{292,406}. It could be inferred that patient 1 has a defect in granule polarization, which has been observed in a recent study, while for patient 2 it could be presumed that the defect lies in degranulation despite proper granule polarization, in agreement with the study by Randzavola et al. in which defects in granule polarization and degranulation were reported²⁹². However, the differences between the two patients could be explained by the fact that they harbor two different mutations, indicating that nature of the mutation most likely impacts the IS assembly and therefore morphological features. For that reason, even though it might be hard in the field of rare diseases, it could be of interest to study how different mutations in one gene could affect IS morphology, and how the IS morphology could translate into functional defects.

As introduced earlier, several PIDs caused by mutations in actin regulatory genes are often accompanied by a cytotoxic defect. Therefore, such an approach as the one developed during my PhD could be useful to screen samples from these patients in parallel and perform a robust morphological profiling to potentially determine the common traits observed during an impaired IS formation that may be causative of the cytotoxic defect. Creating such a database would not only be helpful in trying to establish the morphological features of a defective IS, but such a database could also be used to compare patients with unknown PID mutations to patients in said database, in an attempt to narrow down the potential gene mutations underlying their defects. The more patients that are added to such a database, the more accurate it would become to build a network of possible gene interactions of actin-regulating genes.

5. HCI of the immunological synapse reveals discrepancies in the regulation between cell lines and primary cells.

In our assays, we denote a difference in the response of immortalized NK-92 cell lines treated with SMIFH2 and CK-869, and primary NK cells isolated from the PBMCs of three donors to the same drugs. This raises the question of discrepancies between the responses of cell lines and primary material. The use of immortalized cell lines is more advantageous, as these cells are easily grown and expanded in culture, and may be amenable to different manipulations such as gene knock-down and knock-in. However, the fact that cell lines are grown in culture over a long period of time has been shown to cause phenotypically altered populations⁴⁰⁷. The question of how actin dynamics may differ between immortalized cell lines and primary cells arises due to this fact.

Our results show that NK-92 cells appear to be more affected by treatment with CK-869 than by SMIFH2 and Blebbistatin. This most likely indicates that retrograde actin flow in NK-92 cells is more dependent on the ARP2/3 complex than the formins. In primary NK cells, treatment with CK-869 and SMIFH2 lead to a decrease in actin intensity, most likely implying a control of actin dynamics by both the formins and the ARP2/3 complex. This could imply a difference in the regulation of the IS assembly between cell lines and primary cells isolated from PBMCs. A recent study has addressed this question and compared the actin dynamics between Jurkat cells and primary mouse CD4⁺ T cells, and they showed that Jurkat cells lack actin arcs, that primary cells are more dynamic at the lamellar leading edge, and that the cortical actin network in primary cells undergoes more undulation^{146,280}. Moreover, upon treatment with CK-666 and SMIFH2, they show that the retrograde actin flow in primary cells is mainly generated by MyoII, while it is more dependent on nucleation and polymerization in Jurkat cells²⁸⁰. Therefore, it can be concluded that despite the advantages cell lines present, they may not always be the best model from which conclusions should be drawn.

6. HCI reveals the lack of a standard “normal” or “disease” phenotype

Our results reveal that treating primary NK cells isolated from the PBMCs of three normal donors leads to a unique response in each donor. We show that as a general response to CK-869 treatment, primary NK cells show a general increase in perforin-related parameters. However, when examined closely, we denote that in one donor, perforin-related parameters are decreased. This could imply that the regulation of the immunological synapse is fine-tuned with slight differences among healthy donors. Interestingly, our pipeline also reveals a difference in IS morphological features among the three different normal donors. This most likely indicates that the fine-tuning of the immunological synapse in normal conditions might differ among people based on differences in differentiation status, ongoing infection or treatments, as well as possibly the genetic background. Testing this hypothesis would require the analysis of much larger pools of donors. It should be noted that a solid conclusion cannot be made on inter-donor heterogeneity, and such a conclusion would require a larger number of donors to rule out the possibility that the differences observed are not due to different activation states.

Previous studies have shown that differentiated CD8⁺ T cells from patients deficient in ARPC1B have aberrant IS morphologies^{288,292}. Indeed, they reveal a defective radial spreading and a reduced cell area, and they appear to emit filopodia in response to TCR stimulation. Our images reveal the same IS morphology shown in that study (P1 and P2 are the P1 and P7 in that study), and our analysis confirms the reduced cell area. In addition, we observe different responses to stimulation with ICAM-1 and anti-CD3 Ab for each patient, which shows in the radar plots, the UMAP and the performance of the classifier which can distinguish between the two patients. Patient one has a mutated ARPC1B, while patient 2 has no ARPC1B^{288,408}. Our approach therefore confirms that the immunological synapse of two patients harboring different genetic mutations will have different morphologies. It is therefore possible that due to different expression levels of ARPC1B that different compensation mechanisms (such as by formins) acting at different levels may explain the difference in IS morphologies among the two patients.

7. HCI as a first step preceding functional assays

The immunological synapse has been referred to as a molecular machinery behind lymphocyte activation, as it involves a complex interplay between a myriad of signaling molecules¹⁰⁸. Our results show that a defective immunological synapse assembly distinguishes normal cells from cells drug treated or patient cells. By examining ARPC1B patient CD8+ T lymphocytes and performing cytotoxicity assays, we confirm that a defective immunological synapse relates to a defect in cytotoxicity. However, we only stained F-actin, perforin, LFA-1 and the nucleus, therefore we cannot conclude the molecular mechanism behind the defective cytotoxicity and answering that question would require analysis of the degranulation process in these cells, as our observation of the IS of these patients imply. Therefore, our approach, despite its usefulness in allowing us to extrapolate a functional defect, cannot be a replacement to functional assays, and must be coupled with them for an accurate depiction of the functional defect.

Since our approach is versatile in terms of the cells that may be imaged and the molecules to be stained, one could stain for a multitude of signaling molecules and functional molecules (LFA-1, granzymes, granulysin, LAMP-1) as well as tubulin in cytotoxic cells from different PID patients in an effort to narrow down the source of the functional defect. Such an approach would be of high value if applied on patient cell material, as it has a low requirement of cell numbers. Indeed, with only half a million cells, one could potentially image a hundred different conditions.

Additionally, a gene defect is usually determined by genetic sequencing. Once a mutation is confirmed, the expression of the normal proteins is usually determined by Western Blot analyses^{208,213,224,409}. One potential application of our high content imaging pipeline is to, as an alternative to NGS and Western Blot, start by imaging patient lymphocytes. Indeed, if a patient presents with symptoms that are closely related to a known PID where the IS is also defective, one could image the immunological synapse of the lymphocytes of this patient by staining for the suspected defective protein and proteins from the same family or from the same signaling pathway. Such a process could aid in directing researchers towards where the mutation could lie.

8. HCI of the immunological synapse as a useful tool in the field of personalized medicine

Our results show that HCI can aid in shaping a morphological profile of the IS of each donor. Such interesting findings could be applied in cases of personalized medicine, where the response to treatments can be assessed on a per patient basis. This could be promising if applied to the immunological synapse as a pharmacological target. Indeed, pharmacological compounds that target the IS have been tested and are being optimized, and understanding the mechanisms underlying IS assembly and maintenance is essential for the development of new successful immunotherapeutic strategies. Namely, treatments with specific inhibitors of perforin activity are being tested as immunosuppressive treatment in autoimmunity⁴¹⁰. Blocking CD3 by compounds such as chimeric, humanized and fully human anti-CD3 mAbs is being tested as potential treatment for patients with Crohn's disease and hepatitis⁴¹¹. The blockade of co-stimulatory molecules such as binding of CTLA4-IgG to CD80 to suppress CD28 co-stimulatory signaling is being employed to treat patients with autoimmune disorders⁴¹².

Our HCI approach could be of value when determining responders from non-responders to these treatments, by the assessment of alterations occurring to their IS parameters upon treatment. Assessing the IS morphology in these patients could be an indicator of treatment impact on IS assembly, and examination of several patient responses in parallel could be carried out in an effort to draw conclusions.

In fact, one project we are currently setting up in our lab is the high content imaging of CLL cells from patients before and after treatment with Ibrutinib, an agent that has been shown to destabilize IS assembly, as assess whether different responses to Ibrutinib treatment may be linked to its distinct IS morphologies of leukemic cells in each patient.

9. HCI could be the method study different functional steps of cytotoxicity

To successfully eliminate their targets, cytotoxic cells must migrate towards the site of infection, recognize target cells, form stable conjugates with them and secrete their lytic granule content into the target cells to ensure their elimination.

Motility can be studied in several setups, including transwell assay and migration chambers where the cells migrate in response to a chemokine gradient. Such results would be assessed by flow cytometry and live microscopy respectively. The motility can also be predicted by stimulating the cells with chemokines and seeding them on a matrix, and the morphological changes can be captured by fixed confocal microscopy²⁰⁸. This has been done in a low throughput format, and our experimental approach offers the potential to assess the response to chemokines in a high content fashion, where the response to several chemokines and on different matrices can be tested in parallel. Testing several conditions in parallel while doing only one staining, imaging and analysis process not only saves time but would also allow for the parallel comparison of these different conditions, as the images would be acquired under the same conditions, decreasing variability in experimental settings. Robust morphological profiling allows to efficiently detect where the response is impaired and reveal intrinsic defects that may be due to the actin cytoskeleton.

Conjugate formation between the cytotoxic cell and the target may be assessed by flow cytometry or low throughput confocal microscopy^{224,246}. However, it could be more interesting to study it by microscopy, as staining for tubulin and lytic granules could be informative of the cells' capacity to polarize their granules. Conjugate formation could be amenable to imaging by high content microscopy, and this would allow the parallel imaging of several patients and normal donors in parallel. When cells are imaged with low throughput confocal microscopy, the usual number of cells imaged per experiment is around 30, which can take around 3 hours and may be subject to bias as the cells are selected manually, and some extreme phenotypes may be ignored. HCI offers the potential to image a large number of cells in a much shorter time, and automated acquisition allows for the elimination of bias. The application of robust statistics allows a lesser sensitivity to extreme phenotypes while still revealing the different phenotypes that may exist within a population, and when comparing different conditions. Imaging of conjugates in expanded CD4 and CD8+ T cells has been implemented in our lab, and I have implemented it for primary NK cells. Therefore, one application of the pipeline set up could be the simultaneous imaging of T and NK cells from the same donors. Coupled to approaches of flow cytometry amenable to be assessed in plate formats, this approach

completes the lack that was present in assessing the function steps of cytotoxicity in a high throughput format.

10.Limitations of HCI of the immunological synapse

One limitation that I encountered during my PhD was the fact that coating the multiwell plates and seeding the cells had to be done manually, due to the absence of robotics. Had robotics been accessible, it would not only have saved time in coating plates, as well as seeding and staining cells, but would have most likely decreased the variation in the number of cells seeded in each well.

It is to be noted that even though we imaged 8 z planes encompassing a height of 4 μm , we only opted for the assessment of the first 2 μm closest to the coated surface. Therefore, our data only captures the events at the synaptic plane and may be missing events occurring at higher planes. Indeed, a 3D study would be more comprehensive, and would reveal more information about the state of the lymphocyte, which can provide a better understanding of granule positioning, and could potentially provide insight into granule polarization defects.

Moreover, our study captures the immunological synapse assembly in the context where the lymphocytes are seeded on an ICAM-1 and stimulatory antibody coated surface. In such a scenario, these ligands are fixed, while when expressed on a target cell, they exhibit intermediate motility, depending on the cell state⁴¹³. For that reason, it might be of interest to optimize the HCI of the immunological synapse of lymphocytes when conjugated to target cells and assess the differences the IS morphology that may arise. Another alternative could also be the optimization of this approach on planar lipid bilayers.

In our results upon drug treatment, we observed an increase in perforin-related parameters, implying that the perforin granules were at the IS surface at the time of imaging. However, since the images we captured were of fixed cells, one question that cannot be answered accurately is whether or not this increase in granules at the IS is due to an increased granule recruitment to the IS, or to a defect in granule exocytosis. To accurately answer this question our approach would need to be coupled to a degranulation assay, or a more resolute live imaging microscopy to be more precise in determining whether the granules fail to fuse with the membrane or cannot exit through the actin clearances. In some instances, we also observed a decrease in perforin-related parameters. However, HCI of the IS could be helpful in this case but the whole height of the cell would be imaged to determine whether the cells have degranulated too fast (by a decreased lytic granule count) or if the cells fail to polarize.

Despite the fact that we report different IS morphologies for each of the two patients, the end result for both is a defective cytotoxic activity. For that reason, it could be of interest to study the steps of cytotoxicity of these patients by live microscopy, in order to confirm at which step the defect lies, and confirm the results seen and the assumption made by examining IS morphology. Therefore, despite

the usefulness of HCI screens of the immunological synapse, it is not yet able to replace live microscopy. Additionally, it would be of high informative value to apply high content imaging to decipher ongoing at the nanoscale, and even determine single molecule localization. The compromise between high throughput and high resolution is slowly beginning to become narrower, as we are seeing developments in high throughput super resolution microscopy techniques⁴¹⁴.

The value of HCI is the ability to perform screens using this technology. In fact, an aspect of my PhD project that I have attempted to set up was an HCI screen of the IS of NK-92 cells that were knocked-down with an arrayed library of 85 genes known to play a role in the actin cytoskeleton regulation, and their neighbors. The aim of that screen was to build an interactome of these genes, based on the obtained IS morphologies for the generated knock-downs. However, that project was discontinued due to the difficulty in transducing NK-92 cells with the lentiviral particles. An alternative that could make mapping these interactions possible would be imaging PID patient material. Additionally, if one could image the different cell types from several patients simultaneously, it could give an idea of the variations to this interactome in different cellular subsets.

References

1. Dranoff G. Cytokines in cancer pathogenesis and cancer therapy. *Nat Rev Cancer*. 2004;4(1):11-22. doi:10.1038/nrc1252
2. Hato T, Dagher PC. How the Innate Immune System Senses Trouble and Causes Trouble. *Clin J Am Soc Nephrol*. 2015;10(8):1459-1469. doi:10.2215/CJN.04680514
3. Mazzurana L, Rao A, Van Acker A, Mjösberg J. The roles for innate lymphoid cells in the human immune system. *Semin Immunopathol*. 2018;40(4):407-419. doi:10.1007/s00281-018-0688-7
4. Campbell KS, Hasegawa J. Natural killer cell biology: An update and future directions. *J Allergy Clin Immunol*. 2013;132(3):536-544. doi:10.1016/j.jaci.2013.07.006
5. Wu L, Van Kaer L. Natural killer T cells in health and disease. *Front Biosci (Schol Ed)*. 2011;3:236-251. <http://www.ncbi.nlm.nih.gov/pubmed/21196373>.
6. Holtmeier W, Kabelitz D. γ ; δ ; T Cells Link Innate and Adaptive Immune Responses. In: *Mechanisms of Epithelial Defense*. Basel: KARGER; 2005:151-183. doi:10.1159/000086659
7. Ferreira LMR. Gammadelta T Cells: Innately Adaptive Immune Cells? *Int Rev Immunol*. 2013;32(3):223-248. doi:10.3109/08830185.2013.783831
8. Lawand M, Déchanet-Merville J, Dieu-Nosjean M-C. Key Features of Gamma-Delta T-Cell Subsets in Human Diseases and Their Immunotherapeutic Implications. *Front Immunol*. 2017;8. doi:10.3389/fimmu.2017.00761
9. Bassing CH, Swat W, Alt FW. The Mechanism and Regulation of Chromosomal V(D)J Recombination. *Cell*. 2002;109(2):S45-S55. doi:10.1016/S0092-8674(02)00675-X
10. Krangel MS. Mechanics of T cell receptor gene rearrangement. *Curr Opin Immunol*. 2009;21(2):133-139. doi:10.1016/j.coi.2009.03.009
11. Vogelzang A, McGuire HM, Yu D, Sprent J, Mackay CR, King C. A Fundamental Role for Interleukin-21 in the Generation of T Follicular Helper Cells. *Immunity*. 2008;29(1):127-137. doi:10.1016/j.immuni.2008.06.001
12. Juno JA, van Bockel D, Kent SJ, Kelleher AD, Zaunders JJ, Munier CML. Cytotoxic CD4 T Cells—Friend or Foe during Viral Infection? *Front Immunol*. 2017;8. doi:10.3389/fimmu.2017.00019
13. Bengsch B, Ohtani T, Herati RS, Bovenschen N, Chang K-M, Wherry EJ. Deep immune profiling by mass cytometry links human T and NK cell differentiation and cytotoxic molecule expression patterns. *J Immunol Methods*. 2018;453:3-10. doi:10.1016/j.jim.2017.03.009
14. Rak GD, Mace EM, Banerjee PP, Svitkina T, Orange JS. Natural Killer cell lytic granule secretion occurs through a pervasive actin network at the immune synapse. *PLoS Biol*. 2011;9(9). doi:10.1371/journal.pbio.1001151
15. Kärre K, Ljunggren HG, Piontek G, Kiessling R. Selective rejection of H-2-deficient lymphoma variants suggests alternative immune defence strategy. *Nature*. 1986;319(6055):675-

678. doi:10.1038/319675a0

16. Baume DM, Robertson MJ, Levine H, Manley TJ, Schow PW, Ritz J. Differential responses to interleukin 2 define functionally distinct subsets of human natural killer cells. *Eur J Immunol.* 1992;22(1):1-6. doi:10.1002/eji.1830220102
17. Long EO, Burshtyn DN, Clark WP, et al. Killer cell inhibitory receptors: diversity, specificity, and function. *Immunol Rev.* 1997;155(1):135-144. doi:10.1111/j.1600-065X.1997.tb00946.x
18. Lanier LL. NK CELL RECEPTORS. *Annu Rev Immunol.* 1998;16(1):359-393. doi:10.1146/annurev.immunol.16.1.359
19. Anegón I. Interaction of Fc receptor (CD16) ligands induces transcription of interleukin 2 receptor (CD25) and lymphokine genes and expression of their products in human natural killer cells. *J Exp Med.* 1988;167(2):452-472. doi:10.1084/jem.167.2.452
20. Lanier LL, Ruitenberg JJ, Phillips JH. Functional and biochemical analysis of CD16 antigen on natural killer cells and granulocytes. *J Immunol.* 1988;141(10):3478-3485. <http://www.ncbi.nlm.nih.gov/pubmed/2903193>.
21. Srpan K, Ambrose A, Karampatzakis A, et al. Shedding of CD16 disassembles the NK cell immune synapse and boosts serial engagement of target cells. *J Cell Biol.* 2018;217(9):3267-3283. doi:10.1083/jcb.201712085
22. Sivori S, Vitale M, Morelli L, et al. p46, a Novel Natural Killer Cell-specific Surface Molecule That Mediates Cell Activation. *J Exp Med.* 1997;186(7):1129-1136. doi:10.1084/jem.186.7.1129
23. Pessino A, Sivori S, Bottino C, et al. Molecular Cloning of NKp46: A Novel Member of the Immunoglobulin Superfamily Involved in Triggering of Natural Cytotoxicity. *J Exp Med.* 1998;188(5):953-960. doi:10.1084/jem.188.5.953
24. Moretta A, Bottino C, Vitale M, et al. A *CTIVATING* *R* *ECEPTORS* AND *C* *ORECEPTORS* *I* *NVOLVED* *I* *N* *U* *M* *A* *N* *N* *A* *T* *U* *R* *A* *L* *K* *I* *L* *L* *E* *R* *C* *E* *L* *L* *M* *E* *D* *I* *A* *T* *E* *D* *C* *Y* *T* *O* *L* *Y* *S* *I* *S*. *Annu Rev Immunol.* 2001;19(1):197-223. doi:10.1146/annurev.immunol.19.1.197
25. Freud AG, Zhao S, Wei S, et al. Expression of the Activating Receptor, NKp46 (CD335), in Human Natural Killer and T-Cell Neoplasia. *Am J Clin Pathol.* 2013;140(6):853-866. doi:10.1309/AJCPWGG69MCZOWMM
26. Wiesmayr S, Webber SA, Macedo C, et al. Decreased NKp46 and NKG2D and elevated PD-1 are associated with altered NK-cell function in pediatric transplant patients with PTLD. *Eur J Immunol.* 2012;42(2):541-550. doi:10.1002/eji.201141832
27. Hsieh CL, Nagasaki K, Martinez OM, Krams SM. NKp30 is a functional activation receptor on a subset of rat natural killer cells. *Eur J Immunol.* 2006;36(8):2170-2180. doi:10.1002/eji.200635982
28. Reiners KS, Topolar D, Henke A, et al. Soluble ligands for NK cell receptors promote evasion of chronic lymphocytic leukemia cells from NK cell anti-tumor activity. *Blood.* 2013;121(18):3658-3665. doi:10.1182/blood-2013-01-476606
29. Reiners KS, Kessler J, Sauer M, et al. Rescue of Impaired NK Cell Activity in Hodgkin

- Lymphoma With Bispecific Antibodies In Vitro and in Patients. *Mol Ther.* 2013;21(4):895-903. doi:10.1038/mt.2013.14
30. Wang W, Guo H, Geng J, et al. Tumor-released Galectin-3, a Soluble Inhibitory Ligand of Human NKp30, Plays an Important Role in Tumor Escape from NK Cell Attack. *J Biol Chem.* 2014;289(48):33311-33319. doi:10.1074/jbc.M114.603464
31. Semeraro M, Rusakiewicz S, Minard-Colin V, et al. Clinical impact of the NKp30/B7-H6 axis in high-risk neuroblastoma patients. *Sci Transl Med.* 2015;7(283):283ra55-283ra55. doi:10.1126/scitranslmed.aaa2327
32. Pogge von Strandmann E, Simhadri VR, von Tresckow B, et al. Human Leukocyte Antigen-B-Associated Transcript 3 Is Released from Tumor Cells and Engages the NKp30 Receptor on Natural Killer Cells. *Immunity.* 2007;27(6):965-974. doi:10.1016/j.immuni.2007.10.010
33. Yabe T, McSherry C, Bach F, et al. A multigene family on human chromosome 12 encodes natural killer-cell lectins. *Immunogenetics.* 1993;37(6). doi:10.1007/BF00222470
34. Bauer S. Activation of NK Cells and T Cells by NKG2D, a Receptor for Stress-Inducible MICA. *Science (80-).* 1999;285(5428):727-729. doi:10.1126/science.285.5428.727
35. Raulet DH. Roles of the NKG2D immunoreceptor and its ligands. *Nat Rev Immunol.* 2003;3(10):781-790. doi:10.1038/nri1199
36. Sutherland CL, Chalupny NJ, Schooley K, VandenBos T, Kubin M, Cosman D. UL16-Binding Proteins, Novel MHC Class I-Related Proteins, Bind to NKG2D and Activate Multiple Signaling Pathways in Primary NK Cells. *J Immunol.* 2002;168(2):671-679. doi:10.4049/jimmunol.168.2.671
37. Wu J. An Activating Immunoreceptor Complex Formed by NKG2D and DAP10. *Science (80-).* 1999;285(5428):730-732. doi:10.1126/science.285.5428.730
38. Moretta L, Bottino C, Pende D, Castriconi R, Mingari MC, Moretta A. Surface NK receptors and their ligands on tumor cells. *Semin Immunol.* 2006;18(3):151-158. doi:10.1016/j.smim.2006.03.002
39. Carbone E. HLA class I, NKG2D, and natural cytotoxicity receptors regulate multiple myeloma cell recognition by natural killer cells. *Blood.* 2005;105(1):251-258. doi:10.1182/blood-2004-04-1422
40. Vitale M, Bottino C, Sivori S, et al. NKp44, a novel triggering surface molecule specifically expressed by activated natural killer cells, is involved in non-major histocompatibility complex-restricted tumor cell lysis. *J Exp Med.* 1998;187(12):2065-2072. doi:10.1084/jem.187.12.2065
41. Parodi M, Favoreel H, Candiano G, et al. NKp44-NKp44 Ligand Interactions in the Regulation of Natural Killer Cells and Other Innate Lymphoid Cells in Humans. *Front Immunol.* 2019;10. doi:10.3389/fimmu.2019.00719
42. Cantoni C, Bottino C, Vitale M, et al. NKp44, A Triggering Receptor Involved in Tumor Cell Lysis by Activated Human Natural Killer Cells, Is a Novel Member of the Immunoglobulin Superfamily. *J Exp Med.* 1999;189(5):787-796. doi:10.1084/jem.189.5.787
43. Braud VM, Allan DSJ, O'Callaghan CA, et al. HLA-E binds to natural killer cell receptors CD94/NKG2A, B and C. *Nature.* 1998;391(6669):795-799. doi:10.1038/35869

44. Dustin ML, Long EO. Cytotoxic immunological synapses: NK and CTL synapses. *Immunol Rev.* 2010;235(1):24-34. doi:10.1111/j.0105-2896.2010.00904.x
45. Brown MH, Boles K, van der Merwe PA, Kumar V, Mathew PA, Barclay AN. 2B4, the natural killer and T cell immunoglobulin superfamily surface protein, is a ligand for CD48. *J Exp Med.* 1998;188(11):2083-2090. doi:10.1084/jem.188.11.2083
46. Bottino C, Falco M, Parolini S, et al. NTB-A [correction of GNTB-A], a novel SH2D1A-associated surface molecule contributing to the inability of natural killer cells to kill Epstein-Barr virus-infected B cells in X-linked lymphoproliferative disease. *J Exp Med.* 2001;194(3):235-246. doi:10.1084/jem.194.3.235
47. Falco M, Marcenaro E, Romeo E, et al. Homophilic interaction of NTBA, a member of the CD2 molecular family: induction of cytotoxicity and cytokine release in human NK cells. *Eur J Immunol.* 2004;34(6):1663-1672. doi:10.1002/eji.200424886
48. Chuang SS, Kim MH, Johnson LA, et al. 2B4 stimulation of YT cells induces natural killer cell cytolytic function and invasiveness. *Immunology.* 2000;100(3):378-383. doi:10.1046/j.1365-2567.2000.00031.x
49. Sivori S, Parolini S, Falco M, et al. 2B4 functions as a co-receptor in human NK cell activation. *Eur J Immunol.* 2000;30(3):787-793. doi:10.1002/1521-4141(200003)30:3<787::AID-IMMU787>3.0.CO;2-I
50. Bida AT, Upshaw Neff JL, Dick CJ, et al. 2B4 utilizes ITAM-containing receptor complexes to initiate intracellular signaling and cytolysis. *Mol Immunol.* 2011;48(9-10):1149-1159. doi:10.1016/j.molimm.2011.02.008
51. Wilson JL, Charo J, Martín-Fontecha A, et al. NK cell triggering by the human costimulatory molecules CD80 and CD86. *J Immunol.* 1999;163(8):4207-4212. <http://www.ncbi.nlm.nih.gov/pubmed/10510357>.
52. Long EO, Sik Kim H, Liu D, Peterson ME, Rajagopalan S. Controlling Natural Killer Cell Responses: Integration of Signals for Activation and Inhibition. *Annu Rev Immunol.* 2013;31(1):227-258. doi:10.1146/annurev-immunol-020711-075005
53. Brown ACN, Oddos S, Dobbie IM, et al. Remodelling of Cortical Actin Where Lytic Granules Dock at Natural Killer Cell Immune Synapses Revealed by Super-Resolution Microscopy. Marrack P, ed. *PLoS Biol.* 2011;9(9):e1001152. doi:10.1371/journal.pbio.1001152
54. Bryceson YT, March ME, Ljunggren H-G, Long EO. Synergy among receptors on resting NK cells for the activation of natural cytotoxicity and cytokine secretion. *Blood.* 2006;107(1):159-166. doi:10.1182/blood-2005-04-1351
55. Hsu H-T, Mace EM, Carisey AF, et al. NK cells converge lytic granules to promote cytotoxicity and prevent bystander killing. *J Cell Biol.* 2016;215(6):875-889. doi:10.1083/jcb.201604136
56. Segovis CM, Schoon RA, Dick CJ, Nacusi LP, Leibson PJ, Billadeau DD. PI3K Links NKG2D Signaling to a CrkL Pathway Involved in Natural Killer Cell Adhesion, Polarity, and Granule Secretion. *J Immunol.* 2009;182(11):6933-6942. doi:10.4049/jimmunol.0803840
57. Orange JS, Harris KE, Andzelm MM, Valter MM, Geha RS, Strominger JL. The mature activating natural killer cell immunologic synapse is formed in distinct stages. *Proc Natl Acad Sci U S A.* 2003;100(SUPPL. 2):14151-14156. doi:10.1073/pnas.1835830100

58. Butler B, Cooper JA. Distinct Roles for the Actin Nucleators Arp2/3 and hDia1 during NK-Mediated Cytotoxicity. *Curr Biol*. 2009;19(22):1886-1896. doi:10.1016/j.cub.2009.10.029
59. Shibuya K, Lanier LL, Phillips JH, et al. Physical and Functional Association of LFA-1 with DNAM-1 Adhesion Molecule. *Immunity*. 1999;11(5):615-623. doi:10.1016/S1074-7613(00)80136-3
60. Bryceson YT, Ljunggren H-G, Long EO. Minimal requirement for induction of natural cytotoxicity and intersection of activation signals by inhibitory receptors. *Blood*. 2009;114(13):2657-2666. doi:10.1182/blood-2009-01-201632
61. Culley FJ, Johnson M, Evans JH, et al. Natural Killer Cell Signal Integration Balances Synapse Symmetry and Migration. Marrack P, ed. *PLoS Biol*. 2009;7(7):e1000159. doi:10.1371/journal.pbio.1000159
62. Mace EM, Zhang J, Siminovitch KA, Takei F. Elucidation of the integrin LFA-1-mediated signaling pathway of actin polarization in natural killer cells. *Blood*. 2010;116(8):1272-1279. doi:10.1182/blood-2009-12-261487
63. Ramarao N, Le Clainche C, Izard T, et al. Capping of actin filaments by vinculin activated by the Shigella IpaA carboxyl-terminal domain. *FEBS Lett*. 2007;581(5):853-857. doi:10.1016/j.febslet.2007.01.057
64. Stinchcombe JC, Bossi G, Booth S, Griffiths GM. The immunological synapse of CTL contains a secretory domain and membrane bridges. *Immunity*. 2001;15(5):751-761. <http://www.ncbi.nlm.nih.gov/pubmed/11728337>.
65. Mace EM, Monkley SJ, Critchley DR, Takei F. A Dual Role for Talin in NK Cell Cytotoxicity: Activation of LFA-1-Mediated Cell Adhesion and Polarization of NK Cells. *J Immunol*. 2009;182(2):948-956. doi:10.4049/jimmunol.182.2.948
66. Mace EM, Dongre P, Hsu H-T, et al. Cell biological steps and checkpoints in accessing NK cell cytotoxicity. *Immunol Cell Biol*. 2014;92(3):245-255. doi:10.1038/icb.2013.96
67. Wood SM, Meeths M, Chiang SCC, et al. Different NK cell-activating receptors preferentially recruit Rab27a or Munc13-4 to perforin-containing granules for cytotoxicity. *Blood*. 2009;114(19):4117-4127. doi:10.1182/blood-2009-06-225359
68. Kurowska M, Goudin N, Nehme NT, et al. Terminal transport of lytic granules to the immune synapse is mediated by the kinesin-1/Slp3/Rab27a complex. *Blood*. 2012;119(17):3879-3889. doi:10.1182/blood-2011-09-382556
69. Mace EM, Wu WW, Ho T, Mann SS, Hsu H-T, Orange JS. NK Cell Lytic Granules Are Highly Motile at the Immunological Synapse and Require F-Actin for Post-Degranulation Persistence. *J Immunol*. 2012;189(10):4870-4880. doi:10.4049/jimmunol.1201296
70. Andzelm MM, Chen X, Krzewski K, Orange JS, Strominger JL. Myosin IIA is required for cytolytic granule exocytosis in human NK cells. *J Exp Med*. 2007;204(10):2285-2291. doi:10.1084/jem.20071143
71. Sanborn KB, Rak GD, Maru SY, et al. Myosin IIA Associates with NK Cell Lytic Granules to Enable Their Interaction with F-Actin and Function at the Immunological Synapse. *J Immunol*. 2009;182(11):6969-6984. doi:10.4049/jimmunol.0804337
72. Carisey AF, Mace EM, Saeed MB, Davis DM, Orange JS. Nanoscale Dynamism of Actin Enables Secretory Function in Cytolytic Cells. *Curr Biol*. 2018;28(4):489-502.e9.

doi:10.1016/j.cub.2017.12.044

73. Wang B, Norbury CC, Greenwood R, Bennink JR, Yewdell JW, Frelinger JA. Multiple Paths for Activation of Naive CD8 + T Cells: CD4-Independent Help. *J Immunol.* 2001;167(3):1283-1289. doi:10.4049/jimmunol.167.3.1283
74. Zhang N, Bevan MJ. CD8+ T Cells: Foot Soldiers of the Immune System. *Immunity.* 2011;35(2):161-168. doi:10.1016/j.immuni.2011.07.010
75. Rudolph MG, Stanfield RL, Wilson IA. HOW TCRS BIND MHCS, PEPTIDES, AND CORECEPTORS. *Annu Rev Immunol.* 2006;24(1):419-466. doi:10.1146/annurev.immunol.23.021704.115658
76. Matsui K, Boniface J, Reay P, Schild H, Fazekas de St Groth B, Davis M. Low affinity interaction of peptide-MHC complexes with T cell receptors. *Science (80-).* 1991;254(5039):1788-1791. doi:10.1126/science.1763329
77. Weber S, Traunecker A, Oliveri F, Gerhard W, Karjalainen K. Specific low-affinity recognition of major histocompatibility complex plus peptide by soluble T-cell receptor. *Nature.* 1992;356(6372):793-796. doi:10.1038/356793a0
78. Huang J, Zarnitsyna VI, Liu B, et al. The kinetics of two-dimensional TCR and pMHC interactions determine T-cell responsiveness. *Nature.* 2010;464(7290):932-936. doi:10.1038/nature08944
79. Huppa JB, Axmann M, Mörtelmaier MA, et al. TCR-peptide-MHC interactions in situ show accelerated kinetics and increased affinity. *Nature.* 2010;463(7283):963-967. doi:10.1038/nature08746
80. Irvine DJ, Purbhoo MA, Krogsgaard M, Davis MM. Direct observation of ligand recognition by T cells. *Nature.* 2002;419(6909):845-849. doi:10.1038/nature01076
81. Purbhoo MA, Irvine DJ, Huppa JB, Davis MM. T cell killing does not require the formation of a stable mature immunological synapse. *Nat Immunol.* 2004;5(5):524-530. doi:10.1038/ni1058
82. Huse M, Klein LO, Girvin AT, et al. Spatial and Temporal Dynamics of T Cell Receptor Signaling with a Photoactivatable Agonist. *Immunity.* 2007;27(1):76-88. doi:10.1016/j.immuni.2007.05.017
83. Jiang N, Huang J, Edwards LJ, et al. Two-Stage Cooperative T Cell Receptor-Peptide Major Histocompatibility Complex-CD8 Trimolecular Interactions Amplify Antigen Discrimination. *Immunity.* 2011;34(1):13-23. doi:10.1016/j.immuni.2010.12.017
84. Valitutti S. Sustained signaling leading to T cell activation results from prolonged T cell receptor occupancy. Role of T cell actin cytoskeleton. *J Exp Med.* 1995;181(2):577-584. doi:10.1084/jem.181.2.577
85. McKeithan TW. Kinetic proofreading in T-cell receptor signal transduction. *Proc Natl Acad Sci.* 1995;92(11):5042-5046. doi:10.1073/pnas.92.11.5042
86. Dustin ML, Olszowy MW, Holdorf AD, et al. A Novel Adaptor Protein Orchestrates Receptor Patterning and Cytoskeletal Polarity in T-Cell Contacts. *Cell.* 1998;94(5):667-677. doi:10.1016/S0092-8674(00)81608-6
87. Brownlie RJ, Zamoyska R. T cell receptor signalling networks: branched, diversified

- and bounded. *Nat Rev Immunol.* 2013;13(4):257-269. doi:10.1038/nri3403
88. Hynes RO. Integrins. *Cell.* 2002;110(6):673-687. doi:10.1016/S0092-8674(02)00971-6
89. Takada Y, Ye X, Simon S. The integrins. *Genome Biol.* 2007;8(5):215. doi:10.1186/gb-2007-8-5-215
90. Campana D, Sheridan B, Tidman N, Hoffbrand AV, Janossy G. Human leukocyte function-associated antigens on lympho-hemopoietic precursor cells. *Eur J Immunol.* 1986;16(5):537-542. doi:10.1002/eji.1830160513
91. Anderson DC, Springer TA. Leukocyte Adhesion Deficiency: An Inherited Defect in the Mac-1, LFA-1, and p150,95 Glycoproteins. *Annu Rev Med.* 1987;38(1):175-194. doi:10.1146/annurev.me.38.020187.001135
92. Marlin SD, Springer TA. Purified intercellular adhesion molecule-1 (ICAM-1) is a ligand for lymphocyte function-associated antigen 1 (LFA-1). *Cell.* 1987;51(5):813-819. doi:10.1016/0092-8674(87)90104-8
93. Rothlein R, Dustin ML, Marlin SD, Springer TA. A human intercellular adhesion molecule (ICAM-1) distinct from LFA-1. *J Immunol.* 1986;137(4):1270-1274. <http://www.ncbi.nlm.nih.gov/pubmed/3525675>.
94. Long EO. ICAM-1: Getting a Grip on Leukocyte Adhesion. *J Immunol.* 2011;186(9):5021-5023. doi:10.4049/jimmunol.1100646
95. Comrie WA, Babich A, Burkhardt JK. F-actin flow drives affinity maturation and spatial organization of LFA-1 at the immunological synapse. *J Cell Biol.* 2015;208(4):475-491. doi:10.1083/jcb.201406121
96. Chakraborty S, Núñez D, Hu S-Y, et al. FRET Based Quantification and Screening Technology Platform for the Interactions of Leukocyte Function-Associated Antigen-1 (LFA-1) with InterCellular Adhesion Molecule-1 (ICAM-1). D'Auria S, ed. *PLoS One.* 2014;9(7):e102572. doi:10.1371/journal.pone.0102572
97. Carman C V, Springer TA. Integrin avidity regulation: are changes in affinity and conformation underemphasized? *Curr Opin Cell Biol.* 2003;15(5):547-556. doi:10.1016/j.ceb.2003.08.003
98. Hogg N, Patzak I, Willenbrock F. The insider's guide to leukocyte integrin signalling and function. *Nat Rev Immunol.* 2011;11(6):416-426. doi:10.1038/nri2986
99. Verma NK, Kelleher D. Not Just an Adhesion Molecule: LFA-1 Contact Tunes the T Lymphocyte Program. *J Immunol.* 2017;199(4):1213-1221. doi:10.4049/jimmunol.1700495
100. Shamri R, Grabovsky V, Gauguet J-M, et al. Lymphocyte arrest requires instantaneous induction of an extended LFA-1 conformation mediated by endothelium-bound chemokines. *Nat Immunol.* 2005;6(5):497-506. doi:10.1038/ni1194
101. Houmadi R, Guipouy D, Rey-Barroso J, et al. The Wiskott-Aldrich Syndrome Protein Contributes to the Assembly of the LFA-1 Nanocluster Belt at the Lytic Synapse. *Cell Rep.* 2018;22(4):979-991. doi:10.1016/j.celrep.2017.12.088
102. Fooksman DR, Vardhana S, Vasiliver-Shamis G, et al. Functional Anatomy of T Cell Activation and Synapse Formation. *Annu Rev Immunol.* 2010;28(1):79-105.

doi:10.1146/annurev-immunol-030409-101308

103. Kabanova A, Zurli V, Baldari CT. Signals Controlling Lytic Granule Polarization at the Cytotoxic Immune Synapse. *Front Immunol.* 2018;9. doi:10.3389/fimmu.2018.00307
104. Deguine J, Breart B, Lemaître F, Di Santo JP, Bousso P. Intravital Imaging Reveals Distinct Dynamics for Natural Killer and CD8+ T Cells during Tumor Regression. *Immunity.* 2010;33(4):632-644. doi:10.1016/j.immuni.2010.09.016
105. Martin MD, Badovinac VP. Defining Memory CD8 T Cell. *Front Immunol.* 2018;9. doi:10.3389/fimmu.2018.02692
106. Bousso P, Robey E. Dynamics of CD8+ T cell priming by dendritic cells in intact lymph nodes. *Nat Immunol.* 2003;4(6):579-585. doi:10.1038/ni928
107. Stoll S. Dynamic Imaging of T Cell-Dendritic Cell Interactions in Lymph Nodes. *Science (80-).* 2002;296(5574):1873-1876. doi:10.1126/science.1071065
108. Grakoui A, Bromley SK, Sumen C, et al. The immunological synapse: A molecular machine controlling T cell activation. *Science (80-).* 1999;285(5425):221-227. doi:10.1126/science.285.5425.221
109. Dustin ML, Bromley SK, Kan Z, Peterson DA, Unanue ER. Antigen receptor engagement delivers a stop signal to migrating T lymphocytes. *Proc Natl Acad Sci.* 1997;94(8):3909-3913. doi:10.1073/pnas.94.8.3909
110. Friedl P, den Boer AT, Gunzer M. Tuning immune responses: diversity and adaptation of the immunological synapse. *Nat Rev Immunol.* 2005;5(7):532-545. doi:10.1038/nri1647
111. Faroudi M, Zaru R, Paulet P, Müller S, Valitutti S. Cutting Edge: T Lymphocyte Activation by Repeated Immunological Synapse Formation and Intermittent Signaling. *J Immunol.* 2003;171(3):1128-1132. doi:10.4049/jimmunol.171.3.1128
112. Clark CE, Hasan M, Bousso P. A Role for the Immediate Early Gene Product c-fos in Imprinting T Cells with Short-Term Memory for Signal Summation. Kanellopoulos J, ed. *PLoS One.* 2011;6(4):e18916. doi:10.1371/journal.pone.0018916
113. Dustin ML. Insights into Function of the Immunological Synapse from Studies with Supported Planar Bilayers. In: ; 2010:1-24. doi:10.1007/978-3-642-03858-7_1
114. Skokos D, Shakhar G, Varma R, et al. Peptide-MHC potency governs dynamic interactions between T cells and dendritic cells in lymph nodes. *Nat Immunol.* 2007;8(8):835-844. doi:10.1038/ni1490
115. Samelson LE, Patel MD, Weissman AM, Harford JB, Klausner RD. Antigen activation of murine T cells induces tyrosine phosphorylation of a polypeptide associated with the T cell antigen receptor. *Cell.* 1986;46(7):1083-1090. doi:10.1016/0092-8674(86)90708-7
116. Timmerman LA, Clipstone NA, Ho SN, Northrop JP, Crabtree GR. Rapid shuttling of NF-AT in discrimination of Ca²⁺ signals and immunosuppression. *Nature.* 1996;383(6603):837-840. doi:10.1038/383837a0
117. Quintana A, Schwindling C, Wenning AS, et al. T cell activation requires mitochondrial translocation to the immunological synapse. *Proc Natl Acad Sci.* 2007;104(36):14418-14423. doi:10.1073/pnas.0703126104
118. Halle S, Halle O, Förster R. Mechanisms and Dynamics of T Cell-Mediated

- Cytotoxicity In Vivo. *Trends Immunol.* 2017;38(6):432-443. doi:10.1016/j.it.2017.04.002
119. Dieckmann NMG, Frazer GL, Asano Y, Stinchcombe JC, Griffiths GM. The cytotoxic T lymphocyte immune synapse at a glance. *J Cell Sci.* 2016;129(15):2881-2886. doi:10.1242/jcs.186205
120. Hutz JE, Nelson T, Wu H, et al. The Multidimensional Perturbation Value. *J Biomol Screen.* 2013;18(4):367-377. doi:10.1177/1087057112469257
121. Stinchcombe JC, Griffiths GM. Secretory Mechanisms in Cell-Mediated Cytotoxicity. *Annu Rev Cell Dev Biol.* 2007;23(1):495-517. doi:10.1146/annurev.cellbio.23.090506.123521
122. Ming M, Schirra C, Becherer U, Stevens DR, Rettig J. Behavior and Properties of Mature Lytic Granules at the Immunological Synapse of Human Cytotoxic T Lymphocytes. Cebeacauer M, ed. *PLoS One.* 2015;10(8):e0135994. doi:10.1371/journal.pone.0135994
123. Higgs HN, Pollard TD. Regulation of Actin Polymerization by Arp2/3 Complex and WASp/Scar Proteins. *J Biol Chem.* 1999;274(46):32531-32534. doi:10.1074/jbc.274.46.32531
124. Li F, Higgs HN. The Mouse Formin mDia1 Is a Potent Actin Nucleation Factor Regulated by Autoinhibition. *Curr Biol.* 2003;13(15):1335-1340. doi:10.1016/S0960-9822(03)00540-2
125. Le Clairche C, Carlier M-F. Regulation of Actin Assembly Associated With Protrusion and Adhesion in Cell Migration. *Physiol Rev.* 2008;88(2):489-513. doi:10.1152/physrev.00021.2007
126. Samstag Y. Actin cytoskeletal dynamics in T lymphocyte activation and migration. *J Leukoc Biol.* 2003;73(1):30-48. doi:10.1189/jlb.0602272
127. Batista FD, Treanor B, Harwood NE. Visualizing a role for the actin cytoskeleton in the regulation of B-cell activation. *Immunol Rev.* 2010;237(1):191-204. doi:10.1111/j.1600-065X.2010.00943.x
128. Freeman SA, Lei V, Dang-Lawson M, Mizuno K, Roskelley CD, Gold MR. Cofilin-Mediated F-Actin Severing Is Regulated by the Rap GTPase and Controls the Cytoskeletal Dynamics That Drive Lymphocyte Spreading and BCR Microcluster Formation. *J Immunol.* 2011;187(11):5887-5900. doi:10.4049/jimmunol.1102233
129. Nejedla M, Sadi S, Sulimenko V, et al. Profilin connects actin assembly with microtubule dynamics. Blanchoin L, ed. *Mol Biol Cell.* 2016;27(15):2381-2393. doi:10.1091/mbc.e15-11-0799
130. Mattila PK, Lappalainen P. Filopodia: molecular architecture and cellular functions. *Nat Rev Mol Cell Biol.* 2008;9(6):446-454. doi:10.1038/nrm2406
131. Dupré L, Houmadi R, Tang C, Rey-Barroso J. T Lymphocyte Migration: An Action Movie Starring the Actin and Associated Actors. *Front Immunol.* 2015;6. doi:10.3389/fimmu.2015.00586
132. Monks CRF, Freiberg BA, Kupfer H, Sciaky N, Kupfer A. Three-dimensional segregation of supramolecular activation clusters in T cells. *Nature.* 1998;395(6697):82-86. doi:10.1038/25764
133. Johnson KG, Bromley SK, Dustin ML, Thomas ML. A supramolecular basis for CD45 tyrosine phosphatase regulation in sustained T cell activation. *Proc Natl Acad Sci.*

2000;97(18):10138-10143. doi:10.1073/pnas.97.18.10138

134. Freiberg BA, Kupfer H, Maslanik W, et al. Staging and resetting T cell activation in SMACs. *Nat Immunol*. 2002;3(10):911-917. doi:10.1038/ni836

135. Dustin ML. The Immunological Synapse. *Cancer Immunol Res*. 2014;2(11):1023-1033. doi:10.1158/2326-6066.CIR-14-0161

136. Krummel MF. Differential Clustering of CD4 and CD3zeta During T Cell Recognition. *Science (80-)*. 2000;289(5483):1349-1352. doi:10.1126/science.289.5483.1349

137. Krummel MF, Davis MM. Dynamics of the immunological synapse: finding, establishing and solidifying a connection. *Curr Opin Immunol*. 2002;14(1):66-74. doi:10.1016/S0952-7915(01)00299-0

138. Sims TN, Soos TJ, Xenias HS, et al. Opposing Effects of PKC θ and WASp on Symmetry Breaking and Relocation of the Immunological Synapse. *Cell*. 2007;129(4):773-785. doi:10.1016/j.cell.2007.03.037

139. Campi G, Varma R, Dustin ML. Actin and agonist MHC-peptide complex-dependent T cell receptor microclusters as scaffolds for signaling. *J Exp Med*. 2005;202(8):1031-1036. doi:10.1084/jem.20051182

140. Hashimoto-Tane A, Yokosuka T, Sakata-Sogawa K, et al. Dynein-Driven Transport of T Cell Receptor Microclusters Regulates Immune Synapse Formation and T Cell Activation. *Immunity*. 2011;34(6):919-931. doi:10.1016/j.immuni.2011.05.012

141. Combs J, Kim SJ, Tan S, et al. Recruitment of dynein to the Jurkat immunological synapse. *Proc Natl Acad Sci*. 2006;103(40):14883-14888. doi:10.1073/pnas.0600914103

142. Yokosuka T, Kobayashi W, Sakata-Sogawa K, et al. Spatiotemporal Regulation of T Cell Costimulation by TCR-CD28 Microclusters and Protein Kinase C θ Translocation. *Immunity*. 2008;29(4):589-601. doi:10.1016/j.immuni.2008.08.011

143. Hammer JA, Wang JC, Saeed M, Pedrosa AT. Origin, Organization, Dynamics, and Function of Actin and ActoMyosin Networks at the T Cell Immunological Synapse. *Annu Rev Immunol*. 2019;37(1):201-224. doi:10.1146/annurev-immunol-042718-041341

144. Yi J, Wu XS, Crites T, Hammer JA. Actin retrograde flow and actoMyosin II arc contraction drive receptor cluster dynamics at the immunological synapse in Jurkat T cells. Pollard TD, ed. *Mol Biol Cell*. 2012;23(5):834-852. doi:10.1091/mbc.e11-08-0731

145. Babich A, Li S, O'Connor RS, Milone MC, Freedman BD, Burkhardt JK. F-actin polymerization and retrograde flow drive sustained PLC γ 1 signaling during T cell activation. *J Cell Biol*. 2012;197(6):775-787. doi:10.1083/jcb.201201018

146. Murugesan S, Hong J, Yi J, et al. Formin-generated actoMyosin arcs propel T cell receptor microcluster movement at the immune synapse. *J Cell Biol*. 2016;215(3):383-399. doi:10.1083/jcb.201603080

147. Orange JS. Formation and function of the lytic NK-cell immunological synapse. *Nat Rev Immunol*. 2008;8(9):713-725. doi:10.1038/nri2381

148. Burnet M. Cancer--A Biological Approach: I. The Processes Of Control. II. The Significance of Somatic Mutation. *BMJ*. 1957;1(5022):779-786. doi:10.1136/bmj.1.5022.779

149. Li X, Gruosso T, Zuo D, et al. Infiltration of CD8 + T cells into tumor cell clusters in

- triple-negative breast cancer. *Proc Natl Acad Sci.* 2019;116(9):3678-3687. doi:10.1073/pnas.1817652116
150. Smyth MJ, Crowe NY, Godfrey DI. NK cells and NKT cells collaborate in host protection from methylcholanthrene-induced fibrosarcoma. *Int Immunol.* 2001;13(4):459-463. doi:10.1093/intimm/13.4.459
151. Rubtsova K, Marrack P, Rubtsov A V. Sexual dimorphism in autoimmunity. *J Clin Invest.* 2015;125(6):2187-2193. doi:10.1172/JCI78082
152. Marson A, Housley WJ, Hafler DA. Genetic basis of autoimmunity. *J Clin Invest.* 2015;125(6):2234-2241. doi:10.1172/JCI78086
153. Zenewicz LA, Abraham C, Flavell RA, Cho JH. Unraveling the Genetics of Autoimmunity. *Cell.* 2010;140(6):791-797. doi:10.1016/j.cell.2010.03.003
154. Root-Bernstein R, Fairweather D. Complexities in the Relationship Between Infection and Autoimmunity. *Curr Allergy Asthma Rep.* 2014;14(1):407. doi:10.1007/s11882-013-0407-3
155. Mikuls TR, Payne JB, Yu F, et al. Periodontitis and Porphyromonas gingivalis in Patients With Rheumatoid Arthritis. *Arthritis Rheumatol.* 2014;66(5):1090-1100. doi:10.1002/art.38348
156. Mills KHG. TLR-dependent T cell activation in autoimmunity. *Nat Rev Immunol.* 2011;11(12):807-822. doi:10.1038/nri3095
157. Kuhn A, Wenzel J, Weyd H. Photosensitivity, Apoptosis, and Cytokines in the Pathogenesis of Lupus Erythematosus: a Critical Review. *Clin Rev Allergy Immunol.* 2014;47(2):148-162. doi:10.1007/s12016-013-8403-x
158. Steinman RM. The Induction of Tolerance by Dendritic Cells That Have Captured Apoptotic Cells. *J Exp Med.* 2000;191(3):411-416. doi:10.1084/jem.191.3.411
159. Mathis D, Benoist C. Microbiota and Autoimmune Disease: The Hosted Self. *Cell Host Microbe.* 2011;10(4):297-301. doi:10.1016/j.chom.2011.09.007
160. Rosenblum MD, Remedios KA, Abbas AK. Mechanisms of human autoimmunity. *J Clin Invest.* 2015;125(6):2228-2233. doi:10.1172/JCI78088
161. Bouneaud C, Kourilsky P, Bousso P. Impact of Negative Selection on the T Cell Repertoire Reactive to a Self-Peptide. *Immunity.* 2000;13(6):829-840. doi:10.1016/S1074-7613(00)00080-7
162. Yu W, Jiang N, Ebert PJR, et al. Clonal Deletion Prunes but Does Not Eliminate Self-Specific $\alpha\beta$ CD8(+) T Lymphocytes. *Immunity.* 2015;42(5):929-941. doi:10.1016/j.immuni.2015.05.001
163. Targownik LE, Bernstein CN. Infectious and Malignant Complications of TNF Inhibitor Therapy in IBD. *Am J Gastroenterol.* 2013;108(12):1835-1842. doi:10.1038/ajg.2013.294
164. Kim SY, Solomon DH. Tumor necrosis factor blockade and the risk of viral infection. *Nat Rev Rheumatol.* 2010;6(3):165-174. doi:10.1038/nrrheum.2009.279
165. Picard C, Bobby Gaspar H, Al-Herz W, et al. International Union of Immunological Societies: 2017 Primary Immunodeficiency Diseases Committee Report on Inborn Errors of

- Immunity. *J Clin Immunol*. 2018;38(1):96-128. doi:10.1007/s10875-017-0464-9
166. Jordan MB, Hildeman D, Kappler J, Marrack P. An animal model of hemophagocytic lymphohistiocytosis (HLH): CD8+ T cells and interferon gamma are essential for the disorder. *Blood*. 2004;104(3):735-743. doi:10.1182/blood-2003-10-3413
167. de Saint Basile G, Ménasché G, Fischer A. Molecular mechanisms of biogenesis and exocytosis of cytotoxic granules. *Nat Rev Immunol*. 2010;10(8):568-579. doi:10.1038/nri2803
168. Morimoto A, Nakazawa Y, Ishii E. Hemophagocytic lymphohistiocytosis: Pathogenesis, diagnosis, and management. *Pediatr Int*. 2016;58(9):817-825. doi:10.1111/ped.13064
169. Voskoboinik I, Trapani JA. Perforinopathy: A Spectrum of Human Immune Disease Caused by Defective Perforin Delivery or Function. *Front Immunol*. 2013;4. doi:10.3389/fimmu.2013.00441
170. Stepp SE. Perforin Gene Defects in Familial Hemophagocytic Lymphohistiocytosis. *Science (80-)*. 1999;286(5446):1957-1959. doi:10.1126/science.286.5446.1957
171. Osińska I, Popko K, Demkow U. Perforin: an important player in immune response. *Cent Eur J Immunol*. 2014;1:109-115. doi:10.5114/ceji.2014.42135
172. Benezech S, Walzer T, Charrier E, et al. Late-onset hemophagocytic lymphohistiocytosis with neurological presentation. *Clin Case Reports*. 2017;5(11):1743-1749. doi:10.1002/ccr3.1135
173. Williams NS, Engelhard VH. Perforin-dependent cytotoxic activity and lymphokine secretion by CD4+ T cells are regulated by CD8+ T cells. *J Immunol*. 1997;159(5):2091-2099. doi:9278294
174. Ghosh S, Carmo M, Calero-Garcia M, et al. T-cell gene therapy for perforin deficiency corrects cytotoxicity defects and prevents hemophagocytic lymphohistiocytosis manifestations. *J Allergy Clin Immunol*. 2018;142(3):904-913.e3. doi:10.1016/j.jaci.2017.11.050
175. Marcenaro S, Gallo F, Martini S, et al. Analysis of natural killer–cell function in familial hemophagocytic lymphohistiocytosis (FHL): defective CD107a surface expression heralds Munc13-4 defect and discriminates between genetic subtypes of the disease. *Blood*. 2006;108(7):2316-2323. doi:10.1182/blood-2006-04-015693
176. Feldmann J, Callebaut I, Raposo G, et al. Munc13-4 Is Essential for Cytolytic Granules Fusion and Is Mutated in a Form of Familial Hemophagocytic Lymphohistiocytosis (FHL3). *Cell*. 2003;115(4):461-473. doi:10.1016/S0092-8674(03)00855-9
177. Elstak ED, Neeft M, Nehme NT, et al. The munc13-4–rab27 complex is specifically required for tethering secretory lysosomes at the plasma membrane. *Blood*. 2011;118(6):1570-1578. doi:10.1182/blood-2011-02-339523
178. Bryceson YT, March ME, Barber DF, Ljunggren HG, Long EO. Cytolytic granule polarization and degranulation controlled by different receptors in resting NK cells. *J Exp Med*. 2005;202(7):1001-1012. doi:10.1084/jem.20051143
179. Bryceson YT, Rudd E, Zheng C, et al. Defective cytotoxic lymphocyte degranulation in syntaxin-11–deficient familial hemophagocytic lymphohistiocytosis 4 (FHL4) patients. *Blood*. 2007;110(6):1906-1915. doi:10.1182/blood-2007-02-074468

180. zur Stadt U, Rohr J, Seifert W, et al. Familial Hemophagocytic Lymphohistiocytosis Type 5 (FHL-5) Is Caused by Mutations in Munc18-2 and Impaired Binding to Syntaxin 11. *Am J Hum Genet.* 2009;85(4):482-492. doi:10.1016/j.ajhg.2009.09.005
181. Côte M, Ménager MM, Burgess A, et al. Munc18-2 deficiency causes familial hemophagocytic lymphohistiocytosis type 5 and impairs cytotoxic granule exocytosis in patient NK cells. *J Clin Invest.* 2009;119(12):3765-3773. doi:10.1172/JCI40732
182. Ménasché G, Pastural E, Feldmann J, et al. Mutations in RAB27A cause Griscelli syndrome associated with haemophagocytic syndrome. *Nat Genet.* 2000;25(2):173-176. doi:10.1038/76024
183. Haddad EK, Wu X, Hammer JA, Henkart PA. Defective Granule Exocytosis in Rab27a-Deficient Lymphocytes from Ashen Mice. *J Cell Biol.* 2001;152(4):835-842. doi:10.1083/jcb.152.4.835
184. Sepulveda FE, Debeurme F, Ménasché G, et al. Distinct severity of HLH in both human and murine mutants with complete loss of cytotoxic effector PRF1, RAB27A, and STX11. *Blood.* 2013;121(4):595-603. doi:10.1182/blood-2012-07-440339
185. Kaya Z, Ehl S, Albayrak M, et al. A novel single point mutation of the LYST gene in two siblings with different phenotypic features of Chediak Higashi syndrome. *Pediatr Blood Cancer.* 2011;56(7):1136-1139. doi:10.1002/pbc.22878
186. Certain S, Barrat F, Pastural E, et al. Protein truncation test of LYST reveals heterogenous mutations in patients with Chediak-Higashi syndrome. *Blood.* 2000;95(3):979-983. doi:10648412
187. Baetz K, Isaaz S, Griffiths GM. Loss of cytotoxic T lymphocyte function in Chediak-Higashi syndrome arises from a secretory defect that prevents lytic granule exocytosis. *J Immunol.* 1995;154(11):6122-6131. doi:7751653
188. Grossi C, Crist W, Abo T, Velardi A, Cooper M. Expression of the Chediak-Higashi lysosomal abnormality in human peripheral blood lymphocyte subpopulations. *Blood.* 1985;65(4):837-844. doi:10.1182/blood.V65.4.837.837
189. Gil-Krzewska A, Wood SM, Murakami Y, et al. Chediak-Higashi syndrome: Lysosomal trafficking regulator domains regulate exocytosis of lytic granules but not cytokine secretion by natural killer cells. *J Allergy Clin Immunol.* 2016;137(4):1165-1177. doi:10.1016/j.jaci.2015.08.039
190. Notarangelo LD. Primary immunodeficiencies. *J Allergy Clin Immunol.* 2010;125(2):S182-S194. doi:10.1016/j.jaci.2009.07.053
191. Cirillo E, Cancrini C, Azzari C, et al. Clinical, Immunological, and Molecular Features of Typical and Atypical Severe Combined Immunodeficiency: Report of the Italian Primary Immunodeficiency Network. *Front Immunol.* 2019;10. doi:10.3389/fimmu.2019.01908
192. Chinn IK, Shearer WT. Severe Combined Immunodeficiency Disorders. *Immunol Allergy Clin North Am.* 2015;35(4):671-694. doi:10.1016/j.iac.2015.07.002
193. McCusker C, Upton J, Warrington R. Primary immunodeficiency. *Allergy, Asthma Clin Immunol.* 2018;14(S2):61. doi:10.1186/s13223-018-0290-5
194. ALDRICH RA, STEINBERG AG, CAMPBELL DC. Pedigree demonstrating a sex-linked recessive condition characterized by draining ears, eczematoid dermatitis and bloody

- diarrhea. *Pediatrics*. 1954;13(2):133-139. <http://www.ncbi.nlm.nih.gov/pubmed/13133561>.
195. Massaad MJ, Ramesh N, Geha RS. Wiskott-Aldrich syndrome: a comprehensive review. *Ann N Y Acad Sci*. 2013;1285(1):26-43. doi:10.1111/nyas.12049
196. Buchbinder D, Nugent D, Fillipovich A. Wiskott–Aldrich syndrome: diagnosis, current management, and emerging treatments. *Appl Clin Genet*. April 2014;55. doi:10.2147/TACG.S58444
197. Dovas A, Cox D. Regulation of WASp by phosphorylation: Activation or other functions? *Commun Integr Biol*. 2010;3(2):101-105. doi:10.4161/cib.3.2.10759
198. Cotta-de-Almeida V, Dupr   L, Guipouy D, Vasconcelos Z. Signal Integration during T Lymphocyte Activation and Function: Lessons from the Wiskott   Aldrich Syndrome. *Front Immunol*. 2015;6. doi:10.3389/fimmu.2015.00047
199. Dupr   L, Aiuti A, Trifari S, et al. Wiskott-Aldrich Syndrome Protein Regulates Lipid Raft Dynamics during Immunological Synapse Formation. *Immunity*. 2002;17(2):157-166. doi:10.1016/S1074-7613(02)00360-6
200. Krzewski K, Chen X, Orange JS, Strominger JL. Formation of a WIP-, WASp-, actin-, and Myosin IIA-containing multiprotein complex in activated NK cells and its alteration by KIR inhibitory signaling. *J Cell Biol*. 2006;173(1):121-132. doi:10.1083/jcb.200509076
201. Orange JS, Ramesh N, Remold-O'Donnell E, et al. Wiskott-Aldrich syndrome protein is required for NK cell cytotoxicity and colocalizes with actin to NK cell-activating immunologic synapses. *Proc Natl Acad Sci U S A*. 2002;99(17):11351-11356. doi:10.1073/pnas.162376099
202. De Meester J, Calvez R, Valitutti S, Dupr   L. The Wiskott-Aldrich syndrome protein regulates CTL cytotoxicity and is required for efficient killing of B cell lymphoma targets. *J Leukoc Biol*. 2010;88(5):1031-1040. doi:10.1189/jlb.0410197
203. Gismondi A, Cifaldi L, Mazza C, et al. Impaired natural and CD16-mediated NK cell cytotoxicity in patients with WAS and XLT: ability of IL-2 to correct NK cell functional defect. *Blood*. 2004;104(2):436-443. doi:10.1182/blood-2003-07-2621
204. Orange JS, Roy-Ghanta S, Mace EM, et al. IL-2 induces a WAVE2-dependent pathway for actin reorganization that enables WASp-independent human NK cell function. *J Clin Invest*. 2011;121(4):1535-1548. doi:10.1172/JCI44862
205. Sasahara Y, Rachid R, Byrne MJ, et al. Mechanism of Recruitment of WASP to the Immunological Synapse and of Its Activation Following TCR Ligation. *Mol Cell*. 2002;10(6):1269-1281. doi:10.1016/S1097-2765(02)00728-1
206. Fried S, Reicher B, Pauker MH, et al. Triple-Color FRET Analysis Reveals Conformational Changes in the WIP-WASP Actin-Regulating Complex. *Sci Signal*. 2014;7(331):ra60-ra60. doi:10.1126/scisignal.2005198
207. Lanzi G, Moratto D, Vairo D, et al. A novel primary human immunodeficiency due to deficiency in the WASP-interacting protein WIP. *J Exp Med*. 2012;209(1):29-34. doi:10.1084/jem.20110896
208. Pfajfer L, Seidel MG, Houmadi R, et al. WIP deficiency severely affects human lymphocyte architecture during migration and synapse assembly. *Blood*. 2017;130(17):1949-1953. doi:10.1182/blood-2017-04-777383

209. Glaven JA, Whitehead IP, Nomanbhoy T, Kay R, Cerione RA. Lfc and Lsc Oncoproteins Represent Two New Guanine Nucleotide Exchange Factors for the Rho GTP-binding Protein. *J Biol Chem*. 1996;271(44):27374-27381. doi:10.1074/jbc.271.44.27374
210. Bouafia A, Lofek S, Bruneau J, et al. Loss of ARHGEF1 causes a human primary antibody deficiency. *J Clin Invest*. 2019;129(3):1047-1060. doi:10.1172/JCI120572
211. Toffali L, Montresor A, Mirenda M, Scita G, Laudanna C. SOS1, ARHGEF1, and DOCK2 rho-GEFs Mediate JAK-Dependent LFA-1 Activation by Chemokines. *J Immunol*. 2017;198(2):708-717. doi:10.4049/jimmunol.1600933
212. Kuhns DB, Fink DL, Choi U, et al. Cytoskeletal abnormalities and neutrophil dysfunction in WDR1 deficiency. *Blood*. 2016;128(17):2135-2143. doi:10.1182/blood-2016-03-706028
213. Pfajfer L, Mair NK, Jiménez-Heredia R, et al. Mutations affecting the actin regulator WD repeat-containing protein 1 lead to aberrant lymphoid immunity. *J Allergy Clin Immunol*. 2018;142(5):1589-1604.e11. doi:10.1016/j.jaci.2018.04.023
214. Standing ASI, Malinova D, Hong Y, et al. Autoinflammatory periodic fever, immunodeficiency, and thrombocytopenia (PFIT) caused by mutation in actin-regulatory gene WDR1. *J Exp Med*. 2017;214(1):59-71. doi:10.1084/jem.20161228
215. Uetrecht AC, Bear JE. Coronins: the return of the crown. *Trends Cell Biol*. 2006;16(8):421-426. doi:10.1016/j.tcb.2006.06.002
216. Punwani D, Pelz B, Yu J, et al. Coronin-1A: Immune Deficiency in Humans and Mice. *J Clin Immunol*. 2015;35(2):100-107. doi:10.1007/s10875-015-0130-z
217. Suzuki K, Nishihata J, Arai Y, et al. Molecular cloning of a novel actin-binding protein, p57, with a WD repeat and a leucine zipper motif. *FEBS Lett*. 1995;364(3):283-288. doi:10.1016/0014-5793(95)00393-N
218. Shioh LR, Paris K, Akana MC, Cyster JG, Sorensen RU, Puck JM. Severe combined immunodeficiency (SCID) and attention deficit hyperactivity disorder (ADHD) associated with a coronin-1A mutation and a chromosome 16p11.2 deletion. *Clin Immunol*. 2009;131(1):24-30. doi:10.1016/j.clim.2008.11.002
219. Stray-Pedersen A, Jouanguy E, Crequer A, et al. Compound Heterozygous CORO1A Mutations in Siblings with a Mucocutaneous-Immunodeficiency Syndrome of Epidermodysplasia Verruciformis-HPV, Molluscum Contagiosum and Granulomatous Tuberculoid Leprosy. *J Clin Immunol*. 2014;34(7):871-890. doi:10.1007/s10875-014-0074-8
220. Mori M, Mode R, Pieters J. From Phagocytes to Immune Defense: Roles for Coronin Proteins in Dictyostelium and Mammalian Immunity. *Front Cell Infect Microbiol*. 2018;8. doi:10.3389/fcimb.2018.00077
221. Foger N. Requirement for Coronin 1 in T Lymphocyte Trafficking and Cellular Homeostasis. *Science (80-)*. 2006;313(5788):839-842. doi:10.1126/science.1130563
222. Nal B. Coronin-1 expression in T lymphocytes: insights into protein function during T cell development and activation. *Int Immunol*. 2004;16(2):231-240. doi:10.1093/intimm/dxh022
223. Gandhi M, Achard V, Blanchoin L, Goode BL. Coronin Switches Roles in Actin Disassembly Depending on the Nucleotide State of Actin. *Mol Cell*. 2009;34(3):364-374.

doi:10.1016/j.molcel.2009.02.029

224. Mace EM, Orange JS. Lytic immune synapse function requires filamentous actin deconstruction by Coronin 1A. *Proc Natl Acad Sci U S A*. 2014;111(18):6708-6713. doi:10.1073/pnas.1314975111
225. Billadeau DD, Burkhardt JK. Regulation of Cytoskeletal Dynamics at the Immune Synapse: New Stars Join the Actin Troupe. *Traffic*. 2006;7(11):1451-1460. doi:10.1111/j.1600-0854.2006.00491.x
226. Makrogianneli K, Carlin LM, Keppler MD, et al. Integrating Receptor Signal Inputs That Influence Small Rho GTPase Activation Dynamics at the Immunological Synapse. *Mol Cell Biol*. 2009;29(11):2997-3006. doi:10.1128/MCB.01008-08
227. Cannon JL, Labno CM, Bosco G, et al. WASP Recruitment to the T Cell:APC Contact Site Occurs Independently of Cdc42 Activation. *Immunity*. 2001;15(2):249-259. doi:10.1016/S1074-7613(01)00178-9
228. Stowers L, Yelon D, Berg LJ, Chant J. Regulation of the polarization of T cells toward antigen-presenting cells by Ras-related GTPase CDC42. *Proc Natl Acad Sci*. 1995;92(11):5027-5031. doi:10.1073/pnas.92.11.5027
229. Gernez Y, de Jesus AA, Alsaleem H, et al. Severe autoinflammation in 4 patients with C-terminal variants in cell division control protein 42 homolog (CDC42) successfully treated with IL-1 β inhibition. *J Allergy Clin Immunol*. 2019;144(4):1122-1125.e6. doi:10.1016/j.jaci.2019.06.017
230. Aspenström P. The Intrinsic GDP/GTP Exchange Activities of Cdc42 and Rac1 Are Critical Determinants for Their Specific Effects on Mobilization of the Actin Filament System. *Cells*. 2019;8(7):759. doi:10.3390/cells8070759
231. Vielkind S, Gallagher-Gambarelli M, Gomez M, Hinton HJ, Cantrell DA. Integrin Regulation by RhoA in Thymocytes. *J Immunol*. 2005;175(1):350-357. doi:10.4049/jimmunol.175.1.350
232. Montresor A, Bolomini-Vittori M, Toffali L, Rossi B, Constantin G, Laudanna C. JAK tyrosine kinases promote hierarchical activation of Rho and Rap modules of integrin activation. *J Cell Biol*. 2013;203(6):1003-1019. doi:10.1083/jcb.201303067
233. Bros, Haas, Moll, Grabbe. RhoA as a Key Regulator of Innate and Adaptive Immunity. *Cells*. 2019;8(7):733. doi:10.3390/cells8070733
234. Kinashi T. Intracellular signalling controlling integrin activation in lymphocytes. *Nat Rev Immunol*. 2005;5(7):546-559. doi:10.1038/nri1646
235. Tybulewicz VLJ, Henderson RB. Rho family GTPases and their regulators in lymphocytes. *Nat Rev Immunol*. 2009;9(9):630-644. doi:10.1038/nri2606
236. Dorn T, Kuhn U, Bungartz G, et al. RhoH is important for positive thymocyte selection and T-cell receptor signaling. *Blood*. 2007;109(6):2346-2355. doi:10.1182/blood-2006-04-019034
237. Gu Y, Chae H-D, Siefring JE, Jasti AC, Hildeman DA, Williams DA. RhoH GTPase recruits and activates Zap70 required for T cell receptor signaling and thymocyte development. *Nat Immunol*. 2006;7(11):1182-1190. doi:10.1038/ni1396

238. Chae H-D, Siefiring JE, Hildeman DA, Gu Y, Williams DA. RhoH Regulates Subcellular Localization of ZAP-70 and Lck in T Cell Receptor Signaling. Unutmaz D, ed. *PLoS One*. 2010;5(11):e13970. doi:10.1371/journal.pone.0013970
239. Baker CM, Comrie WA, Hyun Y-M, et al. Opposing roles for RhoH GTPase during T-cell migration and activation. *Proc Natl Acad Sci*. 2012;109(26):10474-10479. doi:10.1073/pnas.1114214109
240. Crequer A, Troeger A, Patin E, et al. Human RHOH deficiency causes T cell defects and susceptibility to EV-HPV infections. *J Clin Invest*. 2012;122(9):3239-3247. doi:10.1172/JCI62949
241. Cote J-F. Identification of an evolutionarily conserved superfamily of DOCK180-related proteins with guanine nucleotide exchange activity. *J Cell Sci*. 2002;115(24):4901-4913. doi:10.1242/jcs.00219
242. Fukui Y, Hashimoto O, Sanui T, et al. Haematopoietic cell-specific CDM family protein DOCK2 is essential for lymphocyte migration. *Nature*. 2001;412(6849):826-831. doi:10.1038/35090591
243. Sanui T, Inayoshi A, Noda M, et al. DOCK2 regulates Rac activation and cytoskeletal reorganization through interaction with ELMO1. *Blood*. 2003;102(8):2948-2950. doi:10.1182/blood-2003-01-0173
244. Dobbs K, Domínguez Conde C, Zhang S-Y, et al. Inherited DOCK2 Deficiency in Patients with Early-Onset Invasive Infections. *N Engl J Med*. 2015;372(25):2409-2422. doi:10.1056/NEJMoa1413462
245. Harada Y, Tanaka Y, Terasawa M, et al. DOCK8 is a Cdc42 activator critical for interstitial dendritic cell migration during immune responses. *Blood*. 2012;119(19):4451-4461. doi:10.1182/blood-2012-01-407098
246. Ham H, Guerrier S, Kim J, et al. Deducator of Cytokinesis 8 Interacts with Talin and Wiskott-Aldrich Syndrome Protein To Regulate NK Cell Cytotoxicity. *J Immunol*. 2013;190(7):3661-3669. doi:10.4049/jimmunol.1202792
247. Zhang Q, Davis JC, Lamborn IT, et al. Combined Immunodeficiency Associated with DOCK8 Mutations. *N Engl J Med*. 2009;361(21):2046-2055. doi:10.1056/NEJMoa0905506
248. Engelhardt KR, McGhee S, Winkler S, et al. Large deletions and point mutations involving the dedicator of cytokinesis 8 (DOCK8) in the autosomal-recessive form of hyper-IgE syndrome. *J Allergy Clin Immunol*. 2009;124(6):1289-1302.e4. doi:10.1016/j.jaci.2009.10.038
249. Randall KL, Chan SS-Y, Ma CS, et al. DOCK8 deficiency impairs CD8 T cell survival and function in humans and mice. *J Exp Med*. 2011;208(11):2305-2320. doi:10.1084/jem.20110345
250. Mizesko MC, Banerjee PP, Monaco-Shawver L, et al. Defective actin accumulation impairs human natural killer cell function in patients with dedicator of cytokinesis 8 deficiency. *J Allergy Clin Immunol*. 2013;131(3):840-848. doi:10.1016/j.jaci.2012.12.1568
251. Geusau A, Mothes-Luksch N, Nahavandi H, et al. Identification of a Homozygous PSTPIP1 Mutation in a Patient With a PAPA-Like Syndrome Responding to Canakinumab Treatment. *JAMA Dermatology*. 2013;149(2):209. doi:10.1001/2013.jamadermatol.717

252. Janssen WJM, Grobarova V, Leleux J, et al. Proline-serine-threonine phosphatase interacting protein 1 (PSTPIP1) controls immune synapse stability in human T cells. *J Allergy Clin Immunol*. 2018;142(6):1947-1955. doi:10.1016/j.jaci.2018.01.030
253. Nesterovitch AB, Hoffman MD, Simon M, Petukhov PA, Tharp MD, Glant TT. Mutations in the PSTPIP1 gene and aberrant splicing variants in patients with pyoderma gangrenosum. *Clin Exp Dermatol*. 2011;36(8):889-895. doi:10.1111/j.1365-2230.2011.04137.x
254. Zeeli T, Padalon-Brauch G, Ellenbogen E, Gat A, Sarig O, Sprecher E. Pyoderma gangrenosum, acne and ulcerative colitis in a patient with a novel mutation in the PSTPIP1 gene. *Clin Exp Dermatol*. 2015;40(4):367-372. doi:10.1111/ced.12585
255. Côté J-F, Chung PL, Théberge J-F, et al. PSTPIP Is a Substrate of PTP-PEST and Serves as a Scaffold Guiding PTP-PEST Toward a Specific Dephosphorylation of WASP. *J Biol Chem*. 2002;277(4):2973-2986. doi:10.1074/jbc.M106428200
256. Abdollahpour H, Appaswamy G, Kotlarz D, et al. The phenotype of human STK4 deficiency. *Blood*. 2012;119(15):3450-3457. doi:10.1182/blood-2011-09-378158
257. Nehme NT, Schmid JP, Debeurme F, et al. MST1 mutations in autosomal recessive primary immunodeficiency characterized by defective naive T-cell survival. *Blood*. 2012;119(15):3458-3468. doi:10.1182/blood-2011-09-378364
258. Halacli SO, Ayvaz DC, Sun-Tan C, et al. STK4 (MST1) deficiency in two siblings with autoimmune cytopenias: A novel mutation. *Clin Immunol*. 2015;161(2):316-323. doi:10.1016/j.clim.2015.06.010
259. Cheng J, Jing Y, Kang D, et al. The Role of Mst1 in Lymphocyte Homeostasis and Function. *Front Immunol*. 2018;9. doi:10.3389/fimmu.2018.00149
260. Chen Y, Ci X, Gorentla B, et al. Differential Requirement of RasGRP1 for $\gamma\delta$ T Cell Development and Activation. *J Immunol*. 2012;189(1):61-71. doi:10.4049/jimmunol.1103272
261. Warnecke N, Poltorak M, Kowtharapu BS, et al. TCR-mediated Erk activation does not depend on Sos and Grb2 in peripheral human T cells. *EMBO Rep*. 2012;13(4):386-391. doi:10.1038/embor.2012.17
262. Salzer E, Cagdas D, Hons M, et al. RASGRP1 deficiency causes immunodeficiency with impaired cytoskeletal dynamics. *Nat Immunol*. 2016;17(12):1352-1360. doi:10.1038/ni.3575
263. Miralles F, Posern G, Zaromytidou A-I, Treisman R. Actin Dynamics Control SRF Activity by Regulation of Its Coactivator MAL. *Cell*. 2003;113(3):329-342. doi:10.1016/S0092-8674(03)00278-2
264. Vartiainen MK, Guettler S, Larijani B, Treisman R. Nuclear Actin Regulates Dynamic Subcellular Localization and Activity of the SRF Cofactor MAL. *Science (80-)*. 2007;316(5832):1749-1752. doi:10.1126/science.1141084
265. Record J, Malinova D, Zenner HL, et al. Immunodeficiency and severe susceptibility to bacterial infection associated with a loss-of-function homozygous mutation of MKL1. *Blood*. 2015;126(13):1527-1535. doi:10.1182/blood-2014-12-611012
266. Ben-Aissa K, Patino-Lopez G, Belkina N V., et al. Activation of Moesin, a Protein That Links Actin Cytoskeleton to the Plasma Membrane, Occurs by Phosphatidylinositol 4,5-bisphosphate (PIP2) Binding Sequentially to Two Sites and Releasing an Autoinhibitory Linker.

J Biol Chem. 2012;287(20):16311-16323. doi:10.1074/jbc.M111.304881

267. Satooka H, Nagakubo D, Sato T, Hirata T. The ERM Protein Moesin Regulates CD8 + Regulatory T Cell Homeostasis and Self-Tolerance. *J Immunol.* 2017;199(10):3418-3426. doi:10.4049/jimmunol.1700074

268. Lagresle-Peyrou C, Luce S, Ouchani F, et al. X-linked primary immunodeficiency associated with hemizygous mutations in the moesin (MSN) gene. *J Allergy Clin Immunol.* 2016;138(6):1681-1689.e8. doi:10.1016/j.jaci.2016.04.032

269. Delmonte OM, Biggs CM, Hayward A, et al. First Case of X-Linked Moesin Deficiency Identified After Newborn Screening for SCID. *J Clin Immunol.* 2017;37(4):336-338. doi:10.1007/s10875-017-0391-9

270. Sun CX, Magalhães MAO, Glogauer M. Rac1 and Rac2 differentially regulate actin free barbed end formation downstream of the fMLP receptor. *J Cell Biol.* 2007;179(2):239-245. doi:10.1083/jcb.200705122

271. Alkhairy OK, Rezaei N, Graham RR, et al. RAC2 loss-of-function mutation in 2 siblings with characteristics of common variable immunodeficiency. *J Allergy Clin Immunol.* 2015;135(5):1380-1384.e5. doi:10.1016/j.jaci.2014.10.039

272. Hsu AP, Donkó A, Arrington ME, et al. Dominant activating RAC2 mutation with lymphopenia, immunodeficiency, and cytoskeletal defects. *Blood.* 2019;133(18):1977-1988. doi:10.1182/blood-2018-11-886028

273. Ambruso DR, Knall C, Abell AN, et al. Human neutrophil immunodeficiency syndrome is associated with an inhibitory Rac2 mutation. *Proc Natl Acad Sci.* 2000;97(9):4654-4659. doi:10.1073/pnas.080074897

274. Murugesan S, Hong J, Yi J, et al. Formin-generated actoMyosin arcs propel T cell receptor microcluster movement at the immune synapse. *J Cell Biol.* 2016;215(3):383-399. doi:10.1083/jcb.201603080

275. Morin NA, Oakes PW, Hyun Y-M, et al. Nonmuscle Myosin heavy chain IIA mediates integrin LFA-1 de-adhesion during T lymphocyte migration. *J Exp Med.* 2008;205(1):195-205. doi:10.1084/jem.20071543

276. Jacobelli J, Chmura SA, Buxton DB, Davis MM, Krummel MF. A single class II Myosin modulates T cell motility and stopping, but not synapse formation. *Nat Immunol.* 2004;5(5):531-538. doi:10.1038/ni1065

277. Ilani T, Vasiliver-Shamis G, Vardhana S, Bretscher A, Dustin ML. T cell antigen receptor signaling and immunological synapse stability require Myosin IIA. *Nat Immunol.* 2009;10(5):531-539. doi:10.1038/ni.1723

278. Kumari S, Vardhana S, Cammer M, et al. T Lymphocyte Myosin IIA is Required for Maturation of the Immunological Synapse. *Front Immunol.* 2012;3. doi:10.3389/fimmu.2012.00230

279. Yu Y, Fay NC, Smoligovets AA, Wu H-J, Groves JT. Myosin IIA Modulates T Cell Receptor Transport and CasL Phosphorylation during Early Immunological Synapse Formation. Kanellopoulos J, ed. *PLoS One.* 2012;7(2):e30704. doi:10.1371/journal.pone.0030704

280. Colin-York H, Javanmardi Y, Skamrahl M, et al. Cytoskeletal Control of Antigen-Dependent T Cell Activation. *Cell Rep.* 2019;26(12):3369-3379.e5.

doi:10.1016/j.celrep.2019.02.074

281. Mace EM, Orange JS. Insights into primary immune deficiency from quantitative microscopy. *J Allergy Clin Immunol*. 2015;136(5):1150-1162. doi:10.1016/j.jaci.2015.03.049
282. Hoogeboom R, Natkanski EM, Nowosad CR, et al. Myosin IIa Promotes Antibody Responses by Regulating B Cell Activation, Acquisition of Antigen, and Proliferation. *Cell Rep*. 2018;23(8):2342-2353. doi:10.1016/j.celrep.2018.04.087
283. Seri M, Pecci A, Di Bari F, et al. MYH9-Related Disease. *Medicine (Baltimore)*. 2003;82(3):203-215. doi:10.1097/01.md.0000076006.64510.5c
284. Pecci A, Panza E, De Rocco D, et al. MYH9 related disease: four novel mutations of the tail domain of Myosin-9 correlating with a mild clinical phenotype. *Eur J Haematol*. 2010;84(4):291-297. doi:10.1111/j.1600-0609.2009.01398.x
285. Goley ED, Welch MD. The ARP2/3 complex: an actin nucleator comes of age. *Nat Rev Mol Cell Biol*. 2006;7(10):713-726. doi:10.1038/nrm2026
286. Padrick SB, Doolittle LK, Brautigam CA, King DS, Rosen MK. Arp2/3 complex is bound and activated by two WASP proteins. *Proc Natl Acad Sci U S A*. 2011;108(33):472-479. doi:10.1073/pnas.1100236108
287. Boczkowska M, Rebowski G, Kast DJ, Dominguez R. Structural analysis of the transitional state of Arp2/3 complex activation by two actin-bound WCAs. *Nat Commun*. 2014;5(1):3308. doi:10.1038/ncomms4308
288. Brigida I, Zoccolillo M, Cicalese MP, et al. T-cell defects in patients with ARPC1B germline mutations account for combined immunodeficiency. *Blood*. 2018;132(22):2362-2374. doi:10.1182/blood-2018-07-863431
289. Volpi S, Cicalese MP, Tuijnenburg P, et al. A combined immunodeficiency with severe infections, inflammation, and allergy caused by ARPC1B deficiency. *J Allergy Clin Immunol*. 2019;143(6):2296-2299. doi:10.1016/j.jaci.2019.02.003
290. Kuijpers TW, Tool ATJ, van der Bijl I, et al. Combined immunodeficiency with severe inflammation and allergy caused by ARPC1B deficiency. *J Allergy Clin Immunol*. 2017;140(1):273-277.e10. doi:10.1016/j.jaci.2016.09.061
291. Kopitar AN, Markelj G, Oražem M, et al. Flow Cytometric Determination of Actin Polymerization in Peripheral Blood Leukocytes Effectively Discriminate Patients With Homozygous Mutation in ARPC1B From Asymptomatic Carriers and Normal Controls. *Front Immunol*. 2019;10. doi:10.3389/fimmu.2019.01632
292. Randzavola LO, Strege K, Juzans M, et al. Loss of ARPC1B impairs cytotoxic T lymphocyte maintenance and cytolytic activity. *J Clin Invest*. November 2019. doi:10.1172/JCI129388
293. Hetrick B, Han MS, Helgeson LA, Nolen BJ. Small Molecules CK-666 and CK-869 Inhibit Actin-Related Protein 2/3 Complex by Blocking an Activating Conformational Change. *Chem Biol*. 2013;20(5):701-712. doi:10.1016/j.chembiol.2013.03.019
294. Gil-Krzewska A, Saeed MB, Oszmiana A, et al. An actin cytoskeletal barrier inhibits lytic granule release from natural killer cells in patients with Chediak-Higashi syndrome. *J Allergy Clin Immunol*. 2018;142(3):914-927.e6. doi:10.1016/j.jaci.2017.10.040

295. Albeanu DF, Soucy E, Sato TF, Meister M, Murthy VN. LED Arrays as Cost Effective and Efficient Light Sources for Widefield Microscopy. Wong ROL, ed. *PLoS One*. 2008;3(5):e2146. doi:10.1371/journal.pone.0002146
296. ROBERTSON JB, ZHANG Y, JOHNSON CH. Light-emitting diode flashlights as effective and inexpensive light sources for fluorescence microscopy. *J Microsc*. 2009;236(1):1-4. doi:10.1111/j.1365-2818.2009.03208.x
297. Thorn K. A quick guide to light microscopy in cell biology. *Mol Biol Cell*. 2016;27(2):219-222. doi:10.1091/mbc.E15-02-0088
298. Zernike F. Phase contrast, a new method for the microscopic observation of transparent objects. *Physica*. 1942;9(7):686-698. doi:10.1016/S0031-8914(42)80035-X
299. Nomarski G, Weill AR. Application à la métallographie des méthodes interférentielles à deux ondes polarisées. *Rev Métallurgie*. 1955;52(2):121-134. doi:10.1051/metal/195552020121
300. Coons AH, Creech HJ, Jones RN. Immunological Properties of an Antibody Containing a Fluorescent Group. *Exp Biol Med*. 1941;47(2):200-202. doi:10.3181/00379727-47-13084P
301. SHIMOMURA O, JOHNSON FH, SAIGA Y. Extraction, purification and properties of aequorin, a bioluminescent protein from the luminous hydromedusan, *Aequorea*. *J Cell Comp Physiol*. 1962;59:223-239. <http://www.ncbi.nlm.nih.gov/pubmed/13911999>.
302. Chalfie M, Tu Y, Euskirchen G, Ward W, Prasher D. Green fluorescent protein as a marker for gene expression. *Science* (80-). 1994;263(5148):802-805. doi:10.1126/science.8303295
303. Wang S, Hazelrigg T. Implications for bcd mRNA localization from spatial distribution of exu protein in *Drosophila* oogenesis. *Nature*. 1994;369(6479):400-403. doi:10.1038/369400a0
304. Heim R, Prasher DC, Tsien RY. Wavelength mutations and posttranslational autoxidation of green fluorescent protein. *Proc Natl Acad Sci*. 1994;91(26):12501-12504. doi:10.1073/pnas.91.26.12501
305. Matz M V., Fradkov AF, Labas YA, et al. Fluorescent proteins from nonbioluminescent Anthozoa species. *Nat Biotechnol*. 1999;17(10):969-973. doi:10.1038/13657
306. Tsien RY. New calcium indicators and buffers with high selectivity against magnesium and protons: design, synthesis, and properties of prototype structures. *Biochemistry*. 1980;19(11):2396-2404. doi:10.1021/bi00552a018
307. Forster T. Energiewanderung und Fluoreszenz. *Naturwissenschaften*. 1946;33(6):166-175. doi:10.1007/BF00585226
308. Stryer L, Haugland RP. Energy transfer: a spectroscopic ruler. *Proc Natl Acad Sci*. 1967;58(2):719-726. doi:10.1073/pnas.58.2.719
309. Clegg RM, Feddersen BA, Gratton E, Jovin TM. <title>Time-resolved imaging fluorescence microscopy</title>. In: Lakowicz JR, ed. ; 1992:448-460. doi:10.1117/12.58237
310. Curtis ASG. THE MECHANISM OF ADHESION OF CELLS TO GLASS: A Study by Interference Reflection Microscopy. *J Cell Biol*. 1964;20(2):199-215. doi:10.1083/jcb.20.2.199

311. Fish KN. Total Internal Reflection Fluorescence (TIRF) Microscopy. In: *Current Protocols in Cytometry*. Hoboken, NJ, USA: John Wiley & Sons, Inc.; 2009. doi:10.1002/0471142956.cy1218s50
312. Denk W, Strickler J, Webb W. Two-photon laser scanning fluorescence microscopy. *Science (80-)*. 1990;248(4951):73-76. doi:10.1126/science.2321027
313. Brakenhoff GJ, Blom P, Barends P. Confocal scanning light microscopy with high aperture immersion lenses. *J Microsc.* 1979;117(2):219-232. doi:10.1111/j.1365-2818.1979.tb01178.x
314. Pawley JB. *Handbook of Biological Confocal Microscopy*. Third edit. Madison, Wisconsin: Springer New York; 2006.
315. Hell SW, Wichmann J. Breaking the diffraction resolution limit by stimulated emission: stimulated-emission-depletion fluorescence microscopy. *Opt Lett.* 1994;19(11):780. doi:10.1364/OL.19.000780
316. Klar TA, Hell SW. Subdiffraction resolution in far-field fluorescence microscopy. *Opt Lett.* 1999;24(14):954. doi:10.1364/OL.24.000954
317. Panchuk-Voloshina N, Haugland RP, Bishop-Stewart J, et al. Alexa Dyes, a Series of New Fluorescent Dyes that Yield Exceptionally Bright, Photostable Conjugates. *J Histochem Cytochem.* 1999;47(9):1179-1188. doi:10.1177/002215549904700910
318. Hess ST, Girirajan TPK, Mason MD. Ultra-High Resolution Imaging by Fluorescence Photoactivation Localization Microscopy. *Biophys J.* 2006;91(11):4258-4272. doi:10.1529/biophysj.106.091116
319. Betzig E, Patterson GH, Sougrat R, et al. Imaging Intracellular Fluorescent Proteins at Nanometer Resolution. *Science (80-)*. 2006;313(5793):1642-1645. doi:10.1126/science.1127344
320. Rust MJ, Bates M, Zhuang X. Sub-diffraction-limit imaging by stochastic optical reconstruction microscopy (STORM). *Nat Methods.* 2006;3(10):793-796. doi:10.1038/nmeth929
321. Brenner S. The genetics of *Caenorhabditis elegans*. *Genetics.* 1974;77(1):71-94. <http://www.ncbi.nlm.nih.gov/pubmed/4366476>.
322. Nüsslein-Volhard C, Wieschaus E. Mutations affecting segment number and polarity in *Drosophila*. *Nature.* 1980;287(5785):795-801. doi:10.1038/287795a0
323. Bickle M. The beautiful cell: high-content screening in drug discovery. *Anal Bioanal Chem.* 2010;398(1):219-226. doi:10.1007/s00216-010-3788-3
324. Munoz DM, Cassiani PJ, Li L, et al. CRISPR Screens Provide a Comprehensive Assessment of Cancer Vulnerabilities but Generate False-Positive Hits for Highly Amplified Genomic Regions. *Cancer Discov.* 2016;6(8):900-913. doi:10.1158/2159-8290.CD-16-0178
325. Sun J, Katz S, Dutta B, Wang Z, Fraser IDC. Genome-wide siRNA screen of genes regulating the LPS-induced TNF- α response in human macrophages. *Sci Data.* 2017;4(1):170007. doi:10.1038/sdata.2017.7
326. Adelman CH, Wang T, Sabatini DM, Lander ES. Genome-Wide CRISPR/Cas9 Screening for Identification of Cancer Genes in Cell Lines. In: ; 2019:125-136.

doi:10.1007/978-1-4939-8967-6_10

327. Carlin LM, Evans R, Milewicz H, et al. A Targeted siRNA Screen Identifies Regulators of Cdc42 Activity at the Natural Killer Cell Immunological Synapse. *Sci Signal*. 2011;4(201):ra81-ra81. doi:10.1126/scisignal.2001729
328. Sharma S, Petsalaki E. Application of CRISPR-Cas9 Based Genome-Wide Screening Approaches to Study Cellular Signalling Mechanisms. *Int J Mol Sci*. 2018;19(4):933. doi:10.3390/ijms19040933
329. Simpson JC, Joggerst B, Laketa V, et al. Genome-wide RNAi screening identifies human proteins with a regulatory function in the early secretory pathway. *Nat Cell Biol*. 2012;14(7):764-774. doi:10.1038/ncb2510
330. Zhang X, Boutros M. A novel phenotypic dissimilarity method for image-based high-throughput screens. *BMC Bioinformatics*. 2013;14(1):336. doi:10.1186/1471-2105-14-336
331. Bray M-A, Singh S, Han H, et al. Cell Painting, a high-content image-based assay for morphological profiling using multiplexed fluorescent dyes. *Nat Protoc*. 2016;11(9):1757-1774. doi:10.1038/nprot.2016.105
332. Mattiazzi Usaj M, Styles EB, Verster AJ, Friesen H, Boone C, Andrews BJ. High-Content Screening for Quantitative Cell Biology. *Trends Cell Biol*. 2016;26(8):598-611. doi:10.1016/j.tcb.2016.03.008
333. Wu LS, Li J. High-Content Imaging Phenotypic Screen for Neurogenesis Using Primary Neural Progenitor Cells. In: ; 2018:101-113. doi:10.1007/978-1-4939-7847-2_8
334. Kepiro M, Varkuti BH, Davis RL. High Content, Phenotypic Assays and Screens for Compounds Modulating Cellular Processes in Primary Neurons. In: ; 2018:219-250. doi:10.1016/bs.mie.2018.09.021
335. Puls TJ, Tan X, Husain M, Whittington CF, Fishel ML, Voytik-Harbin SL. Development of a Novel 3D Tumor-tissue Invasion Model for High-throughput, High-content Phenotypic Drug Screening. *Sci Rep*. 2018;8(1):13039. doi:10.1038/s41598-018-31138-6
336. Lang P, Yeow K, Nichols A, Scheer A. Cellular imaging in drug discovery. *Nat Rev Drug Discov*. 2006;5(4):343-356. doi:10.1053/j.gastro.2006.06.028
337. Sieprath T, Corne T, Robijns J, Koopman WJH, de Vos WH. Cellular redox profiling using high-content microscopy. *J Vis Exp*. 2017;2017(123). doi:10.3791/55449
338. Szalai P, Engedal N. An Image-based Assay for High-throughput Analysis of Cell Proliferation and Cell Death of Adherent Cells. *BIO-PROTOCOL*. 2018;8(9). doi:10.21769/BioProtoc.2835
339. Massey AJ. A high content, high throughput cellular thermal stability assay for measuring drug-target engagement in living cells. Xu B, ed. *PLoS One*. 2018;13(4):e0195050. doi:10.1371/journal.pone.0195050
340. Bai SW, Herrera-Abreu MT, Rohn JL, et al. Identification and characterization of a set of conserved and new regulators of cytoskeletal organization, cell morphology and migration. *BMC Biol*. 2011;9. doi:10.1186/1741-7007-9-54
341. Chia N-Y, Chan Y-S, Feng B, et al. A genome-wide RNAi screen reveals determinants of human embryonic stem cell identity. *Nature*. 2010;468(7321):316-320.

doi:10.1038/nature09531

342. Vizeacoumar FJ, van Dyk N, S.Vizeacoumar F, et al. Integrating high-throughput genetic interaction mapping and high-content screening to explore yeast spindle morphogenesis. *J Cell Biol.* 2010;188(1):69-81. doi:10.1083/jcb.200909013
343. Billmann M, Horn T, Fischer B, Sandmann T, Huber W, Boutros M. A genetic interaction map of cell cycle regulators. Solomon MJ, ed. *Mol Biol Cell.* 2016;27(8):1397-1407. doi:10.1091/mbc.E15-07-0467
344. Heigwer F, Scheeder C, Miersch T, et al. Time-resolved mapping of genetic interactions to model rewiring of signaling pathways. *Elife.* 2018;7. doi:10.7554/eLife.40174
345. Fischer B, Sandmann T, Horn T, et al. A map of directional genetic interactions in a metazoan cell. *Elife.* 2015;4. doi:10.7554/eLife.05464
346. Huh W-K, Falvo J V., Gerke LC, et al. Global analysis of protein localization in budding yeast. *Nature.* 2003;425(6959):686-691. doi:10.1038/nature02026
347. Chong YT, Koh JLY, Friesen H, et al. Yeast Proteome Dynamics from Single Cell Imaging and Automated Analysis. *Cell.* 2015;161(6):1413-1424. doi:10.1016/j.cell.2015.04.051
348. Caldera M, Müller F, Kaltenbrunner I, et al. Mapping the perturbome network of cellular perturbations. *Nat Commun.* 2019;10(1):5140. doi:10.1038/s41467-019-13058-9
349. Rolland T, Taşan M, Charloreaux B, et al. A Proteome-Scale Map of the Human Interactome Network. *Cell.* 2014;159(5):1212-1226. doi:10.1016/j.cell.2014.10.050
350. Priestley RS, Cheung J, Murphy EJ, Ehebauer MT, Davis JB, Di Daniel E. A novel high-content imaging-based technique for measuring binding of Dickkopf-1 to low-density lipoprotein receptor-related protein 6. *J Pharmacol Toxicol Methods.* 2019;95(June 2018):47-55. doi:10.1016/j.vascn.2018.11.003
351. Schulte J, Sepp KJ, Wu C, Hong P, Littleton JT. High-Content Chemical and RNAi Screens for Suppressors of Neurotoxicity in a Huntington's Disease Model. Cookson MR, ed. *PLoS One.* 2011;6(8):e23841. doi:10.1371/journal.pone.0023841
352. Zahir T, Camacho R, Vitale R, et al. High-throughput time-resolved morphology screening in bacteria reveals phenotypic responses to antibiotics. *Commun Biol.* 2019;2(1):269. doi:10.1038/s42003-019-0480-9
353. Simm J, Klambauer G, Arany A, et al. Repurposing High-Throughput Image Assays Enables Biological Activity Prediction for Drug Discovery. *Cell Chem Biol.* 2018;25(5):611-618.e3. doi:10.1016/j.chembiol.2018.01.015
354. Pegoraro G, Misteli T. High-Throughput Imaging for the Discovery of Cellular Mechanisms of Disease. *Trends Genet.* 2017;33(9):604-615. doi:10.1016/j.tig.2017.06.005
355. Carpenter AE, Jones TR, Lamprecht MR, et al. CellProfiler: image analysis software for identifying and quantifying cell phenotypes. *Genome Biol.* 2006;7(10):R100. doi:10.1186/gb-2006-7-10-r100
356. Lamprecht MR, Sabatini DM, Carpenter AE. CellProfiler™: free, versatile software for automated biological image analysis. *Biotechniques.* 2007;42(1):71-75. doi:10.2144/000112257

357. Lau YS, Xu L, Gao Y, Han R. Automated muscle histopathology analysis using CellProfiler. *Skelet Muscle*. 2018;8(1):32. doi:10.1186/s13395-018-0178-6
358. McQuin C, Goodman A, Chernyshev V, et al. CellProfiler 3.0: Next-generation image processing for biology. Misteli T, ed. *PLoS Biol*. 2018;16(7):e2005970. doi:10.1371/journal.pbio.2005970
359. Pau G, Fuchs F, Sklyar O, Boutros M, Huber W. EBImage--an R package for image processing with applications to cellular phenotypes. *Bioinformatics*. 2010;26(7):979-981. doi:10.1093/bioinformatics/btq046
360. Breinig M, Klein FA, Huber W, Boutros M. A chemical-genetic interaction map of small molecules using high-throughput imaging in cancer cells. *Mol Syst Biol*. 2015;11(12):846. doi:10.15252/msb.20156400
361. Pampaloni F, Reynaud EG, Stelzer EHK. The third dimension bridges the gap between cell culture and live tissue. *Nat Rev Mol Cell Biol*. 2007;8(10):839-845. doi:10.1038/nrm2236
362. Haycock JW. 3D Cell Culture: A Review of Current Approaches and Techniques. In: ; 2011:1-15. doi:10.1007/978-1-60761-984-0_1
363. Joshi P, Lee M-Y. High Content Imaging (HCI) on Miniaturized Three-Dimensional (3D) Cell Cultures. *Biosensors*. 2015;5(4):768-790. doi:10.3390/bios5040768
364. Caicedo JC, Cooper S, Heigwer F, et al. Data-analysis strategies for image-based cell profiling. *Nat Methods*. 2017;14(9):849-863. doi:10.1038/nmeth.4397
365. Boutros M, Heigwer F, Laufer C. Microscopy-Based High-Content Screening. *Cell*. 2015;163(6):1314-1325. doi:10.1016/j.cell.2015.11.007
366. Smith K, Li Y, Piccinini F, et al. CIDRE: an illumination-correction method for optical microscopy. *Nat Methods*. 2015;12(5):404-406. doi:10.1038/nmeth.3323
367. SINGH S, BRAY M-A, JONES TR, CARPENTER AE. Pipeline for illumination correction of images for high-throughput microscopy. *J Microsc*. 2014;256(3):231-236. doi:10.1111/jmi.12178
368. Bray M-A, Carpenter A, Imaging Platform BI of M and H. *Advanced Assay Development Guidelines for Image-Based High Content Screening and Analysis*.; 2004. <http://www.ncbi.nlm.nih.gov/pubmed/23469374>.
369. Yan Q, Chen J, De Strycker L. An Outlier Detection Method Based on Mahalanobis Distance for Source Localization. *Sensors*. 2018;18(7):2186. doi:10.3390/s18072186
370. Woehrmann MH, Bray WM, Durbin JK, et al. Large-scale cytological profiling for functional analysis of bioactive compounds. *Mol Biosyst*. 2013;9(11):2604. doi:10.1039/c3mb70245f
371. Bakal C, Aach J, Church G, Perrimon N. Quantitative Morphological Signatures Define Local Signaling Networks Regulating Cell Morphology. *Science (80-)*. 2007;316(5832):1753-1756. doi:10.1126/science.1140324
372. Rohban MH, Singh S, Wu X, et al. Systematic morphological profiling of human gene and allele function via Cell Painting. *Elife*. 2017;6. doi:10.7554/eLife.24060
373. Abdi H, Williams LJ. Principal component analysis. *Wiley Interdiscip Rev Comput Stat*. 2010;2(4):433-459. doi:10.1002/wics.101

374. Jolliffe IT, Cadima J. Principal component analysis: a review and recent developments. *Philos Trans R Soc A Math Phys Eng Sci.* 2016;374(2065):20150202. doi:10.1098/rsta.2015.0202
375. Tenenbaum JB. A Global Geometric Framework for Nonlinear Dimensionality Reduction. *Science (80-).* 2000;290(5500):2319-2323. doi:10.1126/science.290.5500.2319
376. Coifman RR, Lafon S, Lee AB, et al. Geometric diffusions as a tool for harmonic analysis and structure definition of data: Diffusion maps. *Proc Natl Acad Sci.* 2005;102(21):7426-7431. doi:10.1073/pnas.0500334102
377. Maaten L van der. Visualizing data using t-SNE. *J.* 2008;9:2579-2605.
378. van Unen V, Li N, Molendijk I, et al. Mass Cytometry of the Human Mucosal Immune System Identifies Tissue- and Disease-Associated Immune Subsets. *Immunity.* 2016;44(5):1227-1239. doi:10.1016/j.immuni.2016.04.014
379. Becht E, McInnes L, Healy J, et al. Dimensionality reduction for visualizing single-cell data using UMAP. *Nat Biotechnol.* 2019;37(1):38-44. doi:10.1038/nbt.4314
380. McInnes L, Healy J, Saul N, Großberger L. UMAP: Uniform Manifold Approximation and Projection. *J Open Source Softw.* 2018;3(29):861. doi:10.21105/joss.00861
381. Holmström L. Nonlinear Dimensionality Reduction by John A. Lee, Michel Verleysen. *Int Stat Rev.* 2008;76(2):308-309. doi:10.1111/j.1751-5823.2008.00054_10.x
382. Zhang Z. A gentle introduction to artificial neural networks. *Ann Transl Med.* 2016;4(19):370-370. doi:10.21037/atm.2016.06.20
383. Cheerla A, Gevaert O. Deep learning with multimodal representation for pancancer prognosis prediction. *Bioinformatics.* 2019;35(14):i446-i454. doi:10.1093/bioinformatics/btz342
384. Kraus OZ, Grys BT, Ba J, et al. Automated analysis of high-content microscopy data with deep learning. *Mol Syst Biol.* 2017;13(4):924. doi:10.15252/msb.20177551
385. Grys BT, Lo DS, Sahin N, et al. Machine learning and computer vision approaches for phenotypic profiling. *J Cell Biol.* 2017;216(1):65-71. doi:10.1083/jcb.201610026
386. Roosing S, Hofree M, Kim S, et al. Functional genome-wide siRNA screen identifies KIAA0586 as mutated in Joubert syndrome. *Elife.* 2015;4. doi:10.7554/eLife.06602
387. Cleret de Langavant L, Bayen E, Yaffe K. Unsupervised Machine Learning to Identify High Likelihood of Dementia in Population-Based Surveys: Development and Validation Study. *J Med Internet Res.* 2018;20(7):e10493. doi:10.2196/10493
388. Lopez C, Tucker S, Salameh T, Tucker C. An unsupervised machine learning method for discovering patient clusters based on genetic signatures. *J Biomed Inform.* 2018;85:30-39. doi:10.1016/j.jbi.2018.07.004
389. Lim S, Tucker CS, Kumara S. An unsupervised machine learning model for discovering latent infectious diseases using social media data. *J Biomed Inform.* 2017;66:82-94. doi:10.1016/j.jbi.2016.12.007
390. Lipton ZC, Elkan C, Naryanaswamy B. Optimal Thresholding of Classifiers to Maximize F1 Measure. In: ; 2014:225-239. doi:10.1007/978-3-662-44851-9_15

391. Kozak K. Data Mining Techniques in High Content Screening: A Survey. *J Comput Sci Syst Biol.* 2009;02(04). doi:10.4172/jcsb.1000035
392. N. A, C. S, Che T. Data Analysis Approaches in High Throughput Screening. In: *Drug Discovery.* InTech; 2013. doi:10.5772/52508
393. Singh S, Carpenter AE, Genovesio A. Increasing the Content of High-Content Screening. *J Biomol Screen.* 2014;19(5):640-650. doi:10.1177/1087057114528537
394. Poznansky MC, Olszak IT, Foxall R, Evans RH, Luster AD, Scadden DT. Active movement of T cells away from a chemokine. *Nat Med.* 2000;6(5):543-548. doi:10.1038/75022
395. Ojo EO, Sharma AA, Liu R, et al. Membrane bound IL-21 based NK cell feeder cells drive robust expansion and metabolic activation of NK cells. *Sci Rep.* 2019;9(1):14916. doi:10.1038/s41598-019-51287-6
396. Bae DS, Lee JK. Development of NK cell expansion methods using feeder cells from human myelogenous leukemia cell line. *Blood Res.* 2014;49(3):154. doi:10.5045/br.2014.49.3.154
397. Andersen MH, Schrama D, thor Straten P, Becker JC. Cytotoxic T Cells. *J Invest Dermatol.* 2006;126(1):32-41. doi:10.1038/sj.jid.5700001
398. Chávez-Galán L, Arenas-Del Angel MC, Zenteno E, Chávez R, Lascurain R. Cell Death Mechanisms Induced by Cytotoxic Lymphocytes. *Cell Mol Immunol.* 2009;6(1):15-25. doi:10.1038/cmi.2009.3
399. Sermer D, Brentjens R. CAR T-cell therapy: Full speed ahead. *Hematol Oncol.* 2019;37(S1):95-100. doi:10.1002/hon.2591
400. Li D, Li X, Zhou W-L, et al. Genetically engineered T cells for cancer immunotherapy. *Signal Transduct Target Ther.* 2019;4(1):35. doi:10.1038/s41392-019-0070-9
401. Caicedo JC, McQuin C, Goodman A, Singh S, Carpenter AE. Weakly Supervised Learning of Single-Cell Feature Embeddings. In: *2018 IEEE/CVF Conference on Computer Vision and Pattern Recognition.* IEEE; 2018:9309-9318. doi:10.1109/CVPR.2018.00970
402. Roy NH, Burkhardt JK. The actin cytoskeleton: A mechanical intermediate for signal integration at the immunological synapse. *Front Cell Dev Biol.* 2018;6(SEP):1-7. doi:10.3389/fcell.2018.00116
403. Ritter AT, Kapnick SM, Murugesan S, Schwartzberg PL, Griffiths GM, Lippincott-Schwartz J. Cortical actin recovery at the immunological synapse leads to termination of lytic granule secretion in cytotoxic T lymphocytes. *Proc Natl Acad Sci.* 2017;114(32):E6585-E6594. doi:10.1073/pnas.1710751114
404. Tsun A, Qureshi I, Stinchcombe JC, et al. Centrosome docking at the immunological synapse is controlled by Lck signaling. *J Cell Biol.* 2011;192(4):663-674. doi:10.1083/jcb.201008140
405. Barcia C, Thomas CE, Curtin JF, et al. In vivo mature immunological synapses forming SMACs mediate clearance of virally infected astrocytes from the brain. *J Exp Med.* 2006;203(9):2095-2107. doi:10.1084/jem.20060420
406. Ilatovskaya D V, Chubinskiy-Nadezhdin V, Pavlov TS, et al. Arp2/3 complex inhibitors adversely affect actin cytoskeleton remodeling in the cultured murine kidney collecting duct M-

- 1 cells. *Cell Tissue Res.* 2013;354(3):783-792. doi:10.1007/s00441-013-1710-y
407. Sato S, Rancourt A, Sato Y, Satoh MS. Single-cell lineage tracking analysis reveals that an established cell line comprises putative cancer stem cells and their heterogeneous progeny. *Sci Rep.* 2016;6(1):23328. doi:10.1038/srep23328
408. Somech R, Lev A, Lee YN, et al. Disruption of Thrombocyte and T Lymphocyte Development by a Mutation in ARPC1B. *J Immunol.* 2017;199(12):4036-4045. doi:10.4049/jimmunol.1700460
409. Shcherbina A, Rosen FS, Remold-O'Donnell E. WASP levels in platelets and lymphocytes of wiskott-aldrich syndrome patients correlate with cell dysfunction. *J Immunol.* 1999;163(11):6314-6320. doi:10570326
410. Spicer JA, Miller CK, O'Connor PD, et al. Benzenesulphonamide inhibitors of the cytolytic protein perforin. *Bioorg Med Chem Lett.* 2017;27(4):1050-1054. doi:10.1016/j.bmcl.2016.12.057
411. Finetti F, Baldari CT. The immunological synapse as a pharmacological target. *Pharmacol Res.* 2018;134:118-133. doi:10.1016/j.phrs.2018.06.009
412. Adams AB, Ford ML, Larsen CP. Costimulation Blockade in Autoimmunity and Transplantation: The CD28 Pathway. *J Immunol.* 2016;197(6):2045-2050. doi:10.4049/jimmunol.1601135
413. Hsu C-J, Hsieh W-T, Waldman A, et al. Ligand Mobility Modulates Immunological Synapse Formation and T Cell Activation. Gay N, ed. *PLoS One.* 2012;7(2):e32398. doi:10.1371/journal.pone.0032398
414. Beghin A, Kechkar A, Butler C, et al. Localization-based super-resolution imaging meets high-content screening. *Nat Methods.* 2017;14(12):1184-1190. doi:10.1038/nmeth.4486

Annexes

I contributed to the Rey-Barroso et al. paper by performing the immune phenotyping of JY cells for collagen and fibronectin (supplementary figure 1), as well as well as supplementary figure 4, in which the effect of extracellular matrix on the cells' ability to cluster was assessed.

Generating supplementary figure 4 was my first exposure to microscopy in a 96 well plate instead of slides or chambers.

However, imaging 96 wells for the course of 7 hours was a tedious process, despite being able to “save” a specific location in the well to re-image at a later point. By doing this experiment I was made aware of the importance of automation when acquiring images from a large number of wells, whether it be for fixed or live microscopy assays.

Discussions with Javier also exposed me to the different inhibitors of the actin/Myosin components, which was a basis for the drug screen performed during my PhD.

SCIENTIFIC REPORTS

OPEN

Switching between individual and collective motility in B lymphocytes is controlled by cell-matrix adhesion and inter-cellular interactions

Received: 12 July 2017
Accepted: 26 March 2018
Published online: 11 April 2018

Javier Rey-Barroso^{1,2,3}, Daniel S. Calovi⁴, Maud Combe⁴, Yolla German^{1,2,3}, Mathieu Moreau⁴, Astrid Canivet^{1,2,3}, Xiaobo Wang⁵, Clément Sire⁶, Guy Theraulaz⁴ & Loïc Dupré^{1,2,3}

Lymphocytes alternate between phases of individual migration across tissues and phases of clustering during activation and function. The range of lymphocyte motility behaviors and the identity of the factors that govern them remain elusive. To explore this point, we here collected unprecedented statistics pertaining to cell displacements, cell:matrix and cell:cell interactions using a model B cell line as well as primary human B lymphocytes. At low cell density, individual B lymphocytes displayed a high heterogeneity in their speed and diffusivity. Beyond this intrinsic variability, B lymphocytes adapted their motility to the composition of extra-cellular matrix, adopting slow persistent walks over collagen IV and quick Brownian walks over fibronectin. At high cell density, collagen IV favored the self-assembly of B lymphocytes into clusters endowed with collective coordination, while fibronectin stimulated individual motility. We show that this behavioral plasticity is controlled by actomyosin dependent adhesive and Arp2/3-dependent protrusive actin pools, respectively. Our study reveals the adaptive nature of B lymphocyte motility and group dynamics, which are shaped by an interplay between and cell:matrix and cell:cell interactions.

Lymphocytes represent a unique model to study cell motility because they may adopt a vast array of behaviors. These immune cells patrol the organism as isolated individuals endowed with high motility properties favoring the search for pathogens or pathogen-derived determinants¹. Within tissues, lymphocytes can organize into swarms and clusters to sustain specific steps of activation and function²⁻³. Group organization has also been reported to condition tissue residency of memory lymphocyte populations^{6,7}. Furthermore, our recent *in vitro* observations have revealed that the assembly of B and T lymphocytes into clusters confers collective properties leading to distinct chemotactic prowess^{7,8}. Understanding the parameters that govern the transition from individual to group behaviors in lymphocytes would provide insight into the mechanisms that determine collective cell behaviors common to many cellular systems. A key question is to disentangle the relative contribution of cell intrinsic versus extrinsic factors in the emergence of collective cell behaviors. To tackle this question, we here reasoned that the characterization of individual cell motility properties and encounter dynamics would explain the emergence of collective organization.

¹INSERM, UMR1043, Centre de Physiopathologie de Toulouse Purpan, Toulouse, France. ²Université de Toulouse - Paul Sabatier, Toulouse, France. ³CNRS, UMR5282, Toulouse, France. ⁴Centre de Recherches sur la Cognition Animale (CRCA), Centre de Biologie Intégrative (CBI), Centre National de la Recherche Scientifique (CNRS) & Université de Toulouse - Paul Sabatier, Toulouse, France. ⁵Laboratoire de Biologie Cellulaire et Moléculaire du Contrôle de la Prolifération (LBCMCP), Centre de Biologie Intégrative (CBI), Centre National de la Recherche Scientifique (CNRS) & Université de Toulouse - Paul Sabatier, Toulouse, France. ⁶Laboratoire de Physique Théorique - IRSAMC, Centre National de la Recherche Scientifique (CNRS) & Université de Toulouse - Paul Sabatier, Toulouse, France. Clément Sire, Guy Theraulaz and Loïc Dupré contributed equally to this work. Correspondence and requests for materials should be addressed to L.D. (email: loic.dupre@inserm.fr)

As individual cells, lymphocytes face the challenge of patrolling large tissue areas, while scanning locally to discriminate between cells presenting different antigenic determinants⁹. Lymphocyte migrate as amoeboid cells with patterns characterized as a Brownian random walk¹⁰, a persistent random walk^{11,12} or a Lévy walk¹³. While both walking behaviors might accommodate local search and tissue diffusion, it is not yet elucidated which parameters might govern their onset¹⁴. Environmental factors such as extra-cellular matrix (ECM) components affect the motility behavior of lymphocytes¹⁵. Indeed, lymphocytes can adopt walking versus sliding crawling modes depending on substrate attachment^{16,17}. A recent study revealed the presence of “tissue hotspots” that locally influence cell motility properties to favor local search¹⁸. Furthermore, spatial and temporal changes in ECM composition have been demonstrated to control processes such as lymphocyte recruitment, survival and differentiation^{19,20}. Altered expression of fibronectin and collagens I and IV in multiple myeloma is associated to progressive accumulation of malignant lymphocytes in the bone marrow at the different stages of disease progression²¹.

The aim of the present study is to characterize the range of B lymphocyte motility patterns at the single cell level and to decipher which interactions and behavioral mechanisms are involved in the emergence of coordinated groups. Using a well-controlled *in vitro* experimental framework and a dedicated tracking algorithm, we produce unprecedented statistics on B lymphocyte motility properties that highlight both individual heterogeneity and flocking dynamics. Our study reveals that B lymphocyte populations are composed of individuals with distinct diffusion properties that are modulated by interactions with the extracellular matrix. Fibronectin favors B lymphocyte adhesion and increases the proportion of individual cells with high-speed characteristics and chemotactic ability, thereby favoring isolated patrolling. In contrast, reduced adhesion over collagen IV favors group assembly and flocking activity that translate into collective chemotaxis. This study also highlights that actin cytoskeleton remodeling is a key integrator of B lymphocyte adaptive motility properties. Indeed, we identify distinct actin modules that coordinate adhesion to the matrix and protrusive activity involved in cell displacement and encounters with neighbors. Together, our study identifies external cues and intrinsic pathways that explain the wide range of B lymphocyte motility behaviors and control the shift between single versus collective B lymphocyte dynamics.

Results

B lymphocytes adapt their adhesion, protrusive activity and motility behavior to matrices. To investigate the influence of cell-matrix interaction on B lymphocyte motility, the human JY B cell line was used as a model system and deposited at low cell density on non-confined 2D surfaces coated with either collagen IV, a main component of the basement membrane with the ability of self-assembly into networks²² or fibronectin, a stromal matrix fibrillar component²³. These ECM components were chosen for their *in vivo* relevance and distinct effects in pathological processes such as wound healing in the spinal cord²⁰ and multiple myeloma progression in the bone marrow²¹. The JY cells were checked for the expression of the alpha chains of the integrins known to recognize collagen IV (CD49a, CD49b) and fibronectin (CD49d). Notably, JY cells expressed homogeneous integrin levels, which were comparable to those of primary B cells from the peripheral blood of 3 donors (Supplementary Figure S1). In order to record simultaneously the dynamics of cell adhesion and protrusive activity over the two matrices, we devised a combinatorial approach including interference reflection microscopy (IRM), total internal reflection fluorescence (TIRF) imaging of actin dynamics at the contact with the matrix, and wide-field illumination to monitor whole-cell actin remodeling (Supplementary Figure S2). TIRF imaging of LifeAct-GFP (purple) reveals a dense and dynamical actin network that co-localized with the dark areas on parallel IRM snapshots, confirming that it corresponds to the matrix contact area (Supplementary Figure S2). On the other hand, wide-field recording of LifeAct-GFP (green) shows actin enrichment at the cell cortex and within protrusions, which are emitted above the TIRF plane. This combinatorial approach therefore suggests a segregation of the actin cytoskeleton into an adhesive and a protrusive module. This approach indicates that B lymphocytes engage in higher attachment with fibronectin than collagen IV, while they emit various protrusions over both matrices (Fig. 1A). Cell attachment was quantified as a ratio between the TIRF area (adhesive actin) and the cell contour (protrusive actin) (Fig. 1B). This analysis reveals that collagen IV and fibronectin promote very distinct cell attachment, as assessed by the adhesive area. These distinct behaviors are also observed in peripheral blood primary B cells (Supplementary Figure S3A,B).

We then asked how matrix composition would affect B lymphocyte protrusive activity. For that purpose LifeAct-GFP expressing cells were imaged over time as they interacted with collagen IV or fibronectin (Supplementary Video S1) and their shape volatility (Fig. 1C), defined as the standard deviation of the aspect ratio changes over consecutive frames²⁴ was measured. This analysis reveals that cells over fibronectin remodel their shape more dynamically than over collagen IV. We then assessed whether the adhesive and protrusive activities of B lymphocytes over fibronectin and collagen IV would be translated into distinct motility behaviors. For that purpose, the motility of individual B lymphocytes was recorded at high temporal resolution (5-sec time-lapse) and over prolonged time periods (up to 12 h) using bright-field illumination to avoid phototoxicity. A dedicated algorithm based on local light contrast changes around the cell perimeter was designed to automatically recognize and track hundreds of cells on different video-recordings yielding robust motility statistics (see Methods). B lymphocytes display distinct motility behaviors over the two matrices (Supplementary Video S1). First, the speed (indicated by the color code along the trajectories) of B lymphocytes is relatively low over collagen IV (0 to 10 $\mu\text{m min}^{-1}$ range for most of the cells), while it alternates between slow and high values for most of the cells over fibronectin (0 to 20 $\mu\text{m min}^{-1}$ range) (Fig. 1D). Such values are in agreement with the velocities measured for primary lymphocytes *in vitro* and *in vivo*^{13,14,24,25}. Second, analysis of 1-h displacements (Fig. 1E) shows a further distance covered when B lymphocytes were deposited on fibronectin, as compared to collagen IV. Furthermore, analysis of mean square displacement (MSD) over time (Fig. 1F) shows that for both matrices the diffusion exponent is close to 1 indicating that independently from matrix composition, B lymphocytes move as normal

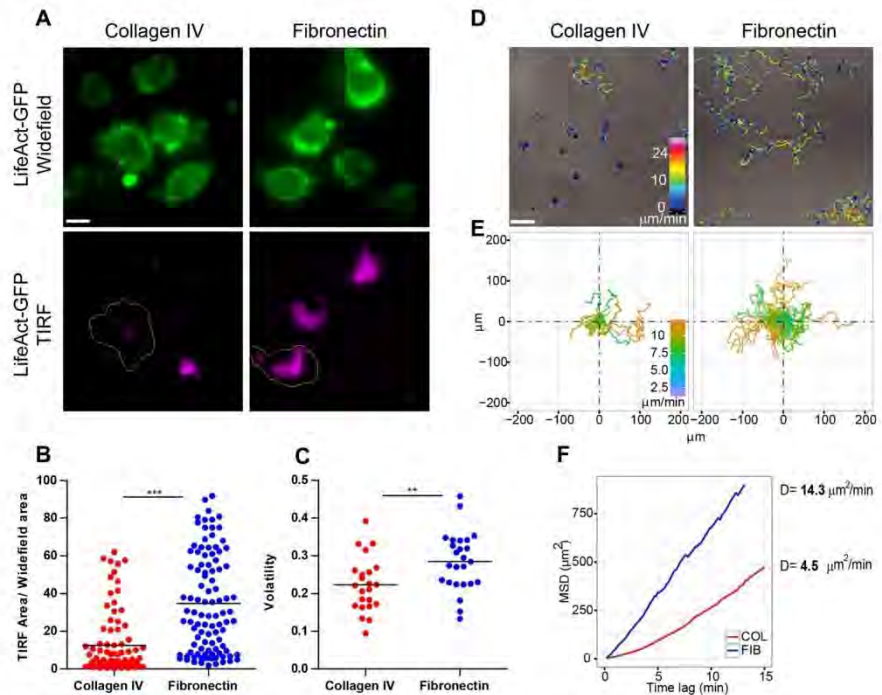


Figure 1. Matrix interaction defines individual motility of B lymphocytes. (A) JY cells were seeded at low density (40 cells mm^{-2}) over $1.5 \mu\text{g ml}^{-1}$ collagen IV or $10 \mu\text{g ml}^{-1}$ fibronectin and imaged after 2 h with combined widefield and TIRF illumination to reveal LifeAct-GFP, respectively throughout the cell body and at the cell/matrix interface. Scale bar, $10 \mu\text{m}$. (B) The proportion of the surface of LifeAct-GFP detected in the TIRF versus widefield images was measured for each cell (collagen IV, 87 cells; fibronectin, 101 cells; data pooled from 3 independent experiments). Bars show mean values. $***p < 0.001$, Student-t test. (C) Cell shape volatility represents the standard deviation of each cell aspect ratio changes over consecutive frames (track length, 20 min; time interval, 1 min) over collagen IV and fibronectin (respectively, 23 and 25 cells; data pooled from 3 independent experiments). Bars show mean values. $*p < 0.01$, Student-t test. (D) JY cells were recorded after 2 h of seeding for 12 h at $12 \text{ frames min}^{-1}$. Images show representative 1-h tracks with color-coded speed (displacement over 1-min intervals). Scale bar, $100 \mu\text{m}$. (E) One-hour tracks of 40 cells per condition were normalized to their x,y starting location and color-coded for their speed. (F) To quantify diffusion properties, the mean square displacement was plotted as a function of time interval (1-min increment). Data stem from 318 cell tracks on collagen IV and 1700 cell tracks on fibronectin. Diffusion coefficient D was calculated as the slope of the curve. See also Supplementary Figures S1 and S2 and Video S1.

diffusers. However, B lymphocytes adopt distinct diffusive characteristics over the two matrices since they move with a diffusion coefficient of $4.5 \mu\text{m}^2 \text{ min}^{-1}$ over collagen IV and of $14.3 \mu\text{m}^2 \text{ min}^{-1}$ over fibronectin. Notably, the higher cell motility over fibronectin as compared to collagen IV also applies to primary B cells (Supplementary Figure S3C). These data highlight that B lymphocytes adapt their motile behavior to matrix composition by modulating both their actin-rich adhesive surface and cell shape dynamics.

B lymphocyte motility at the population and individual cell scales. To further investigate which motility parameters might explain the distinct diffusive characteristics of B lymphocytes over the 2 model matrices, we measured, for each cell, the mean instantaneous speed (time resolution of 5 sec) and the mean displacement over 5-min periods. Our analysis reveals that the distribution of the mean instantaneous speeds of individual B lymphocytes is very similar over the 2 matrices (Fig. 2A), while the average displacement of the cells is three times higher over fibronectin than collagen IV (Fig. 2B). These results suggest that the higher diffusive property of B lymphocytes on fibronectin is not linked to a distinct local scanning activity, but to the ability to translate local movements into more effective exploratory cell displacements. The average displacement over both matrices is distributed over a wide range of values. This might result from a variable behavior of individual cells over time or from stable but heterogeneous properties at the individual cell level. To address this point, the evolution of the average displacement was followed for individual cells over 1 h. This analysis reveals that B lymphocyte motility is characterized by numerous acceleration/deceleration cycles over both matrices and that

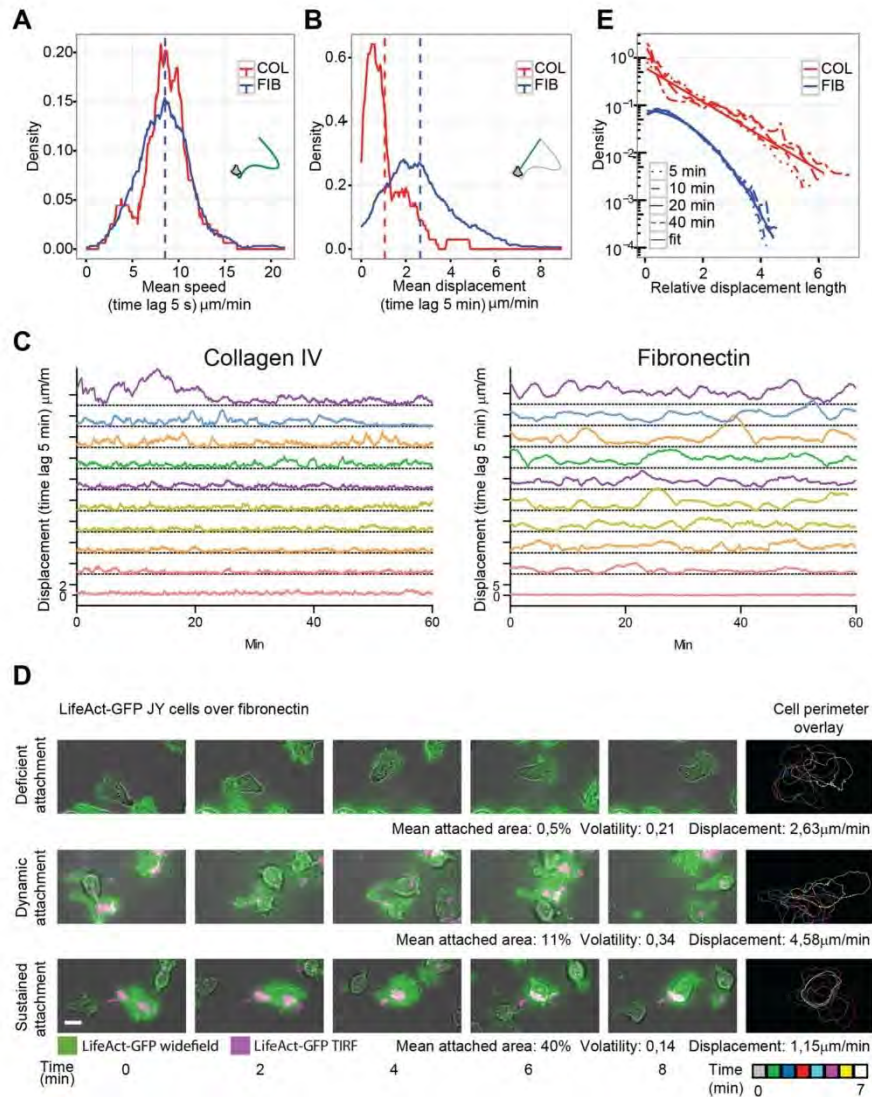


Figure 2. B lymphocytes adopt distinct walking behaviors depending on matrix composition. (A) Mean speed of JY cells migrating for at least 1 h over collagen IV or fibronectin was calculated as full accumulated distance (tracks with 5-sec time resolution) divided by track time length (collagen IV, 90 cells; fibronectin, 330 cells; data from 10 experiments). Dashed bars represent mean values. (B) Mean displacement from the same cell tracks was calculated as the mean of euclidean distances over 5-min time lags. Dashed bars represent mean values. (C) Time evolution of 5-min cell displacements for 10 representative JY cell tracks over each matrix. (D) Representative lifeact-GFP-expressing JY cells migrating over fibronectin and imaged for 10 min with a combination of brightfield, widefield and TIRF modes. Panels to the right represent a color-coded overlay of cell shape and position over 2-min intervals. Mean attached area, volatility and displacement were calculated as described above. Scale bar, 10 μm . (E) Cell displacements over collagen IV or fibronectin were computed using a time lag of 5, 10, 20 and 40 min and normalized to their mean length. Data stem from 63 cell tracks on collagen IV and 229 cell tracks on fibronectin. For readability, the fibronectin curve was shifted downwards by a factor 8. See also Supplementary Video S2.

individual cells undergo these speed variations within a characteristic speed range (Fig. 2C). We then sought to explore whether specific morphological attributes might be associated to the widely distributed diffusive properties. For that purpose, we used our combinatorial microscopy approach to track cell-matrix interaction in cells

displaying different diffusion abilities (Fig. 2D; Supplementary Video S2). Cells that lack a detectable actin-rich matrix attachment, although displaying high protrusive dynamics, have modest diffusion abilities. Cells that distribute adhesive structures into dynamic patches aligned along the cell polarity axis are displaying high displacement. This is reminiscent of the walking behavior described previously in T lymphocytes¹⁷. Cells that display large and sustained matrix attachment fail to displace efficiently, probably because of a reduced ability to detach from the matrix. Together, these observations indicate that the heterogeneity of B lymphocytes diffusive properties is mirrored by distinct actin-rich patterns of matrix attachment.

To further characterize the diffusion properties of B lymphocytes over the two model matrices, we analyzed the distribution of individual displacement lengths normalized by their mean value, for time lags of 5, 10, 20, 40 minutes (Fig. 2E). In both cases, the different densities collapse on the same curve after this normalization. However, while over fibronectin the distribution is nearly Gaussian, like for usual Brownian walkers, displacements over collagen IV display a much wider distribution. These results therefore demonstrate that B lymphocytes adopt different diffusive properties depending on matrix composition, moving as fast Brownian-like random walkers over fibronectin and as slow non-Gaussian walkers over collagen IV, with a much wider range of displacements.

B lymphocyte adhesion to matrix counteracts their assembly into clusters. Although lymphocytes are generally considered as solitary cells, they face multiple physio-pathological settings at high cell density that favor homotypic contacts. It is currently unknown how cell-matrix and cell-cell interactions are integrated to control lymphocyte motility. To address this question, B lymphocytes were seeded at high density (1000 cells mm⁻²) over collagen IV or fibronectin and followed for 12 h with our tracking algorithm, for which a cluster size color-coded classifier and a fusion/fission counter were implemented (Supplementary Video S3). Over collagen IV, B lymphocytes assemble into cell clusters, whose size increases progressively over approximately 6 h, resulting in a large proportion of cells being associated to large-size clusters (Fig. 3A,B). The video recordings also reveal a dynamic exchange of cells between the different categories of clusters' sizes. In comparison, cell aggregation over fibronectin is reduced. Indeed, even if the proportion of isolated cells progressively declines over time, a smaller number of large clusters emerge. This is confirmed by the analysis of the cluster size distribution at the stationary phase (>6 h), which decays much faster over fibronectin than over collagen IV (Fig. 3C). Similarly, interaction with collagen IV favors primary B cells aggregation, while fibronectin tends to limit it (Supplementary Figure S3D,E). To disentangle whether the distinct cellular behaviors observed over the 2 model matrices were related to the nature of the matrix, rather than its coated concentration, we further studied the B cell clustering process using low (1.5 µg/ml) and high (10 µg/ml) concentrations of fibronectin and collagen IV, as well as a non-coated surface (Supplementary Figure S4). Our data clearly support the notion that collagen IV favors assembly of large clusters and that this process is reinforced at high concentration (10 µg/ml). In contrast, fibronectin prevents the clustering behavior at both tested concentrations. These findings indicate that the nature of fibronectin and collagen IV, rather than their local concentrations have diametrically opposite effects on B lymphocyte aggregation. The increased degree of B lymphocyte aggregation observed over collagen IV might result from distinct dynamics of interactions between cells. Indeed, the quantification of fusion probabilities as a function of cluster size reveals that collagen IV favors the fusion of individual cells or small groups together with large groups (>10 cells), while fusion events over fibronectin are mostly limited to individual or small clusters among themselves (Fig. 3D). On the other hand, fission probabilities are comparable over the two matrices, with most fission occurring in small-size clusters (3–5 cells) (Fig. 3D). This implies that interaction with fibronectin hampers B lymphocyte aggregation by decreasing fusion events leading to the assembly of large groups. These data suggest that distinct cell-matrix interactions influence cell-cell interaction dynamics leading to cluster assembly. Such interplay might be controlled via actin cytoskeleton remodeling as recently investigated in the *Dictyostelium* model²⁶. To explore this possibility in our model, LifeAct-GFP transfected JY cells were imaged at high cell density over collagen IV or fibronectin using our combinatorial microscopy approach (Fig. 3E; Supplementary Video S4). Most cells over collagen IV establish limited and unstable actin-rich attachment areas, while they emit actin-rich pseudopodia and lamellipodia in upper planes. The collisions between cells initially occur via the actin-rich protrusions, which then retract and reorient away from the inter-cellular contact. This behavior favors the juxtaposition of cell uropods, which appear to be the preferential structure through which cells engage into stable adhesions. This stepwise behavior results in the generation of clusters made of radially oriented cells, as previously observed for leukemic cells⁷ and neural crest cells²⁷. Over fibronectin, a higher proportion of cells engage in sustained attachment to the substrate. When colliding, cells either reorient their migration or slide along each other without stabilizing inter-cellular contacts. In contrast to the behavior observed over collagen IV, neighbor cells do not appear to attach via their uropods, which are instead strongly engaged into matrix attachment, as revealed by the filamentous structures observed in the TIRF plane. A combination of contact-induced reorientation, sliding and uropod attachment to the matrix therefore contributes to prevent the generation of stable clusters over fibronectin. Together, these data suggest that the actin cytoskeleton integrates the interactions of cells with extracellular matrix and other cells to differentially control cell decision to assemble into groups or remain isolated.

Actin branching and actomyosin contraction control the balance between individual and collective behaviors. To investigate how the identified actin cytoskeleton processes might control emergence of B lymphocyte collective behaviors, we used chemical inhibitors to specifically block ROCK1-dependent actomyosin contractility (Y27632) and Arp2/3-dependent actin branching (CK869). Over collagen IV, both the blockade of ROCK1 and Arp2/3 reduce cell diffusion (Supplementary Figure S5A), as reported in previous studies^{28–31}. While ROCK1 blockade appears to affect cell motility by enhancing cell adherence (Supplementary Figure S5B), Arp2/3 blockade does not alter cell adherence but affects the stability of protrusions. ROCK1 inhibition delays

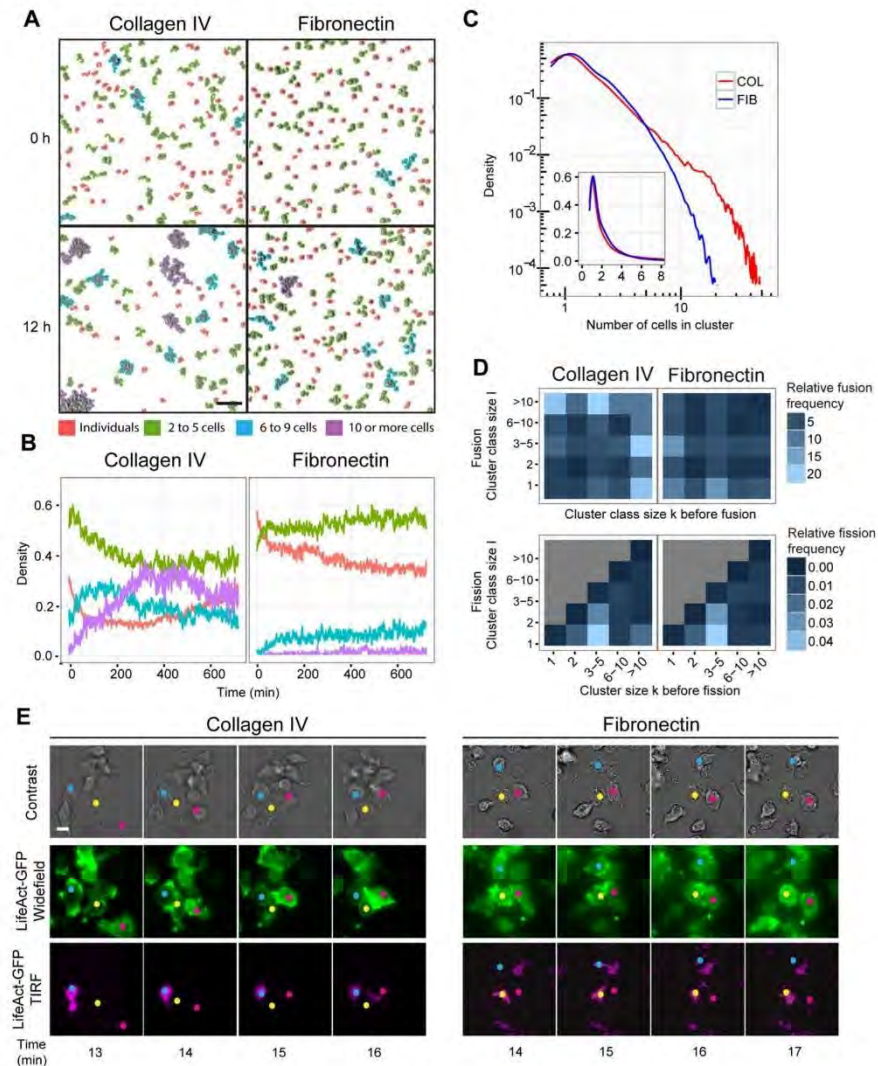


Figure 3. Extracellular matrix conditions assembly of B lymphocytes into clusters. (A) JY cells were seeded at high cell density ($1000 \text{ cells mm}^{-2}$) over collagen IV or fibronectin and recorded for 12 h. Individual cells and cell clusters were color-coded according to the following size categories: individual cells, 2–5 cells, 6–9 and ≥ 10 cells. Representative images at time points 0 and 12 h are shown. Mean cell number: 1831 over Collagen IV and 1788 over fibronectin. Scale bar, $100 \mu\text{m}$. (B) Temporal evolution of the relative area covered by each size category. Data were extracted from 10 videos per condition. (C) Relative distribution of clusters of increasing size studied at the stationary phase (6–12-h time window). (D) Relative frequency of fusion and fission events between clusters of different sizes occurring during the 6–12-h time window. See also Supplementary Figure S2 and Video S3. (E) Representative images of JY cells expressing LifeAct-GFP seeded over collagen IV or fibronectin and recorded over 10 min with a combination of brightfield, widefield and TIRF modes to reveal actin dynamics in cell encounters. Colored dots were added onto cells to keep track of their identity in the successive snap shots. Scale bar, $10 \mu\text{m}$. See also Supplementary Video S4.

the emergence of large clusters over collagen IV (Fig. 4A,B vs Fig. 3A,B). This is mirrored by reduced frequency of both fusion and fission events (Fig. 4C vs Fig. 3D), which reflects the reduced diffusive activity of individual cells, mostly due to a decrease in their mean speed (Supplementary Figure S3). Arp2/3 blockade has an even stronger effect on the aggregation of B lymphocytes over collagen IV, with a marked defect in the assembly of large clusters (Fig. 4A,B vs Fig. 3A,B). The global reduction of fusion events (Fig. 4C vs Fig. 3D) can be explained

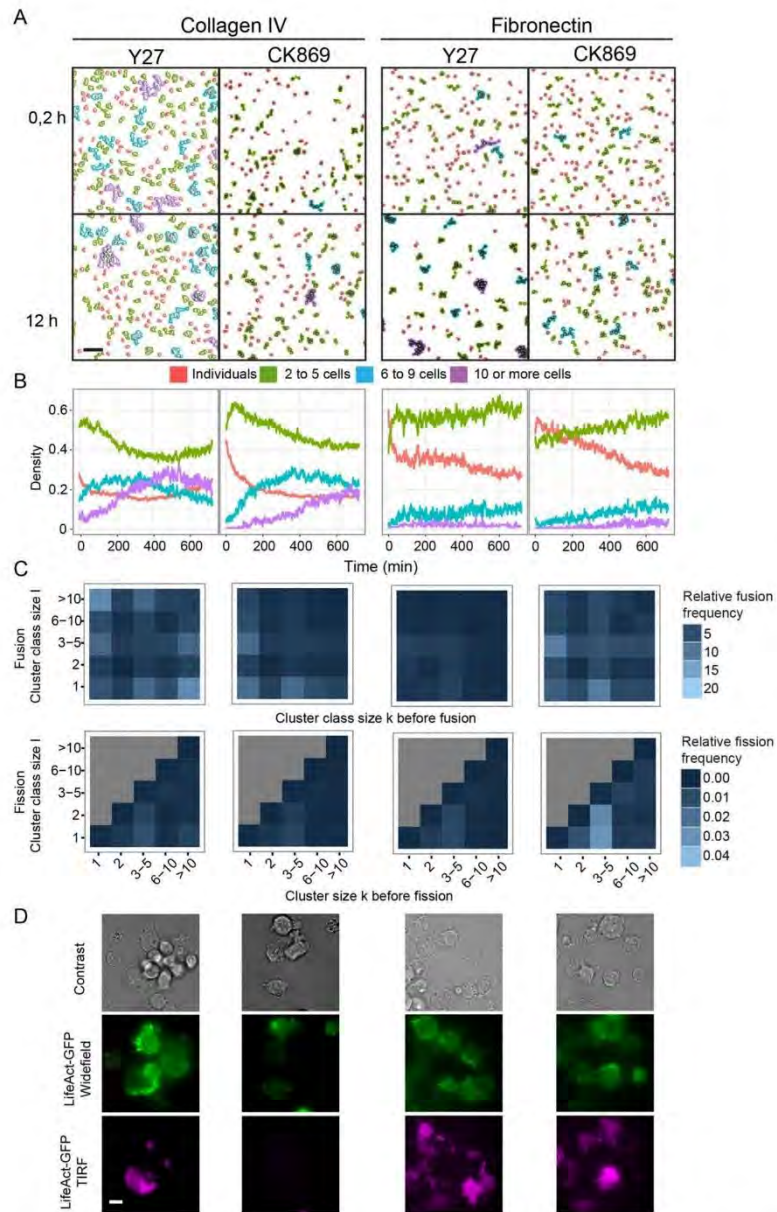


Figure 4. B lymphocyte motility and clustering are differentially controlled by actin branching and actomyosin contraction. **(A)** JY cells pretreated with Y27632 or CK869 were seeded at high cell density over collagen IV or fibronectin and recorded for 12 h. Representative images showing color-coded cells and clusters according to their size are shown at time points 0.5 and 12 h. Scale bar, 100 μ m. **(B)** Temporal evolution of the relative area covered by each size category. Data were extracted from 10 videos per condition (mean cell number: 1831 over collagen IV and 1788 over fibronectin). **(C)** Distribution of relative fusion and fission frequencies according to cell cluster size. Data were extracted from the stationary phase (6–12-h time window). Number of fusions considered: 109549 on collagen IV and 170200 on fibronectin, number of fissions considered: 10737 on collagen IV and 10949 on fibronectin. **(D)** Representative images of JY cells expressing Lifeact-GFP seeded over collagen IV or fibronectin and imaged with a combination of brightfield, widefield and TIRF modes to reveal actin dynamics in cell encounters. Scale bar, 10 μ m. See also Supplementary Figure S3 and Video S5.

by the reduction of B lymphocyte diffusion, caused not only by a speed reduction but also by a decreased ability to translate it into active displacement (Supplementary Figure S5C). CK869 treatment induced the near disappearance of fusions involving medium- to large-size clusters, revealing a qualitative change in cell-cell interactions. We further used our combinatorial microscopy approach to investigate how the blockade of ROCK1 and Arp2/3 might affect the cell-matrix and cell-cell interaction dynamics. While ROCK1 inhibition enhances cell-matrix attachment, it does not appear to affect the ability of cells to engage contacts with neighbors (Fig. 4D; Supplementary Video S5). As previously reported, cells inhibited for Arp2/3 activity display erratic protrusive activity³². Furthermore, treated cells display a reduced ability to stabilize contacts upon encounter, which indicates that the quality of cell protrusions is key to the assembly of B lymphocytes into clusters.

We then investigated how the blockade of ROCK1 and Arp2/3 might modulate the dynamics of cell encounters over fibronectin. Both treatments reduce B lymphocyte diffusion (Supplementary Figure S3). While ROCK1 inhibition mainly affects cell main speed, Arp2/3 inhibition reduces both speed and displacement ability (Supplementary Figure S3). ROCK1 blockade enhances cell adherence, while Arp2/3 blockade decreases it (Fig. 4B). Over fibronectin, which does not promote B lymphocyte aggregation, the blockade of ROCK1 and Arp2/3 has no noticeable impact on clustering, nor on the distribution of fusions and fissions events. At high cell density, ROCK1 blockade appears to impede cell detachment from fibronectin and it does not appear to affect the ability of cells to engage contacts with neighbors (Fig. 4D; Supplementary Video S5). Arp2/3 blockade promotes erratic protrusion dynamics that does not influence the limited ability of cells to aggregate over fibronectin.

These results highlight that actin cytoskeleton dynamics coordinate the interactions of B lymphocytes with matrix and neighbor cells. In particular, Arp2/3-dependent actin branching plays a key role in stabilizing contacts between cells and cluster assembly. On the other hand, actomyosin contraction sustains cell migration by regulating cell-matrix interaction dynamics, while it is dispensable for cluster assembly.

Onset of B lymphocyte collective motility depends on matrix composition. Collective behaviors in biological systems emerge from a complex set of interactions between individual components that are modulated by external conditions in the environment^{33–35}. With the aim of understanding if the interactions of B lymphocytes with the matrix modulate not only aggregation, but also the possible onset of collective motion, individual cell and cluster motility was analyzed on fibronectin and collagen IV. Groups of increasing size were tracked on both matrices to calculate the MSD over time (Fig. 5A) and the diffusion coefficient (Fig. 5B). The data show that over fibronectin diffusion decreases with cluster size, as expected for non-cooperative walkers. In contrast, clusters formed over collagen IV display a sustained diffusive ability, which remains relatively constant whatever the group size. This suggests that clusters over collagen IV might be endowed with a diffusive advantage. Matrix influence on cluster diffusion properties was further studied by analyzing the relationship between diffusion speed and average speed for various cluster sizes (Fig. 5C). Over fibronectin, both motile parameters decay as a function of group size, partially explaining the diffusive defect of the groups by a diminution of their speed. Over collagen IV, the maintenance of diffusion coefficient is independent from changes in average speed. The diffusive property of B lymphocyte clusters over collagen IV might result either from the emergence of a cooperative behavior between cells or from a biased assembly of the most motile B lymphocytes into clusters. To discriminate between these two possibilities, GFP-expressing cells were mixed with unstained ones at a 1/40 ratio in order to track their motility and calculate the time they spent as isolated cells or as members of clusters (Fig. 5D; Supplementary Figure S4; Supplementary Video S6). Over fibronectin, the average displacement of the cells weakly and inversely correlates with the time they remained isolated. This is most probably caused by an increased probability of the most rapid cells to encounter neighbor cells. On the contrary, over collagen IV, cell propensity to remain isolated or to assemble into clusters is independent from their average displacement. This suggests that the sustained diffusion of clusters formed over collagen IV does not result from the aggregation of the fastest cells but arises from a cooperation mechanism between cells. To address whether clustering would affect the motility properties of individual cells, we tracked the stained cells and compared their motility as isolated cells or as part of clusters (Supplementary Figure S4). Over collagen IV, the speed of individual cells increases as they join clusters, indicating that assembly into clusters confers superior motility properties to the cells. Distinctly, over fibronectin, the speed of the cells is similar as they migrate as isolated individuals or as part of clusters. This is in apparent contrast to the loss of diffusive properties of the clusters (Fig. 5B). A possible interpretation is that, over fibronectin, cells remain motile in clusters but slow down cluster displacement because of a lack of coordination. Together, these data indicate that interactions of cells with the matrix condition the emergence of coordination leading to collective migration.

ROCK1 activity plays a pivotal role in the control of B lymphocyte collective chemotaxis. We previously established that malignant lymphocyte clusters display increased chemotactic ability as compared to individual cells⁷. We here tested how B lymphocyte interaction with different matrices might modulate the emergence of chemokine-evoked collective directional motility. For that purpose, JY cells were exposed to a CCL19 chemokine gradient set in dedicated chemotaxis chambers coated with either collagen IV or fibronectin (Fig. 6A; Supplementary Video S7). Isolated cell and cluster trajectories were tracked automatically (Fig. 6B) and the displacement towards the chemokine was computed (Fig. 6C). Over collagen IV, B lymphocyte clusters reach further distances in the direction of the chemokine source as compared to isolated cells. This illustrates how the coordination between cells gives rise to increased chemotactic properties. Over fibronectin, the displacement towards CCL19 of isolated B lymphocytes was higher than that of their counterparts over collagen IV. This is consistent with the fact that B lymphocyte adherence over fibronectin enhances their basal motility, which might translate into enhanced chemotaxis. In contrast to collagen IV, fibronectin does not promote collective chemotaxis. Indeed, B lymphocyte groups display reduced displacement towards CCL19, as their size increases. Our interpretation of these data is that the extended cell interaction with fibronectin favors individual cell chemotaxis, while

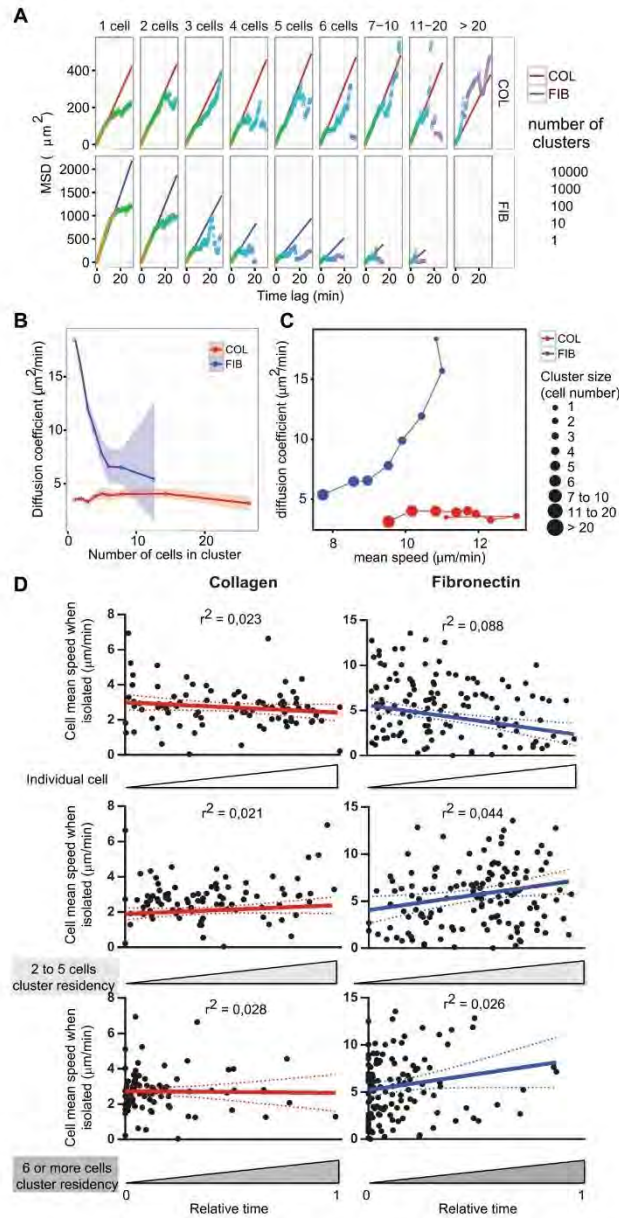


Figure 5. Emergence of B lymphocyte collective motion properties depends on matrix interaction. (A) Mean square displacement was plotted as a function of time interval for JY cell clusters of growing size tracked at high cell density over collagen IV and fibronectin. Linear regressions and shown in red or blue, respectively. The color code indicates the number of tracks available for each time length. Data were pooled from 10 videos per condition. (B) Diffusion coefficient of each cluster category represented with confidence interval. (C) Correlation between diffusion coefficient and mean speed (time lag of 5 s) is shown for clusters of each category. (D) JY-GFP cells diluted 1/40 with unstained JY cells, seeded at high cell density over collagen IV or fibronectin and imaged after 6 h for another 6 h, each 30 s. GFP cells were automatically tracked and their time as isolated cells or as part of clusters were quantified. The plots represent the mean speed of each cell as it migrated alone, as a function to the relative time of those cells as isolated cells, as part of small clusters or as part of large clusters. Linear regression and 95% confidence interval were plotted (collagen IV, 90 cells; fibronectin, 132 cells; data from one representative experiment out of 3). See also Supplementary Figure S4 and Video S6.

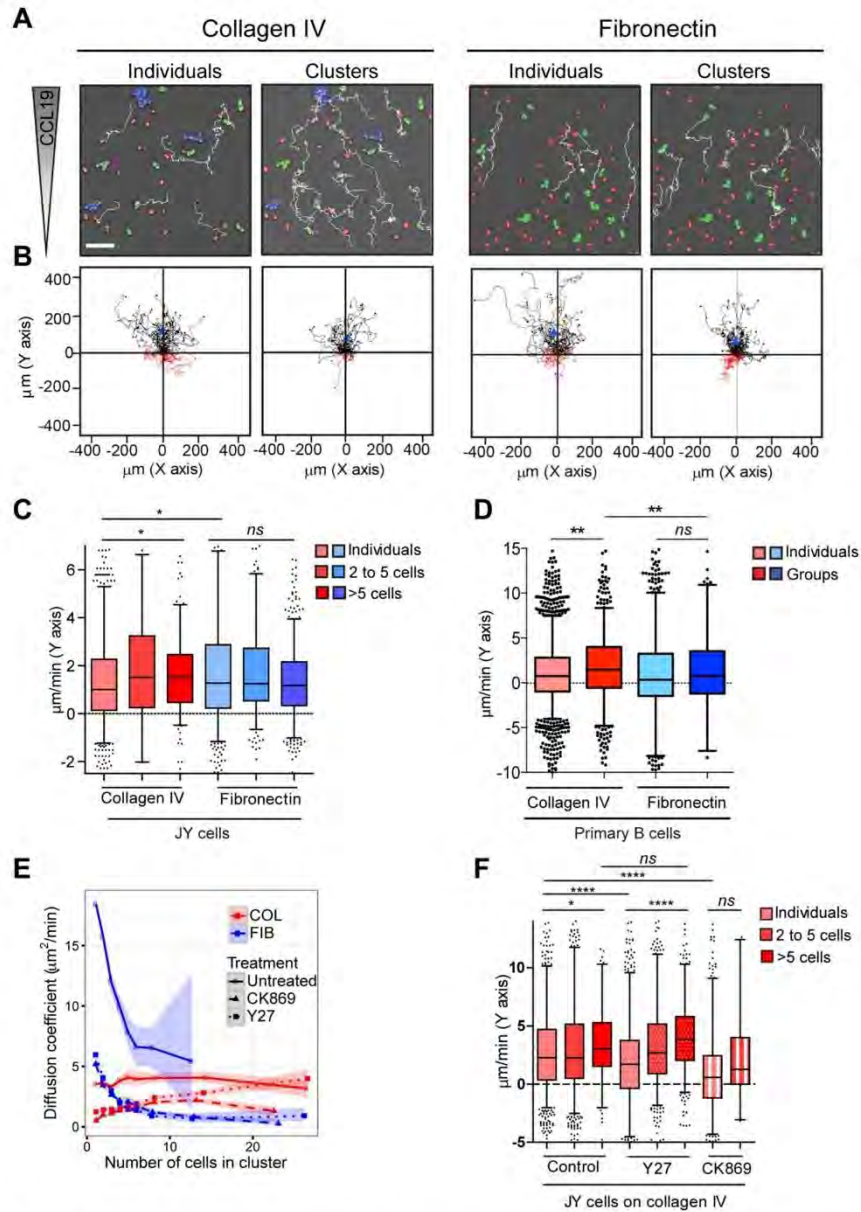


Figure 6. Collective chemotaxis of B lymphocytes depends on matrix interaction and is differentially controlled by actin branching and actomyosin contraction. (A) JY cells migrating over collagen IV or fibronectin in Ibidi chemotaxis chambers in which a $0\text{--}500\text{ ng ml}^{-1}$ CCL19 gradient was established. Colors represent the following size categories: individual cells (red), 2–5 cell clusters (green) and ≥ 6 cell clusters (blue). Representative tracks of individual cells and cell clusters are shown. Scale bar, $100\text{ }\mu\text{m}$. (B) One-hour tracks of 40 cells or clusters per condition were normalized to their x,y starting location. Blue triangles mark the population center of mass at 1 h. Black and red tracks indicate displacement over 1 h, respectively towards and away from the chemokine source. (C) Chemotactic speed calculated as the mean displacement per min along the gradient axis is shown for each size category, with a 5 to 95% data range and values out of the range as single points. Data were pooled from 3 experiments, yielding 249 to 921 values, depending on the size group and matrix. $*p < 0.05$, ANOVA test with Sidak-Holms correction for multiple pairs-comparisons. (D) Primary B cells were seeded over collagen IV or fibronectin, exposed to a $0\text{--}100\text{ ng ml}^{-1}$ CCL19 gradient and tracked for 12 h. Chemotactic speed is shown

for each size category, with a 5 to 95% data range and values out of the range as single points. Data correspond to the pool of 2 experiments, including 213 to 2192 values, depending on the size group and matrix. ** $p < 0.01$, ANOVA test with Sidak-Holms correction for multiple pairs-comparisons. See also Supplementary Figure S4 and Video S7. (E) JY cells were treated with Y27632 or CK869 and tracked over collagen IV or fibronectin. Diffusion coefficients of the indicated size categories are represented with confidence intervals. For comparison, diffusion from untreated cells and clusters is also represented. (F) JY cells were treated with Y27632, CK869 or 0,1% DMSO, seeded over collagen IV and exposed to a 0–500 ng ml⁻¹ CCL19 gradient. Chemotactic speed is shown for each size category, with a 5 to 95% data range and values out of the range as single points. Data were pooled from 2 experiments, yielding 137 to 1924 values, depending on the size group and matrix. * $p < 0.05$, *** $p < 0.0001$, ANOVA test with Sidak-Holms correction for multiple pairs-comparisons. See also Supplementary Figure S4 and Video S8.

preventing cell coordination required for collective chemotaxis. Primary B cells also undergo a higher chemotactic speed over fibronectin than over collagen IV (Fig. 6D). Importantly, primary B cells are also capable of collective chemotaxis since clusters over collagen IV display increased chemotactic speed as compared to isolated cells. Differently, over fibronectin, primary B cell clusters do not display chemotactic advantage over individual cells.

Our experimental model shows that both diffusion coefficient and chemotactic speed decrease with group size over fibronectin, whereas they both increase over collagen IV. This is reminiscent of the fluctuation-dissipation theorem derived from the Einstein relation³⁶, which states that for physical particles, the diffusion coefficient is proportional to the response to the applied field (Supplementary Figure S4).

We then explored which aspects of actin cytoskeleton remodeling might contribute to the emergence of B lymphocyte collective motility. Groups of increasing size were tracked on both matrices to calculate the MSD over time (Supplementary Figure S4) and the diffusion coefficient (Fig. 6E). The data show that over fibronectin, although the actin blocking treatments alter cluster diffusion, the reduction of diffusion as a function of size is maintained. Over collagen IV, Arp2/3 blockade reduces diffusion independently from cluster size. Interestingly, although ROCK1 blockade affects the diffusion of individual cells and small clusters, it spares that of large clusters. This result, combined to the observation that ROCK1 blockade reduces cell cluster speed (Supplementary Figure S4), indicates that this treatment promotes effective displacement of clusters, possibly by reinforcing a cell-to-cell cooperative process.

We further studied how the differential effect of ROCK1 blockade on the diffusion of individual cells and clusters in the absence of gradient would translate in the context of a chemokine field. While Y27632 treatment results in a reduction of individual cell chemotactic ability, it enhances the chemotactic speed of large clusters (Fig. 6F; Supplementary Video S8). Differently, CK869 treatment affects both the chemotaxis speed of individual cells and of the few stable clusters that are formed under this condition. Together, our study reveals that ROCK1-controlled actomyosin contractility plays a pivotal role in the adaptive motility behavior of B lymphocytes by tuning differentially individual cell motility and collective chemotaxis.

Discussion

Our study reveals a wide range of B lymphocyte motility behaviors that emerge from the interplay between cell-matrix and cell-cell interactions. In particular, interactions of cells with the extracellular matrix determines not only their motility behavior as individual cells, but also their propensity to assemble into homotypic clusters and to undergo collective chemotaxis. Our study further highlights the key role played by apparently distinct actin cytoskeleton compartments to integrate the effects of cell-matrix and cell-cell interactions to control the onset of collective dynamics in B lymphocyte populations.

A first key finding of our study is that B lymphocytes adapt their motility behavior to their environment. Indeed, depending on matrix composition, B lymphocytes are either standard Gaussian random walkers or persistent random walkers characterized by a wide distribution of displacements. The adaptive property of lymphocytes could reconcile the different motility behaviors assigned to lymphocytes in different studies^{10,13,14}. Interestingly, lymphocytes have been suggested to adopt either Brownian random walks or persistent random walks within non-inflamed lymph nodes¹⁴. In light of our data, this apparent dichotomy might result from the adaptability of lymphocyte populations in response to distinct ECM components composing the lymph node^{17,37}. Beyond the motility behaviors identified with our simplified *in vitro* assays, lymphocytes may adopt additional motility behaviors when facing more complex environments^{1,38,39}. As lymphocytes extravasate, they migrate successively through ECM environments made of distinct molecular compositions and architectures, such as collagen IV-containing basement membranes and fibronectin-rich fibrillar matrices⁴⁰. Although combinations of matrix components were not assessed in our work, our data suggest that lymphocytes may adapt their motility behaviors as they shift ECM environments. Tissue-specific ECM composition or inflammatory triggers linked to infection may drive additional motility patterns, such as Levy walks described for CD8⁺ T lymphocytes in *T. gondii* infected brain tissues¹⁵. Additionally, tissue architecture is sought to provide favored routes and to impose physical constraints that dictate lymphocyte deformation and motility⁴¹. Independently from the complexity of *in vivo* environments, our data point to the fact that the random motility behaviors of lymphocytes are intrinsic properties of those cells and that they adapt their random motility to ECM composition and possibly related environmental cues, such as matrix fiber spacing and ECM gradients. The plasticity of lymphocyte motility is probably tuned to ensure optimal activation and effector function. Furthermore, we postulate that lymphocytes belonging to distinct subsets and maturation stages may tune differently their motility behavior, because of specific interactions with ECM components.

Our study further highlights that at high cell densities, B lymphocytes alternate between individual and collective behaviors. Importantly, cell-matrix interaction appears to affect cell-cell interaction dynamics, which control the assembly into clusters. Such interplay between cell-matrix and cell-cell interactions has previously been described for neural crest cells⁴² and *Dictyostelium discoideum*²⁶. The low adherence condition (Collagen IV) favors aggregation of cells into radial clusters via their uropods in a way reminiscent of previous observations²⁷. On the other hand, B lymphocytes over fibronectin fail to engage in stable cell-cell contacts. Our data point to a contact inhibition of locomotion mechanism, as described in other cells^{42–44}. Our data show that the nature of the matrix, rather than its local concentration conditions specific cell behaviors. This calls for further exploration of whether the physical properties of the matrices, rather than their biochemical nature or the specificities of the corresponding adhesion receptors might explain the distinct cell behaviors. Interestingly, cell-matrix and cell-cell interactions are associated to seemingly distinct actin cytoskeleton modules. We therefore speculate that the interplay between cell-matrix and cell-cell interactions is controlled via a crosstalk between those 2 actin-rich areas. Along this concept, the different adhesive areas over the 2 matrices are associated to distinct protrusive activities impacting on the establishment of cell-cell contacts. This is reinforced by the finding that Arp2/3 is involved in cell-cell adhesion stabilization, rather than in matrix interaction. Given its role in protrusion stability and LFA-1 activation^{45,46}, Arp2/3 could prime lamellipodia-like extensions that favor extensive contacts between cells, further eliciting LFA-1 driven homotypic adhesions as described for leukemic cells⁷. This is in agreement with the recent finding that the lamellipodium of lymphocytes is dispensable for cell traction during motility, but holds an exploratory role⁴⁷.

The concept that hematopoietic cells are solitary cells and migrate independently from each other has recently been challenged by reports showing that both myeloid and lymphoid cells can switch from single cell to group behaviors^{5,48,49}. Our study indicates that B lymphocyte clusters form cellular hubs that could combine the necessity for B lymphocytes to cooperate during activation and/or function, with the necessity to scan actively tissue surfaces and to recirculate. Indeed the equilibrium between clusters and individual cells is highly dynamical since groups are undergoing active fusion and fission events allowing most cells to temporally contribute to clusters. Like for the grazing dynamics in flocks of sheep⁵⁰, B lymphocyte populations appear to balance the conflicting needs of spreading and gathering. Whereas Merino sheep alternate between group spreading and aggregation phases, B lymphocytes establish a rather stable equilibrium between compact groups and freely moving cells at the population level. Those properties might contribute to the ability of B lymphocytes to both circulate as isolated cells and to assemble into dense follicles in lymphoid organs. Additionally, the specific nature of the reticular ECM fibers composing the scaffold of the B cell follicles is expected to play a key role in the compartmentalization and dynamic behaviors of those cells⁴⁰. A further challenge will be to investigate how the multiple 3D cell-matrix adhesions and inter-cellular interactions are regulating the multi-cellular dynamics of B cell follicles.

Our study reveals the role of cell matrix interaction on the onset of B lymphocyte collective motility. Over fibronectin, B cell clusters display reduced basal motility and chemotaxis as a function of size, pointing to the lack of coordination among the cells composing the clusters. In contrast, over collagen IV, B cell clusters display increased diffusion and chemotaxis as compared to individual cells. Both behaviors are qualitatively consistent with the Einstein relation for diffusing particles submitted to an external field. Moreover, the onset of collective chemotaxis is not the consequence of the preferential aggregation of the most motile B lymphocytes. This instead points to a cell-cell coordination mechanism. Importantly, we show that the role of extracellular matrix on the onset of collective chemotaxis applies to primary B cells isolated from human peripheral blood. In the context of tumoral lymphocytes displaying a similar collective chemotaxis, we previously established that cell coordination was ensured by the turn-over of leader cells expressing high levels of chemokine receptor and protruding toward the chemokine source⁷. Such coordination might apply to the non-tumoral B lymphocytes studied here. In light of our studies, a possible explanation for B lymphocyte coordination over collagen IV would be that cell clusters are pulled by exchanging leader cells that transiently engage in strong attachment to the matrix. Concomitantly, pulling of the cell clusters by such leader cells would be favored by the stability of cell-cell interactions. On the other hand, under conditions favoring strong attachment of most cells, the loose cell-cell contacts are generating noise that counteracts diffusion and chemotaxis. Such noise might be explained by cell-cell frictions, contact-inhibition of locomotion, or cell-cell interactions weakening cell-matrix interaction. The importance of cell-cell interactions during collective chemotaxis over collagen IV is highlighted by our experiments with the ROCK1 inhibitor. The fact that clusters display increased chemotactic speed upon ROCK1 inhibition suggests that myosin contraction in cell clusters limits cluster compactness and onset of collective chemotaxis. This hypothesis is in line with results obtained in carcinoma cells, in which the DDR1-driven down-modulation of myosin contraction in the core of clusters is required for collective migration⁵¹. It is currently unclear whether collective chemotaxis of lymphoid cells might occur *in vivo* because of space constraints. We favor the view that lymphocytes might exploit collective properties to assemble in areas of high chemokine concentration, such as in the context of B cell follicles.

In conclusion, our study reveals how B lymphocytes integrate cell-matrix adhesion and intercellular interactions to generate a vast array of motility behaviors at the population level. In particular, our work unveils the following rules pertaining to B lymphocyte motility: i) B lymphocytes are uniformly endowed with a local scanning activity, independently from matrix interaction; ii) space exploration by B lymphocyte populations relies on a wide distribution of individual cell diffusive abilities that is additionally tuned by matrix interaction; iii) transition from individual to schooling behaviors is highly dependent on matrix interaction. These rules provide a novel framework to explore how the complexity of physiological tissue environments or the activation status of lymphocytes are tuning their motility patterns.

Methods

Cell culture, transduction and treatments. EBV-transformed B cells (JY line) were cultured in RPMI 1640 GlutaMax, supplemented with 10% Fetal Calf Serum, minimum essential amino acids, HEPES, sodium pyruvate and Streptomycin/penicillin solution (Invitrogen) Cells were routinely screened for mycoplasma

contamination using the MycoAlert mycoplasma detection kit (Lonza). For the stable expression of GFP, LifeAct-GFP, LifeAct-RFP, 1×10^5 JY cells were transduced with a lentiviral vector encoding LifeAct-TagGFP2 or LifeAct-TagRFP (Ibidi) over 6 h in RPMI-1640 containing 5% FCS and polybrene ($4 \mu\text{g ml}^{-1}$). Transfected cells were selected by culturing them in the presence of $2 \mu\text{g ml}^{-1}$ puromycin for 7 days, added 24 h after transfection. Bright GFP-positive cells were further selected by flow cytometry sorting. Where indicated, cells were treated with Y27632 (Abcam) at $10 \mu\text{M}$, CK 869 (Sigma-Aldrich) at $50 \mu\text{M}$ or the equivalent concentration of DMSO (10^{-3}). No treatment toxicity was detected in a window of 16 h. Ibitreat™ (Ibidi) plastic plates were coated with $1,5 \mu\text{g ml}^{-1}$ collagen type IV from human placenta or $10 \mu\text{g ml}^{-1}$ fibronectin from human plasma (both from Sigma-Aldrich) diluted on PBS. Matrices were incubated ON at 4°C and 1 h at 37°C before washing with medium and cell seeding.

Primary B cell purification and culture from peripheral blood. Buffy coats from healthy donors were obtained through the Etablissement Français du Sang (EFS Midi-Pyrénées, Purpan University Hospital, Toulouse, France) and processed following standard ethical procedures (Helsinki protocol), after obtaining written informed consent from each donor and approval by the local ethics committee (Comité de Protection des Personnes Sud-Ouest et Outremer II). B cells were isolated from buffy coats via separation by Ficoll centrifugation and a negative selection kit (EasySep Human B Cell Enrichment Kit; Stem Cell Technologies). Purified B cells were cultured at 5×10^6 cells ml^{-1} in RPMI 1640 GlutaMax, supplemented with 10% Fetal Calf Serum and stimulated for 48 h with the $5 \mu\text{M}$ CpG ODN 2006 (InvivoGen) for 48 h before performing the experiments.

Expression of integrins. JY cells or PBMCs were washed and blocked for 20 min with PBS, 20% human serum at 4°C . Then, cells were stained with antibodies against CD19, CD49a, CD49b or CD49d (Biolegend) at $10 \mu\text{g/ml}$ for 60 min at 4°C . Stained cells were washed several times and analyzed using a Miltenyi MacsQuant VYB flow cytometer. Using the FlowJo software, B cells were selected by gating on the CD19 positive cells and analyzed for their expression of the CD49a, CD49b and CD49d integrin alpha-chains.

Recording and quantification of B lymphocyte motility. JY cells were washed, resuspended in fresh medium and seeded (5×10^3 cells in $120 \mu\text{l}$) onto a collagen IV or fibronectin coated channel from a μ -Slide VI 0,4 (Ibidi) to reach a cell density of 50 cells mm^{-2} . After 2 h incubation at 37°C to allow cell attachment, cells were recorded for 12 h at a rate of 1 image each 5 s on an Eclipse TE2000-E fully-motorized inverted microscope (Nikon) and a $10\times/0.45$ NA objective. The microscope was equipped with an incubation chamber (OKOLab) for temperature and CO_2 control. Images were acquired using a Evolve 512 emCCD camera (Photometrics) and the Metamorph software (Molecular Devices). Image processing was performed with a program written in C++ using the open source OpenCV library. To identify the interactions, the first step consisted in detecting and outlining the individual cells and groups. The images were binarized using Otsu method and a morphological closure was applied to reduce noise. Edge detection was implemented with the Suzuki method and the further blob labeling provided a map at any time point (t). Secondly, fusion and scission dynamics were analyzed over time by matching blobs at time t-1 with the ones found at time t. Briefly, distance, size and cell density index combination provided a score for the best blob matching. In case of several blobs with the same match, a fusion or scission event was considered. In case of a missing match, the cell (or cluster) passed to “standby mode” being considered as definitively lost if it did not reappear for 10 frames (50 sec). This method helped us to overcome the problem of over-labeling of “intermittent” cells/clusters due to faint contrasted contours. The proportion of lost cells or clusters in the analyzed video-recordings ranged between 0.44% and 1.33%, depending on ECM coating and cell density. The proportion of gaps in the analyzed tracks ranged between 1.94% and 3.10%, depending on ECM coating and cell density.

B lymphocyte clustering by fixed imaging. JY cells were seeded at 1.2×10^4 cells per well in an angiogenesis μ -plate (Ibidi) containing either uncoated wells or wells precoated with collagen IV (1,5 or $10 \mu\text{g/ml}$) or fibronectin (1,5 or $10 \mu\text{g/ml}$). The plate was placed under a Zeiss apotome microscope equipped with a chamber (37°C , 5% CO_2) and imaged in a bright field mode at 0, 1, 2, 4 and 6 h, using a $10\times/0.45$ NA objective and an Axiocam HRm Rev.3 camera. The image treatment from previous experiments was applied to recognize the perimeter of all cell groups present at each time point. Then, the mean size of individual cells was calculated for each experimental condition and each group area was referred to that value in order to estimate the number of cells composing it. We further checked that the area of clusters remained proportional to the number of cells composing them by staining and counting individual cell nuclei.

B lymphocyte clustering by video recording. JY cells were seeded over the different matrices at 10^3 cells mm^{-2} . Cells were imaged for 12 h with the same settings as in the above section, except that single frames at a few time intervals were replaced by continuous imaging at a rate of 1 frame each 30 s. Where indicated, cells under were treated for 2 h before seeding with either Y27 or CK869. These drugs were kept in the cell medium during the entire recording. The same image analysis tools as above were applied to detect, count and estimate the size of cells and cell groups.

Cluster fusion and fission. Data corresponding to the area and position of cells and cell groups recognized along the video-recordings were computed. On that basis, fusion events were identified as the disappearance of two groups in a frame linked to the appearance of a group of a larger area at the same location in the successive frame. Fission events were defined as the disappearance of a group in a frame linked to the appearance of two smaller groups at the same location in the successive frame. Both fusion and fission events were classified by size category (n) and the crossed probability of fusion and fission for the different size established as $P_{\text{fusion}}(n_1, n_2) = [\text{Number of fusions } n_1 + n_2 \text{ per min}] * (\text{Mean number of clusters from all size categories during the 6 h})$

recording)/(Mean number of clusters from n1 size category along the 6 h *Mean number of clusters from n2 size category along the 6 h)] and P fission ($n \rightarrow n1 + n2$, with $n1 \leq n2$) = (Number of fissions $n \rightarrow n1 + n2$ per min/ Mean number of clusters during the 6 h recording).

Tracking of individual cell association to clusters. JY cells were prepared at a 1/40 GFP positive cell proportion, seeded over collagen IV or fibronectin as before and incubated for 6 h at 37 °C. The bright field and GFP channels were imaged for 6 h each 30 s on an Apotome microscope (Zeiss) and a 10x/0.45 NA objective, as described in the above section. The Image J software was used for video quantification. Briefly, the bright field channel was used to generate a binary image. Then specific masks for individual cells, groups from 2 to 5 cells and groups composed of 6 cells or more were applied and a specific signal intensity was associated to each mask. The three masks were added to recompose the original binary image, this time with an intensity code to distinguish between the three size classes. The GFP channel was used to generate a mask that identified each cell for the full video. Combination of the recomposed bright field and GFP masks and analysis with the TrackMate Image J plugin⁵² provided a tool to follow motility and clustering simultaneously. Cell speed and relative time in each size category were extracted. Speed values obtained from individual tracks shorter than 5 min were discarded. Correlation between speed and time of cluster residence/isolation represented for each cell by using GraphPad Prism.

Combinatorial TIRF, IRM, and widefield analysis of actin dynamics. JY cells expressing LifeAct-GFP were prepared and seeded on collagen IV or fibronectin at low or high cell density as in previous experiments. After 2 h at 37 °C for cell adhesion and, in case, treatment action, cells were placed on a Nikon inverted spinning disk confocal microscope equipped with a back-thinned charge-coupled device camera (Evolve; Photometrics, Tucson, AZ, 512 × 512 pixels), equipped with a temperature and CO₂ controlled chamber and imaged with an oil immersion 100x/1.49 NA objective. 491 nm laser was used to obtain TIRF and widefield at the cell-matrix contact focus, while IRM image was obtained by using 561 nm laser. Added to that, widefield 491 nm signal and brightfield were obtained at cell midbody focus, where cell protrusion where extended. Fixed images or live videos with a 10 s temporal resolution were taken. Relative cell attachment area was calculated by dividing TIRF LifeAct-GFP area by widefield area for each cell. Cell shape volatility was calculated using widefield LifeAct signal as reference for cell shape. Aspect ratio was calculated by dividing the major axis by the minor axis of each cell at each frame using Image J. Volatility was calculated as the standard deviation of the aspect ratio changes over consecutive frames.

Primary B cell attachment, motility and dynamics. Primary B cells were seeded over collagen IV or fibronectin and cultured for 2 h. Cells were imaged on a Nikon inverted spinning disk confocal microscope with a 100X objective for brightfield and IR illumination. Fixed images from random fields with at least 3 cells were taken and cells showing a contact area with the matrix (altering the IR signal pattern) were quantified. For motility studies, 10⁵ cells were seeded at 10³ cells mm⁻² and imaged for 16 h at a frame rate of 1 image each 30 s on a Zeiss apotome microscope equipped with a chamber (37 °C, 5% CO₂) and imaged in a bright field mode with a 10x/0.45 NA objective. For motility quantification, images were treated using Image J to select individual cells by their size and contrast to background and tracks over 20 min appearing after 3 h of recording were automatically registered and quantified using Trackmate. For population dynamics, individual cells, small (2 to 5 cells) and large clusters (6 or more cells) were detected and their covered surface quantified with Image J. The relative proportion of each size category was quantified and plotted with Graphpad Prism.

Chemotaxis assays and 2D migration. JY cells or primary B cells (10⁵ in 6 µl of culture medium) were loaded into the central transversal channel of Ibitreat 3D chemotaxis µ-slides (Ibidi) coated with collagen IV or fibronectin and incubated at 37 °C for 30 min to allow cell attachment. CCL19 0–500 ng ml⁻¹ gradient was created following the manufacturer's instructions. To verify the linearity of the obtained gradients, control slides were prepared using a 10% dextran-FITC solution. Analysis of fluorescence intensity profiles showed that linear gradients were established within 3 h and were stable over at least 24 h. Cell migration was recorded after 5 h by taking 1 image per 30 s for 14 h by an Apotome microscope (Zeiss) and a 5x/0.15 NA objective in temperature and CO₂ controlled conditions. Obtained images were treated and binarized using Image J to create masks corresponding to individual cells, small (2 to 5 cells) and large (6 or more cells) clusters. For primary B cells, the relative paucity of clusters led us to consider only one cluster category. Migration tracks of each category were obtained using the TrackMate plugin of the FIJI software. Only tracks lasting more than 20 min were considered. Chemotaxis plots and migration parameters (FMI-Y and total speed) were obtained with the Chemotaxis and Migration tool from Ibidi. Chemotactic speed was calculated by multiplying mean speed by FMI-Y for each cell or cluster.

Availability of data and material. The datasets used and analyzed during the current study are available from the corresponding author on reasonable request.

Ethics approval and consent to participate. Primary B cells were purified from blood samples collected from healthy adult donors. Samples were obtained as buffy coats generated upon altruistic donation of blood at the Etablissement Français du Sang (EFS Midi-Pyrénées, Purpan University Hospital, Toulouse, France). All samples were collected after signing an informed consent, following standard ethical procedures (Helsinki protocol) and with the approval by the local ethics committee (Comité de Protection des Personnes Sud-Ouest et Outremer II).

References

1. Friedl, P. & Weigel, B. Interstitial leukocyte migration and immune function. *Nat Immunol* **9**, 960–969, <https://doi.org/10.1038/nri.212> (2008).
2. Muppidi, J. R., Lu, E. & Cyster, J. G. The G protein-coupled receptor P2RY8 and follicular dendritic cells promote germinal center confinement of B cells, whereas S1PR3 can contribute to their dissemination. *J Exp Med* **212**, 2213–2222, <https://doi.org/10.1084/jem.20151250> (2015).
3. Miller, M. J., Wei, S. H., Parker, I. & Cahalan, M. D. Two-photon imaging of lymphocyte motility and antigen response in intact lymph node. *Science* **296**, 1869–1873, <https://doi.org/10.1126/science.1070051> (2002).
4. Gerard, A. *et al.* Secondary T cell-T cell synaptic interactions drive the differentiation of protective CD8+ T cells. *Nat Immunol* **14**, 356–363, <https://doi.org/10.1038/ni.2547> (2013).
5. Liu, Z. *et al.* Immune homeostasis enforced by co-localized effector and regulatory T cells. *Nature* **528**, 225–230, <https://doi.org/10.1038/nature16169> (2015).
6. Iijima, N. & Iwasaki, A. T cell memory. A local macrophage chemokine network sustains protective tissue-resident memory CD4 T cells. *Science* **346**, 93–98, <https://doi.org/10.1126/science.1257530> (2014).
7. Malet-Engra, G. *et al.* Collective cell motility promotes chemotactic prowess and resistance to chemorepulsion. *Current Biology* **25**, 242–250, <https://doi.org/10.1016/j.cub.2014.11.030> (2015).
8. Copenhagen, K. *et al.* Frustration induced phases in migrating cell clusters. *arXiv:1705.00025* [physics.bio-ph] (2017).
9. Qi, H., Kastentmuller, W. & Germain, R. N. Spatiotemporal basis of innate and adaptive immunity in secondary lymphoid tissue. *Annu Rev Cell Dev Biol* **30**, 141–167, <https://doi.org/10.1146/annurev-cellbio-100913-013254> (2014).
10. Miller, M. J., Wei, S. H., Cahalan, M. D. & Parker, I. Autonomous T cell trafficking examined *in vivo* with intravital two-photon microscopy. *Proc Natl Acad Sci USA* **100**, 2604–2609, <https://doi.org/10.1073/pnas.2628040100> (2003).
11. Linderman, J. J. *et al.* Characterizing the dynamics of CD4+ T cell priming within a lymph node. *J Immunol* **184**, 2873–2885, <https://doi.org/10.4049/jimmunol.0903117> (2010).
12. Textor, J. *et al.* Random migration and signal integration promote rapid and robust T cell recruitment. *PLoS Comput Biol* **10**, e1003752, <https://doi.org/10.1371/journal.pcbi.1003752> (2014).
13. Harris, T. H. *et al.* Generalized Levy walks and the role of chemokines in migration of effector CD8+ T cells. *Nature* **486**, 545–548, <https://doi.org/10.1038/nature1098> (2012).
14. Banigan, E. J., Harris, T. H., Christian, D. A., Hunter, C. A. & Liu, A. J. Heterogeneous CD8+ T cell migration in the lymph node in the absence of inflammation revealed by quantitative migration analysis. *PLoS Comput Biol* **11**, e1004058, <https://doi.org/10.1371/journal.pcbi.1004058> (2015).
15. Smaniotto, S. *et al.* Combined role of extracellular matrix and chemokines on peripheral lymphocyte migration in growth hormone transgenic mice. *Brain Behav Immun* **24**, 451–461, <https://doi.org/10.1016/j.bbi.2009.11.014> (2010).
16. Friedl, P. & Wolf, K. Plasticity of cell migration: a multiscale tuning model. *J Cell Biol* **188**, 11–19, <https://doi.org/10.1083/jcb.200909003> (2010).
17. Jacobelli, J., Bennett, E. C., Pandurangi, P., Tooley, A. J. & Krummel, M. F. Myosin-IIA and ICAM-1 regulate the interchange between two distinct modes of T cell migration. *J Immunol* **182**, 2041–2050, <https://doi.org/10.4049/jimmunol.0803267> (2009).
18. Fricke, G. M., Letendre, K. A., Moses, M. E. & Cannon, J. L. Persistence and Adaptation in Immunity: T Cells Balance the Extent and Thoroughness of Search. *PLoS Comput Biol* **12**, e1004818, <https://doi.org/10.1371/journal.pcbi.1004818> (2016).
19. Song, J. *et al.* Extracellular matrix of secondary lymphoid organs impacts on B-cell fate and survival. *Proc Natl Acad Sci USA* **110**, E2915–E2924, <https://doi.org/10.1073/pnas.1218131110> (2013).
20. Schreiber, J., Schachner, M., Schumacher, U. & Lorke, D. E. Extracellular matrix alterations, accelerated leukocyte infiltration and enhanced axonal sprouting after spinal cord hemisection in tenascin-C-deficient mice. *Acta Histochem* **115**, 865–878, <https://doi.org/10.1016/j.acthis.2013.04.009> (2013).
21. Tancred, T. M., Belch, A. R., Reiman, T., Pilarski, L. M. & Kirshner, J. Altered expression of fibronectin and collagens I and IV in multiple myeloma and monoclonal gammopathy of undetermined significance. *J Histochem Cytochem* **57**, 239–247, <https://doi.org/10.1369/jhc.2008.952200> (2009).
22. Yurchenco, P. D. & Patton, B. L. Developmental and pathogenic mechanisms of basement membrane assembly. *Curr Pharm Des* **15**, 1277–1294 (2009).
23. Korpos, E., Wu, C., Song, J., Hallmann, R. & Sorokin, L. Role of the extracellular matrix in lymphocyte migration. *Cell Tissue Res* **339**, 47–57, <https://doi.org/10.1007/s00441-009-0853-3> (2010).
24. Zhang, L. *et al.* A lateral signalling pathway coordinates shape volatility during cell migration. *Nat Commun* **7**, 11714, <https://doi.org/10.1038/ncomms11714> (2016).
25. Hauser, A. E. *et al.* Definition of germinal-center B cell migration *in vivo* reveals predominant intrazonal circulation patterns. *Immunity* **26**, 655–667, <https://doi.org/10.1016/j.immuni.2007.04.008> (2007).
26. Wang, C. *et al.* The interplay of cell-cell and cell-substrate adhesion in collective cell migration. *J R Soc Interface* **11**, 20140684, <https://doi.org/10.1098/rsif.2014.0684> (2014).
27. Theveneau, E. & Mayor, R. Integrating chemotaxis and contact-inhibition during collective cell migration: Small GTPases at work. *Small GTPases* **1**, 113–117, <https://doi.org/10.4161/sgtp.1.2.13673> (2010).
28. Smith, A., Bracke, M., Leitinger, B., Porter, J. C. & Hogg, N. LFA-1-induced T cell migration on ICAM-1 involves regulation of MLCK-mediated attachment and ROCK-dependent detachment. *J Cell Sci* **116**, 3123–3133, <https://doi.org/10.1242/jcs.00606> (2003).
29. Bardi, G., Niggli, V. & Loetscher, P. Rho kinase is required for CCR7-mediated polarization and chemotaxis of T lymphocytes. *FEBS Lett* **542**, 79–83 (2003).
30. Haddad, E. *et al.* The interaction between Cdc42 and WASP is required for SDF-1-induced T-lymphocyte chemotaxis. *Blood* **97**, 33–38 (2001).
31. Dang, I. *et al.* Inhibitory signalling to the Arp2/3 complex steers cell migration. *Nature* **503**, 281–284, <https://doi.org/10.1038/nature12611> (2013).
32. Nicholson-Dykstra, S. M. & Higgs, H. N. Arp2 depletion inhibits sheet-like protrusions but not linear protrusions of fibroblasts and lymphocytes. *Cell Motil Cytoskeleton* **65**, 904–922, <https://doi.org/10.1002/cm.20312> (2008).
33. Mehes, E. & Vicssek, T. Collective motion of cells: from experiments to models. *Integr Biol (Camb)* **6**, 831–854, <https://doi.org/10.1039/c4ib00115j> (2014).
34. Sumpter, D. J. T. *Collective animal behavior*. (Princeton University Press, 2010).
35. Camazine, S. *Self-organization in biological systems*. (Princeton University Press, 2001).
36. Kubo, R. The fluctuation-dissipation theorem. *Reports on Progress in Physics* **29**, 255–284, <https://doi.org/10.1088/0034-4885/29/1/306> (1966).
37. Te Boekhorst, V., Preziosi, L. & Friedl, P. Plasticity of Cell Migration *In Vivo* and *In Silico*. *Annu Rev Cell Dev Biol* **32**, 491–526, <https://doi.org/10.1146/annurev-cellbio-111315-125201> (2016).
38. Wolf, K., Muller, R., Borgmann, S., Brocker, E. B. & Friedl, P. Amoeboid shape change and contact guidance: T-lymphocyte crawling through fibrillar collagen is independent of matrix remodeling by MMPs and other proteases. *Blood* **102**, 3262–3269, <https://doi.org/10.1182/blood-2002-12-3791> (2003).

39. Renkawitz, J. *et al.* Adaptive force transmission in amoeboid cell migration. *Nat Cell Biol* **11**, 1438–1443, <https://doi.org/10.1038/ncb1992> (2009).
40. Lokmic, Z. *et al.* The extracellular matrix of the spleen as a potential organizer of immune cell compartments. *Semin Immunol* **20**, 4–13, <https://doi.org/10.1016/j.smim.2007.12.009> (2008).
41. Beltman, J. B., Maree, A. F., Lynch, J. N., Miller, M. J. & de Boer, R. J. Lymph node topology dictates T cell migration behavior. *J Exp Med* **204**, 771–780, <https://doi.org/10.1084/jem.20061278> (2007).
42. Scarpa, E. *et al.* Cadherin Switch during EMT in Neural Crest Cells Leads to Contact Inhibition of Locomotion via Repolarization of Forces. *Dev Cell* **34**, 421–434, <https://doi.org/10.1016/j.devcel.2015.06.012> (2015).
43. Zimmermann, J., Camley, B. A., Rappel, W. J. & Levine, H. Contact inhibition of locomotion determines cell-cell and cell-substrate forces in tissues. *Proc Natl Acad Sci USA* **113**, 2660–2665, <https://doi.org/10.1073/pnas.1522330113> (2016).
44. Davis, J. R. *et al.* Inter-cellular forces orchestrate contact inhibition of locomotion. *Cell* **161**, 361–373, <https://doi.org/10.1016/j.cell.2015.02.015> (2015).
45. Lafouresse, F. *et al.* Wiskott-Aldrich syndrome protein controls antigen-presenting cell-driven CD4+ T-cell motility by regulating adhesion to intercellular adhesion molecule-1. *Immunology* **137**, 183–196, <https://doi.org/10.1111/j.1365-2567.2012.03620.x> (2012).
46. Bailly, M. *et al.* The F-actin side binding activity of the Arp2/3 complex is essential for actin nucleation and lamellipod extension. *Curr Biol* **11**, 620–625 (2001).
47. Leithner, A. *et al.* Diversified actin protrusions promote environmental exploration but are dispensable for locomotion of leukocytes. *Nat Cell Biol* **18**, 1253–1259, <https://doi.org/10.1038/ncb3426> (2016).
48. Lammerrmann, T. *et al.* Neutrophil swarms require LTB4 and integrins at sites of cell death *in vivo*. *Nature* **498**, 371–375, <https://doi.org/10.1038/nature12175> (2013).
49. Herault, A. *et al.* Myeloid progenitor cluster formation drives emergency and leukaemic myelopoiesis. *Nature* **544**, 53–58, <https://doi.org/10.1038/nature21693> (2017).
50. Ginelli, F. *et al.* Intermittent collective dynamics emerge from conflicting imperatives in sheep herds. *Proc Natl Acad Sci USA* **112**, 12729–12734, <https://doi.org/10.1073/pnas.1503749112> (2015).
51. Hidalgo-Carcedo, C. *et al.* Collective cell migration requires suppression of actomyosin at cell-cell contacts mediated by DDR1 and the cell polarity regulators Par3 and Par6. *Nat Cell Biol* **13**, 49–58, <https://doi.org/10.1038/ncb2133> (2011).
52. Tinevez, J. Y. *et al.* TrackMate: An open and extensible platform for single-particle tracking. *Methods* **115**, 80–90, <https://doi.org/10.1016/j.ymeth.2016.09.016> (2017).

Acknowledgements

We thank Salvatore Valitutti and Pauline Gonnord for helpful discussion. We also thank Sophie Allart, Astrid Canivet and Danièle Daviaud from the CPTP microscopy platform for expert assistance. This work was supported by the ANR grant TransCoMigr (ANR-13-BSV1-0031) and the INCa grant 2011–148.

Author Contributions


Conceptualization, J.R.B., D.S.C., C.S., G.T. and L.D.; Methodology, J.R.B., D.S.C., Y.G., A.C., C.S. and L.D.; Software, D.S.C., M.M., M.C. and A.C.; Validation, C.S., G.T., and L.D. Formal analysis, J.R.B., D.S.C., M.M. and C.S.; Investigation, J.R.B.; Writing–Original Draft, J.R.B., C.S., G.T. and L.D.; Writing–Review & Editing, J.R.B., D.S.C., X.W., C.S., G.T. and L.D.; Visualization, J.R.B., M.M. and C.S.; Supervision, C.S., G.T. and L.D.; Project Administration, C.S., G.T. and L.D.; Funding Acquisition, G.T. and L.D.

Additional Information

Supplementary information accompanies this paper at <https://doi.org/10.1038/s41598-018-24222-4>.

Competing Interests: The authors declare no competing interests.

Publisher's note: Springer Nature remains neutral with regard to jurisdictional claims in published maps and institutional affiliations.

 **Open Access** This article is licensed under a Creative Commons Attribution 4.0 International License, which permits use, sharing, adaptation, distribution and reproduction in any medium or format, as long as you give appropriate credit to the original author(s) and the source, provide a link to the Creative Commons license, and indicate if changes were made. The images or other third party material in this article are included in the article's Creative Commons license, unless indicated otherwise in a credit line to the material. If material is not included in the article's Creative Commons license and your intended use is not permitted by statutory regulation or exceeds the permitted use, you will need to obtain permission directly from the copyright holder. To view a copy of this license, visit <http://creativecommons.org/licenses/by/4.0/>.

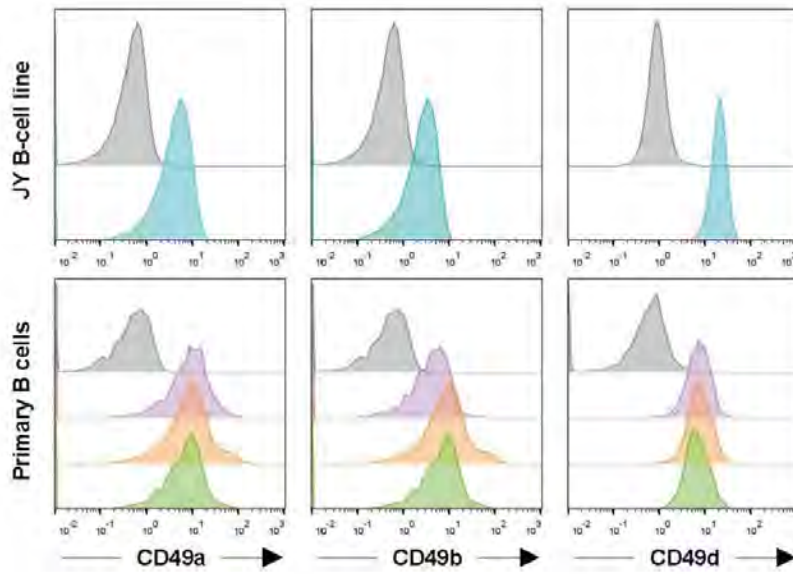
© The Author(s) 2018

**Switching between individual and collective motility in B lymphocytes
is controlled by cell-matrix adhesion and inter-cellular interactions**

Javier Rey-Barroso, Daniel S. Calovi, Maud Combe, Yolla German, Mathieu Moreau, Astrid Canivet, Xiaobo Wang, Clément Sire, Guy Theraulaz and Loïc Dupré

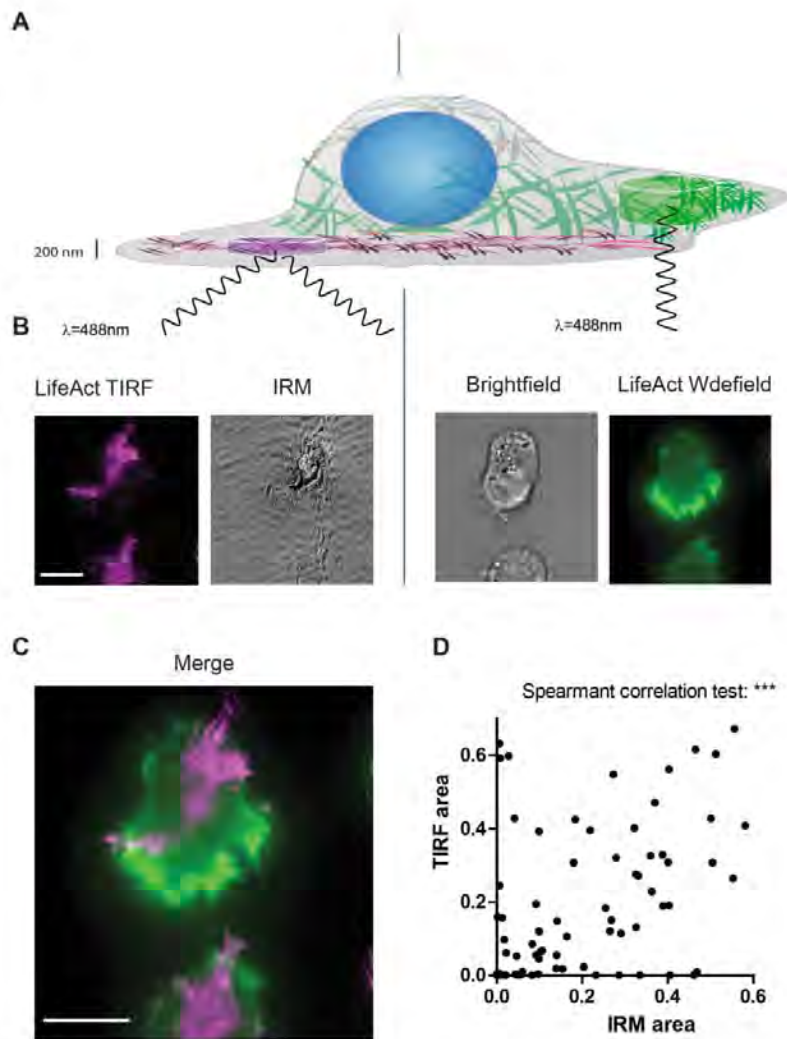
SUPPLEMENTARY INFORMATION

→ Supplementary Figures S1 to S6



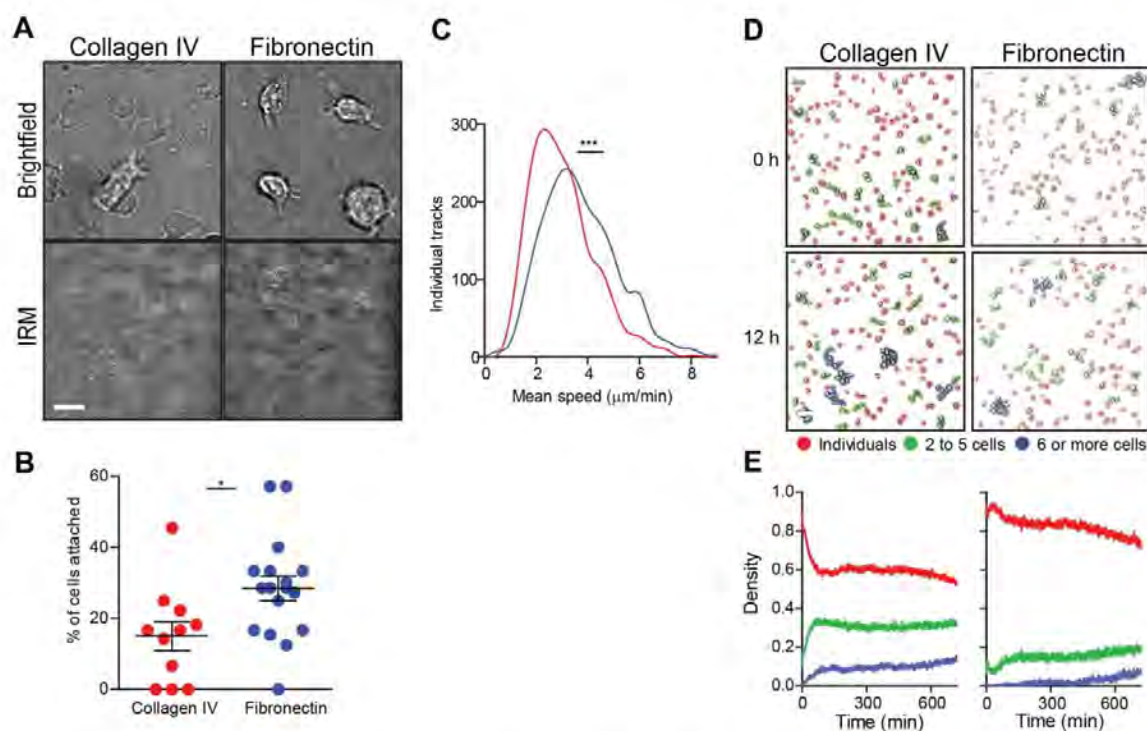
Supplementary Figure S1. B cells from the JY line and primary B cells express comparable and homogeneous levels of integrins.

Expression levels of the integrin alpha chains CD49a, CD49b and CD49d on JY cells or primary B cells from the peripheral blood of three healthy donors were analyzed by flow cytometry and represented as histograms. Negative controls are plotted in grey for comparison.



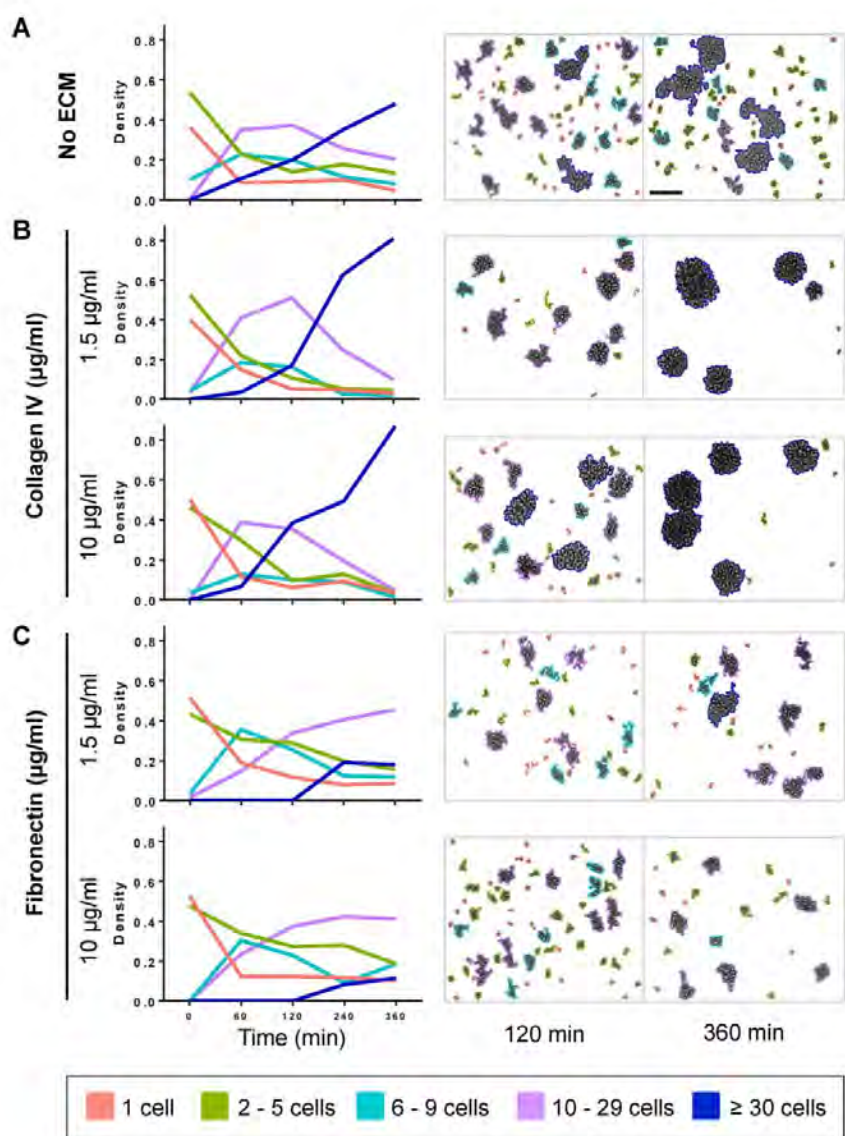
Supplementary Figure S2. Combinatorial microscopy reveals adhesive and protrusive actin modules.

(A) Schematic representation of a LifeAct-GFP expressing cell examined by a real-time microscopy approach combining oblique illumination for TIRF (LifeAct-GFP, represented in magenta) and IRM and widefield illumination (brightfield and LifeAct-GFP, represented in green). (B) Representative LifeAct-GFP expressing JY cell on fibronectin imaged through the combinatorial microscopy approach. Scale bar: 10 μm . (C) Overlay of the LifeAct-GFP images obtained via widefield and TIRF illumination modes. Scale bar: 10 μm . (D) Analysis of the correlation between the LifeAct-GFP TIRF and IRM areas in LifeAct-GFP expressing JY cells ($n=73$ cells).



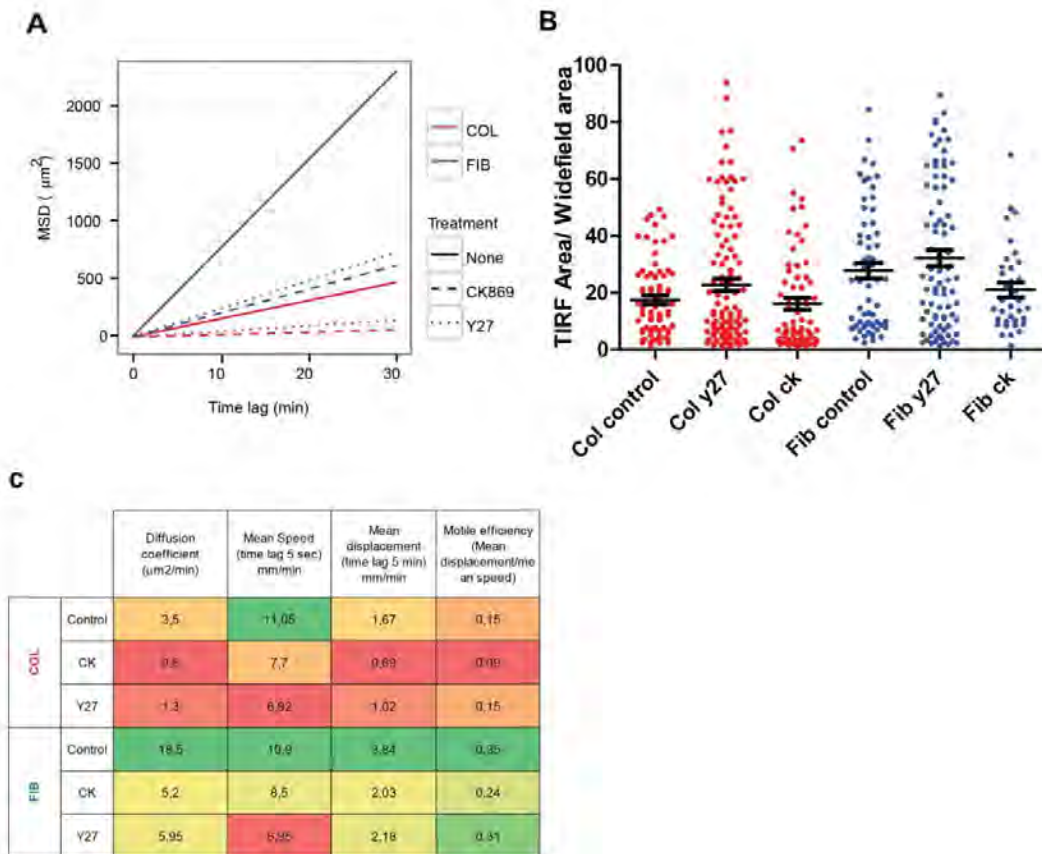
Supplementary Figure S3. Matrix interaction defines primary B cell motility and self-assembly into clusters.

(A) Human primary B cells from peripheral blood stimulated 48 h with CpG2006 were seeded over collagen IV or fibronectin. After 4 h cells were imaged by brightfield and IRM to detect attachment state. **(B)** Quantification of cell attachment to matrix by calculation of percentage of cells showing contact on IRM divided by total number of cells in the image ($n=107$ from 11 images for collagen IV and 137 from 17 images on fibronectin). Bars show mean and SEM. * $p<0.05$, Student-t test. **(C)** Primary B cells seeded over collagen IV or fibronectin were imaged for 12 h and tracks over 10 min recorded and computed. Track mean speed (time lag 30 s) distribution was represented ($n=1694$ and 1687 cells, from two independent experiments) *** $p<0.001$, Student-t test. **(D)** Primary B cells population dynamics over 12 h after seeding over collagen IV or fibronectin at high density were recorded, and individuals, small (2 to 5 cells) and large (6 or more) groups were detected and color coded. Images show a representative population distribution at time 0 and 12 h. **(E)** Evolution of the relative presence of individual and 2 to 5 cell clusters and 6 or more cell clusters (mean from $n=2$ videos).



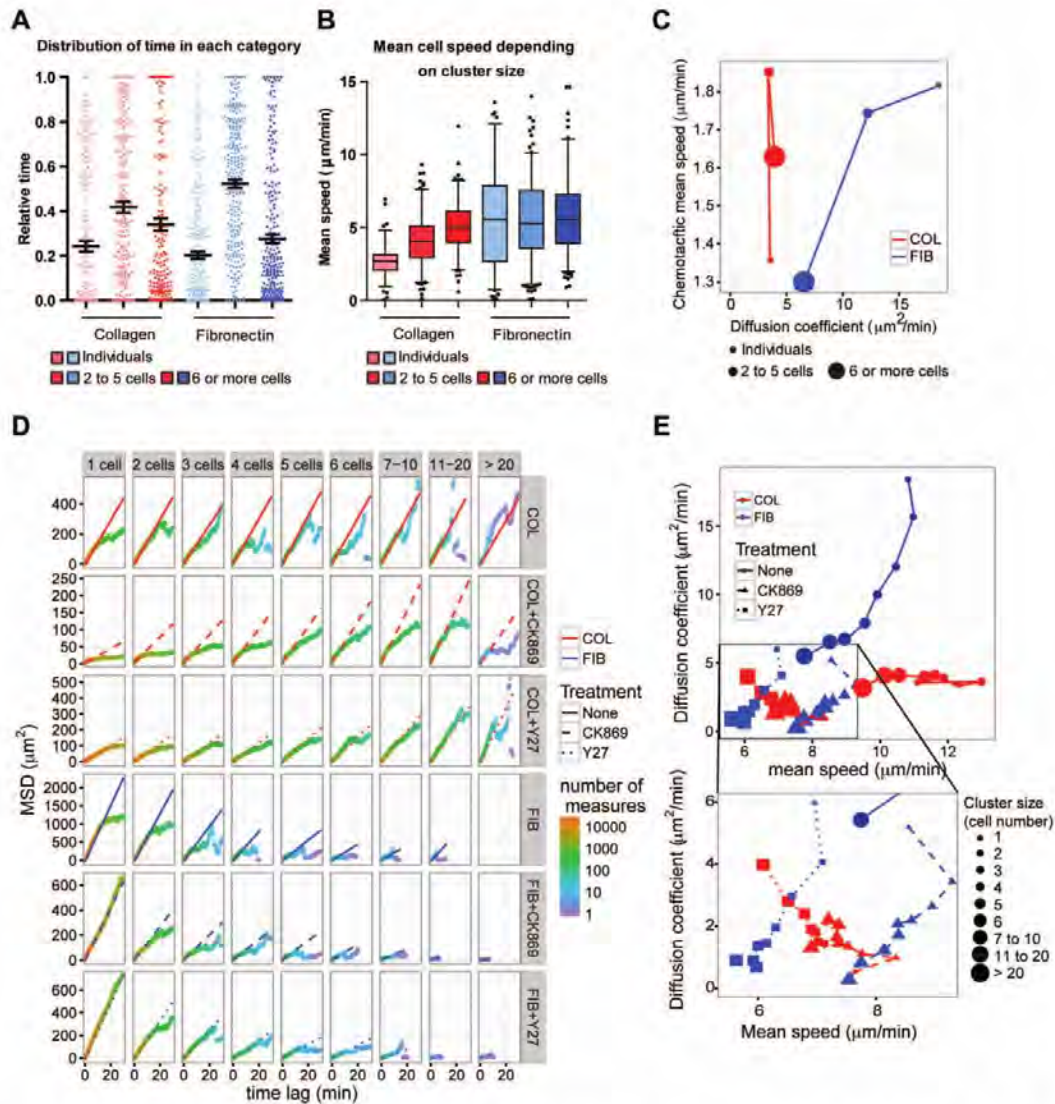
Supplementary Figure S4. Effect of extracellular matrix composition and concentration on lymphocyte assembly into clusters.

JY cells were seeded over (A) plastic, (B) collagen IV (1,5 or 10 µg/ml) or (C) fibronectin (1,5 or 10 µg/ml) and imaged at different time points. Cluster area was recognized and normalized by mean cell size to generate 5 subcategories, as indicated. Relative area covered by each subcategory was calculated and its temporal evolution represented. Representative pictures with colored contours of clusters of each category are shown for each condition at 120 or 360 min. Scale bar, 100 µm. 3 to 6 fields were collected and integrated in the analysis for each condition.



Supplementary Figure S5. Roles of actin branching and actomyosin contraction in lymphocyte attachment and motility.

(A) Tracks from Y27632 or CK869 or non-treated JY individuals seeded over collagen IV or fibronectin were obtained from high cell density videos. All tracks over 1 min were computed for each condition and Mean Square Displacement evolution quantified, fitted and represented. **(B)** Y27632 or CK869 or non treated JY cells were seeded over collagen IV or fibronectin and imaged on TIRF and widefield after 3h. Respective cell areas were calculated and a ratio between them was established and represented. Bars show mean and SEM ($n=79, 119, 76, 65, 89$ and 38 cells). **(C)** Tracks from Y27632 or CK869 or non-treated JY individuals seeded over collagen IV or fibronectin were analyzed to reveal their mean speed. Then diffusion coefficient and mean displacement per min (time lag of 5 min) were extracted from MSD calculation and the motile efficiency was calculated as the ratio between the mean displacement and the mean speed. Results were represented as a table, color-coded respect to their value.



Supplementary Figure S6. Effect of matrix composition on lymphocytes propensity to assemble into clusters or remain isolated, and on their speed during each of these phases.

(A) JY-GFP cells diluted 1/40 into unstained JY were seeded over collagen IV or fibronectin and recorded for 12 h. GFP cells relative time as individual or part of 2 to 5 or 6 or more cells clusters was quantified and plotted ($n=178$ and 250, from three independent experiments). Bars show mean and SEM. (B) Mean speed of JY-GFP cells (considering tracks over 10min) when being isolated or part of clusters was quantified and plotted for each condition ($n=90, 144, 124, 132, 228$ and 177 from a representative experiment). Box and whiskers plot, with a 5 to 95% data range and values out of the range as single points. (C) Cluster size categories in absence of gradient were compiled into the three categories made for gradient experiments and their diffusion coefficient calculated. Plot shows comparison of chemotactic mean speed and diffusion coefficient in the same three categories. (D) MSD of tracks from Y27, CK869 or non-treated JY cell clusters of growing size were obtained from high cell density videos over collagen IV or fibronectin and shown in red or blue, respectively. Color code lines show original values and number of tracks available for each time length. (E) Diffusion coefficients of each cluster category were extracted from previous graph and plotted respect to their mean speed (time lag 5 s).

I contributed to the Guipouy et al. paper by performing the cytotoxicity assays for supplementary figure 2A, which serves as proof that the ova-specific Tregs can kill in an MHC dependent fashion.

For this paper I could use the expertise in cytotoxicity that I had learned from Delphine and apply it to her own project, as well as mine.

Granulysin- and granzyme-dependent elimination of myeloid cells by therapeutic ova-specific type 1 regulatory T cells

Delphine Guipouy¹⁻⁴, Julie Gertner-Dardenne⁴, Laurène Pfajfer¹⁻³, Yolla German¹⁻³, Nathalie Belmonte⁴ and Loïc Dupré^{1-3,✉}

¹INSERM, UMR1043, Centre de Physiopathologie de Toulouse Purpan, Purpan University Hospital, 1 place du Dr Baylac, 31300 Toulouse, France

²Université Toulouse III Paul-Sabatier, 31062 Toulouse, France

³CNRS, UMR5282, 31300 Toulouse, France

⁴TxCell, Allée de la Nertière, 06560 Valbonne Sophia-Antipolis, France

Correspondence to: L. Dupré; E-mail: loic.dupre@inserm.fr

Received 8 February 2018, editorial decision 5 December 2018, accepted 20 December 2019

Abstract

The intrinsic immunosuppressive properties of regulatory T (Treg) cells can be harnessed for therapeutic approaches aiming at down-modulating harmful immune reactions. In this context, expanded type 1 Treg cells (Tr1 cells) specific for ovalbumin (ova-Tr1 cells) have been tested for clinical efficacy in the treatment of autoimmune disorders such as refractory Crohn's disease (CD). The clinical use of these therapeutic products warrants exploration of their mechanism of action. Here, we identified a relationship between the CD activity index and the expression of lytic molecules by the ova-Tr1 cells administered in the previously reported First-in-Man study [Crohn's And Treg cells Study 1 (CATS1) study]. Accordingly, ova-Tr1 cells were found to carry granules containing high levels of lytic molecules, including multiple granzymes and granulysin. These cells displayed a T-cell receptor (TCR)-independent cytotoxic activity, which was preferentially directed toward myeloid cell lines and monocyte-derived dendritic cells. Upon contact with myeloid cells, ova-Tr1 cells induced their apoptosis via a perforin-independent and a granulysin/granzyme-dependent mechanism. As compared to CD8⁺ cytotoxic T cells, ova-Tr1 cells required more time to lyse target cells and displayed a more gradual lytic activity over time. Notably, this activity was sustained over days resulting in the control of myeloid cell populations at a relatively low ratio. Our study reveals that ova-Tr1 cells are endowed with a sustained cytotoxic activity that relies on a unique combination of granulysin and granzymes and that preferentially eliminates myeloid target cells in a TCR-independent manner.

Keywords: cell therapy, crohn's disease, cytotoxic activity, monocytes, Tr1 cells

Introduction

Reinforcing and modulating the immune system has recently become an efficient strategy to tackle the challenges posed by cancers and chronic inflammatory diseases (1–3). Autologous T-cell-based therapies represent one of the immunotherapy approaches being explored today. They include strategies relying on the transfer of either cytotoxic T cells for the elimination of cancer cells (4–6) or regulatory T (Treg) cells to control autoimmune and inflammatory diseases (7, 8). Treg cells are endowed with a suppressive activity (9), which operates through immunosuppressive cytokines (10, 11), metabolism disruption (12) or inhibition of antigen-presenting cell maturation (13). Interestingly, Treg cells can

also mediate a cytotoxic activity toward both effector T cells (14) and myeloid cells, including antigen-presenting cells (15, 16). Importantly, such cytotoxic activity has been reported to be required for the regulatory activity of these cells *in vivo* (17). Type 1 Treg cells (Tr1 cells) are an attractive subset of Treg cells for therapy since they can be generated *in vitro* (18). They also share immunosuppressive and cytotoxic activities (19–21). Nevertheless, the relevance of these activities in the context of therapeutic approaches remains to be evaluated.

An autologous T-cell-based approach consisting of the administration of *in vitro* expanded ovalbumin-specific type

1 Treg cells (ova-Tr1 cells) has been developed for the treatment of Crohn's disease (CD) (20, 22). The phase I/IIa Crohn's And Treg cells Study 1 (CATS1) clinical study showed the safety of this approach in the context of refractory disease and provided a significant clinical improvement in 8 of the 20 treated patients (23). This clinical response was paralleled by a reduction in pro-inflammatory monocytes in the blood of the patients 3 weeks after injection, suggesting that ova-Tr1 cells might dampen CD-associated inflammation via the control of monocytes. In the present study, we explored whether known Tr1-cell-associated mechanisms might contribute to the control of monocytes by ova-Tr1 cells. The phenotypic analysis of markers of the regulatory and cytotoxic activities expressed by the cells administered to CD patients revealed a relationship between levels of cytotoxic molecules and CD activity index (CDAI) reduction. This interrelationship led us to focus on the cytotoxic potential of those cells using a combination of assays based on flow cytometry and quantitative video microscopy (24). Our study demonstrates that therapeutic Tr1 cells are endowed with an alternative cytotoxic activity that eliminates myeloid cells, independently of T-cell receptor (TCR)-mediated signaling, via a granulysin- and granzyme-dependent mechanism.

Methods

Cells

Ova-Tr1 cells. The expansion process of autologous ova-Tr1 cells was optimized from the phase I/IIa study for a phase IIb clinical trial to prevent adverse effects from residues of feeder cells (22). Ova-Tr1 cells were produced using an ex vivo cell culture process, which generates ova-specific T lymphocytes in 8–10 weeks. Peripheral blood mononuclear cells (PBMCs) from individual donors were used as source of ova-Tr1 cells for the manufacturing of the drug substance. Donor PBMCs were enriched in autologous antigen-specific T cells by stimulation with ovalbumin (ova). After limiting dilution plating of the resulting activated cells, T cells demonstrating specificity to ovalbumin and production of ova-Tr1 cytokines were selected for additional expansion and processing. Expansion relied on a stimulation with anti-CD3 and anti-CD28 antibodies in the presence of rIL-2 and rIL-4 (both from Miltenyi). The final drug product consisted of the expanded ova-Tr1 cells that were formulated in a cryopreservation medium, put in vials and frozen.

CD8⁺ cytotoxic T lymphocytes. To generate control cytotoxic T lymphocytes (CTLs), CD8⁺ T cells were sorted from healthy donor PBMCs with a FACS Aria sorter (BD Biosciences) and cloned. CTL clones were cultured in RPMI 1640 glutamax (Gibco) supplemented with 5% human serum (PAA), 100 $\mu\text{g ml}^{-1}$ penicillin/streptomycin, 10 mM HEPES, 0.1 mM minimum essential medium (MEM) non-essential amino acids and 1 mM sodium pyruvate (Invitrogen) and stimulated every 2 weeks with irradiated PBMCs and Epstein-Barr virus-transformed JY cells in the presence of 1 $\mu\text{g ml}^{-1}$ phytohaemagglutinin (PHA), 100 IU ml^{-1} rIL-2 and 5 ng ml^{-1} rIL-15. Control Foxp3⁺ Treg cells were isolated from healthy donor PBMCs on the basis of the expression CD4⁺ CD127^{low} CD25⁺ (EasySep Stemcell isolation kit) according to the manufacturer's protocol.

Target cells. The U937 (ATCC), THP1 (ATCC), JY (ATCC) and K562 cell lines were cultured in RPMI (Gibco) supplemented with 10% fetal calf serum (FCS; PAA) and the components described above. The P815 cell line was cultured in Dulbecco's Modified Eagle's medium (Gibco) supplemented with 10% FCS (PAA) and the components described above. Primary dendritic cells (DCs) were obtained from monocytes following isolation of PBMCs from a healthy donor and 1-h adherence in a flask. DC differentiation was induced during 6 days of culture in RPMI supplemented with 10% FCS and in the presence of 750 IU ml^{-1} granulocyte-macrophage colony-stimulating factor and 100 IU ml^{-1} rIL-4. Where indicated, immature DCs were treated with 1 $\mu\text{g ml}^{-1}$ of lipopolysaccharide to obtain mature DCs.

Phenotypic characterization

Ova-Tr1 cells and Foxp3⁺ Treg cells were stained for extracellular markers with fluorochrome-coupled antibodies recognizing CD4-VioBlue (VIT4, Miltenyi), CD25-APC (4E3, Miltenyi), CD62L-FITC (145/15, Miltenyi), CD127-PE (MB15-18C9, Miltenyi), CTLA-4-PE (BNI3, Miltenyi), ICOS-PECy7 (ISA-3, eBioscience), GITR-AF488 (eBioA1TR, eBioscience), PD-1-PE (PD1.3.1.3, Miltenyi) and CD39-PE (MZ18-23C8, Miltenyi) for 30 min at 4°C. Intracellular staining was performed after fixation and permeabilization using the Cytofix/Cytoperm kit (BD) with the following antibodies: Foxp3-APC (3G3, Miltenyi), perforin-APC (delta G9, Miltenyi), granulysin-AF488 (RB-1, BD Pharmingen), granzyme A-FITC (CB9, BD Pharmingen), granzyme B-PE (GB-11, BD Pharmingen), granzyme H-PE (03, Interchim), granzyme K-efluor660 (G3H69, eBioscience) and granzyme M (rabbit, polyclonal, ClineSciences). For granzyme M staining, a goat anti-rabbit secondary antibody (ClineSciences) coupled with FITC was added. All data were acquired on a Macsquant 10 cytometer and analyzed using MacsQuantify software (Miltenyi).

Phospho-ZAP-70 staining

Control CD4⁺ T cells were stimulated for 30 min with anti-CD3/CD28 beads (1:1 ratio). Ova-Tr1 cells were used upon thawing and harvested from the culture every 3 days (in parallel with the cytotoxic assays performed on the same days). After washing, a first step of fixation with 4% paraformaldehyde (PFA) was performed at room temperature (RT) for 10 min, followed by a permeabilization step with 90% methanol at -20°C overnight. A rabbit polyclonal antibody for phospho-ZAP-70 (Tyr493, Cell Signaling Technology) was used at a dilution of 1:25 for 45 min at RT, then revealed by a secondary anti-rabbit IgG antibody coupled with AF647 (Invitrogen) at a dilution 1:400 for 30 min at RT. Data were acquired on a Macsquant 10 cytometer (Miltenyi) and analyzed using FlowJo software.

Cytotoxic assays

Ova-Tr1 cells were co-incubated with various target cells, at 1:1, 5:1 and 10:1 effector to target cell ratios (reference number of 25,000 target cells against 25,000, 125,000 and 250,000 effector cells). Cells were pelleted for 1 min at 1500 rpm and incubated at 37°C/5% CO₂ from 4 to 72 h. Aphidicolin (Sigma) was used at 0.2 $\mu\text{g ml}^{-1}$ during the assay to block target cell proliferation for all target cell lines, but not primary cells. When indicated, blocking antibodies were used at the

concentration of 10 $\mu\text{g ml}^{-1}$ (anti-DNAM-1, -FasL, -Trail and -HLA-DP/DQ/DR) (25–27). Anti-DNAM-1 (102511), -FasL, (NOK-1) -Trail (RIK2) and -HLA-DP/DQ/DR (7-5-10-1) monoclonal antibodies (mAbs) were purchased from R&D Systems, Thermo Fischer Scientific, BioLegend and Antibodies-online, respectively. The cytotoxic activity was assessed by quantifying the number of residual alive target cells as described previously (24). These data were acquired on a Macsquant 10 and VYB cytometers (Miltenyi) and analyzed using FlowJo software.

Live microscopy recording of cytotoxic activity

Cytotoxic activity was monitored by microscopy in eight-well IBIDI chambers coated with 10 $\mu\text{g ml}^{-1}$ of fibronectin (Sigma-Aldrich) for 1 h at 37°C/5% CO₂. Effector cells were pre-stained with CellTracker green CMFDA dye (Invitrogen) for 30 min at 37°C/5% CO₂ or CellTrace Calcein red/orange dye (Invitrogen) and then transferred into an IBIDI eight-well chamber together with U937 cells. A 2 μM concentration of NucView 488 caspase-3 substrate (Biotium) or a 200 μM concentration of propidium iodide (PI; Sigma) was added. The cells were imaged at a frame rate of 3 min for NucView experiments or 2 min for PI experiments, using a Leica SP8 confocal microscope equipped with a chamber set at 37°C/5% CO₂ and a 20 \times (0.8 NA) objective. To automatically count caspase-3⁺ cells through time, images were binarized and further processed using erosion, dilatation and watershed tools from the ImageJ software (National Institutes of Health). The percentage of caspase-3⁺ cells was calculated based on the number of alive target cells enumerated at the beginning of the recording. Measurements of interaction time and PI entry delay were done by cropping regions of interest containing isolated conjugates made of one T cell and one target cell.

Analysis of lytic granules by confocal microscopy

Ova-Tr1 cells were seeded onto poly-L-lysine-coated slides. Cells were fixed with 4% PFA for 10 min at 37°C, washed with phosphate-buffered saline (PBS) 3% bovine serum albumin (BSA) and permeabilized with PBS 3% BSA 0.1% saponin for 15 min at RT. F-actin was stained with phalloidin-AF555 for 1 h at RT. Granulysin and granzyme B were revealed with coupled-mAb (anti-granulysin-AF488, RB-1 and anti-granzyme B-AF647, GB-11 both from BD Pharmingen). LAMP-1 was first stained with a primary rabbit antibody (Abcam), then revealed by a goat anti-rabbit-AF405 secondary antibody (Invitrogen). Slides were mounted with Vectashield mounting medium (Vector Laboratories). Images were acquired on a LSM 710 confocal microscope equipped with a 63 \times (1.4 NA) oil immersion Plan-Apochromat objective (Carl Zeiss AG).

SiRNA transfection

Ova-Tr1 cells were harvested and re-suspended in OPTI-MEM medium at 1.10⁶ cells in 100 μl and transferred in a 2 mm cuvette (Bio-Rad) alone or together with 2 μg final either of two control SiRNA or three SiRNA targeting granulysin (Life Technologies, ID 17933, 18028 and 135803). The transfection was performed by electroporation using the Gene Pulser

system (Bio-Rad) with the square wave program: 300 V and 1 pulse of 2 ms. Cells were immediately put back in culture in their culture medium added with cytokines.

Suppression assays

Conventional T cells (Tconv) consisted of CD4⁺ T-cell blasts generated from human PBMCs with a PHA/IL-2 stimulation. Tconv cells were stained with CellTrace Violet (CTV, ThermoFisher Scientific) while Ova-Tr1 cells were stained with CMFDA (ThermoFisher Scientific). The Tconv and ova-Tr1 cells were plated at the indicated ratio, in the presence of IL-2 (100 U ml⁻¹ final) and in the presence or not of anti-IL-10 antibody (40 $\mu\text{g ml}^{-1}$) (Miltenyi, clone JES3-9D7). For the stimulation, CD3/CD28-coated beads were added to the wells at a bead/Tconv cell ratio of 1:2. After 96 h of incubation, each condition was acquired using a MACSQuant10 cytometer and analyzed using FlowJo software.

To assess the suppressive activity of Ova-Tr1 cells toward T_H17 CD4⁺ T cells, CD4⁺ T cells were purified from human blood and cultured in T_H17-skewing conditions. These T_H17 CD4⁺ T cells were characterized by *RORC* expression and IL-17A production, as measured by RT-PCR and ELISA, respectively. During the differentiation process, these cells were exposed to the culture supernatant of ova-Tr1 cells that had been stimulated for 48 h with anti-CD3/CD28 antibody-coated beads. *RORC* expression and IL-17A production were compared to the basal levels in order to assess the suppressive activity of different Ova-Tr1 cells.

Statistical analysis

Statistical analyses were performed using GraphPad software. Statistical significance was determined by performing a one sample *t*-test or a two-tailed unpaired *t*-test, as indicated. Graphs show mean values \pm SEM. Resulting *P* values are indicated as follows: ns *P* > 0.05; *0.01 < *P* < 0.05; **0.001 < *P* < 0.01; ***0.0001 < *P* < 0.0001; *****P* < 0.0001.

Results

Expression of granzymes and granulysin by ova-Tr1 cells is linked to clinical response in CD patients

In order to get insight into the mechanism by which ova-Tr1 cells might control refractory CD in the context of adoptive cell therapy, we analyzed the expression of molecules known to mediate regulatory and cytotoxic activities in these cells. Ova-Tr1 cells were defined as CD4⁺ T cells expressing high levels of CD25 but low or undetectable expression of Foxp3 and CD62L, in contrast to thymus-derived Treg cells (Fig. 1A). As previously described, ova-Tr1 cells secreted high amounts of IL-10 and IL-13, low amounts of IFN- γ , but no IL-4 (23). This analysis also confirms that these cells harbor a Tr1 cytokine profile (19, 28). Analysis of immune checkpoint surface molecules on ova-Tr1 cells showed expression of ICOS and GITR but low levels of CTLA-4 and PD-1. Furthermore, ova-Tr1 cells expressed high levels of the ATP-degrading ectonucleotidase CD39 (29). The suppressive ability of ova-Tr1 cells was first tested as their capacity to inhibit the proliferation of Tconv cells (Supplementary Figure S1A). A partial control of Tconv

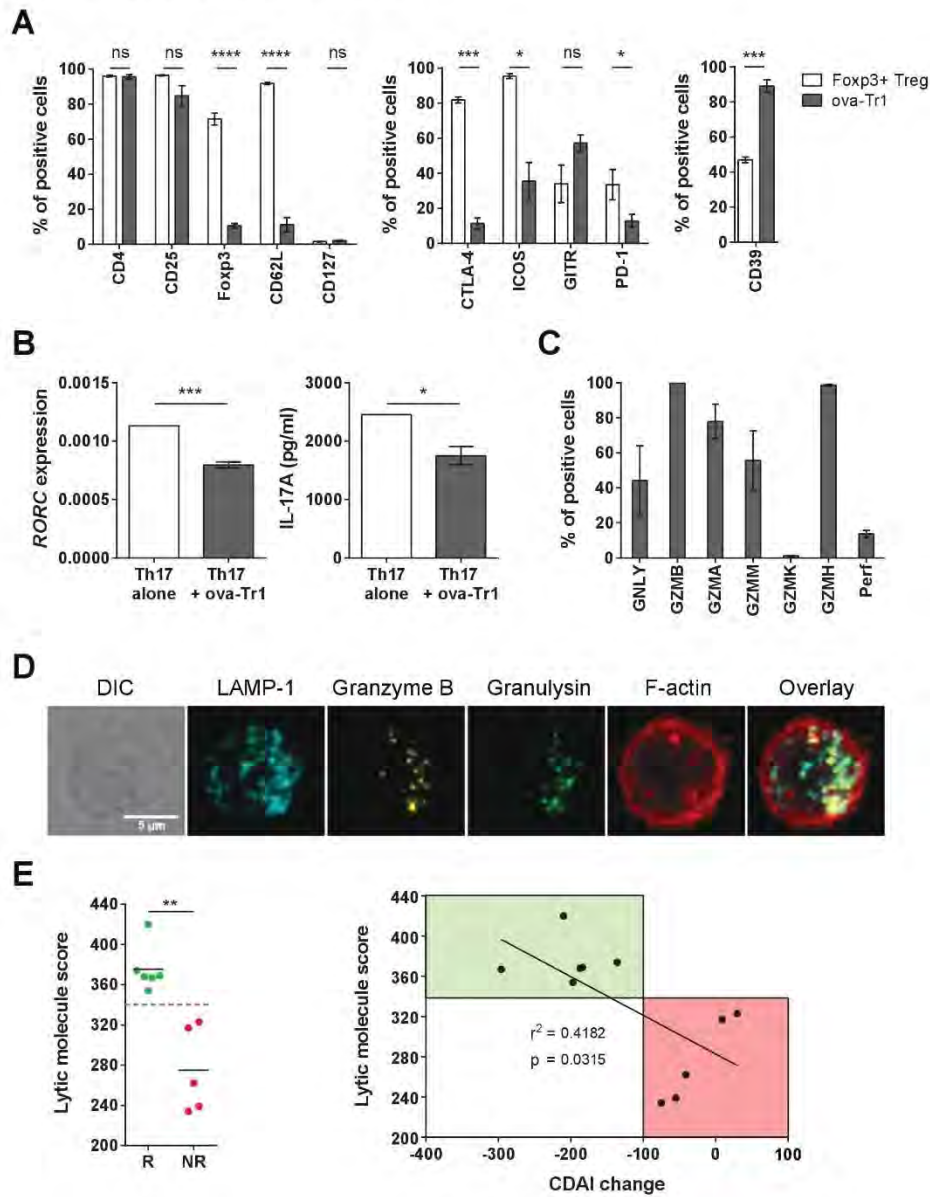


Fig. 1. Phenotypic characterization of ova-Tr1 cells produced for cellular therapy. (A) Expression of characteristic markers of Treg cells, as indicated. Mean \pm SEM, $n = 2$ for control Foxp3⁺ Treg cells and $n = 6$ for ova-Tr1 clones. (B) Suppressive activity of four ova-Tr1 clones toward a test T_H17 cell line, measured as *RORC* mRNA expression and IL-17A production. The white bars indicate reference values for untreated T_H17 cells while the black bars represent mean \pm SEM values following exposure with supernatants from four ova-Tr1 clones. (C) Expression of lytic molecules measured by flow cytometry, shown as percentage of positive cells. Mean \pm SEM, $n = 6$ ova-Tr1 clones. (D) Visualization of granzyme B and granulysin together with LAMP-1 by confocal microscopy, represented as a maximum intensity projection of a z-stack acquisition through the entire cell. (E) Compiled expression of lytic molecules (addition of percentages of positive cells for each lytic molecule) in ova-Tr1 cells transfused to responder (green) and non-responder (red) patients from the CATS1 phase II/IIa clinical trial. CD4I change corresponds to the difference of CD4I scores at the beginning and the end of the trial. Statistical significances were obtained with unpaired *t*-tests (A and E) or a one sample *t*-test (B). ns $P > 0.05$; * $0.01 < P < 0.05$; ** $0.001 < P < 0.01$; *** $0.0001 < P < 0.001$; **** $P < 0.0001$.

cell proliferation was observed at the 10:1 ova-Tr1:Tconv ratio. This suppressive activity appeared to not depend on IL-10 as indicated by the apparent lack of effect of anti-IL-10 antibody treatment (Supplementary Figure S1B). Given the central role of T_H17 cells in CD inflammation, we then tested the ability of ova-Tr1 cells to counteract T_H17 cell differentiation. For that purpose, we applied the culture supernatant of ova-Tr1 cells that had been stimulated with anti-CD3/CD28 antibody-coated beads onto purified CD4⁺ T cells cultured in T_H17 -skewing conditions (Fig. 1B). The supernatants of ova-Tr1 cells dampened both the expression of *RORγ* and the production of IL-17A. Together these data show that ova-Tr1 cells have a moderate suppressive activity toward Tconv cell proliferation and T_H17 cell differentiation.

Tr1 cells have been shown to also mediate their suppressive function via the release of lytic molecules, including granzyme B and perforin (21). We checked the expression of all described granzymes (A, B, H, K and M), as well as perforin and granulysin in the ova-Tr1 cells (Fig. 1C). The tested clones consistently expressed high levels of granzymes A, B, H and M but almost no granzyme K. Interestingly, while the ova-Tr1 cells expressed very low levels of perforin, they expressed granulysin, a cytotoxic molecule that was recently described to be able to cooperate with granzymes to kill pathogens (30). We then studied these cells by confocal microscopy to investigate whether the identified lytic molecules would be localized in granules as expected for cytotoxic T cells. Our analysis confirms the expression of granzyme B and granulysin and shows that these molecules colocalized with the lysosomal marker LAMP-1 (Fig. 1D). Together, these data indicate that ova-Tr1 cells harbor a cytotoxic potential, although they express very low levels of perforin.

Our characterization of the ova-Tr1 cells points to their potential to control inflammatory responses such as those underlying CD *via* suppression of pathogenic T cells and/or *via* a cytotoxic mechanism. We therefore investigated, retrospectively, in the remaining drug products from CATS1 study patients whether the expression of markers of these activities might correlate with the change in CDAI scores. Ova-Tr1 cells infused to patients were studied for the expression of several markers of immunosuppressive and cytotoxic functions, such as costimulatory molecules, CD39, various chemokines receptors, as well as IL-10 secretion. Moreover, the proportion of cells expressing granzymes (A, B, H, K and M), perforin and granulysin was monitored by flow cytometry (representative dot plots are presented in Supplementary Figure S1C) and compiled into a lytic molecule score corresponding to the sum of the percentages of cells expressing each of the lytic molecules separately. This score was compared to the patient CDAI change reached at 5 weeks after injection, when the peak of response was observed in CATS1 (Fig. 1E). A clinical response was defined as a reduction of at least 100 points of the patient CDAI score. The analysis revealed that the lytic molecule score of the infused cells was associated with the clinical response. Indeed, responder patients displayed high lytic molecule scores. In contrast, non-responder patients displayed lower lytic molecule scores than responder patients. While the expression of lytic molecules appeared to be related to the clinical response, we failed to detect any relationship between markers of

immunosuppressive functions and the CDAI of the infused patients (data not shown). Together, these data indicate that the *in vivo* efficacy of ova-Tr1 cells in the context of CD might be related to the cytotoxic potential of these cells, on the basis of their high expression of numerous granzymes and granulysin. This observation raises the question as to whether ova-Tr1 cells are endowed with a lytic activity and, if so, which pathogenic cells they might target.

Ova-Tr1 cells preferentially eliminate myeloid cells independently from TCR re-stimulation

We tested the intrinsic cytotoxic activity of ova-Tr1 cells against various hematopoietic cell lineages using a cytometry-based method designed to assess both short-term and long-term cytotoxic activity at reduced effector to target cell ratios (24). Although ova-Tr1 cells displayed only minimal elimination of the myeloid cell lines U937 and THP1 in a 4-h assay, they efficiently eliminated these cells over 24 h, in a ratio-dependent manner (Fig. 2A). The ability of ova-Tr1 cells to eliminate myeloid cells was confirmed with the use of primary cells. Indeed, ova-Tr1 cells efficiently eliminated monocyte-derived DCs, independently from their maturation status. Ova-Tr1 cells displayed only minimal effects on the viability of cells belonging either to the granulocytic series (K562 cells), the B cell lineage (JY cells) or the T-cell lineage (primary CD8⁺ T cells) (Fig. 2B). Therefore, the cytotoxic activity of ova-Tr1 cells appears to be preferentially directed toward cell lines and primary cells belonging to the monocytic lineage. To further dissect the cytotoxic activity of ova-Tr1 cells, we chose to use the U937 cell line as a model. In the clinical setting, frozen batches of ova-Tr1 cells are thawed and directly administered to patients. We assessed how long the cytotoxic property of ova-Tr1 cells would be maintained in that setting (Fig. 2C). Upon thawing, ova-Tr1 cells displayed a low, but detectable, target cell reduction activity at 4 h, which strongly increased at 24 h. This cytotoxic activity was maintained over the 9 days of *in vitro* culture. To further evaluate their functional stability, ova-Tr1 cells were re-stimulated with anti-CD3- and anti-CD28-coated beads. Three days after stimulation, ova-Tr1 cells remained as efficient at eliminating U937 cells as they were following thawing. Remarkably, the lytic activity of ova-Tr1 cells appeared to not require TCR triggering upon target cell encounter. This notion was reinforced by the fact that addition of a pan blocking antibody against HLA-DP/DQ/DR failed to inhibit ova-Tr1 cell mediated cytotoxicity (Supplementary Figure S2A). The independence from TCR triggering might be explained by a tonic status of the TCR. In support of this hypothesis, ova-Tr1 cells displayed a high level of phosphorylated form of Zap-70 upon thawing, after 9 days of *in vitro* culture and after re-stimulation (Supplementary Figure S2B and C). Together, these data indicate that the TCR-independent cytotoxic activity of ova-Tr1 cells directed toward myeloid cells is a very stable property that is not affected by *in vitro* culture nor by re-stimulation.

Gradual onset of lytic activity by ova-Tr1 cells against myeloid cells

Given the increase in cytotoxic activity measured between 4 and 24 h of co-culture with the target cells, we investigated

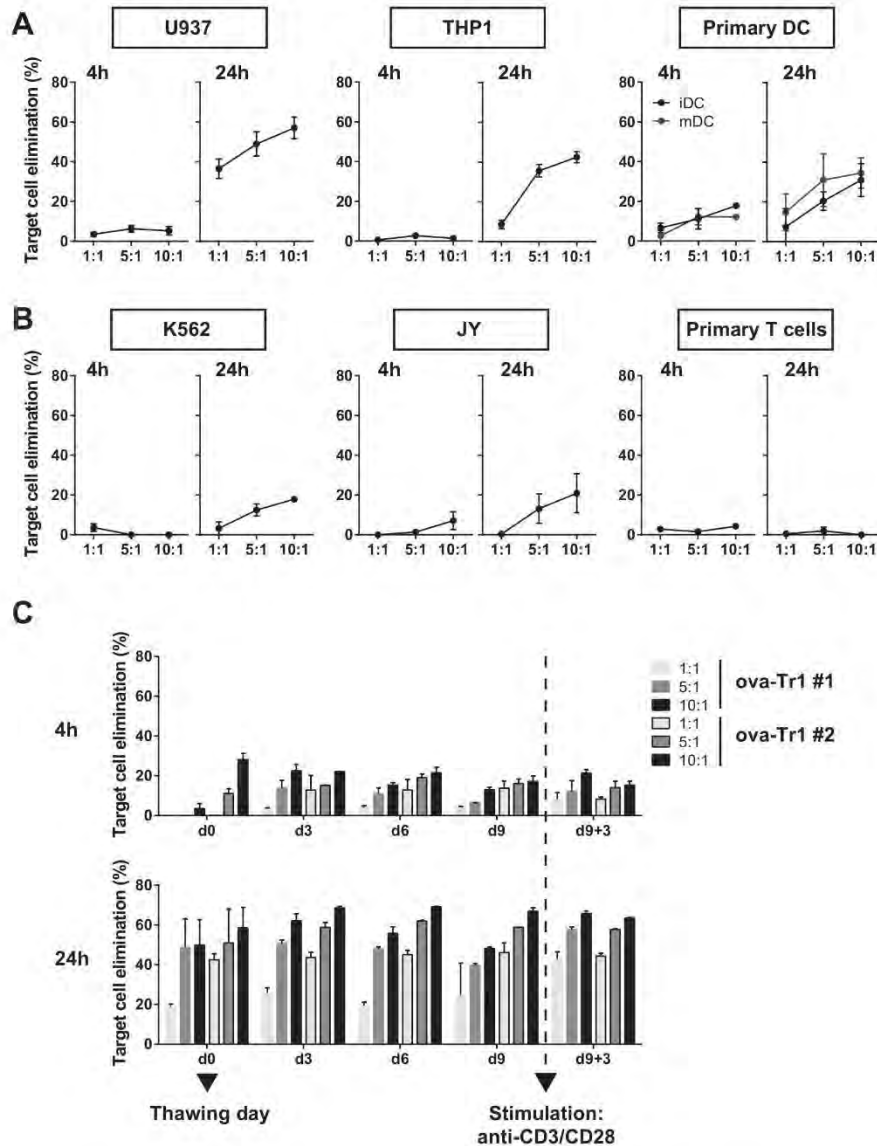


Fig. 2. Ova-Tr1 cells preferentially kill myeloid cells. (A) Short-term (4 h) and long-term (24 h) killing assay against different myeloid cell lines (U937, THP1) and primary monocyte-derived myeloid cells (iDC and mDC). Mean \pm SEM $n = 4$ ova-Tr1 clones. (B) Short-term (4 h) and long-term (24 h) killing assay against a granulocyte cell line (K562), a lymphoid cell line (JY) and primary CD8⁺ T cells. Mean \pm SEM $n = 4$ ova-Tr1 clones. (C) Sustainment of lytic activity by ova-Tr1 cells during a cycle of *in vitro* culture, from thawing up to after re-stimulation, against U937 target cells. Mean \pm SD of an experiment in duplicates with $n = 2$ ova-Tr1 clones.

the kinetics of the ova-Tr1 cell cytotoxic activity by monitoring the events of U937 cell death by live microscopy (Fig. 3A and B). For that purpose, U937 cells were loaded with the NucView fluorescent probe that reveals caspase-3 activation. We used this approach to compare in parallel the cytotoxic

activity of ova-Tr1 cells, CTLs and Foxp3⁺ Treg cells. As expected, CTLs did not display any cytotoxic activity toward U937 cells without an exogenous stimulus. However, in the presence of anti-CD3 antibody, expected to bind Fc receptors on the target cells (31), they eliminated a high proportion

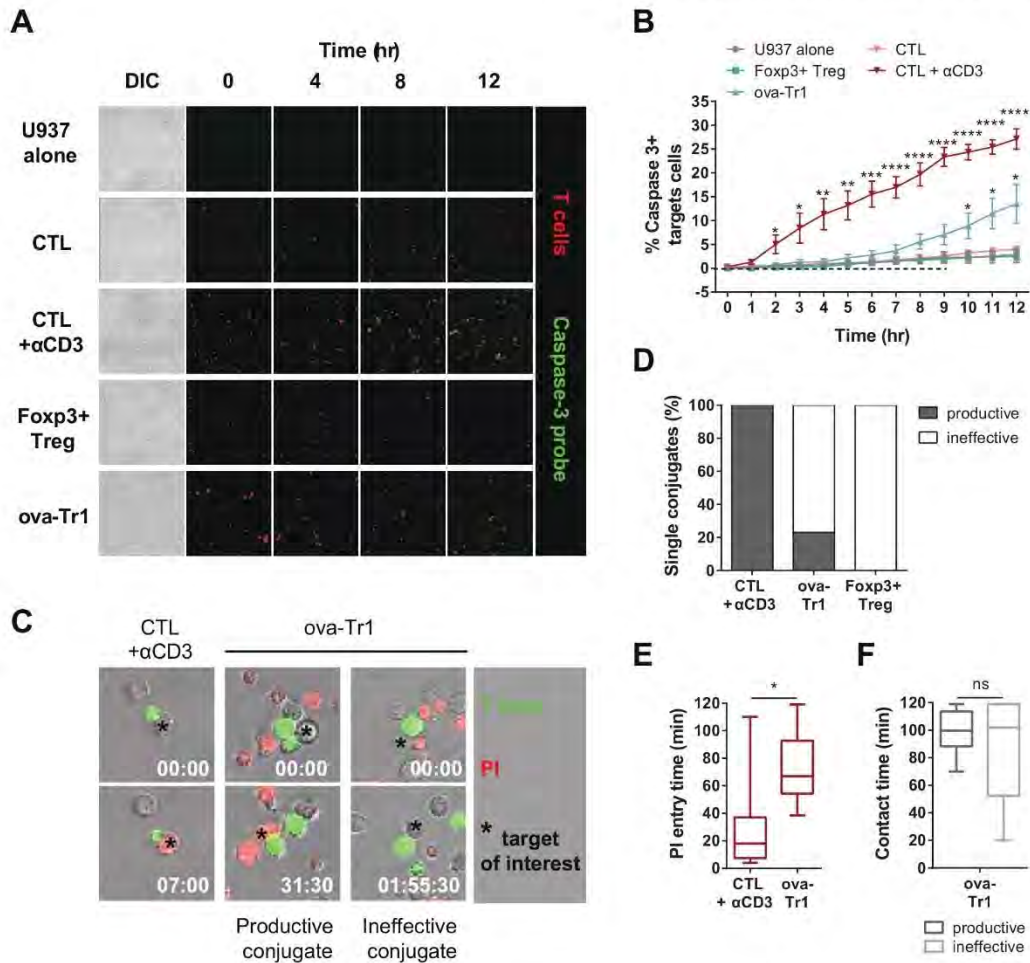


Fig. 3. Killing kinetics of ova-Tr1 cells. Target U937 cells were seeded in the presence of ova-Tr1 cells, Fxp3⁺ Treg cells or CTLs (red) at an E:T ratio of 1:1 for 12 h. The Nucview 488 caspase-3 substrate was used to track individual target cell apoptosis by live microscopy. (A) Representative snapshots showing the activation of caspase-3⁺ target cells after co-culture with the indicated effector cells. (B) Quantification of videos as the percentage of target cells activating caspase-3 over time. Mean \pm SEM of $n = 2$ experiments in triplicates. The same experiment for 2 h, PI was used to track the lethal hit delivery by live microscopy. (C) Representative snapshots showing conjugates triggering PI entry in the target cell. $n = 26$ conjugates per T-cell type. (E) Delay between the first contact with the target cell and PI entry. (F) Contact time with target cells, either for 'productive' or 'ineffective' contacts. Statistical significances were calculated with unpaired *t*-tests. ns $P > 0.05$; * $0.01 < P < 0.05$; ** $0.001 < P < 0.01$; *** $0.0001 < P < 0.001$; **** $P < 0.0001$.

of target cells within a few hours. Distinctly from CTLs, ova-Tr1 cells were able to activate caspase-3 in U937 cells without addition of anti-CD3 antibody. This apoptosis activation further demonstrates that ova-Tr1 cells are endowed with a cytotoxic activity leading to the apoptosis of myeloid target cells. The cytotoxic activity of ova-Tr1 cells was characterized by a slow onset followed by a gradual increase of apoptotic target cells. As an additional control, we tested the ability of Fxp3⁺ Treg cells to eliminate U937 cells. However, Fxp3⁺

Treg cells did not display any lytic activity in this experimental model system.

To further explore the mode of action of ova-Tr1-cell-mediated elimination of myeloid target cells, we performed live microscopy experiments in the presence of a high concentration of PI to reveal target cell membrane permeabilization as a consequence of a lethal hit delivery (32). These experiments reveal that upon contact with U937 cells, ova-Tr1 cells were able to deliver a lethal hit, confirming their identity as genuine

cytotoxic T cells (Fig. 3C). However, while every CTL forming a conjugate with a U937 cell, in the presence of an anti-CD3 antibody, led to an event of PI burst within 2 h, only one fourth of the ova-Tr1 cells were able to do so (Fig. 3D). The limited proportion of ova-Tr1 cells demonstrating a killing activity within the 2-h observation time frame might be explained by the increased delay with which they eventually killed target cells. Indeed, the time between contact and PI entry was on average 65 min for ova-Tr1 cells as compared to 20 min for CTLs (Fig. 3E). The ova-Tr1 cells that did not kill within the 2-h time frame formed conjugates with U937 cells that were as prolonged as some from killer cells, thereby excluding the failure to recognize target cells as a reason for the lack of cytotoxicity (Fig. 3F). As expected from the previous set of experiments, Foxp3 Treg cells failed to induce a detectable PI burst in the U937 cells, confirming the specificity of ova-Tr1 cells in the killing of myeloid target cells. In conclusion, the gradual onset of U937 cell lysis by ova-Tr1 cells observed at the population level might be explained, at least in part, by a delay between initial contact and lethal hit delivery.

Ova-Tr1 cells sustain their lytic activity toward myeloid cells over days

Given the gradual onset of lytic activity in the ova-Tr1 cells, we investigated their ability to control myeloid cell populations over prolonged interaction times. For this purpose, ova-Tr1 cells were co-cultured with U937 cells for 4, 24, 48 and 72 h at the E:T ratios of 1:1, 5:1 and 10:1. Several of the ova-Tr1 clones tested demonstrated a cumulative killing activity over 48–72 h, leading to near elimination of the U937 cell population at the 10:1 ratio in the absence of exogenous TCR stimulation (Fig. 4A). A CTL clone tested in parallel as a control displayed only minor spontaneous killing activity toward the U937 cells. Although ova-Tr1 cells did not require TCR triggering to eliminate U937 cells, we tested whether TCR triggering might potentiate the cytotoxic activity of these cells. Upon addition of anti-CD3 antibodies, the five tested clones displayed increased cytotoxic activity toward the U937 cells (Fig. 4B). Indeed, the exogenous trigger of the TCR in ova-Tr1 cells raised their killing kinetics and increased their overall efficiency at a low E:T ratio. Remarkably, two of the five tested clones displayed comparable killing kinetics and efficiency as the CTL clone tested in parallel. The potentiating effect of the anti-CD3 antibody might be explained by an accelerated onset of the lytic activity, as observed by video microscopy (Supplementary Figure S3A). This was related to a slight increase in the proportion of ova-Tr1 cells that inflicted a PI burst in their opposing target cells (Supplementary Figure S3B) and to a trend toward shortened lethal hit delivery (Supplementary Figure S3C). This analysis highlights the fact that the cytotoxic activity of ova-Tr1 cells against myeloid cells is sustained over days and can be potentiated upon TCR triggering.

The cytotoxic activity of ova-Tr1 cells is mediated by granzymes and granulysin

To further elucidate the mechanism of action of ova-Tr1 cells, we investigated which effector molecules might mediate their

cytotoxic activity. The relatively slow, gradual and sustained activity is suggestive of a lytic molecular pathway relying on 'low triggering' death receptors such as TRAIL or Fas/FasL. To test this hypothesis, we performed cytotoxic assays in the presence or absence of blocking antibodies against TRAIL and FasL (Fig. 5A and B). Neither antibody inhibited the cytotoxic activity of the ova-Tr1 cells, implying that the corresponding molecular pathways are not involved in this process. DNAM-1 has previously been identified as the major trigger of the lytic activity of Tr1 cells (21). However, this receptor appeared not to be involved in the cytotoxic activity of the ova-Tr1 cells since the blocking antibody approach also failed to affect this activity (Fig. 5C), although it was able to reduce the lytic activity of NK-92 cells used as a control (Supplementary Figure S4A).

We have previously reported that the cumulative killing activity of CTLs over a prolonged time is mediated by perforin and granzymes, rather than the Fas/FasL pathway (24). Given the expression of high levels of granzymes within vesicles resembling lytic granules, we tested their contribution to the cytotoxic activity of ova-Tr1 cells. The serine protease inhibitor 3.4DCI, known to block the activity of granzymes, totally inhibited ova-Tr1-cell-mediated lysis of U937 cells (Fig. 5D), thereby identifying granzymes as major effectors of the cytotoxic activity of these cells. Unlike classical cytotoxic lymphocytes, ova-Tr1 cells express very low levels of perforin, which is required to allow membrane permeabilization and delivery of granzymes in cytotoxic T cells and NK cells. We investigated whether those levels might, however, permit a slow release of granzymes in accordance with the killing kinetics of those cells. When concanamycin A was used to inhibit the maturation of perforin, it failed to affect the cytotoxic activity of ova-Tr1 cells (Fig. 5E), although it was able to reduce the lytic activity of control CTLs (Supplementary Figure S4B). This experiment indicates that perforin is not involved in the cytotoxic activity of ova-Tr1 cells. Our phenotypic characterization revealed that ova-Tr1 cells expressed high levels of granulysin, a molecule of activated cytotoxic lymphocytes that mediates killing of bacteria via membrane destabilization properties (30, 33). Since no specific inhibitor of granulysin has been described, we tested its contribution to the cytotoxic activity of ova-Tr1 by inhibiting its expression with siRNA. As assessed by flow cytometry, a substantial inhibition of granulysin expression (up to 70%) was reached 72 h after electroporation of ova-Tr1 cells with specific siRNA (Supplementary Figure S4C). Very clearly, the 24-h lytic activity of ova-Tr1 cells was reduced (>50%) upon electroporation with the siRNA targeting granulysin as compared to the control siRNA (Fig. 5F). We then plotted the level of cytotoxic activity and granulysin expression stemming from two independent experiments in which two ova-Tr1 clones were electroporated, either without siRNA or with control or granulysin siRNA (Supplementary Figure S4D). This analysis shows a positive relationship between granulysin expression in these different cells and their lytic activity, reinforcing the notion that granulysin is a key molecule to control Tr1-cell-mediated cytotoxic activity. Together, our data point to a combined action of granulysin and granzymes as the mechanism by which ova-Tr1 cells kill myeloid target cells.

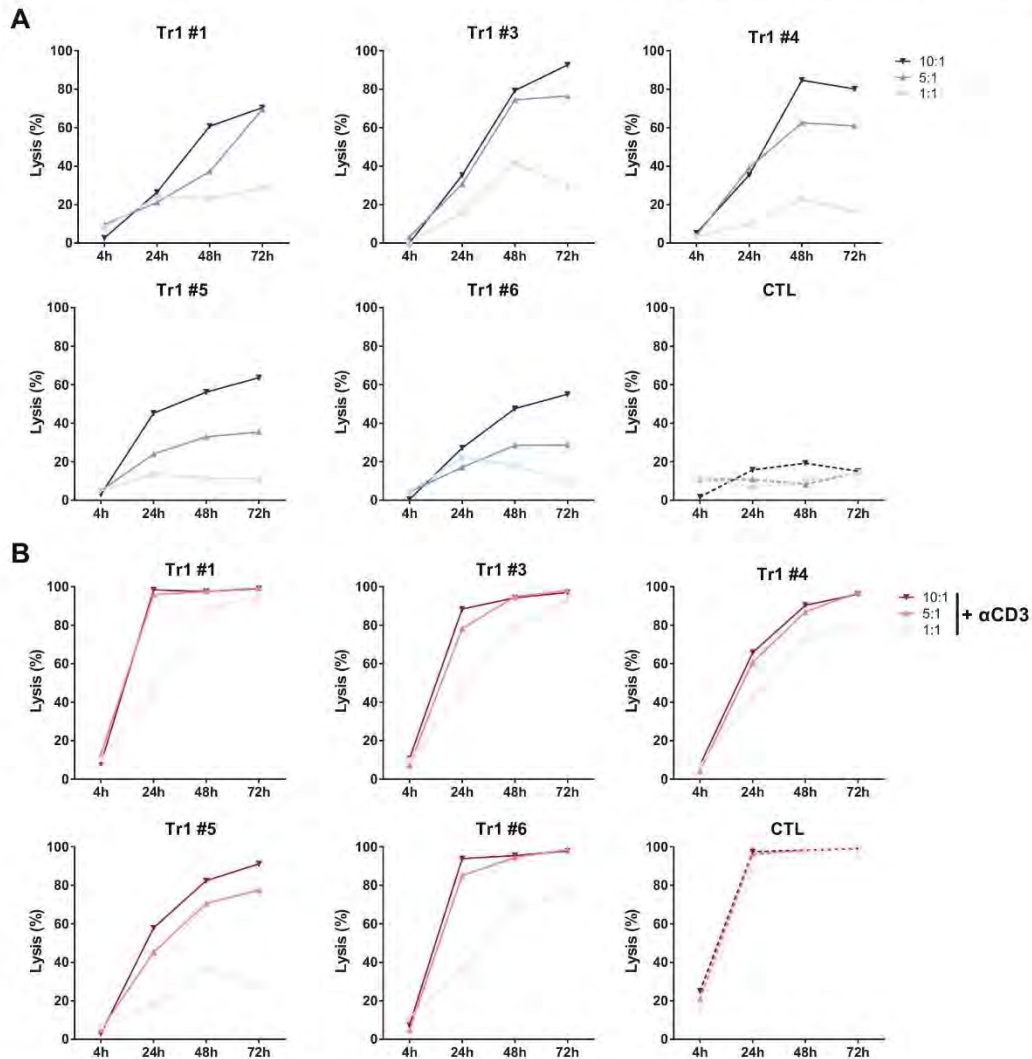


Fig. 4. Sustained lytic activity of ova-Tr1 cells over prolonged time periods. (A) U937 target cells were co-incubated with different ova-Tr1 clones and CTLs at the E:T ratios 1:1, 5:1 and 10:1. Absolute counts of residual live target cells were measured after 4, 24, 48 and 72 h of co-culture. Lysis percentage was obtained based on the number of target cells alone. (B) The same experiments as in A with $10 \mu\text{g ml}^{-1}$ anti-CD3 antibodies added during the co-culture. Representative experiment of two ($n = 5$ ova-Tr1 clones and $n = 2$ CTL clones).

Discussion

Our study aimed at exploring the biology of therapeutic ova-Tr1 cells and identified cytotoxicity toward myeloid cells as a clinically relevant activity. The retrospective analysis of the cells infused to CD patients in the phase I/IIa CATS1 clinical study (23) indicated that expression of lytic molecules, rather than markers of suppression, is related to the CDAI change in individual patients. Analysis of lytic molecule

expression revealed that the ova-Tr1 cells administered to the patients expressed a wide array of lytic molecules including the granzymes A, B, H and M as well as granulysin. To our knowledge, we are the first to report the expression of granzymes H, granzyme M and granulysin in a Treg cell population (14–16, 34, 35). Importantly, our analysis shows that the cumulative expression of lytic molecules in the administered ova-Tr1 cells correlated with the reduction of the CDAI score

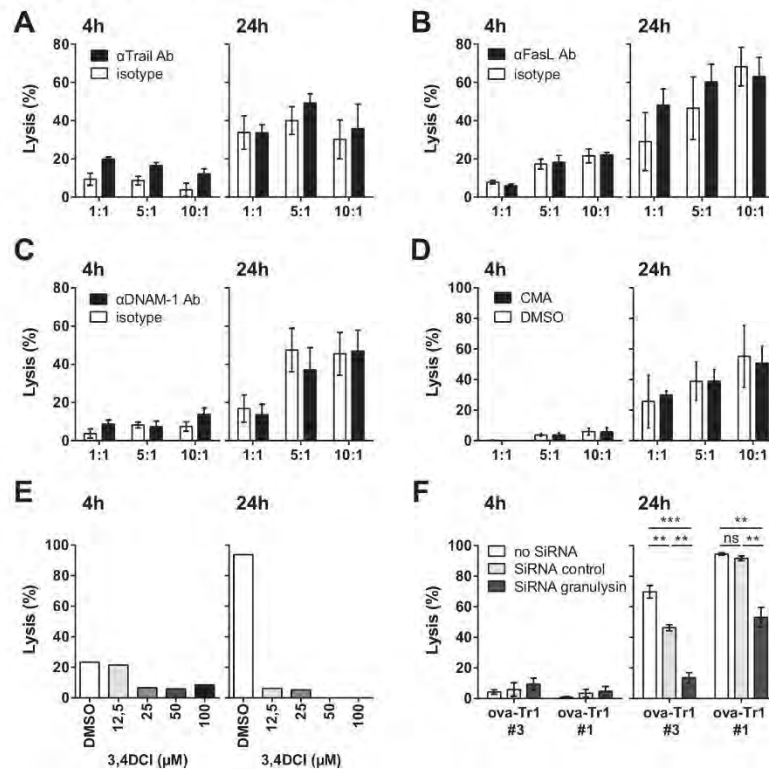


Fig. 5. Identification of the molecular pathway for ova-Tr1 cell lytic activity. (A) Cytotoxic assay in the presence of a blocking antibody against TRAIL or isotype control at the indicated E:T ratio. Mean \pm SEM, $n = 4$ ova-Tr1 clones. (B) Cytotoxic assay in the presence of a blocking antibody against FasL or isotype control. Mean \pm SEM, $n = 4$ ova-Tr1 clones. (C) Cytotoxic assay in the presence of a blocking antibody against DNAM-1 or isotype control. Mean \pm SEM, $n = 4$ ova-Tr1 clones. (D) Cytotoxic assay at a 5:1 E:T ratio in the presence of a serine proteases inhibitor (3,4 DCI) or DMSO. $N = 1$ ova-Tr1 clone. (E) Cytotoxic assay in the presence of concanamycin A or dimethyl sulfoxide (DMSO). Mean \pm SEM, $n = 4$ ova-Tr1 clones. (F) Cytotoxic assay at a 5:1 ratio using electroporated ova-Tr1 cells (no SiRNA, control SiRNA or granulysin-targeting SiRNA pools). This assay was initiated 48 h after electroporation. Mean \pm SD of a representative experiment out of two, each performed in triplicates.

measured in the treated patients. This finding justified a further exploration of the biology of ova-Tr1 cells, with a focus on their potential cytotoxic activity.

By employing a combination of flow cytometry, confocal microscopy and live cell imaging, we demonstrated that ova-Tr1 cells are genuine cytotoxic lymphocytes. Indeed, these cells were able to efficiently kill cells of the monocytic lineage in a contact-dependent manner. Ova-Tr1 cells were found to establish prolonged contacts with target cells. Upon contact, they destabilized the plasma membrane of the target cells as observed by the entry of PI. Furthermore, target cells were found to undergo apoptosis as shown by the activation of caspase-3. Similarly to other cytotoxic lymphocytes such as CTLs or NK cells, ova-Tr1 cells were loaded with a high content of LAMP-1⁺ granules containing lytic molecules. However, our in-depth characterization of the cytotoxic activity of ova-Tr1 cells revealed that in many aspects they used an alternative lytic pathway as compared with CD8⁺ CTLs. Indeed, they appeared to preferentially target cells of the

monocytic lineage, to kill over prolonged time periods independently from TCR triggering and to rely on granulysin, rather than perforin, for the lytic process. Given the described cross-talk between NK cells and monocytes (36), it is tempting to speculate that ova-Tr1 cells might resemble NK cells and utilize an NK cell receptor as a trigger for their cytotoxic activity toward myeloid cells. Our experiments indicate that the receptors NKG2D, NKp46 and NKp30 expressed at the surface of ova-Tr1 cells were not involved (data not shown). We can, however, not exclude that an additional NK cell receptor might mediate or contribute to the ova-Tr1 cell killing of myeloid cells.

Our study demonstrates a preferential lytic activity of therapeutic ova-Tr1 cells toward myeloid cells, especially monocytic cells. This information is in line with the observation that in the CATS1 clinical study, responder CD patients displayed a reduction of circulating pro-inflammatory monocytes after ova-Tr1 infusion. A comparable specificity for target cells of the myeloid lineage has been previously reported for Tr1 cells (21, 37). Such

specificity might be a property of the Tr1 cell subset since classical human Treg cells are able to lyse a broader spectrum of target cells, such as T cells, B cells, monocytes and DCs (16).

The lytic capacity of Tr1 cells was previously described to occur via a mechanism based on the lytic molecules perforin and granzyme B and a requirement of DNAM-1 and CD2 for activation, independently of TCR engagement (21). Despite a similar TCR independence, DNAM-1 did not seem to be involved in the lytic activity of the ova-Tr1 cells studied here. Interestingly, we show that although the TCR was not the trigger for the lytic activity of ova-Tr1 cells, it could potentiate it. The reactivity of the TCR might be explained by the recurrent *in vitro* stimulation applied to the ova-Tr1 cells during their generation that may lead to a tonic state. Accordingly, a high level of phosphorylated ZAP-70 was measured in the expanded ova-Tr1 cells. This feature applied both to the drug product upon thawing and following *in vitro* culture and re-stimulation. We therefore favor a model in which such tonic TCR signals might combine with signals originating from co-receptors to trigger the lytic activity of ova-Tr1 cells.

Whereas high granzyme loads are usually accompanied by perforin expression in both CD4⁺ and CD8⁺ cytotoxic T cells (38), we observed here that the ova-Tr1 lytic activity relied on granzymes but was independent of perforin. Interestingly, these cells were found to express high levels of granulysin, a protein shown to facilitate granzyme diffusion and to exert additional cytotoxic activities (30, 39). The antibody used in our study does not distinguish the two reported granulysin isoforms. However, the fact that the granulysin staining colocalized with LAMP-1 by confocal microscopy (Fig. 1D) suggests that the 9 kDa cytolytic isoform of granulysin was detected. Indeed, it has been reported that the 9 kDa and not the 15 kDa isoform colocalizes with LAMP-1 in NK cells (40). Using siRNA, we provide clear evidence that granulysin is mediating the killing of myeloid cells by the ova-Tr1 cells. To our knowledge, we are the first to report on the activity of granulysin in a Treg cell subset. Interestingly, our data suggest that granulysin might operate as a "spare wheel" for perforin to deliver granzymes within target myeloid cells. Indeed, granulysin is able to perturb membranes and was shown in particular to allow granzyme delivery into intracellular pathogens (30, 33). Alternatively, granulysin might activate target cell apoptosis directly, as shown previously for CTLs and NK cells (39). However, the observation that serine protease inhibition in ova-Tr1 cells led to full inhibition of their lytic activity indicates that granulysin did not promote killing independently from the granzyme molecules.

Ova-Tr1 cells displayed a sustained lytic activity over very prolonged time periods relying on a gradual onset of their cytotoxicity. Indeed, ova-Tr1 cells appeared to kill slowly with an increased delay between contact and lethal hit delivery as compared to CTLs. In addition, ova-Tr1 cells did not all engage at once in killing target cells; at least over the 2-h observation period. Such features are expected to contribute to the sustainment of the lytic activity measured over 3 days of interaction with target cells. The sustained lytic activity of ova-Tr1 cells might be the reflection of an alternative lytic pathway involving granulysin instead of perforin. It is also possible that the latter activity is intrinsic to CD4⁺ cytotoxic T cells, since those cells have been shown to exhibit a delayed

onset of their lytic activity compared to CD8⁺ cytotoxic T cells (41). The cytotoxic activity of ova-Tr1 cells characterized here might limit exhaustion or activation-induced cell death. This type of activity would be an advantage to sustain activity in the context of a chronic disease.

In summary, we here provide evidence that ova-Tr1 cells, used in refractory CD adoptive cell therapy, eliminate pro-inflammatory myeloid cells as a major mechanism of action. Ova-Tr1 cells mediate the killing of myeloid cells via an alternative lytic pathway, which does not require TCR re-stimulation nor perforin. Ova-Tr1 cells are unique cytotoxic lymphocytes in that they use a combination of granulysin and granzymes to mediate a sustained lytic activity. Moreover, in the context of CD, in which inflammatory myeloid cells contribute to the pathogenesis (42–44), a cytotoxic activity toward these cells is relevant for therapy. Finally, our precise characterization of the cytotoxic activity of ova-Tr1 toward myeloid targets unveils their mechanism of action and provides relevant assays to monitor their activity in the context of clinical trials.

Funding

This work was funded by the Cifre convention (2014/0916) between the Association Nationale de la Recherche et de la Technologie (ANRT), France. The ANRT funder had no role in study design, data collection and analysis, decision to publish or preparation of the manuscript.

Acknowledgements

We wish to thank the entire Cell Processing Team at TxCell and in particular Nadia Lounnas-Mourey, Fatima Benali and Justine Desnouveau for providing the ova-Tr1 cells for this study. We thank Nabila Jabrane-Ferrat for providing target cell lines. We also wish to thank Fatima-Ezzahra L'Faqihi-Olive, Valérie Duplan-Eche, Anne-Laure Iscache and Paul Menut from the CPTP cytometry platform, as well as Sophie Allart, Raïssa Houmadi, Astrid Canivet and Danièle Daviaud from the CPTP microscopy platform. We are grateful to Hans Yssel, Salvatore Valitutti, Sabina Müller, Pauline Gonnord, Liza Filali, Javier Rey-Barroso, Marie-Pierre Puissegur, Arnaud Foussat, Nathalie Clerget and Hélène Asnagli for support, technical advice and discussion. D.G. performed the experiments, analyzed the results and wrote the paper; J.G.-D. performed the phenotypic characterization of ova-Tr1, designed the research and supervised the experiments; L.P. performed the suppression experiments; Y.G. performed the MHC-II blockade experiments; N.B. participated in the CATS1 study, designed the research and supervised the experiments; L.D. designed the research, supervised the experiment analysis and wrote the paper.

Conflicts of interest statement: The authors disclose the following: D.G., J.G.-D. and N.B. are or were employed by TxCell. L.D., L.P. and Y.G. disclose no conflicts of interest.

References

- Perica, K., Varela, J. C., Oelke, M. and Schneck, J. 2015. Adoptive T cell immunotherapy for cancer. *Rambam Maimonides Med. J.* 6:e0004.
- Gregori, S., Passerini, L. and Roncarolo, M. G. 2015. Clinical outlook for type-1 and FOXP3(+) T regulatory cell-based therapy. *Front. Immunol.* 6:593.
- June, C. H. 2007. Adoptive T cell therapy for cancer in the clinic. *J. Clin. Invest.* 117:1466.
- Dudley, M. E., Wunderlich, J. R., Yang, J. C. *et al.* 2002. A phase I study of nonmyeloablative chemotherapy and adoptive transfer of autologous tumor antigen-specific T lymphocytes in patients with metastatic melanoma. *J. Immunother.* 25:243.

- 5 Rosenberg, S. A., Yang, J. C., Sherry, R. M. *et al.* 2011. Durable complete responses in heavily pretreated patients with metastatic melanoma using T-cell transfer immunotherapy. *Clin. Cancer Res.* 17:4550.
- 6 Mulé, J. J., Shu, S., Schwarz, S. L. and Rosenberg, S. A. 1984. Adoptive immunotherapy of established pulmonary metastases with LAK cells and recombinant interleukin-2. *Science* 225:1487.
- 7 Trzonkowski, P., Bieniaszewska, M., Juścińska, J. *et al.* 2009. First-in-man clinical results of the treatment of patients with graft versus host disease with human *ex vivo* expanded CD4⁺CD25⁺CD127⁻ T regulatory cells. *Clin. Immunol.* 133:22.
- 8 Marek-Trzonkowska, N., Mysliwiec, M., Dobyszuk, A. *et al.* 2012. Regulatory T cells preserves B-cell function in type 1 diabetes in children. *Diabetes Care* 35:1817.
- 9 Sakaguchi, S., Sakaguchi, N., Asano, M., Itoh, M. and Toda, M. 1995. Immunologic self-tolerance maintained by activated T cells expressing IL-2 receptor alpha-chains (CD25). Breakdown of a single mechanism of self-tolerance causes various autoimmune diseases. *J. Immunol.* 155:1151.
- 10 Nakamura, K., Kitani, A., Fuss, I. *et al.* 2004. TGF-beta 1 plays an important role in the mechanism of CD4⁺CD25⁺ regulatory T cell activity in both humans and mice. *J. Immunol.* 172:834.
- 11 Nakamura, K., Kitani, A. and Strober, W. 2001. Cell contact-dependent immunosuppression by CD4⁺CD25⁺ regulatory T cells is mediated by cell surface-bound transforming growth factor beta. *J. Exp. Med.* 194:629.
- 12 Deaglio, S., Dwyer, K. M., Gao, W. *et al.* 2007. Adenosine generation catalyzed by CD39 and CD73 expressed on regulatory T cells mediates immune suppression. *J. Exp. Med.* 204:1257.
- 13 Oderup, C., Cederbom, L., Makowska, A., Cilio, C. M. and Ivars, F. 2006. Cytotoxic T lymphocyte antigen-4-dependent down-modulation of costimulatory molecules on dendritic cells in CD4⁺CD25⁺ regulatory T-cell-mediated suppression. *Immunology* 118:240.
- 14 Gondek, D. C., Lu, L. F., Quezada, S. A., Sakaguchi, S. and Noelle, R. J. 2005. Cutting edge: contact-mediated suppression by CD4⁺CD25⁺ regulatory cells involves a granzyme B-dependent, perforin-independent mechanism. *J. Immunol.* 174:1783.
- 15 Grossman, W. J., Verbsky, J. W., Tollefsen, B. L., Kemper, C., Atkinson, J. P. and Ley, T. J. 2004. Differential expression of granzymes A and B in human cytotoxic lymphocyte subsets and T regulatory cells. *Blood* 104:2840.
- 16 Grossman, W. J., Verbsky, J. W., Barchet, W., Colonna, M., Atkinson, J. P. and Ley, T. J. 2004. Human T regulatory cells can use the perforin pathway to cause autologous target cell death. *Immunity* 21:589.
- 17 Cao, X., Cai, S. F., Fehniger, T. A. *et al.* 2007. Granzyme B and perforin are important for regulatory T cell-mediated suppression of tumor clearance. *Immunity* 27:635.
- 18 Gregori, S., Goudy, K. S. and Roncarolo, M. G. 2012. The cellular and molecular mechanisms of immuno-suppression by human type 1 regulatory T cells. *Front. Immunol.* 3:30.
- 19 Groux, H., Garra, A. O., Bigler, M., Rouleau, M., Antonenko, S., De Vries, J. E. and Roncarolo, M. G. 1998. A CD4⁺ T-cell subset inhibits antigen-specific T-cell responses and prevents colitis. *Transfus. Med. Rev.* 12:230.
- 20 Foussat, A., Cottrez, F., Brun, V., Fournier, N., Breitmayer, J. P. and Groux, H. 2003. A comparative study between T regulatory type 1 and CD4⁺CD25⁺ T cells in the control of inflammation. *J. Immunol.* 171:5018.
- 21 Magnani, C. F., Alberigo, G., Bacchetta, R. *et al.* 2011. Killing of myeloid APCs via HLA class I, CD2 and CD226 defines a novel mechanism of suppression by human Tr1 cells. *Eur. J. Immunol.* 41:1652.
- 22 Brun, V., Bastian, H., Neveu, V. and Foussat, A. 2009. Clinical grade production of IL-10 producing regulatory Tr1 lymphocytes for cell therapy of chronic inflammatory diseases. *Int. Immunopharmacol.* 9:609.
- 23 Desreumaux, P., Foussat, A., Allez, M. *et al.* 2012. Safety and efficacy of antigen-specific regulatory T-cell therapy for patients with refractory Crohn's disease. *Gastroenterology* 143:1207.
- 24 Vasconcelos, Z., Müller, S., Guipouy, D. *et al.* 2015. Individual human cytotoxic T lymphocytes exhibit intracloacal heterogeneity during sustained killing. *Cell Rep.* 11:1474.
- 25 Fernández, L., Valentin, J., Zalacain, M., Leung, W., Patiño-García, A. and Pérez-Martínez, A. 2015. Activated and expanded natural killer cells target osteosarcoma tumor initiating cells in an NKG2D-NKG2DL dependent manner. *Cancer Lett.* 368:54.
- 26 Stel, A. J., Ten Cate, B., Jacobs, S. *et al.* 2007. Fas receptor clustering and involvement of the death receptor pathway in rituximab-mediated apoptosis with concomitant sensitization of lymphoma B cells to fas-induced apoptosis. *J. Immunol.* 178:2287.
- 27 Sato, K., Nakaoka, T., Yamashita, N. *et al.* 2005. TRAIL-transduced dendritic cells protect mice from acute graft-versus-host disease and leukemia relapse. *J. Immunol.* 174:4025.
- 28 Bacchetta, R., Sartirana, C., Levings, M. K., Bordignon, C., Narula, S. and Roncarolo, M. G. 2002. Growth and expansion of human T regulatory type 1 cells are independent from TCR activation but require exogenous cytokines. *Eur. J. Immunol.* 32:2237.
- 29 Mascanfroni, I. D., Takenaka, M. C., Yeste, A. *et al.* 2015. Metabolic control of type 1 regulatory T cell differentiation by AHR and HIF1- α . *Nat. Med.* 21:638.
- 30 Walch, M., Dotiwala, F., Mulik, S. *et al.* 2014. Cytotoxic cells kill intracellular bacteria through granulysin-mediated delivery of granzymes. *Cell* 157:1309.
- 31 Scallan, B., McCarthy, S., Radewonuk, J. *et al.* 2007. Quantitative *in vivo* comparisons of the Fc gamma receptor-dependent agonist activities of different fucosylation variants of an immunoglobulin G antibody. *Int. Immunopharmacol.* 7:761.
- 32 Lopez, J. A., Jenkins, M. R., Rudd-Schmidt, J. A. *et al.* 2013. Rapid and unidirectional perforin pore delivery at the cytotoxic immune synapse. *J. Immunol.* 191:2328.
- 33 Chun, F. Z., Ling, L. M., Jones, G. J., Gill, M. J., Krensky, A. M., Kubes, P. and Mody, C. H. 2007. Cytotoxic CD4⁺ T cells use granulysin to kill *Cryptococcus neoformans*, and activation of this pathway is defective in HIV patients. *Blood* 109:2049.
- 34 Velaga, S., Ukena, S. N., Dringenberg, U. *et al.* 2015. Granzyme a is required for regulatory T-cell mediated prevention of gastrointestinal graft-versus-host disease. *PLoS One* 10:e0124927.
- 35 Loebbermann, J., Thornton, H., Durant, L. *et al.* 2012. Regulatory T cells expressing granzyme B play a critical role in controlling lung inflammation during acute viral infection. *Mucosal Immunol.* 5:161.
- 36 Michel, T., Hentges, F. and Zimmer, J. 2012. Consequences of the crosstalk between monocytes/macrophages and natural killer cells. *Front. Immunol.* 3:403.
- 37 Locafaro, G., Andolfi, G., Russo, F. *et al.* 2017. IL-10-engineered human CD4⁺ Tr1 cells eliminate myeloid leukemia in an HLA class I-dependent mechanism. *Mol. Ther.* 25:2254.
- 38 Takeuchi, A. and Saito, T. 2017. CD4 CTL, a cytotoxic subset of CD4⁺ T cells, their differentiation and function. *Front. Immunol.* 8:1.
- 39 Saini, R. V., Wilson, C., Finn, M. W., Wang, T., Krensky, A. M. and Clayberger, C. 2011. Granulysin delivered by cytotoxic cells damages endoplasmic reticulum and activates caspase-7 in target cells. *J. Immunol.* 186:3497.
- 40 Clayberger, C., Finn, M. W., Wang, T. *et al.* 2012. 15 kDa granulysin causes differentiation of monocytes to dendritic cells but lacks cytotoxic activity. *J. Immunol.* 188:6119.
- 41 Hildemann, S. K., Eberlein, J., Davenport, B., Nguyen, T. T., Victorino, F. and Homann, D. 2013. High efficiency of antiviral CD4⁺ killer T cells. *PLoS One* 8:e60420.
- 42 Linton, L., Karlsson, M., Grundström, J. *et al.* 2012. HLA-DR(hi) and CCR9 define a pro-inflammatory monocyte subset in IBD. *Clin. Transl. Gastroenterol.* 3:e29.
- 43 Griseri, T., McKenzie, B. S., Schiering, C. and Powrie, F. 2012. Dysregulated hematopoietic stem and progenitor cell activity promotes interleukin-23-driven chronic intestinal inflammation. *Immunity* 37:1116.
- 44 Siddiqui, K. R., Laffont, S. and Powrie, F. 2010. E-cadherin marks a subset of inflammatory dendritic cells that promote T cell-mediated colitis. *Immunity* 32:557.

Figure S1

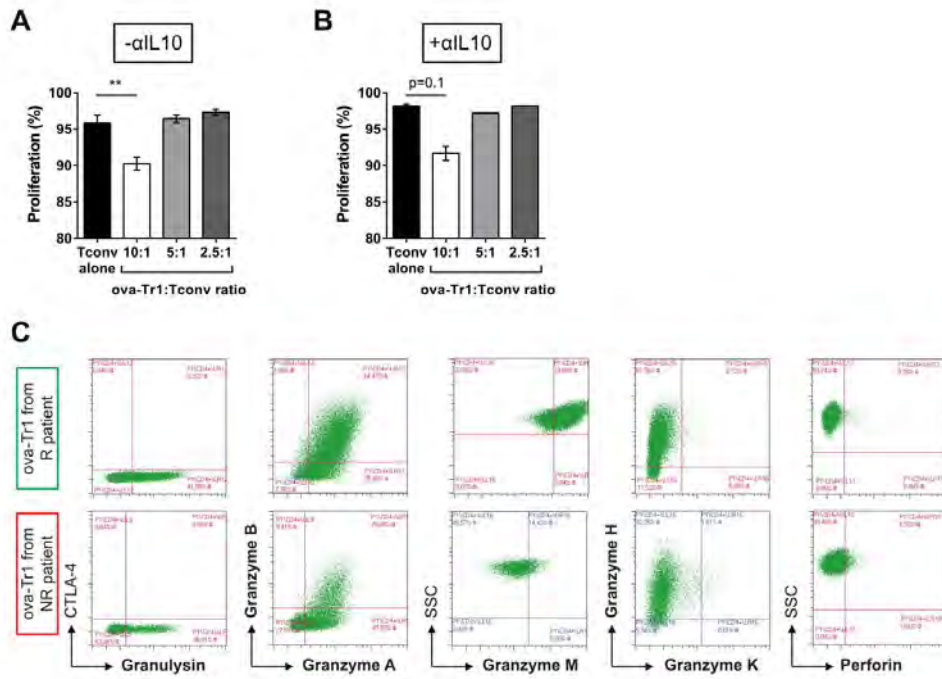


Figure S2

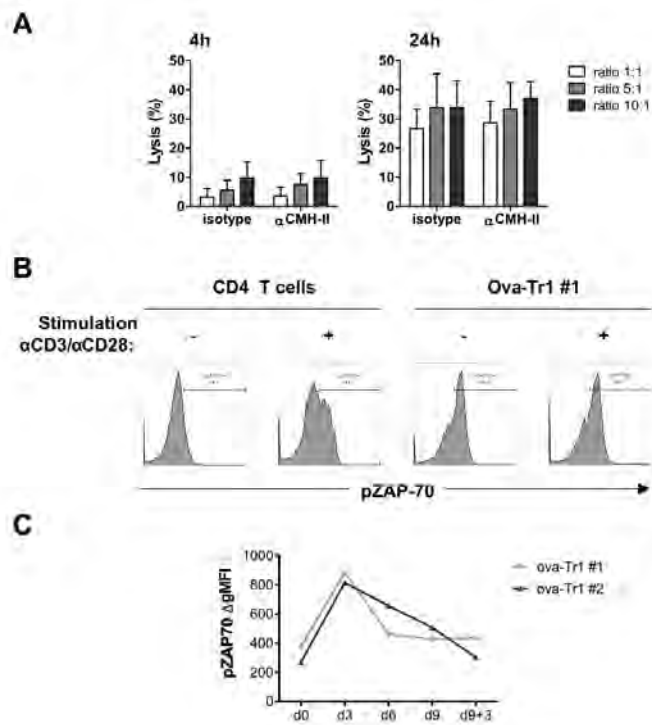


Figure S3

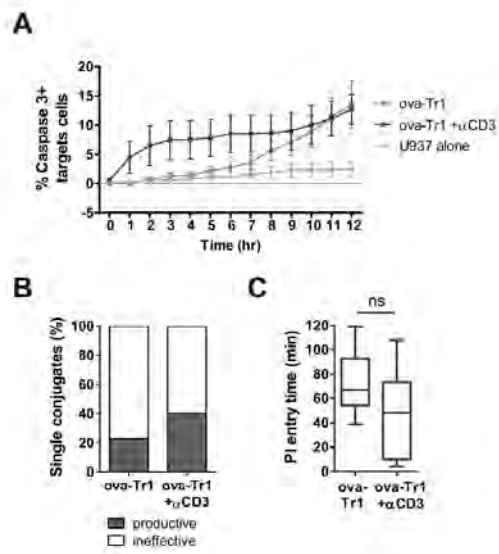
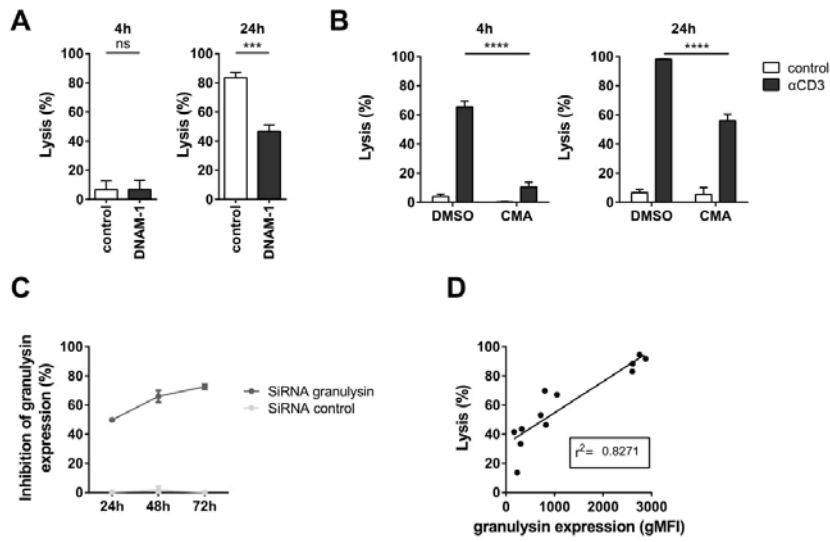


Figure S4



High content cell imaging reveals actin cytoskeleton-mediated control of the immunological synapse

Cytotoxic lymphocytes rely on actin cytoskeleton remodeling to achieve their function. In particular cytotoxic T lymphocytes and NK cells assemble the immunological synapse (IS), a complex actin-rich structure that allows the interaction with target cells, such as infected cells or tumor cells, and permits the polarized delivery of lytic granules. Although actin cytoskeleton remodeling is known to be a driving force of IS assembly and dynamics, our understanding of the molecular control of actin remodeling sustaining IS dynamics remains fragmented. This PhD project consisted in developing a high-content imaging approach to unbiasedly define the metrics of IS from human T and NK lymphocytes and to characterize the requirements for actin cytoskeleton integrity in organizing the IS architecture.

For that purpose, the stimulation and staining of cell lines and primary cells in multiwell plates and acquisition of a unique set of >100.000 confocal images with a fully automatized high-content imager was optimized. The images were analyzed with two complementary CellProfiler analytical pipelines to characterize the morphological features associated with different treatments and disease status. We first extracted 16 morphological features pertaining to F-actin, LFA-1 or lytic molecules based on prior knowledge of IS assembly, and included features pertaining to the nucleus. We show that IS assembly in Jurkat and NK-92 cells is characterized by increased F-actin intensity and cell area. For Jurkat cells, we report an increase in LFA-1 intensity and surface area, and for NK-92 cells an increase in lytic granule detection at the IS plane. We then treated NK-92 cells with seven drugs known to affect different aspects of actin dynamics and investigated the associated effects on IS features. We report concentration dependent effects, not only on F-actin intensity, as expected, but also on lytic granule polarization. Furthermore, using a high-resolution morphological profiling based on >300 features, we show that each drug inflicts distinct alterations of IS morphology. In a next step, we applied our experimental pipeline to primary NK cells isolated from the blood of healthy donors. Distinct morphological features were characterized among the NK cells from different donors, highlighting the sensitivity of our approach, but also revealing an unsuspected variability of immune cell morphologies among donors. We then further applied our approach to primary CD8⁺ T cells from patients with a rare immunodeficiency due to mutations in the gene encoding the actin regulator ARPC1B. ARPC1B deficiency results in decreased F-actin intensity, as well as in lytic granule polarization. This prompted us to assess the ability of these cells to kill target cells, which was markedly reduced. These results illustrate how the systematic analysis of the IS might be used to assist the exploration of functional defects of lymphocyte populations in pathological settings.

In conclusion, our study reveals that although assembly of the IS can be characterized by a few features such as F-actin intensity and cell spreading, capturing fine alterations of that complex structure that arise from cytoskeleton dysregulation requires a high-content analysis. The pipeline we developed through this project holds promises for the morphological profiling of lymphocytes from primary immunodeficiency patients whose genetic defect has not yet been identified. Moreover, the discriminative power of our high-content approach could be exploited to characterize the response of lymphocytes to various stimuli and to monitor lymphocyte activation in multiple immune-related pathologies and treatment settings.

L'imagerie cellulaire à haut débit révèle le contrôle de la synapse immunologique par le cytosquelette d'actine

Les lymphocytes cytotoxiques dépendent du remodelage du cytosquelette d'actine pour atteindre leur fonction. En particulier, les lymphocytes T cytotoxiques et les cellules NK assemblent la synapse immunologique (SI), structure complexe riche en actine qui permet l'interaction avec des cellules cibles et la distribution polarisée de granules lytiques (GL). Bien que le remodelage du cytosquelette d'actine soit connu pour être une force motrice de l'assemblage et de la dynamique de la SI, la compréhension du contrôle moléculaire du remodelage de l'actine soutenant la dynamique de la SI reste fragmentée. Ce projet de thèse a consisté à développer une approche d'imagerie à haut débit pour définir de manière impartiale les métriques de la SI des lymphocytes T et NK et caractériser les exigences d'intégrité du cytosquelette d'actine dans l'organisation de l'architecture de la SI.

À cette fin, la stimulation et coloration des lignées cellulaires et cellules primaires dans des plaques à puits multiples et l'acquisition d'un ensemble unique d'images confocales avec un imageur à haut contenu entièrement automatisé ont été optimisées. Les images ont été analysées avec deux pipelines complémentaires avec CellProfiler pour définir les caractéristiques morphologiques associées aux différents traitements et à l'état de la maladie. Nous avons d'abord extrait 16 caractéristiques morphologiques se rapportant à la F-actine, LFA-1 ou aux GL, sur la base d'une connaissance préalable de l'assemblage de la SI, et inclus des caractéristiques relatives au noyau. Nous montrons que l'assemblage de la SI dans les lignées est caractérisé par une augmentation de l'intensité de la F-actine et la surface cellulaire. Pour les cellules Jurkat, nous rapportons une augmentation de l'intensité et de la surface LFA-1, et de la de la détection des LG sur le plan SI pour les cellules NK-92. Le traitement des cellules NK-92 avec 7 drogues affectant différents aspects de la dynamique de l'actine et l'étude des effets associés sur les caractéristiques de la SI montrent des effets dépendants de la concentration sur l'intensité de l'actine et sur la polarisation des GL. De plus, un profilage morphologique à haute résolution basé sur > 300 caractéristiques montre que chaque drogue inflige des altérations distinctes sur la morphologie de la SI. Nous avons appliqué ce pipeline à des cellules NK primaires isolées du sang de donneurs sains. Des caractéristiques morphologiques distinctes définissent les cellules NK de différents donneurs, soulignant la sensibilité de notre approche, mais révélant également une variabilité insoupçonnée des morphologies des cellules immunitaires parmi les donneurs. Nous avons appliqué notre approche aux cellules T CD8⁺ primaires de patients présentant une immunodéficience rare due à des mutations dans le gène codant pour le régulateur d'actine ARPC1B. La carence en ARPC1B entraîne une diminution de l'intensité de l'actine et de la polarisation des GL. Cela nous a incités à évaluer la capacité lytique de ces cellules, qui a été considérablement réduite. Ces résultats illustrent comment l'analyse systématique de la SI pourrait être utilisée pour aider à l'exploration des défauts fonctionnels des populations de lymphocytes dans des contextes pathologiques.

En conclusion, notre étude révèle que, bien que l'assemblage de la SI puisse être caractérisé par quelques caractéristiques telles que l'intensité de l'actine et la propagation cellulaire, la capture de fines altérations résultant de la dérégulation du cytosquelette nécessite une analyse à haut débit. Le pipeline développé est prometteur pour le profilage morphologique des lymphocytes de patients atteints d'immunodéficiences primaires dont le défaut génétique n'a pas encore été identifié. De plus, le pouvoir discriminant de notre approche pourrait être exploité pour caractériser la réponse des lymphocytes à divers stimuli et surveiller leur activation dans de multiples pathologies et traitements.